



**HAL**  
open science

# MR microscopy of neuronal tissue: acquisition acceleration, modelling and experimental validation of water diffusion

van Khieu Nguyen

► **To cite this version:**

van Khieu Nguyen. MR microscopy of neuronal tissue: acquisition acceleration, modelling and experimental validation of water diffusion. Medical Physics [physics.med-ph]. Université Paris Saclay (COmUE), 2017. English. NNT: 2017SACLS086 . tel-01735295

**HAL Id: tel-01735295**

**<https://theses.hal.science/tel-01735295>**

Submitted on 15 Mar 2018

**HAL** is a multi-disciplinary open access archive for the deposit and dissemination of scientific research documents, whether they are published or not. The documents may come from teaching and research institutions in France or abroad, or from public or private research centers.

L'archive ouverte pluridisciplinaire **HAL**, est destinée au dépôt et à la diffusion de documents scientifiques de niveau recherche, publiés ou non, émanant des établissements d'enseignement et de recherche français ou étrangers, des laboratoires publics ou privés.

NTT: 2017SACLS086

THÈSE DE DOCTORAT  
DE  
L'UNIVERSITÉ PARIS-SACLAY  
PRÉPARÉE À  
L'UNIVERSITÉ PARIS-SUD

LABORATOIRE: I<sup>2</sup>BM/DSV/Neurospin - CEA Saclay

ÉCOLE DOCTORALE N°: 575

Electrical, Optical, Bio - physics and Engineering

Spécialité de doctorat: imagerie et physique médicale

Par

Van Khieu NGUYEN

MR MICROSCOPY OF NEURONAL TISSUE:  
acquisition acceleration, modeling and experimental  
validation of water diffusion

Thèse présentée et soutenue à NeuroSpin-CEA Saclay, le: 10/04/2017

**Composition du jury:**

M. Samuel C. GRANT	Professeur agrégée (Florida State University)	Rapporteur, Président
M. Clair POIGNARD	Chargé de recherche (Université de Bordeaux)	Rapporteur
M. Jean-Christophe GINEFRI	Chargé de recherche (Université de Paris-Sud)	Examinateur
M. Demian WASSERMANN	Chargé de recherche (INRIA Sophia Antipolis)	Examinateur
Mme. Luisa CIOBANU	Ingénieur E5 (Neurospin, CEA-Saclay)	Directeur de thèse
Mme. Jing-Rebecca LI	Chargé de recherche (INRIA Saclay)	Co-directeur de thèse



This thesis is submitted in partial fulfillment of the requirements for the degree of Doctor of Philosophy by Université Paris-Saclay.

© Copyright by Van Khieu NGUYEN, 2017  
All Rights Reserved



---

# MICROSCOPIE DU TISSU NEURONAL PAR IRM: ACCÉLÉRATION DES ACQUISITIONS, MODÉLISATION ET VALIDATION EXPÉRIMENTALE DE LA DIFFUSION DE L'EAU

## Résumé

La technique d'acquisition comprimée ou compressed sensing (CS) exploite la compressibilité de différents types d'images pour reconstruire des données sous-échantillonnées sans perte d'informations. Cette technique peut être appliquée à l'IRM pour réduire les temps d'acquisition. CS est basée sur trois composantes majeures : (1) la représentation parcimonieuse du signal dans un domaine de transformation, (2) des mesures incohérentes et (3) une méthode de reconstruction non-linéaire avec une contrainte de parcimonie. Si le nombre total de points dans une image est plus grand que quatre fois le nombre de coefficients de décomposition alors la reconstruction de données sous-échantillonnées est réalisable. Dans la partie IV de cette thèse, nous proposons un nouveau modèle de sous-échantillonnage basé sur la théorie de l'agrégation limitée par la diffusion (DLA) et montrons qu'il est plus performant que la méthode de sous-échantillonnage aléatoire. Le modèle de sous-échantillonnage DLA a été utilisé pour implémenter la technique de CS pour l'imagerie haute résolution pondérée T2 et T1 sur un champ magnétique très intense (17.2T). Pour chacune des pondérations, le temps d'acquisition a été réduit de 50 % tout en conservant la qualité des images en termes de résolution spatiale, rapport contraste sur bruit et quantification de l'intensité du signal. Les deux nouvelles séquences d'impulsions CS (csRARE et csFLASH) ont été implémentées sur le logiciel commercial ParaVision 5.1. La partie V de la thèse est centrée sur l'étude de la dépendance en temps de la diffusivité dans le ganglion abdominal de l'*Aplysia californica*. Le ganglion abdominal de l'aplysie a été choisi pour cette étude d'imagerie car l'IRM à haute résolution permet la description anatomique fine du réseau cellulaire (taille des neurones individuels et orientation des axones). Utiliser les tissus neuronaux de l'aplysie pour étudier la relation entre la structure cellulaire et le signal d'IRM de diffusion peut permettre de comprendre cette relation pour des organismes plus complexes. Le signal d'IRM de diffusion (IRMd) a été mesuré à différents temps de diffusion dans le ganglion abdominal et des simulations de la diffusion de l'eau dans des géométries obtenues à partir de la segmentation d'images haute résolution pondérées T2 et l'incorporation d'informations sur la structure cellulaire trouvées dans la littérature ont été réalisées. Pour comparer le signal d'IRMd dans des neurones composés d'une seule cellule avec le signal des simulations numériques, des cellules de grande taille ont été segmentées à partir d'images anatomiques pondérées T2. A l'intérieur des cellules, un noyau à forme irrégulière a été généré manuellement (environ 25-30% en fraction volumique). Les petites cellules ont été modélisées comme des petites sphères avec un petit noyau sphérique concentrique (environ 25% en fraction volumique). Le nerf a été modélisé en combinant des axones (cylindres) de différents diamètres en cohérence avec la littérature. Le signal numérique d'IRMd a été simulé en résolvant l'équation de Bloch-Torrey pour les domaines géométriques décrits ci-dessus. En fittant le signal expérimental avec le signal simulé pour différents types de cellules comme les grandes cellules neuronales (diamètre entre 150 et 420  $\mu\text{m}$ ), des agrégats de petites cellules neuronales ayant la forme d'un sac (jusqu'à 400 cellule chez l'aplysie adulte dans chaque sac avec une taille cellulaire entre 40 et 100  $\mu\text{m}$  de diamètre), des nerfs (groupes d'axones de forme cylindrique avec un diamètre de moins de 1 à 25  $\mu\text{m}$ ) pour une grande gamme de temps de diffusion, nous avons obtenu des estimations du coefficient de diffusion intrinsèque dans le noyau et le cytoplasme (pour les neurones) et le coefficient de diffusion intrinsèque dans les axones (pour les nerfs). Nous avons aussi évalué la pertinence d'utiliser une formule préexistante décrivant la dépendance en temps du coefficient de diffusion pour estimer la taille des cellules.

**Mots-clefs** : imagerie par résonance magnétique (IRM) , échantillonnage compressif, microscopie par résonance magnétique (MRM), segmentation cellulaire, agrégation limitée par la

diffusion (DLA), variation totale.

---

## Abstract

Compressed sensing (CS) exploits the compressibility of different types of images to reconstruct undersampled data without loss of information. The technique can be applied to MRI to reduce the acquisition times. The CS is based on three major components: (1) sparsity representation of the signal in some transform domain, (2) incoherent measurements, and (3) sparsity-constrained nonlinear reconstruction method. If the total number of points in the image is larger than four times the number of sparse coefficients then the reconstruction of undersampled data is feasible. In the part IV of this thesis, we propose a new undersampling model based on the diffusion limited aggregation (DLA) theory and show that it performs better than the random variable undersampling method. The DLA undersampling model was used to implement the CS for T2-weighted and T1-weighted high resolution imaging at the ultra-high magnetic field (17.2T). In both cases, the acquisition time was reduced by 50% while maintaining the quality of the images in terms of spatial resolution, contrast to noise ratio, and signal intensity quantification. Both new CS pulse sequences (csRARE and csFLASH) were implemented in ParaVision 5.1 commercial software.

In the part V of the thesis is focused on the study of the time-dependent diffusivity in the abdominal ganglion of *Aplysia californica*. The *Aplysia* abdominal ganglion was chosen in this imaging study because high resolution MR imaging allows the fine anatomical description of the cellular network (size of individual neurons and orientation of axons). Using the *Aplysia* ganglia to study the relationship between the cellular structure and the diffusion MRI signal can shed light on this relationship for more complex organisms. We measured the dMRI signal at several diffusion times in the abdominal ganglion and performed simulations of water diffusion in geometries obtained after segmenting high resolution T2-weighted images and incorporating known information about the cellular structure from the literature. To match the dMRI signal in the single cell neurons with numerical simulations signal, the large cell outline was segmented from the anatomical T2 weighted image. Inside this cell shape, an irregularly shaped nucleus was manually generated (around 25-30% volume fraction). The small cells were modeled as small spheres with a smaller concentric spherical nucleus (around 25% volume fraction). The nerve was modeled by combining axons (cylinders) of different diameters consistent with the literature. The numerical dMRI signal can be simulated by solving Bloch-Torrey equation under the geometries domain described above. By fitting the experimental signal to the simulated signal for several types of cells such as: large cell neurons (diameter between 150  $\mu\text{m}$  and 420  $\mu\text{m}$ ); cluster of small neuron cells gathered in the shape of a bag (up to 400 cells in adult *Aplysia* in each bag with cell size between 40  $\mu\text{m}$  to 100  $\mu\text{m}$  in diameter); and nerves (group of axons cylindrical shape diameter from less than 1  $\mu\text{m}$  to 25  $\mu\text{m}$ ) at a wide range of diffusion times, we obtained estimates of the intrinsic diffusion coefficient in the nucleus and the cytoplasm (for cell neurons) and the intrinsic diffusion coefficient in the axons (for the nerves). We also evaluated the reliability of using an existing formula for the time-dependent diffusion coefficient to estimate cell size.

**Keywords** : magnetic resonance imaging (MRI), compressed sensing (CS), magnetic resonance microscopy (MRM), cell segmentation, diffusion limited aggregation (DLA), total variation (TV) .

---

## Acknowledgments

Firstly, I would like to express my sincere gratitude to my advisors Dr. Luisa CIOBANU and Dr. Jing-Rebecca LI for their patience and motivation, for sharing their immense knowledge with me and for their continuous support during those years of Ph.D. Their guidance helped me at all times of the research work and the writing of the thesis. I could not have imagined having better advisors and mentors for my Ph.D. study.

Besides my advisors, I would like to thank the rest of my thesis committee: Dr. Clair POIGNARD and Dr. Samuel GRANT for reviewing and correcting my thesis; Dr. Jean-Christophe GINEFRI and Dr. Demian WASSERMANN for examining my thesis. I would like to acknowledge Dr. Jean-Christophe GINEFRI from Ecole doctoral EOBÉ for his guidance.

My sincere thanks also goes to Mrs. Jessica GAMEIRO (assistante d'Equipes de Recherche INRIA), Mrs. Valérie BERTHOU (Département des ressources humaines, INRIA-Saclay), and Mrs. Laurence STEPHEN (Ecole doctoral EOBÉ), who always helped me and answered my questions about the administrative, visa, and the registration procedures.

I would like to thank my labmates in the NeuroPhysics Team: Pavel SVEHLA, Dr. Gabrielle FOURNET, Dr. Tangi ROUSSEL, Dr. Tomokazu TSURUGIZAWA, Dr. Yoshifumi ABE, and Dr. Denis LE BIHAN for the stimulating discussions during the monthly team meetings. I would like to thank Gabrielle and Tangi for their help with translating the thesis abstract and thesis summary to French. I gratefully acknowledge Dr. Guillaume RADECKI for his support in the early stages of experiments of this work. I thank all the researchers in NeuroSpin, CEA-Saclay for all the fun we had in the past three years. I would like to acknowledge Boucif DJEMAI for his assistance with the husbandry of *Aplysia*. I would also like to thank my friends Dr. Van Dang NGUYEN and Dr. Tuan Hang NGUYEN for their support when I arrived in Paris.

Last but not the least, I would like to thank my parents, my brothers and my sister, my nephews, and especially my wife Khanh Nga and her parents for supporting me “spiritually” during those years of research, during the writing of this thesis and during my life in general. This accomplishment would not have been possible without them. I want to thank my wife for loving me the way I am. Thank you.

**This Ph.D. thesis is dedicated to my parents and my wife  
for their love, endless support and encouragement.**



# Contents

<b>List of Abbreviations</b>	<b>ix</b>
<b>Thesis summary (in French)</b>	<b>1</b>
<b>General introduction</b>	<b>16</b>
<b>I Important Concepts in Magnetic Resonance Imaging</b>	<b>19</b>
<b>1 NMR</b>	<b>20</b>
1.1 Bloch Equations . . . . .	21
1.2 Signal detection . . . . .	24
<b>2 MRI</b>	<b>26</b>
2.1 Gradient encoding . . . . .	27
2.2 $k$ -space . . . . .	28
2.3 Fourier transform and image reconstruction . . . . .	29
2.4 Frequency encoding . . . . .	30
2.5 2D imaging . . . . .	30
2.6 3D imaging . . . . .	32
2.7 Resolution and FOV . . . . .	33
2.8 SNR . . . . .	34
2.9 Acquisition time . . . . .	35
<b>3 MRI pulse sequences</b>	<b>36</b>
3.1 Spin Echo sequence . . . . .	36
3.2 RARE: T2-weighted images . . . . .	37
3.3 Gradient Echo sequence . . . . .	38
3.4 FLASH: T1-weighted images . . . . .	39
3.5 FISP sequence . . . . .	40
<b>II Diffusion MRI in the <i>Aplysia</i> neuronal tissue</b>	<b>41</b>
<b>4 Water diffusion in biological tissue</b>	<b>42</b>

<b>5</b>	<b>Diffusion-encoding</b>	<b>42</b>
<b>6</b>	<b>Bloch-Torrey equation model</b>	<b>43</b>
<b>7</b>	<b>The relation between the ADC and the cell size</b>	<b>44</b>
<b>8</b>	<b>Aplysia animal model</b>	<b>45</b>
<b>9</b>	<b>Fast dMRI sequences</b>	<b>48</b>
9.1	The Echo-planar imaging . . . . .	48
9.2	DP-FISP . . . . .	49
<b>III</b>	<b>Accelerated acquisition techniques</b>	<b>51</b>
<b>10</b>	<b>Acceleration by partial Fourier imaging and Parallel imaging</b>	<b>52</b>
10.1	Partial Fourier imaging . . . . .	52
10.2	Parallel imaging . . . . .	52
<b>11</b>	<b>Non-Cartesian trajectories</b>	<b>53</b>
<b>12</b>	<b>Compressed sensing</b>	<b>54</b>
12.1	Sparsity of MR images . . . . .	56
12.2	Incoherence . . . . .	58
12.3	Polynomial undersampling patterns . . . . .	58
12.4	Image reconstruction: Discrete Fourier Transform . . . . .	59
12.5	CS image reconstruction . . . . .	60
<b>13</b>	<b>Measuring the quality of accelerated acquisition</b>	<b>67</b>
13.1	Image error . . . . .	67
13.2	Pearson's Correlation Coefficient . . . . .	67
<b>IV</b>	<b>Compressed sensing for high resolution MRI</b>	<b>68</b>
<b>14</b>	<b><math>k</math>-space undersampling patterns</b>	<b>69</b>
14.1	DLA undersampling patterns . . . . .	69
14.2	DLA vs polynomial undersampling . . . . .	70

---

<b>15</b>	<b>The implementation of CS on T2w and T1w pulse sequences</b>	<b>72</b>
<b>16</b>	<b>Image reconstruction</b>	<b>73</b>
<b>17</b>	<b>Cell segmentation algorithm</b>	<b>74</b>
<b>18</b>	<b>CS in T2-weighted imaging: CS-RARE</b>	<b>76</b>
18.1	The choice of undersampling ratio for generating undersampling patterns	76
18.2	Sample preparation and data acquisition . . . . .	76
18.3	Signal to noise ratio and spatial resolution . . . . .	76
<b>19</b>	<b>CS in T1-weighted imaging: CS-FLASH</b>	<b>78</b>
19.1	Undersampling pattern generation . . . . .	80
19.2	Data acquisition . . . . .	80
19.3	Sample preparation . . . . .	81
19.4	Image analysis . . . . .	81
19.5	Results . . . . .	82
<b>20</b>	<b>Conclusion and discussion</b>	<b>85</b>
<b>V</b>	<b>Diffusion magnetic resonance imaging in the <i>Aplysia</i></b>	<b>87</b>
<b>21</b>	<b>Introduction</b>	<b>88</b>
<b>22</b>	<b>Materials and methods</b>	<b>89</b>
22.1	Sample preparation . . . . .	89
22.2	Image acquisition . . . . .	89
22.3	Image analysis . . . . .	90
22.4	Simulations . . . . .	92
<b>23</b>	<b>Results</b>	<b>97</b>
23.1	Experimental time-dependent ADC . . . . .	97
23.2	Estimating cell size using short time ADC formula . . . . .	100
23.3	Simulation of a two compartments model of large cell neurons . . . . .	103
23.4	Simulations of the ADC in bag cell neurons and nerves . . . . .	104

---

<b>24 Conclusion</b>	<b>107</b>
<b>VI Summary and future directions</b>	<b>108</b>
<b>25 Summary</b>	<b>109</b>
<b>26 Future directions</b>	<b>110</b>
26.1 Future work on DLA-CS strategy applications . . . . .	110
26.2 Future work on optimizing the CS image reconstruction and dMRI simulation codes . . . . .	110
26.3 Future work on combining dMRI experiment, simulation and histology imaging . . . . .	111
<b>List of publications</b>	<b>112</b>
<b>List of Figures</b>	<b>117</b>
<b>List of Tables</b>	<b>118</b>
<b>List of Algorithms</b>	<b>119</b>
<b>Index</b>	<b>120</b>
<b>Index</b>	<b>122</b>
<b>Bibliography</b>	<b>123</b>

## List of Abbreviations

<b>2D</b>	Two dimensional.
<b>3D</b>	Three dimensional.
<b>ADC</b>	Apparent Diffusion Coefficient.
<b>ASW</b>	Artificial Sea Water.
<b>BW</b>	Bandwidth.
<b>CS</b>	Compressed sensing.
<b>CS-FLASH</b>	Compressed sensing-FLASH sequence.
<b>CS-RARE</b>	Compressed sensing-RARE sequence.
<b>DLA</b>	Diffusion Limited Aggregation.
<b>dMRI</b>	Diffusion magnetic resonance imaging.
<b>DP-FISP</b>	Diffusion prepared-FISP.
<b>DTI</b>	Diffusion Tensor Imaging.
<b>EPI</b>	Echo Planar Imaging.
<b>FISP</b>	Fast Imaging with Steady-state free Precession.
<b>FLASH</b>	Fast Low Angle Shot.
<b>FOV</b>	Field of View.
<b>FSE</b>	Fast Spin Echo.
<b>FT</b>	Fourier transform.
<b>GRAPPA</b>	GeneRalized Autocalibrating Partially Parallel Acquisitions.
<b>GRE</b>	Gradient Echo.
<b>ID</b>	Inner diameter.
<b>MEMRI</b>	Manganese Enhanced Magnetic Resonance Imaging.
<b>MR</b>	Magnetic Resonance.
<b>MRI</b>	Magnetic Resonance Imaging.
<b>MRM</b>	Magnetic Resonance Microscopy.
<b>NMR</b>	Nuclear Magnetic Resonance.
<b>OGSE</b>	Oscillating-Gradient Spin Echo.
<b>PBS</b>	Phosphate-Buffered Saline.
<b>PCC</b>	Pearson's Correlation Coefficient.
<b>pdf</b>	probability density function.
<b>PGSE</b>	Pulsed-Gradient Spin Echo.
<b>PI</b>	Parallel Imaging.
<b>PSF</b>	Point Spread Function.

<b>RARE</b>	Rapid Acquisition with Refocused Echoes.
<b>RE</b>	Relative Errors.
<b>RF</b>	Radio frequency.
<b>RMSE</b>	Root Mean Square Error.
<b>RSE</b>	Rapid Spin Echo.
<b>SE</b>	Spin Echo.
<b>SENSE</b>	Sensitivity encoding.
<b>SMASH</b>	Simultaneous acquisition of spatial harmonics.
<b>SNR</b>	Signal-to-noise ratio.
<b>T1w</b>	T1-weighted image.
<b>T2w</b>	T2-weighted image.
<b>TE</b>	Echo time first.
<b>TPSF</b>	Transform Point Spread Function.
<b>TSE</b>	Turbo Spin Echo.
<b>TV</b>	Total variation.

# Thesis summary (in French)

## Résumé

Les objectifs de ces travaux de thèse sont (1) l'implémentation de l'acquisition compressée ou *compressed sensing* (CS) pour la réduction du temps d'acquisition d'images haute-résolution par résonance magnétique et (2) l'étude du signal d'IRM de diffusion (IRMd) et de ses dépendances avec la micro-structure du tissu observé, en utilisant particulier l'information obtenue avec l'acquisition de plusieurs temps de diffusion. Le modèle animal choisi pour ces études est l'*Aplysia californica* et plus particulièrement ses ganglions car ces derniers sont constitués de neurones de grande taille (plusieurs centaines de micromètre de diamètre) comparés aux neurones de mammifères (5 à 10 micromètre de diamètre). Ces neurones de grande taille peuvent être identifiés sur des images anatomiques en utilisant l'imagerie par résonance magnétique (IRM). Toutes les données présentées dans cette thèse ont été acquises sur l'IRM ultra-haut champ 17.2T à NeuroSpin, CEA, Saclay. Les antennes radio-fréquences utilisées pour la détection sont de type solénoïde avec un diamètre interne de 2.4 mm et leur conception a été précédemment décrit [Jelescu IO et al., *Neuroimage* 2013].

Ce projet a été financé par l'ANR (ANR-13-BSV5-0014-01, project ANImE) et par l'école doctorale EOBE, Université Paris Sud, Orsay, France.

## Partie I : Principes de l'imagerie par résonance magnétique

L'IRM est une technique d'imagerie couramment utilisée qui se base sur la résonance magnétique nucléaire (RMN). Le principe consiste à polariser l'objet à imager en employant un puissant champ magnétique présent dans le scanner IRM. L'aimantation magnétique obtenue peut alors être manipulée à l'aide d'ondes radio-fréquences et de gradients de champ magnétique pour obtenir une image. Suivant le type d'encodage et de séquence d'acquisition, l'image obtenu peut dépendre de certains paramètres physiologiques comme par exemple la perfusion ou la diffusion. Dans le domaine de l'IRM clinique, les images sont générées en détectant le signal provenant des atomes d'hydrogènes ( $^1\text{H}$ ). D'autres noyaux peuvent être détectés tels que le sodium ( $^{23}\text{Na}$ ) ou le phosphore ( $^{31}\text{P}$ ). Toutefois, le noyau d'hydrogène ( $^1\text{H}$ ), qui n'est constitué que d'un proton, est le plus étudié en IRM car il est très abondant dans les tissus biologiques (sous forme d'eau) et possède le rapport gyromagnétique (relatif à la sensibilité du noyau) le plus important. Le premier chapitre présente les principes de l'IRM tels que le *k-space*, l'encodage de l'espace par les gradients, le champ de vue ou *field-of-view* (FOV), le rapport signal-sur-bruit (RSB), l'imagerie 2D et 3D ainsi que la reconstruction d'image IRM en utilisant la transformée de Fourier. Les séquences d'acquisition RARE, FLASH et FISP utilisées lors de ces travaux de thèse et le contraste qu'elles génèrent, respectivement en T2, en T1 et en diffusion, sont expliquées.

## Partie II : IRM de diffusion dans les tissus neuronaux de l'*Aplysia*

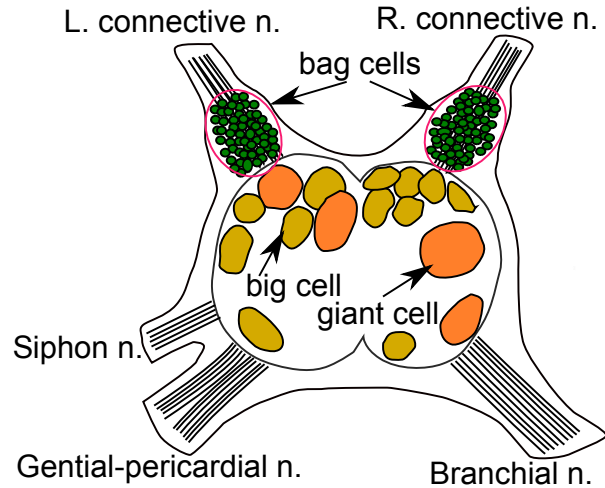
L'IRM de diffusion (IRMd) est une méthode dérivée de l'IRM. C'est une technique d'imagerie non-invasive qui permet de mesurer les caractéristiques de diffusion des molécules d'eau dans les tissus biologiques. La diffusion moléculaire est restreinte dans les tissus car les molécules d'eau rencontrent de nombreux obstacles telles que des fibres ou des membranes. La technique IRMd permet de mettre en évidence des détails dans la micro-structure du tissu en mesurant et en caractérisant la diffusion des molécules d'eau qui s'y trouvent. Toutefois, les relations entre cette micro-structure complexe du tissu et le signal IRMd sont mal connues et nécessitent des approches combinant données expérimentales, modélisations mathématiques et numériques. Le ganglion abdominal de l'*Aplysia* a été choisi pour cette étude car l'imagerie haute-résolution permet une description anatomique du réseau cellulaire (taille des neurones et orientation des axones). Les observations et résultats de cette étude sur les tissus de l'*Aplysia* pourront potentiellement s'étendre par la suite à des tissus et des organismes plus complexes.

Dans cette partie, nous présenterons les concepts majeurs de l'IRMd, les équations qui s'y rapportent et les travaux précédents. La relation entre le coefficient de diffusion apparent (ADC) et la taille des cellules et le modèle animal choisi pour ces simulations de signaux IRMd seront également présentés. En effet, l'*Aplysia* possède des cellules neuronales de grande taille qui constitue un modèle idéal des neurones présents chez les mammifères. Le système nerveux de l'*Aplysia* possède une structure simple constituée de grandes cellules de forme ronde, de cellules plus petites également rondes et disposées sous forme d'agrégats ayant la forme d'un sac et enfin de groupes d'axones non myélinisés de forme cylindrique. Cette structure sert de modèle pour l'étude du système neuronales des mammifères (soma, groupe d'axones et dendrites). Étant donné la taille importante des neurones présents chez l'*Aplysia*, il est possible de vérifier certaines hypothèses relatives aux temps de diffusion courts (en employant les séquence de type OGSE [M. D. Does et al. *MRM* 49(2) 2003]) ou PGSE [B. A. Hargreaves, *JMRI*, 36, 2012]). Le système nerveux de l'*Aplysia californica* est constitué de cinq paires de ganglions : buccale, cérébrales, pédale et abdominale [E. R. Kandel and I. Kupfermann, *Annual Review of Physiology*, 32(1), 1970]. Les ganglions abdominales et buccales ont été choisis pour l'étude IRM car leur réseau de cellules a fait l'objet de nombreuses études en particulier concernant les neurones et l'orientation des axones [P. Conn and L. Kaczmarek, *Molecular neurobiology*, 3(4), 1989]. De plus, le ganglion abdominal et des neurones individuels y appartenant ont été précédemment étudiés avec des techniques de microscopie par résonance magnétique (MRM) et de MRM de diffusion. Un schéma du ganglion abdominal de l'*Aplysia* est montré en Figure I.

L'étude IRM décrite dans ces travaux de thèse se concentre sur trois types de cellules et constituants cellulaires :

1. Les neurones de grande taille
2. Les agrégats de neurones regroupés en forme de sac
3. Les nerfs

Les données relatives à la taille des axones et la distribution des nerfs présentés dans le tableau I ne concerne que le ganglion buccal de l'*Aplysia californica* ; nous n'avons pas

FIGURE I – Le ganglion abdominal de l'*Aplysia californica*.

Nerf	I ( $> 25\mu\text{m}$ )	II ( $10 - 25\mu\text{m}$ )	III ( $1 - 10\mu\text{m}$ )	IV ( $\leq 1\mu\text{m}$ )
1b	0	$5.00 \pm 0.54$	$261 \pm 50$	$7144 \pm 1044$
2b	$2.33 \pm 0.33$	$19.41 \pm 4.04$	$235 \pm 74$	$9415 \pm 1312$
3b	0	$15.00 \pm 1.58$	$67 \pm 9.6$	$2191 \pm 755$
ON	$1.67 \pm 0.33$	$8.67 \pm 2.03$	$681 \pm 191$	$10483 \pm 691$
RN	0	$16.00 \pm 0.60$	$1579 \pm 326$	$2692 \pm 791$
CBC	$2.00 \pm 0.41$	$12.00 \pm 1.44$	$196 \pm 82$	$1591 \pm 206$

TABLE I – Les différents nerfs (1b, 2b, 3b, ON, RN, CBC) présents dans le ganglion buccal et leur composition respective en termes d'axones. Quatre type d'axones ont été établis en fonction de leur diamètre : type I, II, III et IV [C. Musio and C. Bedini, *Zoomorphology*, 110(1), 1990].

trouvé de données similaires pour le ganglion abdominal.

Les nerfs contiennent des groupes d'axones (de forme cylindrique) avec des diamètres variant de moins de  $1 \mu\text{m}$  à plus de  $25 \mu\text{m}$ . Un schéma du ganglion buccal présenté en Figure II montre la disposition symétrique de groupes de neurones tels que B1, B2, B6, B9 ( $200-300 \mu\text{m}$ ) [D. Gardner and E. R. Kandel, *Science*, 176(4035), 1972; D. Gardner, *Science*, 173(3996), 1971] ainsi que des neurones de petites tailles ( $\leq 50 \mu\text{m}$ ) [J. Ono, *Neuroscience*, 18, 1986]. La fin de cette seconde partie est dédiée à la description d'une séquence IRMd rapide intitulée séquence FISP avec préparation pour la diffusion (DPFISP).

### Partie III : Techniques pour l'accélération de l'acquisition IRM

Les avancées technologiques de l'IRM permettent aujourd'hui l'acquisition de signaux avec un RSB important sans le besoin de moyennner. Toutefois, le temps d'acquisition reste long car il dépend principalement de la résolution spatiale et du remplissage du k-space, rendant certaines études inapplicables sur des modèles *in vivo*. Une approche pour la réduction du temps d'acquisition consiste à sous-échantillonner le k-space. Cette approche est utilisée pour l'imagerie parallèle et pour le *compressed sensing*. Lorsque le k-space est sous-échantillonné, la reconstruction de l'image par transformée de Fourier peut

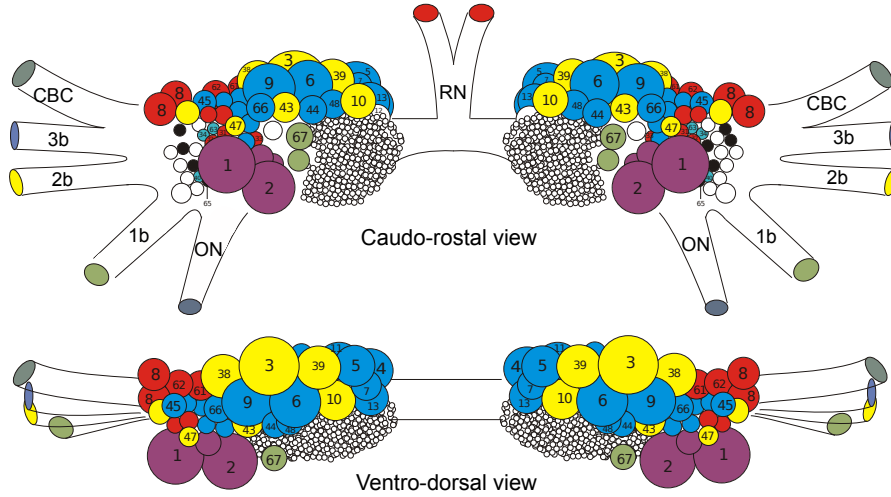


FIGURE II – Le ganglion buccal de l'*Aplysia* (schéma de R. Nargeot).

produire des artefacts de repliements. Les stratégies de sous-échantillonnage irrégulier peuvent réduire ces artefacts mais provoquent également une diminution du RSB de l'image [G. Marseille et al., *JMR series B*, 111(1), 1996]. L'imagerie parallèle permet d'exploiter l'information redondante présente dans le k-space en reconstruisant l'image à partir de données acquises simultanément avec un réseau d'antennes radio-fréquence (RF) [K. P. Pruessmann et al., *MRM*, 42(5), 1999]. Les antennes RF en réseau phasé pour l'imagerie microscopique ont récemment fait l'objet de développements en employant les dernières avancées relatives aux liaisons filaire (*wire bonding*) [O. G. Gruschke et al., *Lab Chip*, 12, 2012]. Toutefois, ce type d'antenne reste difficile à construire lorsque l'objet à imager est de petite taille, ce qui limite toutes application pour la MRM haute-résolution. Les méthodes basées sur le compressed sensing sont de plus en plus utilisées pour l'acquisition et la reconstruction des images IRM. Ainsi, des applications pour l'imagerie cardiaque [M. Lustig et al., *MRM*, 58(6), 2007], l'imagerie spectroscopique hyper-polarisée [S. Hu et al., *MRM*, 63(2), 2010], l'IRM de vélocimétrie [J. Paulsen et al., *JMR*, 205(2), 2010] et enfin plus récemment, l'imagerie de tenseur de diffusion [Y. Wu et al., *MRM*, 71(2), 2014] ont vu le jour. Cette partie comprendra une description des méthodes les plus courantes pour pour l'accélération de l'acquisition basées sur l'acquisition partielle du k-space et l'imagerie parallèle. Les stratégies reposant sur des trajectoires non-cartésiennes dans le k-space seront également mentionnées. Enfin, les principes du compressed sensing (CS) seront énoncés et son implémentation pour la réduction des temps d'acquisition en IRM sera détaillé. CS repose sur trois composantes majeures [M. Lustig et al., *MRM*, 58(6), 2007] : (1) la représentation parcimonieuse du signal dans un domaine de transformation, (2) des mesures incohérentes et (3) une méthode de reconstruction non-linéaire avec une contrainte de parcimonie. Si le nombre total de points dans une image est plus grand que quatre fois le nombre de coefficients de décomposition alors la reconstruction de données sous-échantillonnées est réalisable [Ricardo Otazo et al., *MRM*, 64(3), 2010].

La reconstruction des données sous-échantillonnées a été réalisée en employant des algorithmes existants. Soit  $\mathcal{F}_u$  l'opérateur de transformée de Fourier et  $\mathcal{W}$  l'opérateur de transformée en ondelettes, l'image reconstruite notée  $m$  est obtenue en résolvant le

problème d'optimisation suivant :

$$\begin{aligned} & \underset{m}{\text{minimize}} && \|\mathcal{W}m\|_1 + \alpha \text{TV}(m), \\ & \text{avec la condition} && \|\mathcal{F}_u m - y\|_2 < \epsilon, \end{aligned} \tag{I}$$

Où  $\alpha$  traduit la parcimonie de  $\mathcal{W}$  en différences discrétisées, TV est la variation totale et  $y$  représente le k-space sous-échantillonné. Le paramètre de seuillage  $\epsilon$  correspond au niveau de bruit estimé. L'équation (I) peut se résoudre en utilisant une méthode de descente de gradient conjugué non-linéaire [M. Lustig et al., *MRM*, 58(6), 2007] ou la méthode itérative split de Bregman [T. Goldstein and S. Osher, *SIAM Journal on Imaging Sciences*, 2(2), 2009]. D'après nos expériences, la méthode *iterative split* de Bregman est l'un des solveurs les plus rapides pour la reconstruction d'image à partir des coefficients de Fourier.

## Partie IV : L'acquisition compressée ou *compressed sensing* en IRM haute-résolution

Cette partie traite de l'application du *compressed sensing* (CS) à l'IRM haute-résolution. Le CS est une nouvelle technique de traitement du signal développée par Donoho en 2006 (d'autres nomenclatures existent pour désigner CS : *compressive sensing*, *compressive sampling* ou *sparse sampling*). Entre 2004 et 2006, les auteurs Emmanuel Candes, Terence Tao et David Donoho ont prouvé à travers plusieurs publications que si la condition de parcimonie est respectée, le signal peut être reconstruit avec un nombre d'échantillons inférieur à celui décrit par le critère de Nyquist. Sur le même principe, une image peut être reconstruite sans perte d'informations en utilisant des données sous-échantillonnées.

Cette partie débute avec la description d'une nouvelle approche de CS pour la génération de trajectoires de sous-échantillonnage, reposant sur la théorie de l'agrégation limitée par la diffusion (DLA) [Witten T and Sander L, *Phys. Rev. Lett.* 1981]. Le modèle DLA permet d'extraire un sous-ensemble de points issus d'un k-space échantillonné régulièrement afin d'établir un motif de sous-échantillonnage. DLA a été utilisée pour le sous-échantillonnage d'imagerie haute-résolution pondérée en T2 (séquence RARE) et en T1 (séquence FLASH). La Figure III illustre l'application de la méthode DLA avec un sous-échantillonnage de 50% dans la direction de l'encodage de phase, pour des acquisitions RARE (facteur d'accélération  $A_F = 4$ ) et FLASH.

Nous démontrons que l'approche DLA permet d'obtenir de meilleurs résultats que la méthode polynomiale pour un sous-échantillonnage supérieur à 25% de données issues d'acquisition RARE avec  $A_F = 4$  (Figure IVa) et  $A_F = 1$  (Figure IVb).

La méthode de descente de gradient conjugué a été employé pour la reconstruction d'image CS dans le cas d'acquisition RARE pondérée en T2 (Figure Va). La méthode itérative split de Bergman a été employé pour la reconstruction d'image CS dans le cas d'acquisition pondérée en T1 (Figure Vb). Les performances des deux méthodes sont similaires.

Le sous-échantillonnage DLA a été employé pour implémenter l'acquisition CS pour l'imagerie haute-résolution pondérée en T2 et T1 à ultra-haut champ magnétique (17.2 T). Les performances des méthodes d'acquisitions DLA-CS RARE (Figure IV) et DLA-CS FLASH (Figure VI) ont été évaluées pour différents taux de sous-échantillonnage.

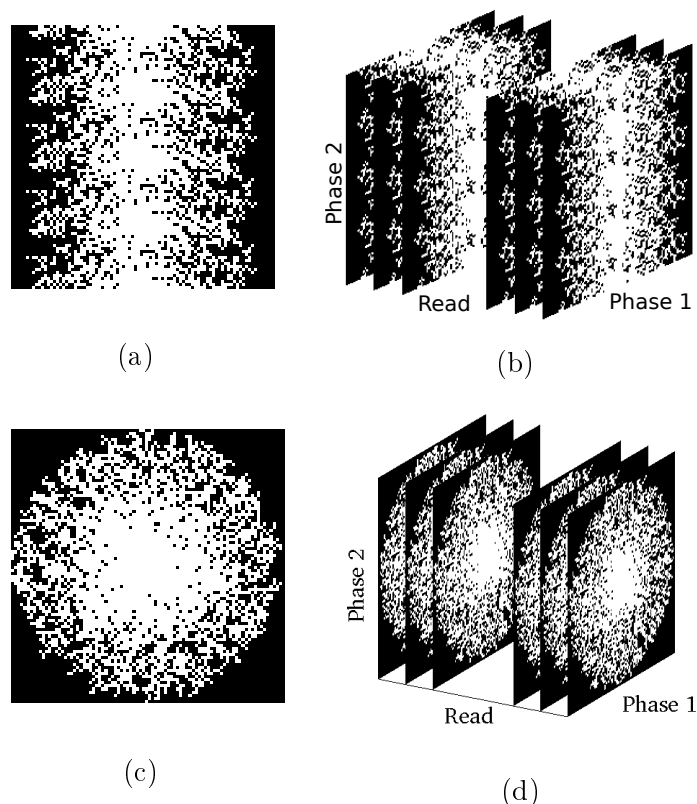


FIGURE III – Exemples de sous-échantillonnages DLA de 50% (a) et 3D DLA (b) employés pour l’encodage de phase pour une acquisition RARE avec  $A_F = 4$  (haut). Exemples de sous-échantillonnages DLA de 50% (c) et 3D DLA (d) employés pour l’encodage de phase pour une acquisition FLASH (bas).

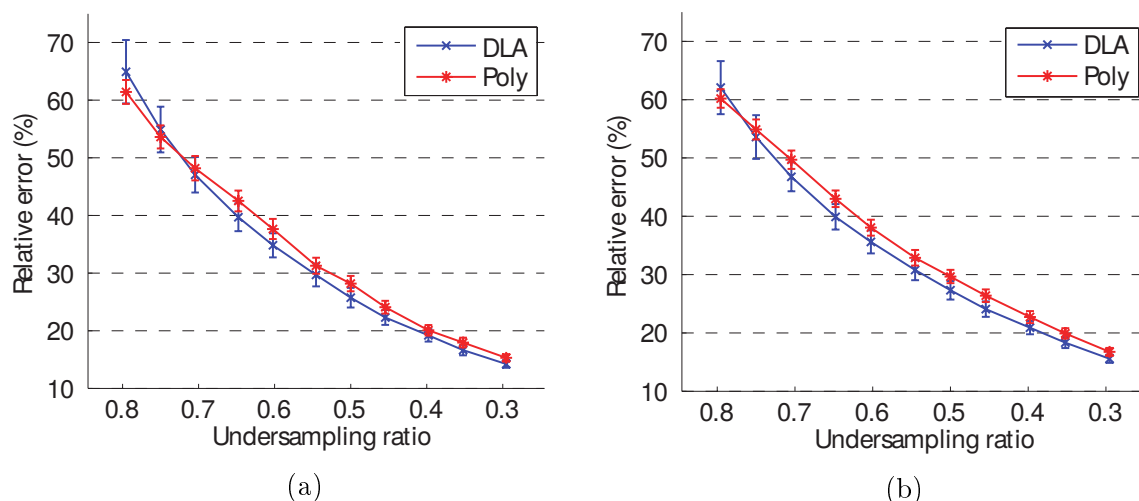


FIGURE IV – Erreurs relatives obtenues entre les images de référence (idéalement échantillonnées) et les images CS obtenues par sous-échantillonnage DLA (bleu) et par sous-échantillonnage polynomiale (rouge) pour des données acquises avec la séquence RARE avec  $A_F = 4$  (a) et  $A_F = 1$  (b). Les barres d’erreur représentent les écart-types ( $n = 300$ ).

Dans les deux cas, un taux de sous-échantillonnage de 50% permet un compromis idéal entre résolution spatiale, rapport contraste-sur-bruit et intensité du signal. Ces deux

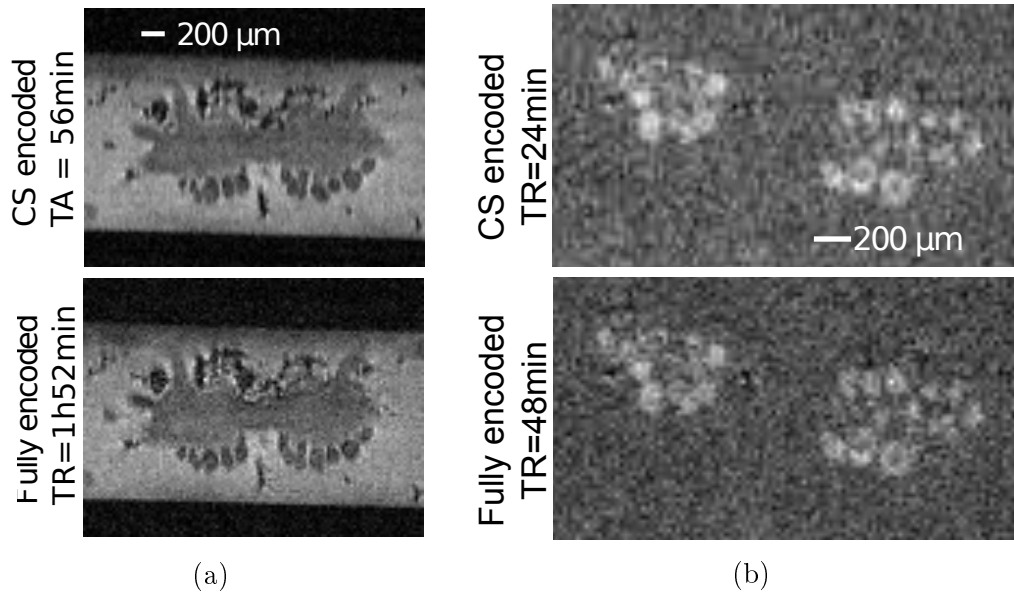


FIGURE V – Images de ganglions buccaux (résolution isotropique de  $25 \mu m$ ) acquises avec un échantillonnage complet (bas) et un sous-échantillonnage CS de 50% (haut). Deux types de séquence d’acquisition et de reconstruction ont été employés : (a) une acquisition RARE pondérée en T2 reconstruite avec une méthode de descente de gradient conjugué ; la durée d’acquisition est de 1h52 minutes pour l’échantillonnage complet et de 56 minutes pour le sous-échantillonnage CS de 50% ; (b) une acquisition pondérée en T1 reconstruite avec la méthode itérative split de Bergman ; la durée d’acquisition est de 48 minutes pour l’échantillonnage complet et de 24 minutes pour le sous-échantillonnage CS de 50%.

séquences d’acquisition CS (*csRARE* et *csFLASH*) ont été implémentées sur le logiciel commercial Bruker Paravision 5.1 ; la reconstruction des images est réalisée sur Matlab.

La séquence d’acquisition *csRARE* a été utilisé pour imager des tissus neuronaux in vivo avec une résolution spatiale et un rapport contraste-sur-bruit suffisant pour identifier la majorité des neurones présent dans le ganglion de l’*Aplysia*. Ces dernières ont été identifiées automatiquement à l’aide d’un algorithme de segmentation développé durant les travaux de thèse. La séquence d’acquisition *csFLASH* a permis de quantifier avec précision l’intensité du signal lors d’expériences d’imagerie du manganèse MEMRI (*Manganese Enhanced MRI*). En moyenne, une différence de 1.37% en intensité de signal provenant d’un neurone a été estimée entre les images échantillonnées de manière idéale et les images CS acquises avec un sous-échantillonnage déterminé pré-acquisition (Figure VII). En comparaison, le sous-échantillonnage post-acquisition de données idéalement échantillonnées produit une erreur plus faible (0.50%). Cette erreur différente suivant le scénario suivi pour le sous-échantillonnage pourrait être due à plusieurs instabilités expérimentales telles que le changement de position de l’échantillon à imager dans le champ  $B_0$  (suite à des vibrations dues aux gradients) ou le changement de certaines propriétés physiologiques de l’échantillon dans le temps. L’estimation du coefficient de corrélation de Pearson (PCC) entre les données idéalement échantillonnées et les données sous-échantillonnées a montré que les performances de la méthode DLA-CS sont influencée par le rapport signal-sur-bruit de l’image, ce qui est en accord avec une étude récente [Prieto C et al., *JMRI*, 36(6), 2012]. Des taux d’accélération et donc

des réductions importantes des durées d'acquisition sont à prévoir lorsque le rapport signal-sur-bruit est important.

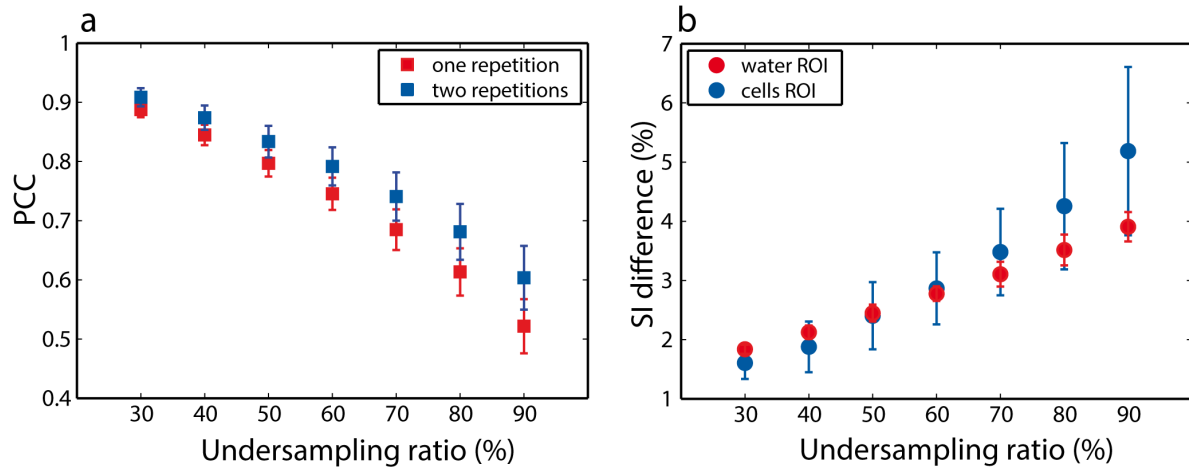


FIGURE VI – Évaluation des performances de la méthode CS-DLA pour différents taux de sous-échantillonnage : (a) Coefficient PCC estimé entre les images idéalement échantillonnées et les images CS en fonction du taux de sous-échantillonnage pour une répétition (rouge) et deux répétitions (bleu). Le coefficient PCC a été calculé pour une région d'intérêt couvrant approximativement 50000 voxels. (b) Différence en intensité entre les images idéalement échantillonnées et les images CS en fonction du taux de sous-échantillonnage (2 acquisitions moyennées) pour une région d'intérêt contenant de l'eau (rouge) et du tissu neuronal (bleu). Les barres d'erreur représentent les écart-types. Ces données sont issues d'une étude contenant  $N=6$  échantillons.

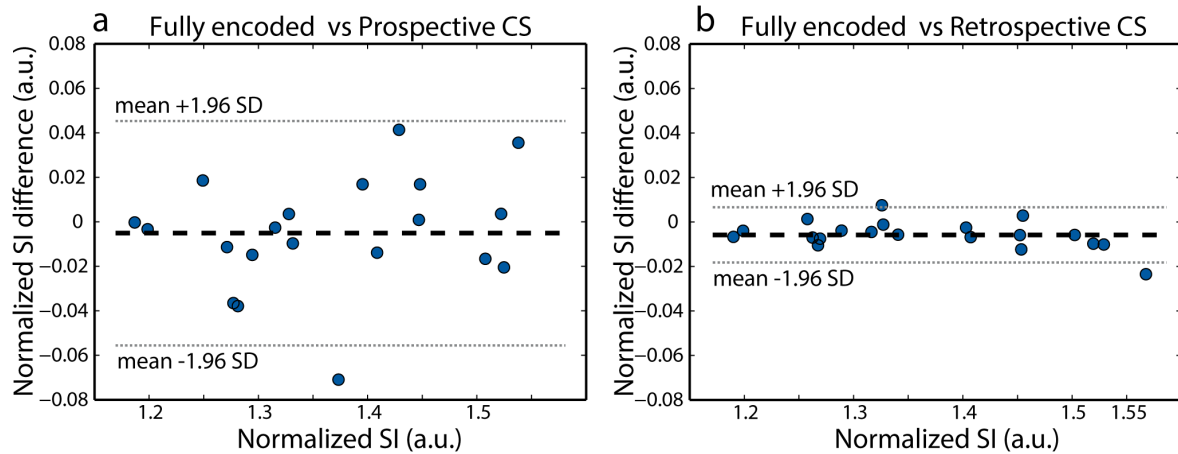


FIGURE VII – Représentation de Bland-Altman montrant la différence de l'intensité du signal entre les images échantillonnées de manière idéale et : (a) les images CS acquises avec un sous-échantillonnage déterminé pré-acquisition (*prospective CS*) (a) et (b) les images CS acquises avec un sous-échantillonnage post-acquisition de données idéalement échantillonnées (*retrospective CS*). Chaque point représente l'intensité du signal mesuré dans un neurone (2 ganglions, 10 neurones par ganglion).

Alors que le sous-échantillonnage DLA a été implémenté pour les acquisitions RARE avec un facteur d'accélération de 4, l'implémentation pour d'autres facteur d'accélération

est directe. Toutefois, nous avons démontré que l'approche DLA est plus performante pour des acquisitions RARE sans accélération, protocole habituellement utilisé pour imager des tissus dont les temps de relaxation T2 sont courts. Enfin, cette approche n'est pas limitée aux acquisitions RARE ou FLASH et peut aisément s'étendre à d'autres types de séquences.

Pour résumer, les résultats présentés dans cette partie démontrent que la méthode DLA est une excellente alternative aux stratégies de sous-échantillonnage polynomial et est capable de ramener à des durées acceptables certains protocoles d'imagerie exigeant habituellement de longs temps d'acquisition. En conséquence, ce type d'approche peut grandement bénéficier à la microscopie par résonance magnétique en permettant l'étude d'échantillons *in vivo*. Les résultats obtenus avec la stratégie DLA-CS ont montré la possibilité d'accélérer l'acquisition des images haute-résolution et quantitative MEMRI pour l'étude de tissu neuronal. Alors que les temps d'acquisition obtenus ne sont pas plus courts en comparaison avec certaines techniques d'imagerie ultra-rapides telle que Echo Planar Imaging (EPI) ou l'imagerie spirale, l'approche DLA-CS reste prometteuse à très haut champ lorsqu'on désire une importante résolution spatiale et que les acquisitions de type *single shot* ne sont pas réalisables. Enfin, DLA-CS ne se limite pas au domaine de la microscopie par résonance magnétique et peut tout à fait être employé dans les domaines d'imagerie préclinique et clinique où la réduction des temps d'acquisitions sont toujours appréciables.

## Partie V : IRM de diffusion pour l'*Aplysia*

La cinquième partie de cette thèse traite de la diffusivité dans le ganglion abdominal de l'*Aplysia californica*. L'étude de la relation entre la structure cellulaire et le signal en IRM de diffusion dans les tissus neuronaux de l'*Aplysia* permet une meilleure compréhension de cette relation pour des organismes plus complexes. Des expériences d'IRMd ont été réalisées sur des échantillons chimiquement fixés de ganglions abdominaux pour une plage de temps de diffusion où l'évolution du signal IRMd est considérée comme étant mono-exponentielle et peut être décrite de manière fiable par le coefficient ADC. L'analyse de ces données ADC en fonction du temps de diffusion a été réalisée pour les cellules de grande taille à l'aide de formules analytiques connues et valides pour les temps de diffusion courts. Il est intéressant de noter qu'une analyse grossière employant ces formules analytiques peuvent échouer du fait de la présence des noyaux cellulaires, rendant l'estimation de la taille des cellules inexacte et très inférieure à leur taille réelle.

Des simulations numériques du coefficient ADC ont été réalisées pour plusieurs types de cellules présentes dans le ganglion abdominal. Pour simuler la géométrie des cellules les plus grandes, ces dernières ont été segmentées à partir d'images anatomiques pondérées en T2 et un noyau a été généré manuellement (Figure VIII). Les petites cellules ont été modélisées à l'aide de géométrie sphérique et cylindrique en accord avec les données relatives à la structure cellulaire présentes dans la littérature. Cette bibliothèque de résultats de simulation a alors été employée afin d'ajuster notre modèle de diffusivité intrinsèque aux données acquises sur des cellules de petite taille et des nerfs.

Le signal d'IRMd a été mesuré pour différents temps de diffusion dans des régions d'intérêt (ROI) comprenant des neurones de grande taille, des agrégats de neurones et des nerfs (Figure IX et X).

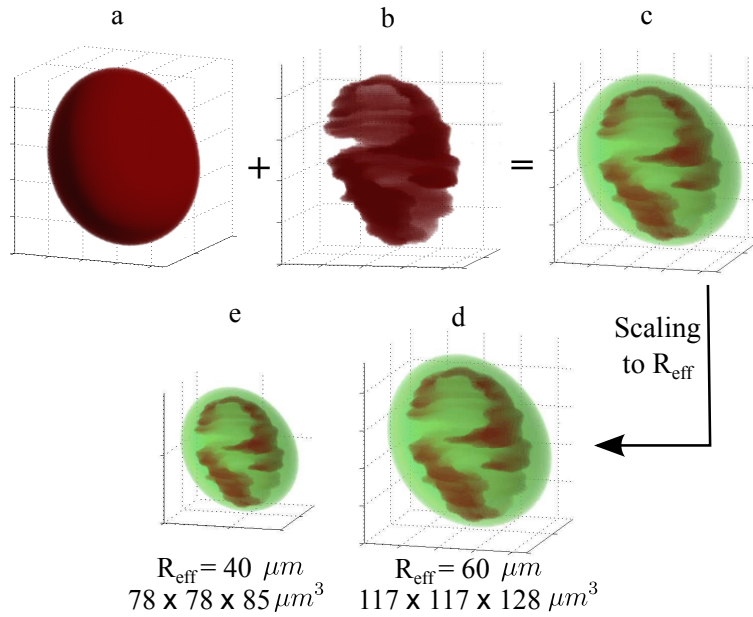


FIGURE VIII – Rendu géométrique 3D d'un neurone de grande taille. Le contour du neurone a été estimé à partir d'images pondérées en T2 (a). Un noyau de forme irrégulière a été ensuite généré manuellement (b) puis inséré dans le neurone (c). Le noyau est représenté en rouge alors que le cytoplasme est en vert. Des cellules de taille différente ont ainsi été modélisées en augmentant la taille du noyau  $R_{eff}$  (par exemple  $R_{eff} = 60 \mu m$  (d) et  $R_{eff} = 40 \mu m$  (e)).

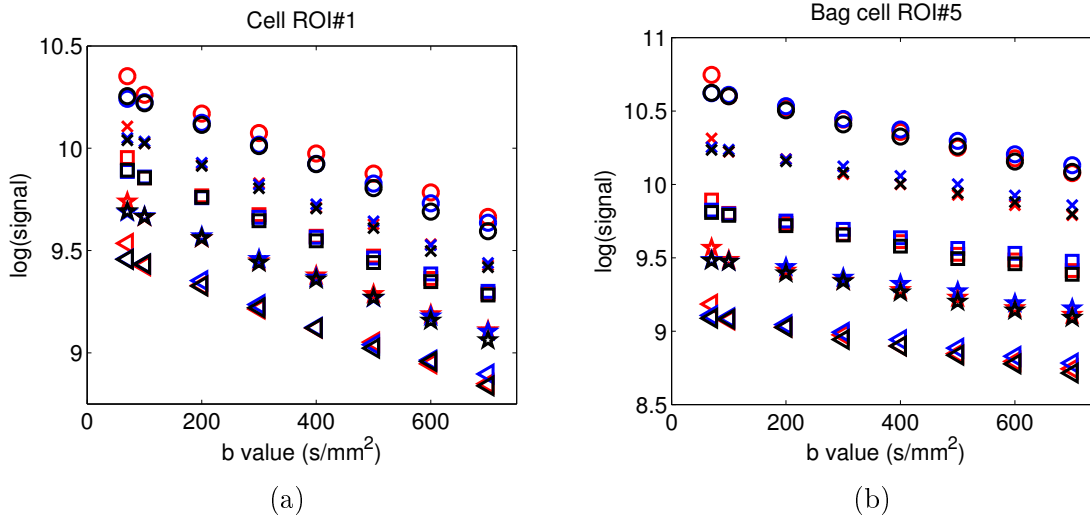


FIGURE IX – Le signal d'IRMd acquis pour plusieurs temps de diffusion sur des neurones de grande taille (a) et des agrégats de neurones (b). Pour chaque graphique, les signaux sont représentés de haut en bas pour des valeurs respectives de temps de diffusion  $\Delta$  allant 5 à 25 ms. Les couleurs représentent la direction des gradients (rouge pour x, bleu pour y et noir pour z).

Le logarithme du signal IRMd acquis évolue de manière linéaire avec le b-value pour une plage allant de 70 à 700  $s/mm^2$ ; le coefficient ADC décrit donc le signal de manière fiable pour cette plage. Les signaux acquis suivant les composantes x, y et z ne montrent pas d'anisotropie significative pour les neurones de grande taille et les agrégats

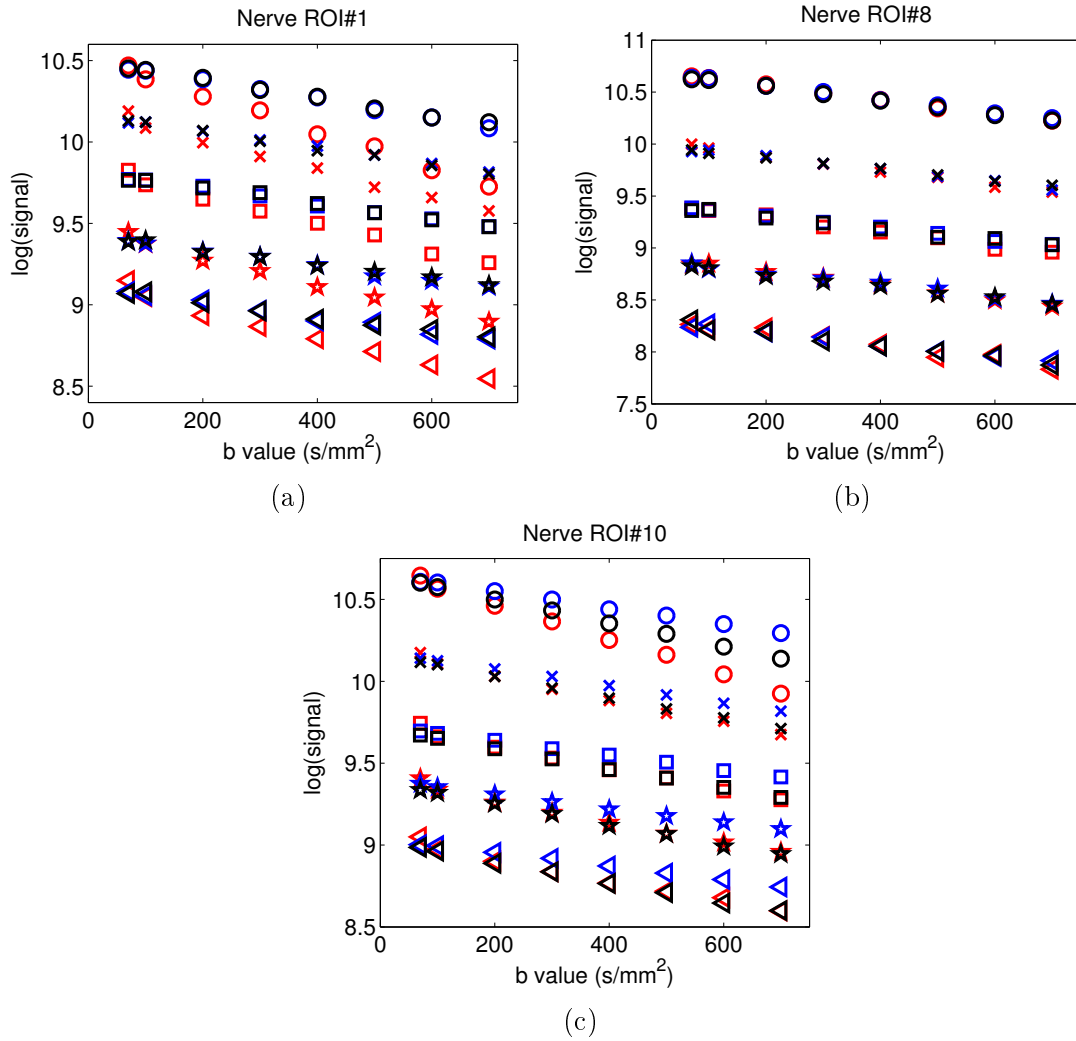


FIGURE X – Le signal IRMd acquis sur la composante nerveuse du neurone pour plusieurs temps de diffusion : (a) l'orientation générale du nerf est suivant la direction x, les composantes y et z étant similaires ; (b) l'orientation du nerf est telle que les trois composantes x, y, et z sont identiques ; (c) l'orientation du nerf suit majoritairement les directions x et z (la composante y est la plus faible). Pour chaque graphique, les signaux sont représentés de haut en bas pour des valeurs respectives de temps de diffusion  $\Delta$  allant 5 à 25 ms. Les couleurs représentent la direction des gradients (rouge pour x, bleu pour y et noir pour z).

de neurones. Lorsque le temps de diffusion augmente de 5 à 25 ms, le coefficient ADC moyen diminue de 9.45% pour les neurones de grande taille, de 20.8% pour les agrégats de neurones ; la diffusivité moyenne (MD) diminue de 14.98% dans les nerfs (Figure XI).

Avec l'hypothèse d'une diffusivité libre de  $2.0 \mu\text{m}^2/\text{ms}$ , le déplacement moyen due à la diffusion est de 7.7 à  $17.3 \mu\text{m}$  pour des temps de diffusion entre 5 et 25 ms. En conséquence, il est possible d'utiliser les modèles mathématiques développés par Mitra et al [P. P. Mitra et al., *Phys. Rev. Lett.*, 68,1992] pour estimer le coefficient ADC pour un temps de diffusion court et ainsi estimer les rayons des cellules ( $R_{\text{est}}$ ) et les comparer aux mesures expérimentales ( $R_{\text{eff}}$ ) (Figure XII).

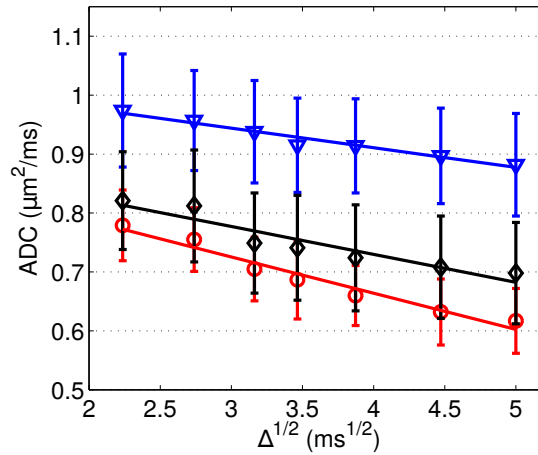


FIGURE XI – Coefficient ADC moyen en fonction du temps de diffusion pour les agrégats de neurones (cercles,  $N=11$  ROIs), pour les neurones de grande taille (triangles,  $N=22$  ROIs) et pour les nerfs (losanges,  $N=12$  ROIs). Les données ont été ajustées par régression linéaire. Le coefficient ADC diminue de 9.45% et 20.8% pour les neurones de grande taille et les agrégats de neurones respectivement ; MD diminue de 14.95% dans les nerfs. Les barres d'erreur correspondent aux écart-types des données expérimentales.

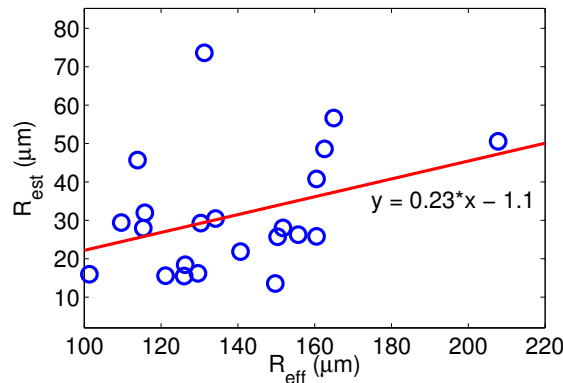


FIGURE XII – La taille de la cellule est largement sous-estimée :  $R_{\text{est}}$  représente en moyenne 25% de  $R_{\text{eff}}$ .

Nous avons étendue l'analyse en procédant à des simulations basées sur un modèle du neurones à deux compartiments avec un échange limitée entre le noyau et le cytoplasme. Nous avons ainsi généré quatre géométries basées sur trois types de forme pour le noyau et sur la position de ce dernier dans la cellule (Figure XIII).

Nous avons étudié les dépendances entre le coefficient ADC, la forme du noyau et la fraction en volume en simulant les valeurs  $ADC(\Delta, R)$  pour une diffusivité intrinsèque dans le cytoplasme de  $D_c = 1 \mu\text{m}^2/\text{ms}$  et une diffusivité intrinsèque dans le noyau de  $D_n = 2 \mu\text{m}^2/\text{ms}$  ( $\Delta$  variant entre 5 et 25 ms). En ajustant les valeurs ADC obtenues suivant le modèle  $ADC(\Delta, R) = A(R) \times \sqrt{\Delta} + B(R)$ , nous avons observé que la pente  $A(R)$  dépend majoritairement de la forme du noyau ; les dépendances avec la fraction en volume ou la position du noyau dans le neurone sont plus faibles (Figure XIV).

Nous avons également comparé l'évolution de l'ADC en fonction du temps de diffu-

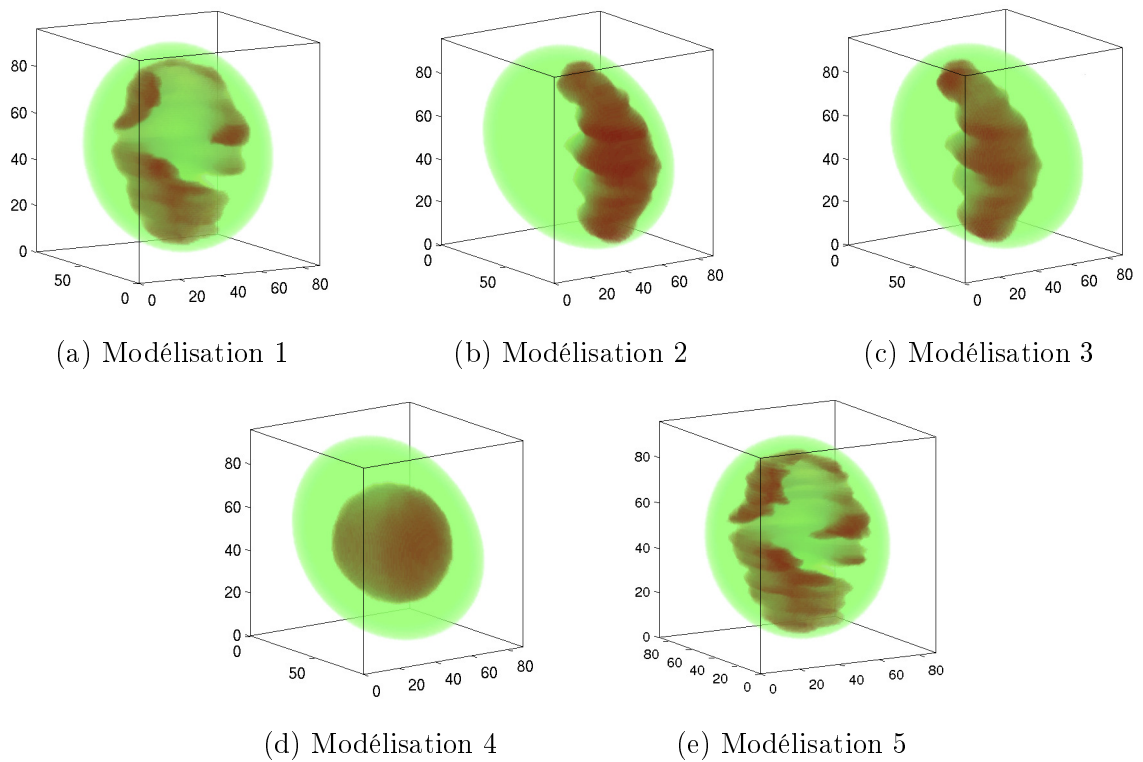


FIGURE XIII – Cinq géométries différentes de neurones ayant la même taille et le même contour, mais ayant une forme de noyau différente (en rouge, a-e) et une position différente du noyau dans la cellule (b, c). Le contour du neurone est le même pour les cinq géométries et a été généré à partir des images pondérées en T2. La fraction en volume du noyau dans la cellule est approximativement de 25%. Les géométries 1 (a) et 5 (e) possèdent la même forme de noyau mais la fraction en volume est différente (respectivement 25% et 29%).

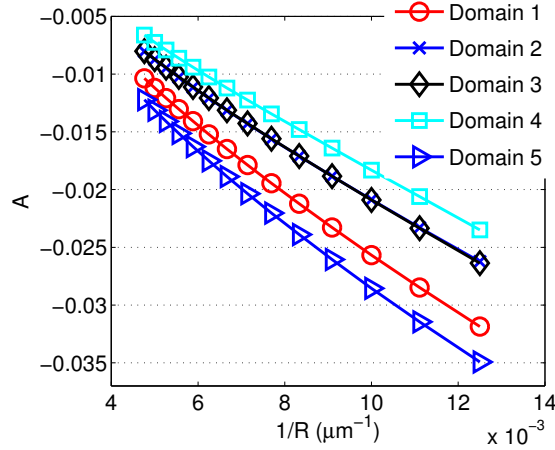


FIGURE XIV – Pente  $A(R)$  en fonction du rayon de cellule  $R$  pour différentes fractions en volume.

sion par simulation pour les agrégats de neurones et les nerfs, et extrait les paramètres de diffusion intrinsèque pour le cytoplasme ( $D_c$ ), pour le noyau ( $D_n$ ) et les axones ( $D_a$ ). Les résultats de simulations ADC pour  $D_c$  variant de 0.50 à 1.00  $\mu\text{m}^2/\text{ms}$  et  $D_n$  variant de 1.25 à 2.00  $\mu\text{m}^2/\text{ms}$  sont représentées Figure XVa. La figure XVb montre les couples ( $D_c, D_n$ ) qui permettent d'obtenir une erreur d'ajustement minimale. Les courbes en trait pointillé représentées en Figure XVa sont les résultats de simulation du coefficient ADC réalisée pour le couple ( $D_c, D_n$ ) de même couleur en Figure XVb.

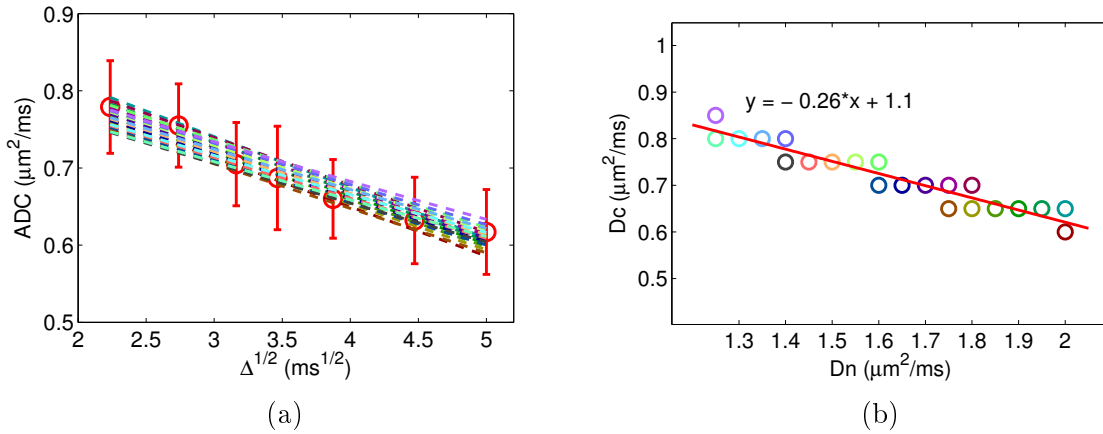


FIGURE XV – (a) Coefficient ADC moyen acquis en fonction du temps de diffusion (cercles) et ajustements optimaux (lignes pointillées). (b) Couples solution ( $D_c, D_n$ ) optimaux (cercles colorés). Les diffusivités intrinsèques sont corrélées :  $D_c + 0.26 \times D_n = 1.1$ . Chaque ajustement numérique représenté en (a) correspond à un couple solution ( $D_c, D_n$ ) en (b) et est repéré par le même code couleur. Les barres d'erreur correspondent aux écart-types des données expérimentales.

Nous avons enfin simulé les valeurs de MD pour  $D_a$  variant de 0.85 à 2.00  $\mu\text{m}^2/\text{ms}$  pour 6 distributions d'axones (Tableau I). En comparant les valeurs de MD simulées aux valeurs expérimentales, nous avons extrait des plages de valeurs pour  $D_a$  (Tableau II).

Nerf	1b	2b	3b	ON	RN	CBC
Plage $D_a$ ( $\mu\text{m}^2/\text{ms}$ )	1.85-2.00	1.55-1.65	1.30-1.40	1.80-1.95	1.75-1.90	1.40-1.50

TABLE II – Les plages de diffusivité intrinsèque  $D_a$  ( $\mu\text{m}^2/\text{ms}$ ) permettant d’obtenir un ajustement optimal des données expérimentales de MD pour les 6 types d’axones présents dans les nerfs du ganglion buccal (1b, 2b, 3b, ON, RN, CBC).

## Conclusion

Ces travaux de thèse ont permis d’aboutir sur deux aspects :

1. Les stratégies DLA-CS ont été implémentées avec succès pour l’imagerie pondérée en T2 et T1 avec une réduction du temps d’acquisition de 50% tout en conservant une qualité d’image satisfaisante en termes de résolution spatiale et d’intensité du signal. De plus, ce type de sous-échantillonnage DLA peut également être employé pour l’imagerie reposant sur l’acquisition d’un  $k$ -space non cartésien. Le développement de telle méthode est capable de ramener à des durées acceptables certains protocoles d’imagerie exigeant habituellement de longs temps d’acquisition. En conséquence, ce type d’approche peut grandement bénéficier à la microscopie par résonance magnétique en permettant l’étude d’échantillons *in vivo*.
2. Nous avons étudié l’évolution du coefficient ADC suivant le temps de diffusion et évalué sa dépendance avec trois structures différentes présentes dans le ganglion abdominal de l’*Aplysia*. Nous avons observé qu’une augmentation du temps de diffusion de 5 à 25 ms provoque une diminution du coefficient ADC de 20.8%, 9.45% et 14.98% respectivement pour les agrégats de neurones, les neurones de grande taille et les nerfs. Le coefficient ADC varie de manière différente suivant les éléments neuronaux observés du fait de leur taille et de leur forme différente. Notre étude a permis de constater que le modèle mono-compartimental n’est pas suffisant pour modéliser de manière adéquate les neurones de grande taille. En se basant sur des résultats de simulation et des données expérimentales, nous avons pu établir un modèle à deux compartiments, par ajout d’un noyau dans la région cytoplasmique du neurone, afin de permettre un ajustement numérique satisfaisant de l’évolution du coefficient ADC sur une plage de temps de diffusion allant de 5 à 25 ms. Nous avons ainsi observé, en accord avec la littérature, que la diffusivité intrinsèque du noyau est plus élevée que celle présente dans le cytoplasme. De plus, la forme et la fraction en volume du noyau influencent grandement l’évolution du coefficient ADC contrairement à sa position dans la cellule. Ces observations démontrent que la méthode d’imagerie IRMd pourrait potentiellement être employée comme outil de diagnostic pour révéler des anomalies cellulaires relatives à la forme et la taille des noyaux cellulaires [M. Webster et al., *Journal of Cell Science*, 122(10), 2009]. Nous avons également observé une dépendance linéaire entre les diffusivités intrinsèques dans le cytoplasme et le noyau pour les agrégats de neurones. Enfin, la diffusivité intrinsèque dans les nerfs et plus particulièrement dans les axones dépend de manière significative du diamètre de ces derniers. Des études supplémentaires combinant simulation et expérimentation sur l’*Aplysia* permettrait de déterminer plus précisément la relation entre la géométrie et le signal IRMd.

## General introduction

Magnetic Resonance Imaging (MRI) is a widely used imaging technique based on Nuclear Magnetic Resonance (NMR). MRI is based on the interaction between an applied strong magnetic field present in the scanner and a nucleus that possesses spin (containing an odd number of protons and/or neutrons). The principle is to “magnetize” the object of interest by a strong magnetic field present in the scanner. Using specific encoding schemes and acquisition parameters one can sensitize MR images to various physiologically relevant parameters (perfusion status and water diffusion among others). In general, in clinical and research MRI, the images are generated by using the signal from the nuclei of hydrogen atoms ( $^1\text{H}$ ), however other nuclei can also be used ( $^{23}\text{Na}$ ,  $^{31}\text{P}$ ,  $^{13}\text{C}$ , etc). The  $^1\text{H}$  nucleus is the most-often used in MRI because of many reasons. The  $^1\text{H}$  nucleus, consisting of a single proton, has a spin of  $1/2$  and is the most abundant isotope of hydrogen, and exists naturally in biological tissues (as it is present in water). In addition, the  $^1\text{H}$  has the highest gyromagnetic ratio (a measure of the MRI sensitivity to detect a particular species) among all nuclei.

Magnetic Resonance Microscopy (MRM) refers to high resolution MRI, higher than  $100\ \mu\text{m}^3$  down to the scale of  $5\text{-}10\ \mu\text{m}^3$ . The MRM imaging technique is useful for the study of fundamental aspects of the nervous system at the level of single neurons or small size networks. In this thesis we use the *Aplysia californica* animal model because of the relatively simple nervous structure with cell sizes much larger compared with mammalian neurons, e.g. several hundred microns in diameter versus  $5\text{-}10$  microns. Given their size, it is possible to image and identify individual neurons from the MR anatomical images (typically acquired with  $25\ \mu\text{m}$  isotropic resolution). In order to achieve high resolutions, we use a high magnetic field ( $17.2\ \text{T}$ ) and custom built solenoidal coils ( $2.4\ \text{mm}$  diameter) developed by our team.

High resolution MRI experiments require long acquisition time. Acceleration methods are therefore highly desirable. Parallel imaging techniques are successfully used to reduce the acquisition time in clinical and preclinical imaging, however they are less popular in MR microscopy due to the limited space available for placing multiple coil elements. The compressed sensing (CS) approach another technique used to accelerate MR acquisitions time by reducing the number of points acquired in k-space. The first objective of this thesis was to implement compressed sensing (CS) strategies to reduce the acquisition time in high resolution magnetic resonance. Specifically, we proposed and validated a new undersampling model based on the diffusion limited aggregation (DLA). We applied this undersampling method to T2-weighted (starting from RARE sequence) and T1-weighted images (starting from FLASH sequence).

A specific application of MRI is diffusion MRI. Diffusion MRI (dMRI) is a non-invasive imaging technique that gives a measure of the diffusion characteristics of water in biological tissues. The molecular diffusion in tissues is restricted, i.e. water molecules interact with many obstacles such as fibers and membranes. By measuring how water molecules diffuse through the tissue, the dMRI technique can be reveal microscopic details about its microstructure. However, understanding the relationship between the complex tissue microstructure and the dMRI signal is not easy task on one needs to make use of mathematical modeling and numerical simulations the dMRI signal tools is very importance. The *Aplysia* nervous tissue facilitates the dMRI studies because high

resolution MR imaging allows the fine anatomical description of the cellular network (size of individual neurons and orientation of axons). Using the *Aplysia* neuronal tissues to study the relationship between the cellular structure and the diffusion MRI signal can shed light on this relationship for more complex organisms. Therefore the second objective of this thesis was to develop and validate a diffusion model in the abdominal ganglion of *Aplysia californica*. We measured the dMRI signal at several diffusion times and performed simulations of water diffusion in cellular geometries obtained after segmenting high resolution T2-weighted images and incorporating known information about the cellular structure from the literature. We have validated certain relationships between the cellular geometry and the dMRI signal in the *Aplysia* neurons and nerves.

This thesis is organized into six main parts as follows. In part 1, we introduce the MRI concepts relevant to this thesis such as k-space, gradient encoding, field-of-view (FOV), signal to noise ratio (SNR), 2D and 3D imaging, as well as the basic image reconstruction principles based on the Fourier transform. In addition, we describe the main pulse sequences used during this thesis and the contrast they generate: the RARE pulse sequence for T2-weighted imaging, the FLASH pulse sequence for T1-weighted imaging. In part 2, we briefly introduce dMRI concepts as well as related equations and existing works. The relation between apparent diffusion coefficient and cell size, the animal model used in dMRI simulations are also introduced here. Furthermore, we describe a fast dMRI sequence, the diffusion prepared FISP sequence. Several accelerated acquisition techniques are presented in part 3. In part 4, we propose a new undersampling scheme based on the DLA model. We detail the development, implementation, validation and the application DLA-CS to T2-weighted (RARE) and T1-weighted (FLASH) images to reduce the acquisition time while maintaining the quality of image in term of resolution and signal quantification. We proposed a cell segmentation algorithm and its application in order to compare the fully encoding and DLA-CS images. Part 5 is dedicated to diffusion MRI both in terms of data acquisition and modeling. The conclusion and future directions are presented in part 6.

In briefly, the main outcomes of this thesis are:

1. We proposed a new undersampling model based on the diffusion limited aggregation (DLA) and have successfully implemented the DLA-CS strategies for T2 and T1-weighted images, with a reduction of the acquisition time of 50% while maintaining the quality of the images both in terms of spatial resolution and signal intensity quantification. The DLA undersampling patterns introduced here are not limited to be subsets of Cartesian k-space points, but it can also be extended to non-Cartesian imaging and for other type of sequences. Such developments are beneficial to magnetic resonance microscopy studies by reducing the notoriously long acquisitions to more reasonable times, thus enabling the expansion of the technique to dynamic investigations. In addition, we proposed a simple cell segmentation algorithm as a tool for image analysis in MR microscopy.
2. We investigated dependence of the ADC on the diffusion time in three different structures within the abdominal ganglia of *Aplysia*. We found that by increasing the diffusion time from 5 to 25 ms, the ADC dropped by 20.8%, 9.45% and 14.98% for bag cell neurons, large cell neurons and the nerve ROI, respectively. The different behavior in the three different regions can be explained by the different sizes and shapes of the cellular components. By analyzed the diffusion time-

dependent ADC using a well-known analytical formula that is valid in the short diffusion time regime, we found that it is not sufficient to approximate the large cell size by using the predicted one compartment model. We went on to perform numerical simulation of the ADC for several cell types of the abdominal ganglia. To create the simulation geometries, for the largest cells, we segmented a high resolution T2-weighted images and incorporated a manually generated nucleus. For small cells and nerve cells, we created spherical and cylindrical geometrical domains that are consistent with known information about the cellular structures from the literature. Using the library of simulation results, we fitted for the intrinsic diffusivities of the small cells and the nerve cells. Based on the results from numerical simulation (by solving the Bloch-Torrey equation on specific domains of large neurons) and evidence from experimental data, we established that it is necessary to include a nucleus region embedded in a cytoplasmic region in order to fit the large drop in ADC observed when varying the diffusion time from 5 to 25 ms. In agreement to the literature we found that the intrinsic diffusivity in the nucleus is higher than in the cytoplasm. Moreover, both shape and nucleus volume fraction were found to significantly influence the ADC behavior, while the position of the nucleus did not seem to be important. This results suggests that dMRI can be used as a diagnostic tool as the shape and size of cell nuclei can reveal cellular abnormalities. Regarding the bag cell neurons, we observed a linear relationship between the intrinsic diffusivities in the cytoplasm and the nucleus for which the fitting of ADC was successful. Moreover, we found regarding the nerve that the extracted intrinsic diffusivity of axons depends significantly on the axons diameter distribution we chose.

All the solution creation (artificial sea water), sample preparation as well as experimental in this thesis were performed by me, except for the sample preparation, solution creation and experimental protocol mentioned in section 19 (CS in T1-weighted imaging: CS-FLASH) were processed by my colleague, Pavel Svehla, the co-authorship in a preparation manuscript. The daily tending for the *Aplysia* was shared by our team members and not to mentioned in this thesis.

This work was funded by grant ANR-13-BSV5-0014-01 (project ANImE) and by the doctoral school EOBE, University Paris Sud, Orsay, France.

---

## Part I

# Important Concepts in Magnetic Resonance Imaging

## Summary

---

<b>1</b>	<b>NMR</b>	<b>20</b>
1.1	Bloch Equations . . . . .	21
1.2	Signal detection . . . . .	24
<b>2</b>	<b>MRI</b>	<b>26</b>
2.1	Gradient encoding . . . . .	27
2.2	$k$ -space . . . . .	28
2.3	Fourier transform and image reconstruction . . . . .	29
2.4	Frequency encoding . . . . .	30
2.5	2D imaging . . . . .	30
2.5.1	Slice selection . . . . .	30
2.5.2	Phase encoding . . . . .	30
2.5.3	2D image reconstruction . . . . .	31
2.6	3D imaging . . . . .	32
2.6.1	Phase 2 encoding . . . . .	32
2.6.2	3D image reconstruction . . . . .	33
2.7	Resolution and FOV . . . . .	33
2.8	SNR . . . . .	34
2.9	Acquisition time . . . . .	35
<b>3</b>	<b>MRI pulse sequences</b>	<b>36</b>
3.1	Spin Echo sequence . . . . .	36
3.2	RARE: T2-weighted images . . . . .	37
3.3	Gradient Echo sequence . . . . .	38
3.4	FLASH: T1-weighted images . . . . .	39
3.5	FISP sequence . . . . .	40

---

Magnetic resonance imaging (MRI) is a widely used imaging technique based on nuclear magnetic resonance (NMR). The principle is to “magnetize” the object of interest by a strong magnetic field present in the scanner. Subsequently, the magnetization is manipulated using radio waves and magnetic field gradients in order to generate images. Using specific encoding schemes and acquisition parameters one can sensitize MR images to various physiologically relevant parameters such as perfusion status and water diffusion among others. In general, in medical MRI, the images are generated by using the signal from the nuclei of hydrogen atoms ( $^1\text{H}$ ), however other nuclei can also be used ( $^{23}\text{Na}$ ,  $^{31}\text{P}$ ,  $^{13}\text{C}$ , etc) [1]. This chapter will introduce MRI concepts relevant to this thesis such as k-space, gradient encoding, field-of-view (FOV), signal-to-noise ratio (SNR), as well as the basic image reconstruction principles based on the Fourier transform. In addition, we describe the main pulse sequences used during this thesis and the contrast they generate: the RARE pulse sequence for T2-weighted imaging, the FLASH pulse sequence for T1-weighted imaging, and the FISP pulse sequence. For more detail about MRI as well as the pulse sequences, one can refer to the literature [1, 2, 3, 4, 5]. Note that, in this thesis, vectors are usually denoted using bold-face font, scalar numbers or complex numbers using regular font.

## 1 NMR

Neutrons and protons have the intrinsic quantum property of spin, characterized by the nuclear spin quantum number  $s$  (for more details see [6]). The absolute value of the spin angular momentum is

$$S = \frac{h}{2\pi} \sqrt{s(s+1)}, \quad (1)$$

where  $h = 6.626 \times 10^{-34} \text{Js}$  is the Planck constant. The magnetic quantum number is denoted by  $m$  and can have  $2s+1$  values:  $m = -s, -s+1, \dots, s-1, s$ . The  $z$ -component of the spin angular momentum vector is

$$S_z = m_s \frac{h}{2\pi}. \quad (2)$$

The  $^1\text{H}$  nucleus has one proton and it has spin value  $s = \frac{1}{2}$ , associated with a magnetic moment

$$\boldsymbol{\mu} = \gamma \mathbf{S}, \quad (3)$$

where  $\gamma$  is the gyromagnetic ratio, a characteristic specific to the considered nucleus (for proton  $\gamma = 2.68 \times 10^8 \text{ rad s}^{-1} \text{ T}^{-1}$ ). In the presence of an external homogeneous magnetic field  $\mathbf{B}$  this results in a torque

$$\mathbf{T} = \boldsymbol{\mu} \times \mathbf{B}, \quad (4)$$

where  $\boldsymbol{\mu}$  is the magnetic moment, with a related potential energy equal to

$$E = -\boldsymbol{\mu} \cdot \mathbf{B}. \quad (5)$$

The  $^1\text{H}$  nucleus can have one of two spin states, referred to as spin-up ( $m_s = \frac{1}{2}$ , also referred to as “parallel” state) and spin-down ( $m_s = -\frac{1}{2}$ , also referred to as “anti-parallel” state). The two states have equal energy and at thermal equilibrium, the number of

spin in the spin-up state is approximately equal to the number of spins in the spin-down state. In the presence of an external magnetic field  $\mathbf{B}_0$ , directed along a particular direction, conventionally denoted by  $\mathbf{z}$ ,  $\mathbf{B}_0 = B_0\mathbf{z}$ , the interaction between the nuclear magnetic moment and the external magnetic field splits the energy level into two levels (for an arbitrary nucleus the energy level splits into  $(2s+1)$  levels called Zeeman levels). Then the  $z$ -component of a nuclear magnetic moment in (3) becomes  $\mu_z = \gamma m \frac{h}{2\pi}$  and the energy level of each state is

$$E_m = -\mu_z B_0 = -\gamma m \frac{h}{2\pi} B_0. \quad (6)$$

Therefore, for proton, the difference in the energy levels for the two states is  $\Delta E = \gamma \frac{h}{2\pi} B_0$ . The excess of spins in the lower energy state gives the equilibrium magnetization  $M_0$  which is oriented along the external field (direction  $\mathbf{z}$ ). The difference in the energy levels can be rewritten as:

$$\nu = \frac{\omega_0}{2\pi} = \frac{\Delta E}{h} = \frac{\gamma}{2\pi} B_0, \quad (7)$$

where  $\omega_0$  is called the Larmor angular frequency.  $\omega_0$  is proportional to the strength of the magnetic field  $B_0$  and can be calculated using the Larmor equation:

$$\omega_0 = \gamma B_0. \quad (8)$$

The Larmor frequency  $\omega_0$  is measured in megahertz (MHz), the gyromagnetic ratio  $\gamma$  is in MHz/T and the magnetic field strength  $B_0$  is in Tesla (T). Following the Boltzmann distribution, the net magnetization is given by

$$\mathbf{M}_0 = M_0\mathbf{z} = \rho \frac{\gamma^2}{4kT} \left( \frac{h}{2\pi} \right)^2 B_0\mathbf{z}, \quad (9)$$

where  $k$  is the Boltzmann constant and  $T$  is the temperature in Kelvin. The unit vector  $\mathbf{z} = (0, 0, 1)$  gives the direction of the external magnetic field. The spin density  $\rho$  is a characteristic of the object being imaged and depends on its chemical content and structure.

## 1.1 Bloch Equations

To detect a NMR signal the bulk magnetization vector must be tipped away from the  $z$ -direction by applying another magnetic field (i.e  $\mathbf{B}_1$  field) perpendicular to  $\mathbf{B}_0$ . When the macroscopic magnetization interacts with this time-varying external magnetic field  $\mathbf{B}(t)$ , its evolution can be described by the equation of motion in completely classical terms, which is the approach we will pursue in what follows. The equation of motion is known as the Bloch equation for the magnetization is the simple equation:

$$\frac{d\mathbf{M}}{dt} = \gamma (\mathbf{M} \times \mathbf{B}), \quad (10)$$

where  $\mathbf{B}$  is the total magnetic field. For the case  $\mathbf{B} = \mathbf{B}_0 = (0, 0, B_0)$ , the coordinate form of (10) is

$$\begin{aligned}\frac{dM_x}{dt} &= \gamma B_0 M_y, \\ \frac{dM_y}{dt} &= -\gamma B_0 M_x, \\ \frac{dM_z}{dt} &= 0.\end{aligned}\tag{11}$$

Under an initial condition

$$\mathbf{M}(t = 0) = [M_x(0), M_y(0), M_z(0)],$$

these equation have the solution (see [7])

$$\begin{aligned}M_x(t) &= M_x(0) \cos(-\omega_0 t) - M_y(0) \sin(-\omega_0 t), \\ M_y(t) &= M_x(0) \sin(-\omega_0 t) + M_y(0) \cos(-\omega_0 t), \\ M_z(t) &= M_z(0),\end{aligned}\tag{12}$$

in which  $\omega_0 = \gamma B_0$ , the Larmor angular frequency, represents the precession frequency of spins located in a magnetic field (Figure 1). Following the application of a radio-

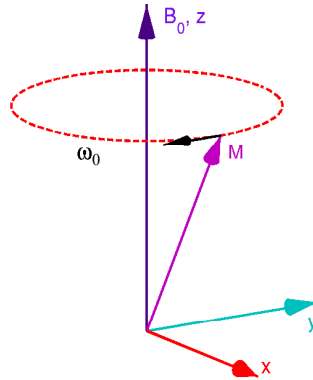


Figure 1 – In presence of a static magnetic field, the spin magnetic moments and the resulting bulk magnetization precesses at the Larmor frequency.

frequency (RF) pulse (a magnetic field, the direction of which is oscillating at the Larmor frequency), the equilibrium magnetization is deviated from the  $\mathbf{B}_0$  direction ( $z$ -direction) by an angle  $\alpha$  (the flip angle) given by:

$$\alpha = \gamma \int_0^\tau B_1(t) dt,\tag{13}$$

where  $\tau$  is the length of time the field with the magnitude  $B_1(t)$  is turned ON.

In the case  $\mathbf{B} = \mathbf{B}_0 = (0, 0, B_0)$  and initial conditions  $\mathbf{M}(t = 0) = M_0(\sin\alpha, 0, \cos\alpha)$ , the solutions of (10) are:

$$\begin{aligned}M_x &= M_0 \sin\alpha \cos(-\omega_0 t), \\ M_y &= M_0 \sin\alpha \sin(-\omega_0 t), \\ M_z &= M_0 \cos\alpha.\end{aligned}$$

The complex transverse component of  $\mathbf{M}$  is a single complex value  $M_{\perp}$  given by

$$M_{\perp} = M_x + iM_y = M_0 \sin(\alpha) e^{-i\omega_0 t},$$

where  $i = \sqrt{-1}$  is the imaginary unit.

If the magnetization vector is tipped (nutated) to the  $x - y$  plane, then the RF pulse is called a 90 degree pulse and the duration of the pulse must satisfy  $\gamma B_1 \tau = \pi/2$ , where  $B_1$  is the magnitude of the RF field and  $\tau$  is the width of the pulse. The nutation magnetization by the angle 90 degree is described in equation (10) with  $\mathbf{B} = (B_1 \cos(\omega t), 0, B_0)$ .

After the RF pulse has been turned off, the magnetization vector starts to return back to the direction of the static magnetic field. It is most advantageous to analyze the magnetization and its differential equations in terms of parallel and perpendicular components relative to the static main magnetic field,  $\mathbf{B} = B_0 \mathbf{z}$ . For the case of non-interacting spins, the parallel, or “longitudinal”, component of the magnetization satisfies:

$$\frac{dM_z}{dt} = 0, \quad (14)$$

and the transverse component  $\mathbf{M}_{\perp} = M_x \mathbf{x} + M_y \mathbf{y}$  satisfies:

$$\frac{d\mathbf{M}_{\perp}}{dt} = \gamma \mathbf{M}_{\perp} \times \mathbf{B}, \quad (15)$$

where

$$\mathbf{B} = \begin{bmatrix} 0 \\ 0 \\ B_0 \end{bmatrix}.$$

Due to the interactions between the spins and the lattice there are terms in equations (14) and (15) which depend on different decay parameters. Specifically, for equation (14) the magnetic moments tend to align with the external magnetic field in order to reach their minimum energy state. As a result, the rate of the change of the longitudinal magnetization  $\frac{dM_z}{dt}$  is proportional to the difference  $M_0 - M_z$ . The proportionality constant,  $T_1$ , is empirically determined and represents the inverse of the growth rate. The equation (14) becomes:

$$\frac{dM_z}{dt} = \frac{1}{T_1} (M_0 - M_z), \quad (16)$$

$T_1$  is the called “spin-lattice relaxation time”. Immediately after the RF pulse is turned off, the time decay of longitudinal magnetization, with initial value  $M_z(0)$ , to the equilibrium value  $M_0$  is described by:

$$M_z(t) = M_z(0) e^{-t/T_1} + M_0 (1 - e^{-t/T_1}). \quad (17)$$

The solution for an arbitrary starting point  $t_0$  can be written as:

$$M_z(t) = M_z(0) e^{-(t-t_0)/T_1} + M_0 (1 - e^{-(t-t_0)/T_1}). \quad (18)$$

For equation (15), the characterization of the overall rate of reduction in the transverse magnetization brings forward another experimental parameter, the “spin-spin” or

transverse relaxation time  $T_2$ . The equation (15) can be rewritten including the  $T_2$  term as:

$$\frac{d\mathbf{M}_\perp}{dt} = \gamma\mathbf{M}_\perp \times \mathbf{B} - \frac{1}{T_2}\mathbf{M}_\perp. \quad (19)$$

The Bloch equation (10) with  $T_1$  and  $T_2$  relaxation becomes

$$\frac{d\mathbf{M}}{dt} = \gamma(\mathbf{M} \times \mathbf{B}) - \frac{(M_x\mathbf{x} + M_y\mathbf{y})}{T_2} - \frac{(M_z - M_0)\mathbf{z}}{T_1}. \quad (20)$$

Under an initial condition  $\mathbf{M}(t=0) = [M_x(0), M_y(0), M_z(0)]$ , the solution is (see [7])

$$\begin{aligned} M_x(t) &= e^{-t/T_2} (M_x(0) \cos(-\omega_0 t) - M_y(0) \sin(-\omega_0 t)), \\ M_y(t) &= e^{-t/T_2} (M_x(0) \sin(-\omega_0 t) + M_y(0) \cos(-\omega_0 t)), \\ M_z(t) &= M_z(0) e^{-t/T_1} + M_0 (1 - e^{-t/T_1}). \end{aligned} \quad (21)$$

The longitudinal component decays from its initial value of  $M_z(0)$  toward its equilibrium value of  $M_0$ . The transverse component rotates at frequency  $\omega_0$  and decays towards zero. The complex transverse component of the magnetization  $M_{xy} = M_x + iM_y$  becomes

$$\begin{aligned} M_{xy}(t) &= M_{xy}(0) e^{-t/T_2} e^{-i\omega_0 t}, \\ &= |M_{xy}(0)| e^{-i\omega_0 t + i\phi_0} e^{-t/T_2}, \end{aligned} \quad (22)$$

where  $\phi_0$  and  $|M_{xy}(0)|$  are the phase and the module of the complex number  $M_{xy}(0)$ , respectively.

## 1.2 Signal detection

To detect the NMR signal it is necessary to have an RF coil which is in the transverse plane, that is, perpendicular to the  $\mathbf{B}_0$  field. The receiver coil, which usually surrounds the sample, is an antenna which ‘‘picks-up’’ the voltage  $V(t)$  induced by the precessing of the magnetization. The voltage induced in the receive coil is given by

$$V(t) = -\frac{d}{dt} \int (\mathbf{M}(\mathbf{r}, t) \cdot \mathbf{B}^{rf}(\mathbf{r})) d\mathbf{r}, \quad (23)$$

where  $\mathbf{B}^{rf}(\mathbf{r})$  describes the sensitivity of the receiver coil at different points in space. More specifically,  $\mathbf{B}^{rf}(\mathbf{r})$  is the ratio of the magnetic field produced by the receiver coil to the current in the coil (magnetic field per unit current).  $\mathbf{B}^{rf}(\mathbf{r})$  can be measured in a given coil, or calculated from for a particular coil geometry. The primary objective of the receiver coil design is to prescribe wire placements so that  $\mathbf{B}^{rf}(\mathbf{r})$  has the largest possible transverse component. The longitudinal component of  $\mathbf{B}^{rf}(\mathbf{r})$  contributes little to the output voltage, and can be ignored. This is a result of the fact that the time derivative of  $M_z(t, \mathbf{r})$  is much smaller than that of the transverse component.  $M_z(\mathbf{r}, t)$  decays exponentially with the time constant  $T_1$ , typically hundreds to thousands milliseconds, while the transverse component oscillates with a period of relaxation  $T_2$  on the order of tens to hundreds of milliseconds for protons in most live tissue. The magnetic resonance (MR) signal measured by some electronics system is proportional to (23) and it depends

on amplifier gain and other system characteristics. The MR signal can be written in terms of the space components,  $\mathbf{r}$ , as

$$s(t) \propto -\frac{d}{dt} \int [M_x(\mathbf{r}, t) \mathbf{B}_x^{rf}(\mathbf{r}) + M_y(\mathbf{r}, t) \mathbf{B}_y^{rf}(\mathbf{r}) + M_z(\mathbf{r}, t) \mathbf{B}_z^{rf}(\mathbf{r})] d\mathbf{r}. \quad (24)$$

Note that the solutions  $M_x(\mathbf{r}, t)$ ,  $M_y(\mathbf{r}, t)$ ,  $M_z(\mathbf{r}, t)$ , and the transverse component  $M_{xy}(\mathbf{r}, t)$  are determined by equations (21) and (22). For static fields with magnitudes of several tesla, the Larmor frequency  $\omega_0$  for proton is at least four orders-of-magnitude larger than typical values of  $\frac{1}{T_1}$  and  $\frac{1}{T_2}$ . Hence the time derivative of the  $e^{-t/T_1}$  and  $e^{-t/T_2}$  can be neglected, compared with the derivative of the  $e^{-i\omega_0 t}$  factor. The time derivative of transverse component is

$$\frac{dM_{xy}(\mathbf{r}, t)}{dt} = -|M_{xy}(\mathbf{r}, 0)| \left( \frac{1}{T_2(\mathbf{r})} + i\omega_0 \right) e^{-t/T_2(\mathbf{r}) - i\omega_0 t + i\phi_0(\mathbf{r})}. \quad (25)$$

Since  $\frac{1}{T_1}$  and  $\frac{1}{T_2}$  are very small compared to  $\omega_0$ , and  $M_x = \text{Re}(M_{xy})$  and  $M_y = \text{Im}(M_{xy})$ , the MR signal can be approximation by

$$\begin{aligned} s(t) &\propto \omega_0 \int e^{-t/T_2(\mathbf{r})} |M_{xy}(\mathbf{r}, 0)| [\text{Re}(ie^{-i\omega_0 t + i\phi_0(\mathbf{r})}) \mathbf{B}_x^{rf}(\mathbf{r}) + \text{Im}(ie^{-i\omega_0 t + i\phi_0(\mathbf{r})}) \mathbf{B}_y^{rf}(\mathbf{r})] d\mathbf{r} \\ &\propto \omega_0 \int e^{-t/T_2(\mathbf{r})} |M_{xy}(\mathbf{r}, 0)| [\sin(\omega_0 t - \phi_0(\mathbf{r})) \mathbf{B}_x^{rf}(\mathbf{r}) + \cos(\omega_0 t - \phi_0(\mathbf{r})) \mathbf{B}_y^{rf}(\mathbf{r})] d\mathbf{r}. \end{aligned} \quad (26)$$

By denoting the magnitude  $\mathbf{B}_\perp^{rf}$  and the phase  $\theta_{\mathbf{B}}$  of the complex number  $\mathbf{B}_{xy}^{rf} = \mathbf{B}_x^{rf} + i\mathbf{B}_y^{rf} = \mathbf{B}_\perp^{rf} e^{i\theta_{\mathbf{B}}}$ , it implies that  $\mathbf{B}_x^{rf} = \mathbf{B}_\perp^{rf} \cos\theta_{\mathbf{B}}$  and  $\mathbf{B}_y^{rf} = \mathbf{B}_\perp^{rf} \sin\theta_{\mathbf{B}}$  and thanks to the trigonometric identity  $\sin(a+b) = \sin a \cos b + \cos a \sin b$ , the equation (26) can be simplified as

$$s(t) \propto \omega_0 \int e^{-t/T_2(\mathbf{r})} |M_{xy}(\mathbf{r}, 0)| \mathbf{B}_\perp^{rf}(\mathbf{r}) \sin(\omega_0 t - \phi_0(\mathbf{r}) + \theta_{\mathbf{B}}(\mathbf{r})) d\mathbf{r}. \quad (27)$$

Assume that the sample volume is  $V_s$ , for the limit case where all quantities in (27) do not depend on in the spatial position  $\mathbf{r}$ , then

$$s(t) \propto \omega_0 V_s e^{-t/T_2} |M_{xy}(0)| \mathbf{B}_\perp^{rf} \sin(\omega_0 t - \phi_0 + \theta_{\mathbf{B}}). \quad (28)$$

In practice, the signal is measured through two channels, which are called real and imaginary, corresponding to the multiplication of the signal by a sinusoid or a cosinusoid with a frequency of  $\omega = \omega_0 + \delta_\omega$  near  $\omega_0$ , where  $\delta_\omega$  is the offset frequency. Through some mathematical approximation with low pass filtering, the real signal is determined by

$$s_{re}(t) \propto \frac{1}{2} \omega_0 \int e^{-t/T_2(\mathbf{r})} |M_{xy}(\mathbf{r}, 0)| \mathbf{B}_\perp^{rf}(\mathbf{r}) \cos(\delta_\omega t + \phi_0(\mathbf{r}) - \theta_{\mathbf{B}}(\mathbf{r})) d\mathbf{r}, \quad (29)$$

and the imaginary signal is determined by

$$s_{im}(t) \propto \frac{1}{2} \omega_0 \int e^{-t/T_2(\mathbf{r})} |M_{xy}(\mathbf{r}, 0)| \mathbf{B}_\perp^{rf}(\mathbf{r}) \sin(\delta_\omega t + \phi_0(\mathbf{r}) - \theta_{\mathbf{B}}(\mathbf{r})) d\mathbf{r}. \quad (30)$$

Now, the complex signal  $s(t) = s_{re}(t) + i s_{im}(t)$  becomes

$$\begin{aligned} s(t) &\propto \frac{1}{2}\omega_0 \int e^{-t/T_2(\mathbf{r})} |M_{xy}(\mathbf{r}, 0)| \mathbf{B}_{\perp}^{rf}(\mathbf{r}) e^{i(\delta_{\omega}t + \phi_0(\mathbf{r}) - \theta_{\mathbf{B}}(\mathbf{r}))} d\mathbf{r} \\ &\propto \frac{1}{2}\omega_0 \int e^{-t/T_2(\mathbf{r})} |M_{xy}(\mathbf{r}, 0)| \mathbf{B}_{\perp}^{rf}(\mathbf{r}) e^{i[(\omega - \omega_0)t + \phi_0(\mathbf{r}) - \theta_{\mathbf{B}}(\mathbf{r})]} d\mathbf{r} \\ &\propto \frac{1}{2}\omega_0 \int M_{xy}(\mathbf{r}, t) \mathbf{B}_{xy}^{rf}(\mathbf{r}) e^{i\omega t} d\mathbf{r}. \end{aligned} \quad (31)$$

Since the usual computer is digital and not analog, it is necessary to convert from the analog complex signal to two arrays of digital signal numbers  $s_n$  (corresponding with real and imaginary signal sampling) given by

$$s_n \propto \omega_0 \int M_{xy}(\mathbf{r}, t) \mathbf{B}_{xy}^{rf}(\mathbf{r}) e^{i\omega n \Delta t} d\mathbf{r}, \quad (32)$$

where the sampling time interval is  $\Delta t$ .

## 2 MRI

As explained before, inside the MRI scanner, there is a strong static magnetic field of magnitude  $B_0$  applied along what is conventionally called the positive  $z$ -direction, resulting in a net magnetization in the positive  $z$ -direction. When a time-varying magnetic field (much weaker than the static magnetic field) is applied for a short time at the resonance frequency,  $\omega_0 = \gamma B_0$ , where  $\gamma/(2\pi) = 42.576$  MHz/Tesla is the gyromagnetic ratio of the water proton, the net magnetization is tipped away from the  $z$ -axis. For simplicity, we assume that the net magnetization is tipped onto the  $x - y$  plane, then the oscillating magnetic field will be called a 90 degree pulse. The magnetization vector will precess around the  $z$ -axis, inducing a voltage in the receiver coil (see Figure 2). The net magnetization will realign along the  $z$ -direction, due to two relaxation effects:

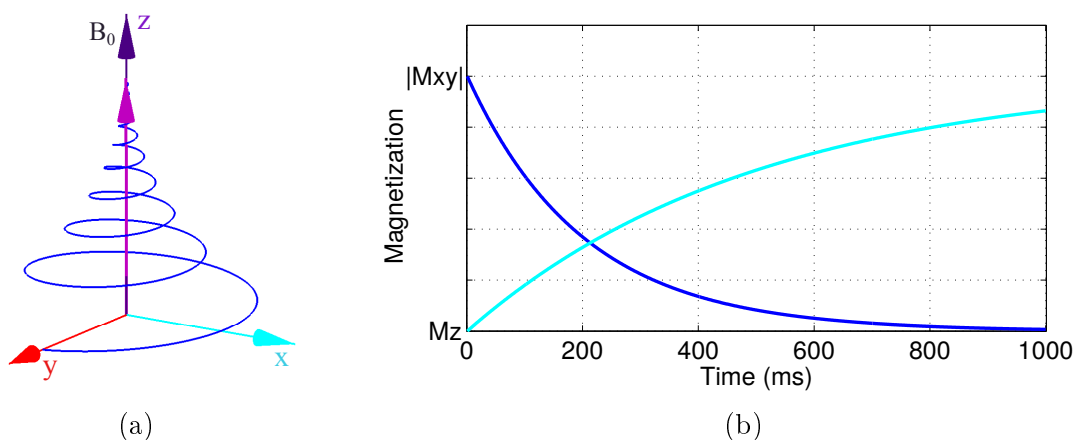


Figure 2 – Effects of relaxation on the magnetization vector after a 90 degree excitation pulse. (a) The magnetization vector precesses around the  $z$ -axis. (b) The measured net magnetization in the  $x - y$  plane ( $M_{xy}$ ) and the  $z$ -component of the relaxing magnetization. In both subfigures,  $T_2 = 200$  ms,  $T_1 = 500$  ms.

the spin-lattice relaxation (recovery the net magnetization along the  $z$ -direction to its original value), and the spin-spin relaxation (the decay of the net magnetization in the  $x - y$  plane to zero). The rate constant of the first relaxation is called  $T_1$  and the rate constant of the second kind of relaxation is called  $T_2$ . Both  $T_1$  and  $T_2$  vary according to the tissue environment and depend on the external magnetic field  $\mathbf{B}_0$ . The MR signal also depends on the spin density varies with the tissue environment.

Usually, in which addition to  $T_2$  (spin-spin) relaxation, local field inhomogeneities also contribute to the signal decay, this effect is called  $T_2^*$  and can be cancelled by a refocusing 180 degree pulse, applied at  $t = TE/2$  after the 90 degree pulse, producing an echo at  $TE$ , that gives a measured signal that will have only the contribution from  $T_2$ . Such a sequence of applied RF pulses is called a spin echo sequence.

## 2.1 Gradient encoding

The spatial encoding of the signal is obtained by applying additional magnetic fields in all three directions called magnetic field gradients or gradient fields  $G_x(t)$ ,  $G_y(t)$  and  $G_z(t)$ . The gradient fields are produced by a set of three independently computer-controlled coils. These coils are referred as the  $x$ -gradient,  $y$ -gradient and  $z$ -gradient coils. In the presence of the magnetic field gradient,  $\mathbf{G}$ , the local magnetic field is given by:

$$\mathbf{B}(\mathbf{r}, t) = (B_0 + \mathbf{G}(t) \cdot \mathbf{r})\mathbf{z}.$$

The spatial varying magnetic field  $\mathbf{B}(\mathbf{r})$  is generated by applying magnetic field gradients in all three directions  $\mathbf{G} = (G_x, G_y, G_z)$ . The magnetic field gradients are given by:

$$\begin{aligned} G_x &= \frac{dB_z}{dx} \\ G_y &= \frac{dB_z}{dy} \\ G_z &= \frac{dB_z}{dz} \end{aligned} \quad (33)$$

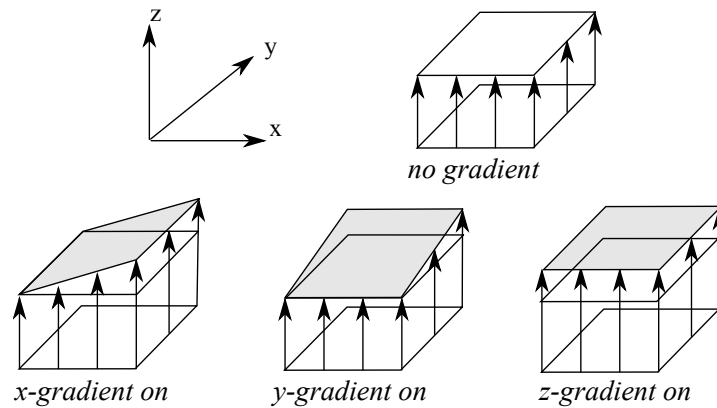


Figure 3 – Diagram of gradient field effects on the main magnetic field  $\mathbf{B}_0$ .

In this case, the Larmor frequency  $\omega_0$  in all the equations mentioned in the previous section will be replaced by the precession frequency of the transverse magnetization

$M_{xy}(\mathbf{r})$ , which is the Larmor frequency plus a frequency offset due to imaging gradient  $\mathbf{G}(t)$ :

$$\begin{aligned}\omega(\mathbf{r}, t) &= \omega_0 + \omega_G(\mathbf{r}, t) \\ &= \gamma B_0 + \gamma \mathbf{G}(t) \cdot \mathbf{r},\end{aligned}$$

where  $\omega_G(\mathbf{r}, t) = \gamma \mathbf{G}(t) \cdot \mathbf{r}$  and  $B_0$  is the main magnetic field. The accumulated phase offset due to the applied gradient, at time  $t$ , is

$$\phi_G(\mathbf{r}, t) = -\gamma \int_0^t \mathbf{G}(t') \cdot \mathbf{r} dt'. \quad (34)$$

In a reference frame rotating at frequency  $\omega_0$ , the complex transverse magnetization in the  $x - y$  plane,  $M(\mathbf{r}, t) := M_x(\mathbf{r}, t) + iM_y(\mathbf{r}, t)$ , obeys the Bloch equation:

$$\frac{\partial M(\mathbf{r}, t)}{\partial t} = -i\gamma \mathbf{r} \cdot \mathbf{G}(t)M(\mathbf{r}, t) - \frac{M(\mathbf{r}, t)}{T_2(\mathbf{r})}, \quad (35)$$

where  $T_2(\mathbf{r})$  is the local spin-spin relaxation rate. The solution of equation (35) is

$$M(\mathbf{r}, t) = \rho(\mathbf{r}) e^{-t/T_2(\mathbf{r})} e^{-i\mathbf{r} \cdot (\gamma \int_0^t \mathbf{G}(s) ds)}, \quad (36)$$

where  $t = 0$  is the start of the 90 degree pulse and  $\rho(\mathbf{r})$  is the spin density.

## 2.2 $k$ -space

One of the most important concepts in MRI is the  $k$ -space, which was introduced in 1981 by Likes [8] and in 1983 by Ljunggren [9] and Twieg [10]. Briefly, *k-space is an array of numbers representing spatial frequencies associated with the MR image*. In MRI,  $k$ -space is the two dimensional (2D) or three dimensional (3D) Fourier transform of the MR image. The  $k$ -space points or Fourier data (complex values) are collected during the MR acquisition. Each  $k$ -space point contains spatial frequency and phase information about every pixel in the final image. Conversely, each pixel in the image maps to every point in  $k$ -space. The individual points in  $k$ -space do **not** correspond one-to-one with individual pixels in the image.

For a general gradient  $\mathbf{G}$ , the  $k$ -space coordinate is defined as:

$$\mathbf{k}(t) = \frac{\gamma}{2\pi} \int_0^t \mathbf{G}(s) ds. \quad (37)$$

Some authors omit the factor of  $2\pi$  in the denominator from the definition of  $k$ -space, this factor is absorbed it into the definition of  $\gamma$ . The  $k$ -space has units of inverse distance, typically inverse centimeters ( $\text{cm}^{-1}$ ). For a time-constant gradient  $G_x$ ,  $G_y$ ,  $G_z$ , we get

$$k_x(t) = \frac{\gamma}{2\pi} G_x t, \quad (38)$$

$$k_y(t) = \frac{\gamma}{2\pi} G_y t, \quad (39)$$

$$k_z(t) = \frac{\gamma}{2\pi} G_z t. \quad (40)$$

Using the k-space definition, the magnetization located at position  $\mathbf{r}$  (Equation (36)) becomes

$$M(\mathbf{r}, t) = \rho(\mathbf{r}) e^{-t/T_2(\mathbf{r})} e^{-i2\pi\mathbf{k}(t)\cdot\mathbf{r}},$$

and the MRI signal can be written as

$$S(\mathbf{k}(t)) = \int \mu(\mathbf{r}) e^{-i2\pi\mathbf{k}(t)\cdot\mathbf{r}} d\mathbf{r}, \quad (41)$$

where  $\mu(\mathbf{r})$  is the effective spin density, which is proportional to the magnitude of the external magnetic field, the spin density and the relaxation constants (see more [1]).

## 2.3 Fourier transform and image reconstruction

The Fourier transform is one of the most important theories in signal processing, especially in MRI. It is thoroughly described in several textbooks [11, 12, 13, 14]. In what follows I will briefly introduce the concept of Fourier transform and its application to MRI.

The Fourier transform defines a relationship between the image domain and its representation in the frequency domain. The original signal can be recovered from knowing the Fourier transform, and vice versa, without loss of information. Theoretically, the Fourier transform is defined by:

$$S(\mathbf{k}) = \int \mu(\mathbf{r}) e^{-i2\pi\mathbf{r}\cdot\mathbf{k}} d\mathbf{r}, \quad (42)$$

and the inverse Fourier transform is defined by:

$$\mu(\mathbf{r}) = \int S(\mathbf{k}) e^{i2\pi\mathbf{r}\cdot\mathbf{k}} d\mathbf{k}, \quad (43)$$

where  $S(\mathbf{k})$  is called Fourier transform of  $\mu(\mathbf{r})$  and vice versa  $\mu(\mathbf{r})$  is called inverse Fourier transform of  $S(\mathbf{k})$ . Briefly, we denote  $\mathcal{F}\mu$  for Fourier transform of  $\mu$  and  $\mathcal{F}^{-1}S$  for inverse Fourier transform of  $S$ . Note that, there are some other forms of Fourier transform definitions. Following the helpful summary provided by T. W. Körner in his book *Fourier Analysis* [14]. We can define

$$S(\mathbf{k}) = \frac{1}{A} \int \mu(\mathbf{r}) e^{iB\mathbf{r}\cdot\mathbf{k}} d\mathbf{r},$$

where  $A = \sqrt{2\pi}$ ,  $B = \pm 1$ ;  $A = 1$ ,  $B = \pm 2\pi$ . In this thesis we have chosen  $A = 1$  and  $B = -2\pi$ .

Equation (41) implies that the MRI signal, acquired at echo time  $t = \text{TE}$ , is the Fourier transform of the effective spin density

$$S(\mathbf{k}) = \int \mu(\mathbf{r}) e^{-i2\pi\mathbf{k}\cdot\mathbf{r}} d\mathbf{r} = \mathcal{F}\mu(\mathbf{k}), \quad (44)$$

and vice versa the effective spin density is the inverse Fourier transform of the MRI signal

$$\mu(\mathbf{r}) = \int S(\mathbf{k}) e^{i2\pi\mathbf{k}\cdot\mathbf{r}} d\mathbf{k} = \mathcal{F}^{-1}S(\mathbf{r}). \quad (45)$$

The 2D and 3D Fourier transform (and inverse Fourier transform) formulas will be mentioned in the following sections in the content of image reconstruction in 2D and 3D.

## 2.4 Frequency encoding

In 2D and 3D MR imaging, the most straightforward type of gradient encoding is the frequency encoding. Keep in mind that the frequency encoding only on one direction. If a gradient  $G_x(t)$  is applied to the sample, the precessing frequency will change linearly with the location  $\mathbf{r} = (x, 0, 0)$ ,

$$\begin{aligned}\omega(\mathbf{r}, t) &= \gamma \mathbf{G}(t) \cdot \mathbf{r} \\ &= \gamma G_x(t)x\end{aligned}\tag{46}$$

If the signal is read out while this gradient is on, contributions from different locations along the  $x$  axis will exhibit different frequencies. This process is called frequency encoding, and corresponding gradient is called frequency encoding gradient (or read gradient). Note that the frequency encoding gradient strength does not change during the acquisition.

## 2.5 2D imaging

### 2.5.1 Slice selection

When performing 2D MRI, the image is acquired in a sub-volume of the sample. Slice selection is used to selectively excite the spins in a “defined plane”. The space dependence of the Larmor frequency in the presence of a gradient can be used to selectively excite the spins within a slice perpendicular to the gradient direction. Since only the excited spins generate a signal, this is used to restrict the imaged volume of sample. As described before, the resonance frequency of the spins during the  $z$  gradient is:

$$\omega(z) = \gamma B_0 + \gamma G_z z = \omega_0 + \omega_G(z).$$

Note that at  $z = 0$  (isocenter) the frequency  $\omega = \gamma B_0 = \omega_0$ . The  $z$  location of the excited spins and thus the slice plane will be  $z = \frac{\omega_G(z)}{\gamma G_z}$  (see Figure 4). If a gradient is applied in the  $z$  direction during an RF excitation pulse of bandwidth  $W = \Delta\omega$  with single frequency  $\omega$ , only the spins in a thin slice (thickness  $\Delta z$ ) are excited :

$$\Delta z = \frac{W}{\gamma G_z}.\tag{47}$$

After the excitation pulse, the selected transverse magnetization in the sample is essentially a two dimensional distribution.

### 2.5.2 Phase encoding

If a magnetic field gradient is applied in the  $y$  direction for a given time interval  $\Delta t_y$ , the Larmor frequency will vary in this direction during that time interval, so that the signal at different positions will accumulate a different phase. After the gradient has been switched off, the precession frequency will return to a constant value, while the

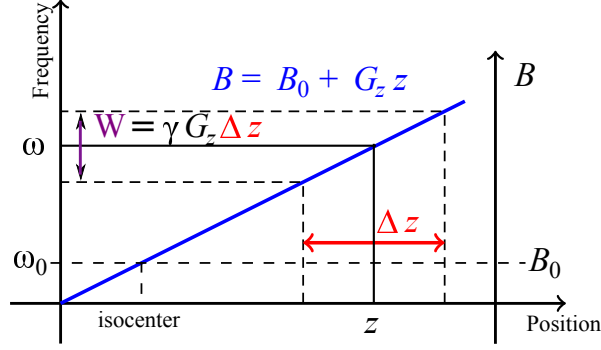


Figure 4 – Diagram of the slice selection when applying an excitation pulse. A gradient  $G_z$  imposes a space dependence on the main magnetic field. An RF pulse with the single frequency  $\omega$  will excite only the spins at the appropriate position. Thus, the slice position depends on the strength of the gradient and the pulse frequency.

imprinted phase remains proportional to  $y$ . This process is called phase encoding.

$$\begin{aligned}\phi(\mathbf{r}) &= (\omega(\mathbf{r}) - \omega_0(\mathbf{r})) \Delta t_y \\ &= \gamma G_y y \Delta t_y \\ &= 2\pi k_y y,\end{aligned}\quad (48)$$

where  $k_y = \frac{\gamma}{2\pi} G_y \Delta t_y$ .

### 2.5.3 2D image reconstruction

Suppose  $z \in [(z_0 - \frac{1}{2}\Delta z), (z_0 + \frac{1}{2}\Delta z)]$  are the limits of the slice of interest. By choosing  $\mathbf{G}(t) = (0, G_y, 0)$  (phase) for a time interval  $\Delta t_y$  and then choosing  $\mathbf{G}(t) = (G_x, 0, 0)$  (read) for a time interval  $\Delta t_x$ , then since the  $z$  component of gradient encoding  $\mathbf{G}(t)$  equal zeros, the magnetization at  $\mathbf{r}$  at TE is

$$M(\mathbf{r}, t) = \rho(x, y, z) e^{-\text{TE}/T_2(\mathbf{r})} e^{-i2\pi(k_x x + k_y y)},$$

where  $k_x = \frac{\gamma}{2\pi} G_x \Delta t_x$  and  $k_y = \frac{\gamma}{2\pi} G_y \Delta t_y$ . The MRI signal in equation (44) can be rewritten as

$$S(k_x, k_y) = \int \int \left[ \int_{(z_0 - \frac{1}{2}\Delta z)}^{(z_0 + \frac{1}{2}\Delta z)} \mu(x, y, z) dz \right] e^{-i2\pi(k_x x + k_y y)} dx dy. \quad (49)$$

The effective spin density in slice  $l$  is:

$$\mu_l(x, y) = \left( \int_{(z_0 - \frac{1}{2}\Delta z)}^{(z_0 + \frac{1}{2}\Delta z)} \mu(x, y, z) dz \right). \quad (50)$$

It is clear that the MRI signal in equation (49) is the 2D Fourier transform of the contrast function in equation (50):

$$\begin{aligned}S(k_x, k_y) &= \int \int \mu_l(x, y) e^{-i2\pi(k_x x + k_y y)} dx dy \\ &= \mathcal{F}_{2D}[\mu_l(x, y)](k_x, k_y).\end{aligned}$$

Therefore,

$$\begin{aligned}\mu_l(x, y) &= \int \int S(k_x, k_y) e^{i2\pi(k_x x + k_y y)} dk_x dk_y \\ &= \mathcal{F}_{2D}^{-1}[S(k_x, k_y)](x, y).\end{aligned}$$

As mentioned in section 2.2, the effective spin density  $\mu(x, y, z)$  is proportional to the magnitude of the external magnetic field, the spin density and the relaxation constants, thus  $\mu_l(x, y)$  proportional these parameters as well.

By the appropriate choice of  $G_x$ ,  $G_y$ , and  $\Delta t_x$  and  $\Delta t_y$  the Fourier transform can be obtained for a set of 2D Fourier points. Then the inverse Fourier transform can be performed and then sampled at physical space points to obtain the image intensity in each voxel,  $V_{i,j,l}$  where

$$\begin{aligned}V_{i,j,l} := & \left[ \left( i - \frac{1}{2} \right) \Delta x, \left( i + \frac{1}{2} \right) \Delta x \right] \times \left[ \left( j - \frac{1}{2} \right) \Delta y, \left( j + \frac{1}{2} \right) \Delta y \right] \\ & \times \left[ \left( z_0 - \frac{1}{2} \Delta z \right), \left( z_0 + \frac{1}{2} \Delta z \right) \right].\end{aligned}$$

An average value of the effective spin density function for  $V_{i,j,l}$ :

$$\begin{aligned}\bar{\mu}_l(i, j, z_0) &\approx \int_{V_{i,j,l}} \mu(x, y, z) dx dy dz, \\ &\approx \int_{(j-\frac{1}{2})\Delta y}^{(j+\frac{1}{2})\Delta y} \int_{(i-\frac{1}{2})\Delta x}^{(i+\frac{1}{2})\Delta x} \left( \int_{(z_0-\frac{1}{2}\Delta z)}^{(z_0+\frac{1}{2}\Delta z)} \mu(x, y, z) dz \right) dx dy, \\ &\approx \int_{(j-\frac{1}{2})\Delta y}^{(j+\frac{1}{2})\Delta y} \int_{(i-\frac{1}{2})\Delta x}^{(i+\frac{1}{2})\Delta x} \mu_l(x, y) dx dy,\end{aligned}\tag{51}$$

can be displayed in an image.

## 2.6 3D imaging

In 3D imaging, instead of using slice selection, a second phase encoding gradient will be applied in  $z$  direction. This second phase encoding axis is typically called phase 2.

### 2.6.1 Phase 2 encoding

As for the primary phase encoding, if the gradient field in the  $z$  direction is applied for a given time interval  $\Delta t_z$ , the Larmor frequency will vary in this direction during that time interval, so that the signal at different positions accumulates a different phase. After the gradient has been switched off, the precession frequency returns to a constant value, while the imprinted phase remains proportional to  $z$ :

$$\begin{aligned}\phi(\mathbf{r}) &= (\omega(\mathbf{r}) - \omega_0(\mathbf{r})) \Delta t_z \\ &= \gamma G_z z \Delta t_z \\ &= 2\pi k_z z,\end{aligned}\tag{52}$$

where  $k_z = \frac{\gamma}{2\pi} G_z \Delta t_z$ .

### 2.6.2 3D image reconstruction

By choosing  $\mathbf{G}(t) = (0, 0, G_z)$  for a time interval  $\Delta t_z$ , then choosing  $\mathbf{G}(t) = (0, G_y, 0)$  for a time interval  $\Delta t_y$ , and finally choosing  $\mathbf{G}(t) = (G_x, 0, 0)$  for a time interval  $\Delta t_x$ , the magnetization at  $\mathbf{r}$  at TE is

$$M(x, y, z) = \rho(x, y, z) e^{-TE/T_2(x,y,z)} e^{-i2\pi(k_x x + k_y y + k_z z)},$$

where  $k_x = \frac{\gamma}{2\pi} G_x \Delta t_x$ ,  $k_y = \frac{\gamma}{2\pi} G_y \Delta t_y$  and  $k_z = \frac{\gamma}{2\pi} G_z \Delta t_z$ . The MRI signal in equation (44) can be rewritten as the 3D Fourier transform:

$$\begin{aligned} S(k_x, k_y, k_z) &= \int \int \int \mu(x, y, z) e^{-i2\pi(k_x x + k_y y + k_z z)} dx dy dz \\ &= \mathcal{F}_{3D}[\mu(x, y, z)](k_x, k_y, k_z). \end{aligned} \quad (53)$$

Therefore, the effective spin density is the inverse Fourier transform of the signal:

$$\begin{aligned} \mu(x, y, z) &= \int \int \int S(k_x, k_y, k_z) e^{i2\pi(k_x x + k_y y + k_z z)} dk_x dk_y dk_z \\ &= \mathcal{F}_{3D}^{-1}[S(k_x, k_y, k_z)](x, y, z). \end{aligned} \quad (54)$$

Then the inverse Fourier transform can be performed and then sampled at physical space points to obtain the image intensity in each voxel,  $V_{i,j,l}$  where

$$\begin{aligned} V_{i,j,l} := & \left[ \left( i - \frac{1}{2} \right) \Delta x, \left( i + \frac{1}{2} \right) \Delta x \right] \times \left[ \left( j - \frac{1}{2} \right) \Delta y, \left( j + \frac{1}{2} \right) \Delta y \right] \\ & \times \left[ \left( l - \frac{1}{2} \right) \Delta z, \left( l + \frac{1}{2} \right) \Delta z \right]. \end{aligned}$$

An average value of the effective spin density function for  $V_{i,j,l}$ :

$$\bar{\mu}(i, j, l) \approx \int_{V_{i,j,l}} \mu(x, y, z) dx dy dz, \quad (55)$$

that can be displayed in an image.

## 2.7 Resolution and FOV

The FOV is defined as the size of the two or three dimensional spatial encoding area of the image. We denote  $FOV_x$ ,  $FOV_y$  and  $FOV_z$  the size of the image in  $x$  (read),  $y$  (phase 1) and  $z$  (phase 2) directions, respectively. The FOV is typically divided into several picture elements (pixels). The number of points in each direction,  $N_x$ ,  $N_y$  and  $N_z$  for  $x$ ,  $y$  and  $z$  direction, respectively, give the acquisition matrix size. The nominal resolution of image (pixel width) is determined by  $\Delta x = \frac{FOV_x}{N_x}$ ,  $\Delta y = \frac{FOV_y}{N_y}$  and  $\Delta z = \frac{FOV_z}{N_z}$ . In the case of 2D imaging,  $N_z = 1$  and  $\Delta z = FOV_z$  is slice thickness as mentioned in the slice selection section.

As shown in Figure 5, the FOV is inversely proportional to the encoding steps (the spacing) samples in  $k$ -space (see more [2, 15]):

$$\Delta k_i = \frac{1}{FOV_i} = \frac{1}{N_i \Delta i}, \quad \forall i = x, y, z.$$

Alternatively, this relation can be based on the spatial resolution:

$$\Delta i = \frac{1}{K_i} = \frac{1}{2k_{i \max}}, \quad \forall i = x, y, z$$

where  $K_i$  is the width of the  $k$ -space region in  $i$  direction,  $i = x, y, z$ , that is sampled in the entire experiment.

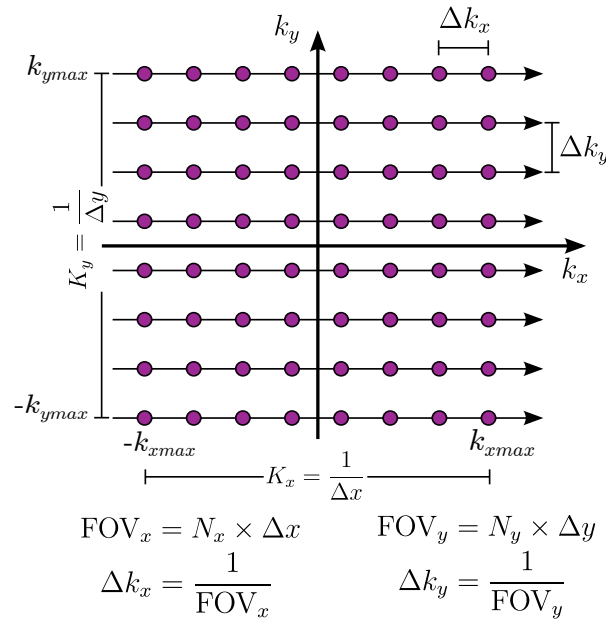


Figure 5 – Diagram of the  $k$ -space and the relationships between  $k$ -space FOV and resolution. The sampled  $k$ -space points are plotted as dots; the arrows show the trajectories during one frequency encoding scan corresponding to one phase encoding step.

## 2.8 SNR

The SNR was introduced by Edelstein et al. in 1986 [16]. The SNR is measure of how much true signal versus how much noise a particular image has. In MRI imaging, the SNR is then defined by

$$SNR = \frac{\text{mean}(signal)}{\text{std}(noise)}. \quad (56)$$

The SNR is proportional to the volume of the voxel and to the square root of the number of averages and phase steps (assuming constant sized voxels). Since averaging and increasing the phase steps takes time, the SNR is depends on the square root of the acquisition time:

$$SNR \propto \Delta x \Delta y \Delta z \sqrt{T_{acq}},$$

where the product of the three pixel dimensions (without zero-filling interpolation)  $\Delta x \Delta y \Delta z$  is the voxel volume, and  $T_{acq}$  is the total acquisition time. The total acquisition times is proportional to number of phase encoding steps, so we have for 3D imaging,

$$\text{SNR}_{3D} \propto \Delta x \Delta y \Delta z \sqrt{N_y N_z \text{TR} N_a},$$

and for 2D imaging

$$\text{SNR}_{2D} \propto \Delta x \Delta y \Delta z \sqrt{N_y \text{TR} N_a},$$

where  $N_a$  is the number of averages, TR is the time between the acquisition of two “read” lines and it is called repetition time. In addition, the SNR does not only depend on the acquisition parameters as mentioned above but also depend on the others parameters as [17, 18]:

$$\text{SNR} = \frac{\gamma^3 \hbar^2 B_0^2 B_1 \rho \Delta x \Delta y \Delta z}{4kT_s} \cdot \frac{1}{\sqrt{8kT_{eff} \text{BW} R_{eff}}},$$

where  $\rho$  is the spin density,  $\hbar = 1.05457 \times 10^{-34}$  Js is the reduced Planck constant,  $k = 1.38 \times 10^{-23}$  J/K is Boltzmann’s constant,  $B_0$  is external field gradient strength,  $B_1$  is RF gradient strength,  $T_s$  is the temperature of the sample,  $T_{eff}$  is the temperature characterizing the noise of the system, BW is the bandwidth of receiver coil and  $R_{eff}$  is the effective resistance.

Glyn Johnson and colleagues reported in [19] that the 2D multislice and 3D MRI sequences are often equally sensitive in terms of SNR per unit imaging time. Moreover, the major advantage of 3D imaging is improved the resolution while the 2D sequences provides higher reliability for image quality as reported in [20] by Niranjan Balu and colleagues. As shown in equation (47), the higher gradient strength in slice direction is necessary to get the lower slice thickness. Therefore, in high-resolution MRI, the 3D MRI sequences usually used instead of 2D multislice due to the limited of gradient strength.

Finally, the SNR can be improved by tweaking scan parameters (note however that there is an interdependence between the acquisition parameters). Assuming all other factors remain the same, the SNR can be improved by

- Reducing resolution
- Decreasing TE
- Increasing the acquisitions times by increasing the number of averages,  $N_a$ , to reduce the standard deviation of noise
- Decreasing the bandwidth.

## 2.9 Acquisition time

Let us consider a 3D k-space data collection and let  $N_y$ ,  $N_z$  denote the number of phase encoding steps for two directions perpendicular to the read axis. Basically, each unique pair of phase encoding gradients is acquired during one TR. Therefore, the total acquisition time for a 3D imaging method is given by

$$T_{acq} = N_y N_z \text{TR}. \quad (57)$$

For a 2D imaging experiment, the total acquisition time is

$$T_{acq} = N_y \text{ TR}. \quad (58)$$

In practice, in order to increase the SNR, one can increase the number of averages, that we denote  $N_a$ , it means that the data is collected  $N_a$  times and then averaged. In this case the total acquisition time is increased by a factor  $N_a$ .

### 3 MRI pulse sequences

A pulse sequence is a series of events comprising of RF pulses, gradient waveforms, and data acquisition. The purpose of the pulse sequence is to manipulate the magnetization in order to produce the desired signal. A wide variety of sequences are used in MRI. The most basic ones are Spin Echo (SE) sequences and the Gradient Echo (GRE) sequences. There are several basic steps which constitute an MR pulse sequence.

- Slice selection (in 2D imaging): Turn on the slice-selection gradient; Excitation pulse (RF pulse); and then turn off slice-selection gradient.
- Phase encoding: Turn on the phase encoding gradient repeatedly with a different strength.
- Read: Turn on the frequency encoding gradient repeatedly during the acquisition with the same strength.
- Generate echo (or FID) and collection of the MR signal.

#### 3.1 Spin Echo sequence

The most common pulse sequence used in MR imaging is based on the detection of a spin echo or Hahn echo [21]. A 90 degree radio frequency pulse is applied to excite the magnetization and one or more 180 degree pulses are applied to refocus the spins and to generate signal echoes named spin echoes (SE). In the pulse sequence timing diagram (Figure 6), the simplest form of a spin echo sequence is illustrated. The 90 degree excitation pulse rotates the longitudinal magnetization ( $M_z$ ) into the xy-plane and the dephasing of the transverse magnetization ( $M_{xy}$ ) starts. The application of a 180 degree refocusing pulse (rotates the magnetization in the x-plane) generates signal echoes. The purpose of the 180 degree pulse is to rephase the spins, causing them to regain coherence and thereby to recover transverse magnetization, producing a spin echo. The recovery of the z-magnetization occurs with the  $T_1$  relaxation time and typically at a much slower rate than the  $T_2$ -decay, because in general  $T_1$  is greater than  $T_2$  for biological tissues and is usually in the range of 50–3000 ms. (Note that  $T_1$  depends on the magnetic field, example at ultra-high magnetic field at 17 T,  $T_1$  can be reach 2800 ms while  $T_2$  around 50 ms.) The SE pulse sequence was devised by Carr and Purcell [22] and exists now in many forms: the multi echo pulse sequence using single or multislice acquisition, the fast spin echo (FSE/TSE) pulse sequence, spin echo planar imaging (EPI) pulse sequence; all are basically spin echo sequences. In the simplest form of SE imaging, the pulse sequence has to be repeated many times as only one k-space line is acquired in one TR.

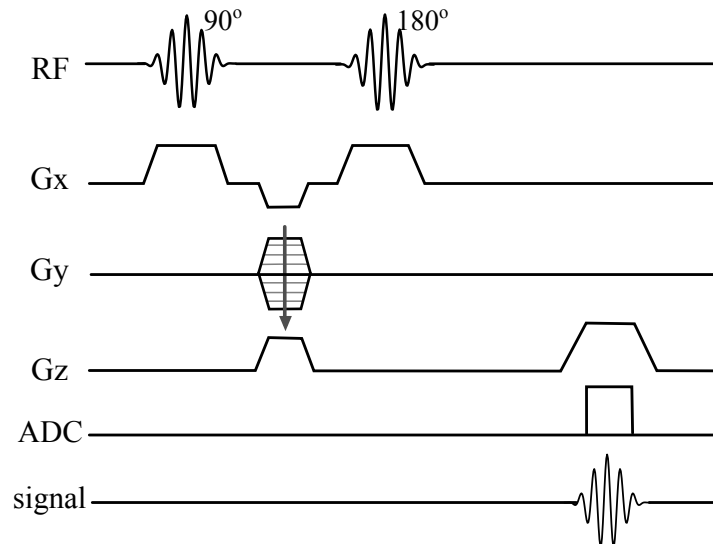


Figure 6 – Spin echo pulse diagram.

### 3.2 RARE: T2-weighted images

The Rapid Acquisition with Refocused Echoes (RARE) sequence, also called Rapid Spin Echoes (RSE) or Fast Spin Echo (FSE) or Turbo Spin Echo (TSE) depending on the manufacturer, was introduced by Jurgen Hennig in 1986 [23] and it is based on the multiple-echo sequence. Over the years, RARE has mostly replaced the conventional multiple spin-echo pulse sequence, which was the most common sequence used in clinical imaging. RARE speeds up the image acquisition by acquiring multiple lines in k-space per repetition (determined by RARE factor parameter,  $A_F$ ). The RARE sequence starts with a  $90^\circ$  pulse excitation and then repeatedly plays  $180^\circ$  refocusing pulses at TE intervals (Figure 7). The number of refocusing pulses determines the rare-factor and therefore the reduction in the acquisition time. However, the amplitude of the successive

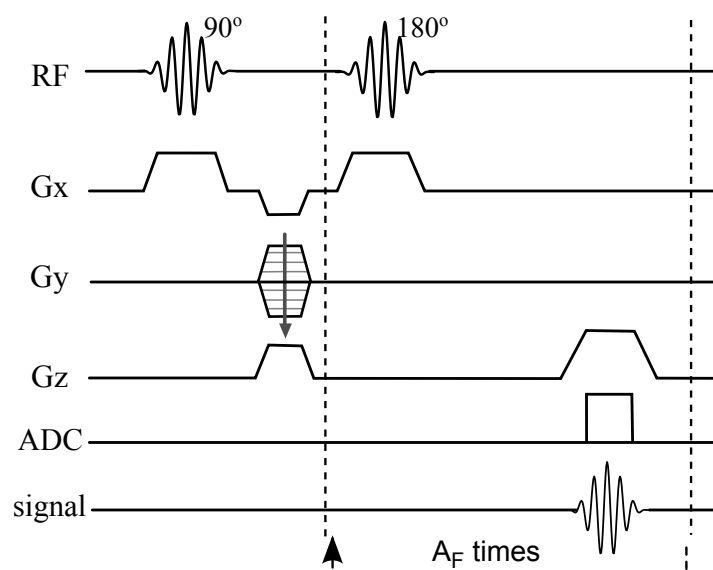


Figure 7 – RARE pulse diagram.

echoes naturally decays with  $T_2$  implying that each line in k-space has a different  $T_2$

weighting. The effective echo time of such acquisition depends on the time when the central line in  $k$ -space is acquired, hence the choice of phase-encoding steps ordering is very important. The RARE sequence typically provides excellent  $T_2$ -weighted image ( $T_2w$ ) contrast but is improper for  $T_2$  quantification because of the mixed  $T_2$  weighting within a single  $k$ -space plane [23].

### 3.3 Gradient Echo sequence

A gradient echo is generated by using a pair of bipolar gradient pulses. In the pulse sequence timing diagram, the basic gradient echo sequence is illustrated (see Figure 8). There is no refocusing 180 degree pulse and the data are sampled during a gradient echo, which is achieved by dephasing the spins with a negatively pulsed gradient before they are rephased by a gradient with opposite polarity to generate the echo. As shown in

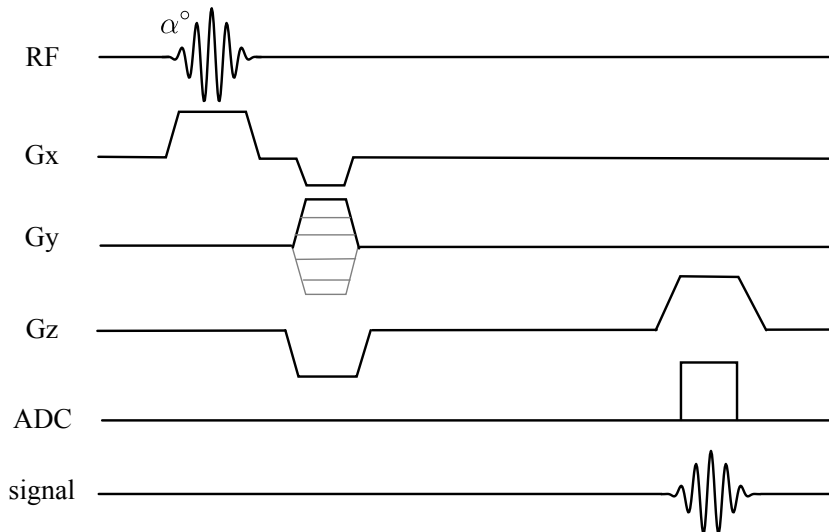


Figure 8 – Gradient echo pulse diagram.

the gradient echo diagram, the excitation pulse is termed the alpha pulse  $\alpha^\circ$ . It tilts the magnetization by a flip angle  $\alpha^\circ$ , which is typically between 0 and 90 degrees. Due to the small flip angle there is a reduction in the value of transverse magnetization that will be used to form the image. The contrast and signal generated by a gradient echo depend on the size of the longitudinal magnetization, the flip angle and the echo time. When  $\alpha = 90^\circ$  the sequence is identical to the so-called partial saturation or saturation recovery pulse sequence. In standard GRE imaging, this basic pulse sequence is repeated as many times as the number of phase encoding points ( $k$ -space lines). Additional gradients or radio frequency pulses are introduced with the aim to spoil the  $xy$ -magnetization at the moment when the spin system is subject to the next pulse. As a result of the short repetition time, the  $z$ -magnetization cannot fully recover and after a few initial pulses there is an equilibrium established between the  $z$ -magnetization recovery and the  $z$ -magnetization reduction due to the pulses (steady-state). Gradient echo sequences are often used for  $T_1$ -weighted image ( $T_1w$ ) imaging and the contrast depends on TR and flip angle.  $T_2^*$  weighting can be minimized by keeping the TE as short as possible, but pure  $T_2$  weighting is not possible. By using a reduced flip angle, some of the magnetization value remains longitudinal (less time needed to achieve full recovery). For a certain  $T_1$

and TR, there exist one flip angle that will give the most signal, known as the "Ernst angle" [24].

### 3.4 FLASH: T1-weighted images

The FLASH (Fast Low Angle SHot) sequence is a basic gradient-echo sequence with two typical features [25]. The TR is generally shorter than the  $T_1$  of the sample, meaning the longitudinal magnetization has not fully recovered between two successive excitation pulses. After a given number of pulse repetitions, the longitudinal magnetization available before each pulse reaches a steady-state level. The transverse magnetization remaining at the end of the read-out block is "spoiled" by a gradient, ensuring that  $M_{xy} = 0$  before the following excitation pulse (see Figure 9). Thus no coherent mag-

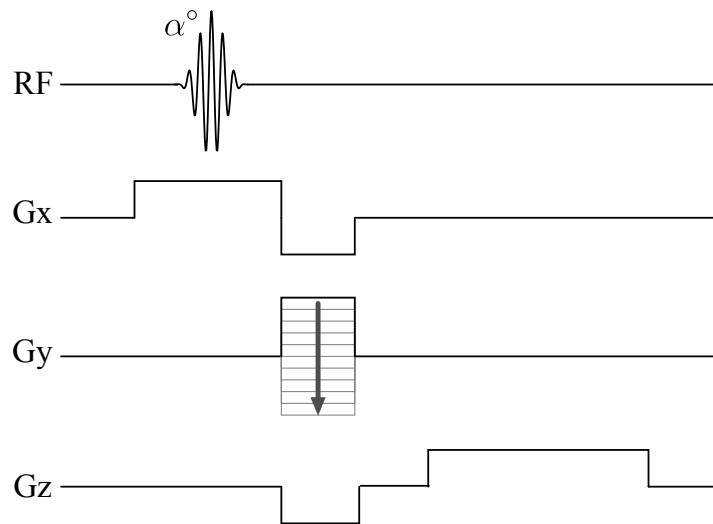


Figure 9 – FLASH pulse diagram.

netization will be tipped from the transverse plane onto the longitudinal axis by the next RF pulse. This spoiling is required for instance if  $TR < 5T_2$ . Combining these conditions the FLASH signal equation in steady-state is:

$$S = M_0 \frac{(1 - e^{-TR/T_1}) \sin(\alpha) e^{-TE/T_2^*}}{1 - \cos(\alpha) e^{-TR/T_1}}.$$

The steady-state therefore depends on the choice of TE, TR and flip angle (usually 5 – 30°). Ideally, all of the data in k-space should be acquired when the system is in steady-state, hence the need for “dummy scans” (all the pulses and gradients are played but the data is not acquired) to reach steady-state prior to the actual acquisition start. In practice, if k-space is acquired linearly starting from the edge, dummy scans are less crucial since steady-state will likely be reached before the center of k-space (which determines the main signal level) is acquired. The advantage of the FLASH sequence is a short acquisition time via a short TR. The short TR will generally introduce T1 weighting, although  $T_2^*$  weighting is also possible through a choice of relatively long TE.

### 3.5 FISP sequence

The Fast Imaging with Steady-state free Precession (FISP) is a fast imaging sequence using a refocusing gradient in the phase encoding direction during the end module to maximize (refocus) remaining transverse magnetization at the time when the next excitation is due the “balanced” (Figure 10). The FISP is usually performed with a short TR

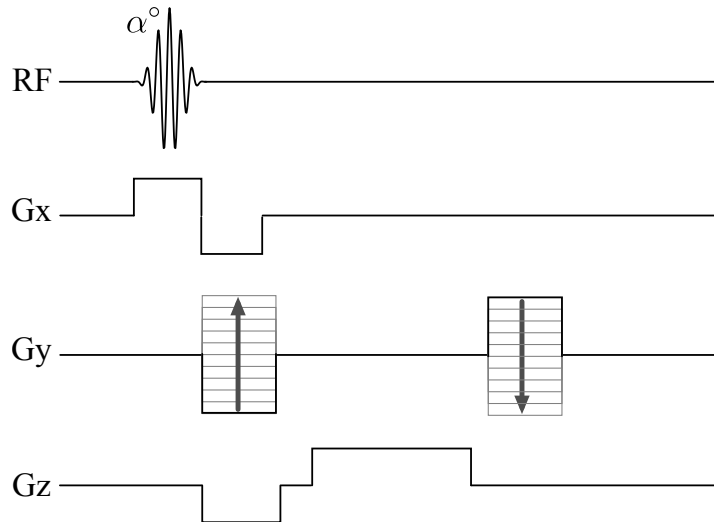


Figure 10 – FISP pulse diagram.

(20-50 ms). Most often this technique is used to generate  $T_2^*$ -weighted images, although other weightings sequence are possible. This sequence is very similar to FLASH, except that the spoiler pulse is eliminated. As a result, there is transverse magnetization still present at the time of application of the next RF pulse. Because there is still some remaining transverse magnetization at the time of the RF pulse, an RF pulse of the degree flips the spins less than the degree from the longitudinal axis. With small flip angles, very little longitudinal magnetization is lost and the image contrast becomes almost independent of T1. Using a very short TE (with TR 20-50 ms, flip angle 30-45°) eliminates  $T_2^*$  effects, so that the images become proton density weighted. As the flip angle is increased, the contrast becomes increasingly dependent on T1 and T2\*. It is in the domain of large flip angles and short TRs that FISP exhibits a vastly different contrast compared to the FLASH sequence. More detail about FISP and some related sequences, one can refer to the literatures [26, 27].

---

## Part II

# Diffusion MRI in the *Aplysia* neuronal tissue

## Summary

---

4	Water diffusion in biological tissue	42
5	Diffusion-encoding	42
6	Bloch-Torrey equation model	43
7	The relation between the ADC and the cell size	44
8	Aplysia animal model	45
9	Fast dMRI sequences	48
9.1	The Echo-planar imaging . . . . .	48
9.2	DP-FISP . . . . .	49

---

## 4 Water diffusion in biological tissue

Besides the spin density and relaxation contrasts, incoherent spin displacement can be another source of contrast in MRI. Such displacement are due to the Brownian motion of water molecules in tissue which is hindered by the presence of biological cell membranes as well as cell nuclei and macro-molecules.

## 5 Diffusion-encoding

The incoherent spin displacement is encoded by the application of additional magnetic field gradients, called diffusion-encoding gradients, which are turned ON for very short durations during the sequence gradient “pulses”. The most commonly used diffusion-encoding pulse sequence is the Pulsed-Gradient Spin Echo (PGSE) [28] sequence. For the PGSE sequence, the effective gradient time profile is:

$$f(t) = \begin{cases} 1 & t_s < t \leq t_s + \delta, \\ -1 & t_s + \Delta < t \leq t_s + \Delta + \delta, \\ 0 & \text{otherwise,} \end{cases} \quad (59)$$

where  $t_s$  is the starting time of the first gradient pulse,  $\delta$  is the duration of the pulses and  $\Delta$  the delay between the start of the pulses (see Figure (11)). The signal is measured at the echo time  $TE$ . Note that the time of the application of the  $180^\circ$  refocusing pulse,  $\frac{TE}{2}$ , satisfies  $t_s + \delta \leq \frac{TE}{2} < t_s + \Delta$  [29, 30].

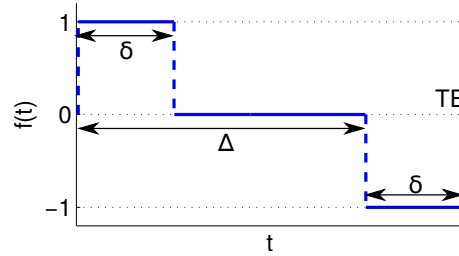


Figure 11 – The PGSE time profile for  $t_s = 0$ , consisting of two rectangular pulses (duration  $\delta$ , separated by a time interval  $\Delta$ )

Under the assumption that spins experience a homogeneous (or homogenized) isotropic diffusion environment characterized by the diffusion coefficient  $D^{hom}$  inside the voxel  $V$  (and neglecting edge effects at the boundary of  $V$ ), the spins starting at position  $\mathbf{r}_0 \in V$  at  $t_s$  diffuse according to the probability density function:

$$P(\mathbf{r}, t) = \frac{e^{-\|\mathbf{r}-\mathbf{r}_0\|^2/4D^{hom}(t-t_s)}}{(4\pi D^{hom}(t-t_s))^{\frac{d}{2}}}, \quad d = 3.$$

Furthermore, under the assumption that  $\delta \ll \Delta$  (narrow pulse assumption) the effect of the first diffusion-encoding magnetic field gradient pulse on spins starting at  $(\mathbf{r}_0, t_s)$  is a gain of a complex phase  $e^{-i\gamma\mathbf{g}\cdot\mathbf{r}_0\delta}$  between  $t_s$  and  $t_s + \delta$ , where  $\mathbf{g} \in \mathbb{R}^3$  is the

diffusion-encoding gradient vector,  $\gamma$  is the gyromagnetic ratio of the water proton. If spins move from  $\mathbf{r}_0$  to a different position, say  $\mathbf{r}$ , at the start of the second pulse, then the cumulative effect of the PGSE sequence is  $e^{-i\gamma\mathbf{g}\cdot(\mathbf{r}-\mathbf{r}_0)\delta}$ . Thus, the effect on the MRI signal, compared to having no diffusion-encoding gradient  $\mathbf{g}$ , is an *attenuation* (loss) of the signal:

$$\int_{\mathbf{r}_0 \in V} \rho(\mathbf{r}_0) \int_{\mathbf{r} \in V} \frac{e^{-\|\mathbf{r}-\mathbf{r}_0\|^2/4D^{hom}\Delta}}{(4\pi D^{hom}\Delta)^{\frac{d}{2}}} e^{-i\gamma\mathbf{g}\cdot(\mathbf{r}-\mathbf{r}_0)\delta} d\mathbf{r} d\mathbf{r}_0 = e^{-\gamma^2\delta^2\|\mathbf{g}\|^2 D^{hom}\Delta} \int_{\mathbf{r}_0 \in V} \rho(\mathbf{r}_0) d\mathbf{r}_0,$$

where we used the formula for the Fourier transform of the Green's function of the heat or diffusion equation. Note that the effective spin density at  $\mathbf{r}_0$ , denoted by  $\rho(\mathbf{r}_0)$ , is proportional to the external magnetic field and relaxation constants ( $e^{-TE/T_2(\mathbf{r})}$  and  $e^{-TR/T_1(\mathbf{r})}$ ).

If  $\delta$  is not small compared to  $\Delta$ , then, in fact, the signal attenuation is [31]:

$$S(b, TE) = e^{-D^{hom}b} \int_{\mathbf{r}_0 \in V} \rho(\mathbf{r}_0) d\mathbf{r}_0,$$

where the b-value is a weighting factor as defined in [32]:

$$b(\mathbf{g}, \delta, \Delta) = \gamma^2\|\mathbf{g}\|^2\delta^2(\Delta - \delta/3), \quad (60)$$

for the PGSE sequence. The replacement of  $\Delta$  by  $\Delta - \delta/3$  accounts for pulses that are not narrow.

To obtain the diffusion coefficient from the MRI signal, one can acquire the MRI signal with a diffusion weighting  $\mathbf{g}$  and another one without diffusion weighting,  $\mathbf{g} = 0$ , and use the formula:

$$D^{hom} = \frac{\log S(\mathbf{g}) - \log S(\mathbf{g} = 0)}{-b}.$$

Because biological tissue is not a homogeneous diffusion environment due to the presence of cell membranes and other cell components (nucleus, macro-molecules) the quantity obtained using the above formula is called the Apparent Diffusion Coefficient (ADC) and it is smaller than the free diffusion coefficient.

## 6 Bloch-Torrey equation model

The mathematical description of the complex transverse magnetization including effects of diffusion is called the Bloch-Torrey equation [31]:

$$\frac{\partial M(\mathbf{r}, t)}{\partial t} = -i\gamma \mathbf{r} \cdot \mathbf{g} f(t) M(\mathbf{r}, t) + \nabla \cdot (D(\mathbf{r})\nabla M(\mathbf{r}, t)), \quad (61)$$

where  $f(t) \in \mathbb{R}$  contains the effective time profile information of the diffusion-encoding gradient. In the above equation, we have neglected relaxation effects and imaging gradients. The intrinsic diffusion coefficient  $D(\mathbf{r})$  depends on the tissue micro-structure. In this thesis, we will neglect permeability effects between cells and cell components so that spins always stay inside any geometrical confinement,  $\Omega$ . In this case, we will add the homogeneous Neumann boundary condition to the PDE above:

$$(D(\mathbf{r})\nabla M(\mathbf{r}, t)) \cdot \mathbf{n}(\mathbf{r}) = 0, \quad \mathbf{r} \in \partial\Omega, \quad (62)$$

to complete the mathematical problem, where  $\mathbf{n}(\mathbf{r})$  is the outward pointing normal vector to  $\Omega$ .

## 7 The relation between the ADC and the cell size

Diffusion magnetic resonance imaging (dMRI) has shown tremendous promise in a wide range of brain imaging applications. The correlation of dMRI-derived metrics with brain micro-structure properties such as axon size, myelin thickness, neurite orientation distribution, is an active area of research. To explain the correlations between the dMRI metrics (the ADC value, signal, etc) and the geometrical parameters, there have been numerous biophysical models (usually subdividing the tissue into compartments described by spheres, ellipsoids, cylinders, and the extra-cellular space) [33, 34, 35, 36, 37, 38, 39]. However, it is difficult to connect the geometrical parameters contained in these models to ground truth values due to the complexity of brain tissue.

To get closer to the ground truth, experiments performed on various artificial phantoms have been conducted including: carrot slices [40], spheres filled with a gel in each cell compartment [41], physical phantoms constructed from resected rat spinal cord [42], polyfil fibers wound on a spherical polyamide spindle [43], straight X-crossings of polyester fibers [44]. Other authors performed histological analysis of the tissue of interest by manual alignment with MRI data [45], co-registration of diffusion tensor imaging (DTI) and Golgi data [46] to get independent information of the microstructure of the imaged object and verify their models described in [39, 47, 48, 46, 45, 49]. This information was then compared with model predictions extracted from the experimental dMRI data. This comparison procedure can be useful in evaluating the quality and usefulness of the proposed dMRI models.

A well-known approximation for the ADC in the short time regime is the following [50, 51]:

$$ADC_{\text{short}} = D_0 \left( 1 - \frac{4\sqrt{D_0}}{3 \dim \sqrt{\pi}} \sqrt{\Delta} \frac{S}{V} \right), \quad (63)$$

where  $\frac{S}{V}$  is the surface to volume ratio. In the above formula the pulse duration  $\delta$  is assumed to be very small compared to  $\Delta$ . A recent correction to the formula in (63) taking into account the finite pulse duration  $\delta$  [52] is the following:

$$ADC_{\text{short}} = D_0 \left[ 1 - \frac{4\sqrt{D_0}}{3 \dim \sqrt{\pi}} C_{\delta, \Delta} \frac{S}{V} \right], \quad (64)$$

where

$$\begin{aligned} C_{\delta, \Delta} &= \frac{4}{35} \frac{(\Delta + \delta)^{7/2} + (\Delta - \delta)^{7/2} - 2(\delta^{7/2} + \Delta^{7/2})}{\delta^2 (\Delta - \delta/3)} \\ &= \sqrt{\Delta} \left( 1 + \frac{1}{3} \frac{\delta}{\Delta} - \frac{8}{35} \left( \frac{\delta}{\Delta} \right)^{3/2} + \dots \right). \end{aligned}$$

When  $\delta \ll \Delta$ , the value  $C_{\delta, \Delta}$  becomes  $\sqrt{\Delta}$ .

For spheres (three dimensions) or disks (two dimensions), the surface to volume ratio  $\frac{S}{V}$  is  $\frac{\dim}{R}$ , where  $R$  is the radius. From the experimental ADC for multiple diffusion times we can fit the experimental ADC as the linear function of  $\sqrt{\Delta}$  or  $C_{\delta, \Delta}$ , and the radius can be estimated.

## 8 *Aplysia* animal model

In this thesis we propose another approach for dMRI model validation, using the much larger neural cells of the *Aplysia californica* as a surrogate phantom. The advantages of this choice lies in the simple structure of the neural system, consisting of large round cells, smaller round cells gathered in bags, and cylindrical bundles of unmyelinated axons. These cell components can be surrogates for mammalian brain cell components (the soma, axon bundles, dendrites). In particular, the large size of the *Aplysia* neural cells make it possible to test claims about short time diffusion imaging (usually implemented with OGSE [53] sequences) using the PGSE [28] sequence.

At moderate  $b$ -values that we will consider in this thesis, the mono-exponential behavior is sufficient to describe the dMRI signal. Thus, we consider only the relationship of the ADC, which contains first order dependence of the signal on the  $b$ -value, to geometrical information on the confining domain  $\Omega$ . This relationship is not completely understood from a theoretical point of view except for some simple geometries. Geometrical models (spherical and oriented cylindrical cells embedded in extra-cellular space [33, 39]). In these case, the dMRI signal is decomposed as the sum of the signals from two different tissue compartments: the signal from the spherical cells and the extra-cellular space being Gaussian with an effective diffusion tensor.

The neural system of the *Aplysia californica* consists of five pairs of ganglia: buccal, cerebral, pleural, pedal, and abdominal ganglia [54]. The abdominal and buccal ganglia were chosen in this imaging study because the cellular network is very well known in terms of single cell neurons and axonal orientation [55, 56]. Moreover, the abdominal ganglion or single neurons from the abdominal ganglion have been investigated using magnetic resonance microscopy (MRM) and diffusion MRM studies. The abdominal ganglia diagram is shown in Figure 12.

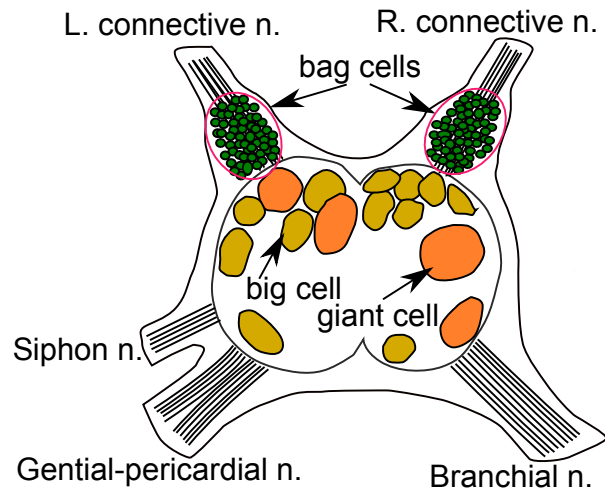


Figure 12 – The *Aplysia* abdominal ganglion diagram.

Several authors have reported ADC values in the cytoplasm and in the nucleus of the L7 neurons of the *Aplysia* abdominal ganglia. The results showed that the ADC values in the cytoplasm are smaller than in the nucleus. For example Grant et al. reported in [57] by using a biexponential signal fit that the average ADC in the cytoplasm is  $0.30 \pm 0.09 \times 10^{-3} \text{ mm}^2/\text{s}$ ; while the average ADC in the nucleus is  $1.17 \pm 0.29 \times 10^{-3}$

$\text{mm}^2/\text{s}$ . Using monoexponential fits, Schoeniger and colleagues [58] found ADCs of  $0.28 \times 10^{-3}$  and  $1.47 \times 10^{-3} \text{ mm}^2/\text{s}$  in the cytoplasm and nucleus, respectively. These results are in good agreement with recent reports by Choong H. Lee and colleagues [59], which also found that the ADC in the nucleus is larger than in the cytoplasm, as shown in Figure 13. In addition, in a study validating cellular diffusion, Grant et al. [57]

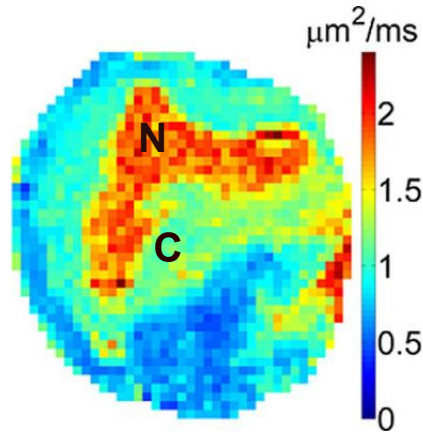


Figure 13 – The ADC in the nucleus (N) is larger than it in the cytoplasm (C) of L7 *Aplysia* neuron. ( $7.8\mu\text{m}$  in-plane resolution, source: Lee et al. [59]: [www.nature.com/articles/srep11147](http://www.nature.com/articles/srep11147) )

demonstrated that the nuclear diffusion is monoexponential while cytoplasm diffusion appears non-monoexponential. In a previous study Hsu et al. [60] concluded that the apparent diffusion isotropy came from sub-cellular diffusion isotropy rather than averaging effects over multiple cells.

In this thesis, we focus on the following three types of cells and cell components for imaging study.

1. Large neuron cells;

There are many large neuron cells in the abdominal ganglion with a diameter of at least  $150 \mu\text{m}$  that are visible by inspection in the high resolution ( $26 \mu\text{m}$  isotropic) T2w images. Some of these include neurons L2 to L9, L11, R2 to R8, R14 and R15 (labeled L or R for left or right hemiganglion, e.g. see in [61]). The single cell neurons with diameter less than  $150 \mu\text{m}$  are not included in this group. We note that the sizes of these identified neurons are not fixed, they vary as a function of the age and the weight of the animal. The large cell neurons contain a nucleus, cytoplasm and are probably surrounded by small satellite (glial) cells [59]. The satellite cells are very small cells,  $6 \mu\text{m}$  maximum in diameter, without a nucleus [55, 56, 59].

Several large cell neurons of diameter greater than  $150 \mu\text{m}$  (up to  $420 \mu\text{m}$ ) that are easily identifiable from the T2w image will be selected for this study.

2. Clusters of neuron cells gathered in the shape of a bag;

The bag shaped clusters comprise of hundreds of neurons that are located on the rostral end of the abdominal ganglion [55]. The actual number and sizes of these neurons depend on the animal age and weight [62]. For example, in young *Aplysia*, there are probably fewer than 100 small (about  $10 \mu\text{m}$  in diameter) cell neurons

in each bag; in adult *Aplysia* the number of cells grows to 400 in each bag with cell sizes between 40 to 100  $\mu\text{m}$  in diameter [55, 63, 64, 65].

There are two clusters of bag cells in each abdominal ganglion. When the abdominal ganglion is slid inside the small imaging capillary (as it will be later described in chapter V), only one cluster of bag cells is easy to identify from the T2w image, the other cluster is usually close to the abdominal body making it harder to identify from the T2w image. Therefore, only the one clearly identifiable cluster of bag cells in each ganglion is selected for this study.

### 3. Nerve;

These are groups of (cylindrically shaped) axons. There are five groups of nerves in the abdominal ganglion: the left/right connective nerves, siphon nerve, genital-pericardial nerve and branchial nerve [61] (see Figure 12). The siphon nerve and left/right connective nerves are of interest in this study because they remain intact as the ganglion is inserted inside the imaging capillary whereas other nerves are cut.

The information of the axon sizes and distributions for the nerves shown in Table 1 are for the buccal ganglia of *Aplysia californica* because we could not find analogous information about the abdominal ganglia. The nerves contain groups of axons (cylindrically shaped) with diameters ranging from very small (less than 1  $\mu\text{m}$ ) to large (greater than 25  $\mu\text{m}$ ). Based the axonal area configuration, small distribution, these

Nerve	I ( $> 25\mu\text{m}$ )	II ( $10 - 25\mu\text{m}$ )	III ( $1 - 10\mu\text{m}$ )	IV ( $\leq 1\mu\text{m}$ )
1b	0	$5.00 \pm 0.54$	$261 \pm 50$	$7144 \pm 1044$
2b	$2.33 \pm 0.33$	$19.41 \pm 4.04$	$235 \pm 74$	$9415 \pm 1312$
3b	0	$15.00 \pm 1.58$	$67 \pm 9.6$	$2191 \pm 755$
ON	$1.67 \pm 0.33$	$8.67 \pm 2.03$	$681 \pm 191$	$10483 \pm 691$
RN	0	$16.00 \pm 0.60$	$1579 \pm 326$	$2692 \pm 791$
CBC	$2.00 \pm 0.41$	$12.00 \pm 1.44$	$196 \pm 82$	$1591 \pm 206$

Table 1 – The nerves (1b, 2b, 3b, ON, RN, CBC) of buccal ganglia. There are four type of axons with different range of axons diameter: type I , II , III and IV. The distribution of axons type of each nerve [56] were shown.

nerve mentioned above can be separated to three groups [56]:

- Nerves consisting of many semicircular-shaped bundles of small axons (nerve 1b).
- Nerves subdivided into two separated regions: the first group mainly contains large-sized axons and the second group contains small and medium sized axons (nerves 2b and ON).
- Nerves which uniform distribution of axons (the separation of axonal areas is missing) (nerve 3b and CBC).

As shown in Figure 14, the buccal ganglia contains several bilaterally symmetrical groups of neurons such as B1, B2, B6, B9 (200 - 300  $\mu\text{m}$ ) [66, 67] as well as small neurons ( $\leq 50\mu\text{m}$ ) [68].

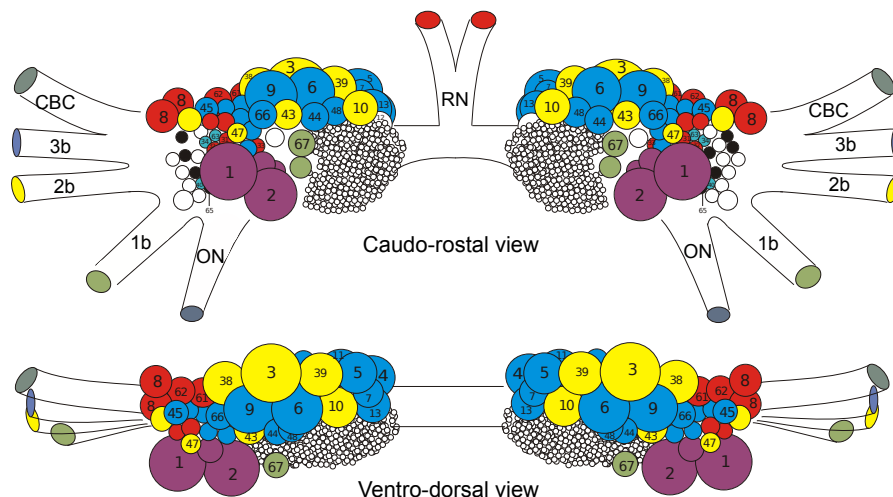


Figure 14 – The *Aplysia* buccal ganglion diagram realized by R. Nargeot.

## 9 Fast dMRI sequences

This section will briefly introduce two fast dMRI sequences: the Echo Planar Imaging (EPI) sequence and diffusion-prepared FISP sequence.

### 9.1 The Echo-planar imaging

EPI is one of the early magnetic resonance imaging sequences, used in numerous applications including diffusion, perfusion, and functional magnetic resonance imaging. EPI uses a different strategy for data collection than what we had presented in chapter I. When the echo planar imaging acquisition strategy is used, a complete image is formed from a single data sample (all k-space lines are measured in one repetition time). EPI can be employed either with a gradient echo or spin echo sequence depending on the contrast desired. Figure 15 shows the pulse sequence timing diagram of a spin echo EPI with eight echo train pulses. In the case of a gradient echo based EPI sequence the initial part (before the acquisition) is very similar to a standard gradient echo sequence. By periodically fast reversing the readout or frequency encoding gradient, a train of echoes is generated. A “blipped” phase encoding technique used on most modern systems applies a small amplitude gradient phase encoding pulse (equal to  $\Delta k_y$ ) prior to each sampling period. No phase encoding gradient is applied during signal detection so that the phase encoding for each echo is constant. When used in the gradient echo mode, EPI sequences are very sensitive to  $T_2^*$  effects. The advantage of EPI is its fast data collection, however, it is extremely sensitive to image artifacts and distortions due to the magnetic susceptibility differences at tissue-air interfaces, making their use problematic in some anatomical regions. Modern gradient amplifiers may be required for single-shot EPI imaging because of the rapid switching of the readout gradient polarity necessary to acquire all the echoes. These artifacts can be reduced by employing segmented or multishot acquisitions to the detriment of increasing the acquisition time which becomes  $TR \times \text{number of segments}$ . Segmented techniques acquire a subset of phase-encoding steps following each excitation pulse. A segmented loop structure with multiple excitation pulses is used to acquire all phase encoding steps. EPI is not very

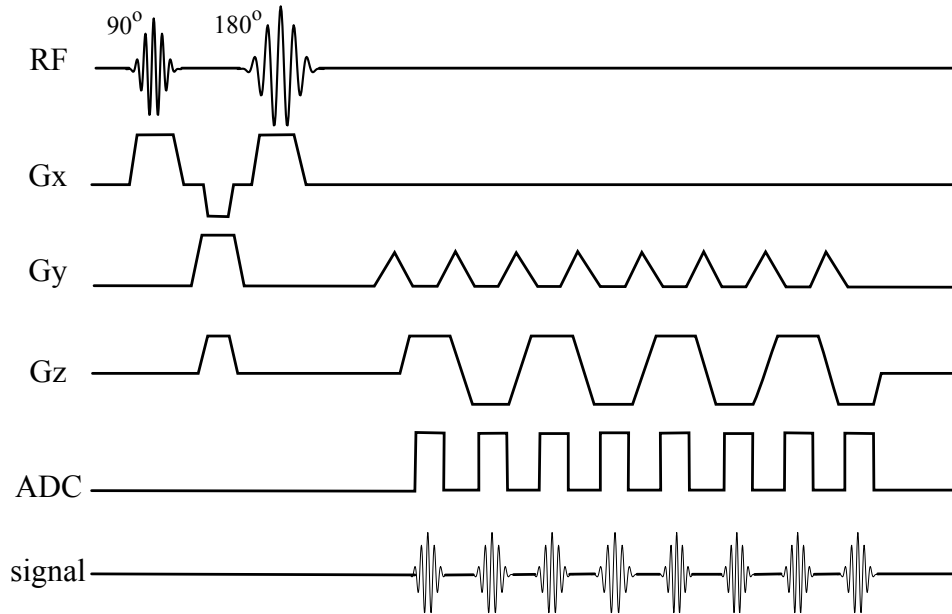


Figure 15 – Echo planar imaging pulse sequence timing diagram. A spin echo excitation scheme and an echo train length of 8 are illustrated.

popular in microscopy studies because the reduced fields of view and voxel sizes lead to severe artifacts related to susceptibility differences, eddy currents, mechanical vibration and errors in gradient trajectory.

## 9.2 DP-FISP

The main limitations of diffusion measurements are long acquisition times and low resolution. Recently, Lu et al. have developed a rapid diffusion prepared-FISP (DP-FISP) MRI acquisition for *in vivo* preclinical imaging [69] (single slice  $0.3 \times 0.3 \times 2 \text{ mm}^3$  resolution). Briefly, the main idea is to combine a slice-selective diffusion preparation ( $90_x - 180_y - 90_{-x}$ ) with a single-shot, centric encoding FISP imaging readout. The diffusion preparation was designed with bipolar diffusion gradients to limit cardiac and respiratory motion artifacts. Gradient spoilers were applied after the diffusion preparation to avoid spurious echoes. Our group extended the DP-FISP sequence proposed by Lu to a 3D DP-FISP version with centric encoding for high resolution microscopy imaging [70] (see Figure 16). More details about the DP-FISP and 3D DP-FISP pulse sequence designs can be found in [69, 71]. The results show that this sequence is much more time-efficient than standard DW-SE and less prone to artifacts than EPI. 3D DP-FISP can be used in the low b-value range for ADC measurements. Higher b-value introduce non-negligible signal recovery from  $T_1$  relaxation. The limiting feature of the total acquisition time in a 3D DP-FISP is the long TR between planes in k-space. This is required to obtain complete longitudinal relaxation before the next diffusion prepared module [71].

The 3D DP-FISP will be used during this thesis for the study of time-dependent ADC measurements in multi-diffusion directions with multiple b-values and validation with numerical simulation of time-dependent ADCs.

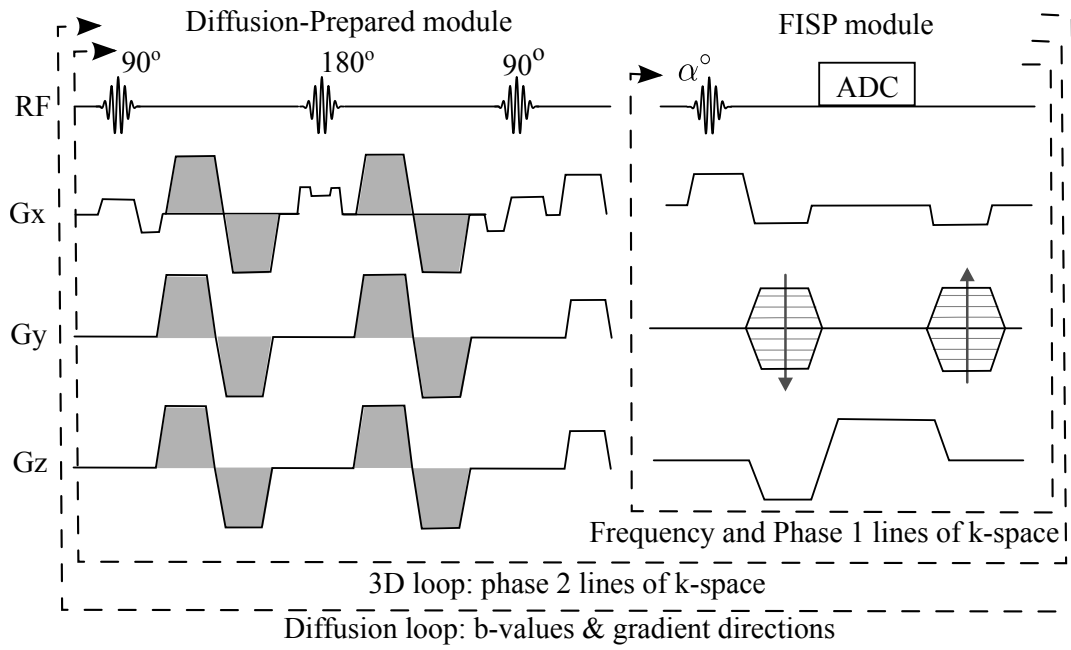


Figure 16 – DP-FISP pulse sequence timing diagram.

---

## Part III

# Accelerated acquisition techniques

## Summary

---

<b>10 Acceleration by partial Fourier imaging and Parallel imaging</b>	<b>52</b>
10.1 Partial Fourier imaging . . . . .	52
10.2 Parallel imaging . . . . .	52
<b>11 Non-Cartesian trajectories</b>	<b>53</b>
<b>12 Compressed sensing</b>	<b>54</b>
12.1 Sparsity of MR images . . . . .	56
12.2 Incoherence . . . . .	58
12.3 Polynomial undersampling patterns . . . . .	58
12.4 Image reconstruction: Discrete Fourier Transform . . . . .	59
12.5 CS image reconstruction . . . . .	60
12.5.1 Nonlinear conjugate-gradient descent method: SpareMRI tool- box . . . . .	62
12.5.2 Split Bregman method . . . . .	63
<b>13 Measuring the quality of accelerated acquisition</b>	<b>67</b>
13.1 Image error . . . . .	67
13.2 Pearson's Correlation Coefficient . . . . .	67

---

Despite the fact that the modern magnetic resonance imaging hardware available today often results in sufficiently high SNR without signal averaging, the total experimental time, dictated only by the requirement for sufficient k-space coverage, can be extremely long, prohibiting the very high resolution imaging of live biological systems. One way to reduce the data acquisition time is by undersampling the k-space, a strategy proposed by several methods including parallel imaging and compressed sensing (CS). When the k-space is undersampled Fourier reconstructions produce aliasing artifacts. Non-uniform undersampling strategies can reduce these artifacts but often with a loss in image signal to noise ratio [72, 73, 74, 75, 76]. Parallel imaging exploits redundancy in k-space reconstructing the image from data acquired simultaneously with an array of radio frequency coils [77, 78]. Using the latest developments in wire bonding technology phase array microcoils have been recently reported [79, 80]. However, the small sample size renders the construction of such micro-arrays difficult and limits the applicability of parallel imaging to high resolution MR microscopy. The use of CS methods in the acquisition and reconstruction of magnetic resonance images has been reported for cardiac imaging [81, 82, 83, 84], hyper-polarized spectroscopic imaging [85] and more recently, diffusion tensor imaging [86] and MRI velocimetry [87].

In the following we will briefly describe the most common methods of acceleration by partial Fourier imaging and parallel imaging. The non-Cartesian k-space trajectory will be also introduced. The next sections will discuss the principles of CS for MRI.

## 10 Acceleration by partial Fourier imaging and Parallel imaging

### 10.1 Partial Fourier imaging

The principle of partial Fourier imaging is based on the property that the Fourier transformation of a purely real function has complex conjugate symmetry in k-space [88, 89]. In theory this means that the fully k-space signals can be extrapolated from only half of the k-space points. When applied to the phase encoding direction, this will reduce the acquisition time by half. In practice, in order to provide robust phase correction slightly more than half (commonly approximation 60%) of the phase encodes are acquired. The resulting image has the same FOV and spatial resolution as that using a full data matrix. The problems associated with partial Fourier imaging are a loss in SNR due to the reduced number of measured lines and an enhanced sensitivity to artifacts due to the artificial replication of the information. It is also possible to apply this technique in the read direction to reduce the echo time, which may permit a slight reduction in repetition time per phase encode [90, 89]; however the scan time is not significantly affected.

### 10.2 Parallel imaging

Parallel imaging (PI) is based on parallel signal detection employing several surface coils placed side by side (so called coil arrays) to reduce the total imaging acquisition time. Most modern human scanner systems employ 8-16 receiver channels capable of

accommodating phased arrays with 8-16 coils elements. The new generation of scanners can allow tens to hundreds of channels, with the limiting factor being the prohibitively high cost of receiver units [91, 92, 93, 89]. Parallel methods do not reduce the acquisition time per spatial phase encoding step such as fast sequences, but instead reduces their number [94].

Phased-array coils were initially developed to improve SNR in MR imaging by reducing coil size and improving the sensitivity, which effectively reduces the amplitude of the noise detected. Multiple overlapping small coils can cover the same volume as a larger coil, and when the signals from individual coils are combined, the noise is substantially reduced and SNR is significantly improved [95]. The basis of PI techniques is the concept that acquisition time is proportional to the number of phase encoding lines reduced by sampling the MR signal in a parallel fashion. Each RF element is associated with a dedicated RF channel whose signals can be processed and combined together. The spatial data yielded by the array of coil elements can be used for partial phase encoding only, to speed up acquisition. Using this technique, the number of phase encoding lines is reduced by increasing the distance between the lines in k-space, effectively reducing the field of view corresponding with phase encoding for the image (see more [4, 89]). The image reconstructed from each coil contains aliasing artifacts, however a correct image can be obtained by using extra information regarding coil positions and sensitivities. The PI techniques can be classified into image-based and k-space based techniques depending on the reconstruction algorithms. Among the image-based techniques the most popular one is Sensitivity encoding (SENSE) [78] which reconstruct the image after Fourier transformation, in the image domain. There are two k-spaces based techniques commonly used: Simultaneous acquisition of spatial harmonics (SMASH) [96] and GeneRalized Autocalibrating Partially Parallel Acquisitions (GRAPPA) [77]. In the k-space based techniques, the final (unaliased) signals are measured by merging the coils signals prior to image reconstruction. The other difference between these two methods is in the calibration scans are acquired. The calibration data for the volume explored by each coil element and the signal produced is subsequently used to map the spatial sensitivity of each coil elements. SMASH acquires the calibration scans separately from primary scan, so that the main scan time reduction is directly proportional to the number of coils. GRAPPA technique acquires the calibration scans as a part of the primary scan, so the scan time savings but presents better the SNR.

## 11 Non-Cartesian trajectories

Almost all MR imaging is performed by acquiring the k-space points along a Cartesian grid, or rectilinear trajectories, however, k-space can also be sampled in an arbitrary non-Cartesian manner. The limiting factor in data acquisition speed is the time needed to play out gradient waveforms. Moreover, the maximum gradient strengths and slew rates in MRI scanner are constrained by physiological considerations. Therefore, imaging speed can only be further improved by increasing the efficiency of gradient waveforms or by reducing the amount of gradient encoding. Non-Cartesian parallel imaging seeks to use both of these approaches simultaneously to significantly reduce the amount of time required to collect MRI data (see in [97]). Many non-Cartesian trajectories have been explored such as radial [98, 99], spiral [100, 101], rosette [102] and stochastic [103], etc.

The most common non-Cartesian trajectories are radial and spiral trajectories. The common feature is that sampling is more dense near the center of k-space than near the edges. As a result, a re-gridding of the raw data must be done prior to performing the Fourier transformation in order to produce images without phase artifacts. Radial sampling uses a constant magnitude gradient for each line while the spiral sampling uses variable  $G$ . The central points of k-space are usually acquired at the beginning of sequence. Re-gridding in spatial encoding is necessary to ensure a constant density k-space. More detail about non-Cartesian trajectories can be found in references [89, 97]. The radial and spiral k-space trajectories diagrams shown in Figure 17.

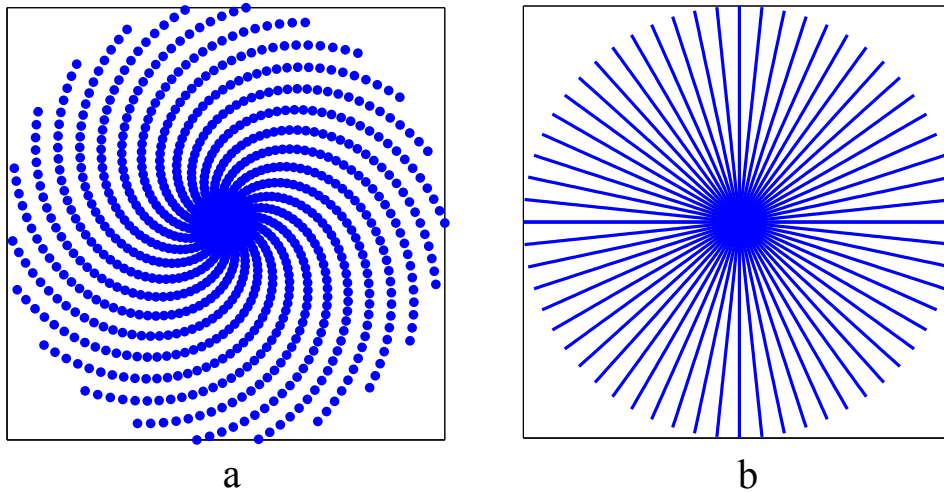


Figure 17 – Non-Cartesian sampling: a) Spiral k-space trajectory and b) Radial trajectory.

## 12 Compressed sensing

In the field of digital signal processing, the Nyquist–Shannon sampling theorem is the fundamental theory connecting between continuous signal and discrete signals in time domain. The Nyquist–Shannon sampling theorem states [104]:

**Theorem 12.1** *If a function  $f(t)$  contains no frequencies higher than  $W$  cycles per second (cps), then it is completely determined by giving its ordinates at a series of points spaced  $\frac{1}{2W}$  seconds apart.*

A sufficient sample-rate is therefore greater than or equal to  $2W$  samples per seconds. Equivalently, for a given sample rate  $f_s$ , perfect reconstruction is guaranteed possible for a bandlimit  $W < f_s/2$ .  $2W$  and  $f_s/2$  are respectively called the Nyquist rate and Nyquist frequency. The notation  $T = 1/f_s$  is usually used to represent the interval between samples and is called the sample period or sampling interval. The Nyquist–Shannon sampling theorem (well know as *Nyquist rate*) propose the sufficient condition for *sampling* the continuous signal to discrete signal for which one can be maintain all information from continuous-time signal. The Shannon sampling theorem states that the sampling rate must be at least twice the highest frequency present in the signal of

interest [104]. The theorem also provides a formula for the reconstruction of the original signal by sinc-interpolation:

$$f(t) = \sum_{n=-\infty}^{\infty} f_n \frac{\sin \pi(2Wt - n)}{\pi(2Wt - n)},$$

where  $f_n = f\left(\frac{n}{2W}\right)$  is the  $n^{\text{th}}$  sample, for all positive and negative integer values of  $n$ . However, the exactly reconstruction may still be possible when the Nyquist criterion is not satisfied. Extensions of Shanon sampling theorem can be found in reference [105]. Basically, if the signal is sparse in the Fourier domain then it can recovered from far fewer samples than required by the Nyquist limit [105, 106, 107]. CS is a novel signal processing technique introduced by Donoho in 2006 [108] (for MRI) which exploits this property. Other nomenclatures used for CS are: compressive sensing, compressive sampling, or sparse sampling. Through papers published between 2004 and 2006, Emmanuel Candès, Terence Tao, and David Donoho proved that, provided the sparsity condition is satisfied, the signal can be recovered with fewer samples than the Nyquist criterion requires and therefore different types of images can be reconstructed from undersampled data without loss of information [109, 110, 108, 81]. The technique can be applied to MRI to reduce the acquisition times. CS is based on three major components [81]:

- (1) a sparse representation of the signal in some transform domain (such as Fourier transform (FT) domain, Wavelet transform domain ...),
- (2) the aliasing artifacts due to k-space undersampling be incoherent (noise like) in that transform domain, and
- (3) a sparsity-constrained nonlinear reconstruction method.

If the total number of points in the image is larger than four times the number of sparse coefficients then the reconstruction of undersampled data is feasible. As discussed in [111], sparsity expresses the idea that the information rate of the continuous time signal may be much smaller than suggested by its bandwidth (BW) (i.e. compressible), and the incoherence expresses the idea that objects having a sparse representation in some known transform domain must be spread out in the acquired domain. Luckily, most of signal are sparse in known transform domain such as Wavelet domain.

Nowadays, CS in MRI is just one of the way application of CS such as imaging compressive, digital camera, astronomy, geophysics and high speed analogue to digital conversion signal, etc.

Starting from the requirement for undersampling k-space data and considering the MR hardware constrains several ways of generating undersampling patterns have been proposed. The most commonly used undersampling schemes, either Cartesian or non-Cartesian, consist of variable-density random undersampling [81, 112] based on a probability density function.

As mentioned above, the CS based on three fundamental premise: *sparsity*, *incoherence* and non-linear *reconstruction*. In this section we will dedicated the sparsity and incoherence in MRI.

Almost image are not sparse in image domain, but it would be sparse in a transform domain via a sparsity transform operator. A sparsity transform operator is an operator mapping a vector of image data to a sparse vector [81]. For example, a piece wise constant images (example Shepp-Logan image in Figure 18) can be sparsely represented under finite difference operator. The finite difference operator here mean computing the differences between neighbouring pixels and is often referred to as total variation (TV) [113]. Actually, the MR images are not piecewise constant, but in case of images in which the boundaries contain the most important information, like angiograms images, will be sparsely presented in a finite differences transform. Nowadays, the multi-scale

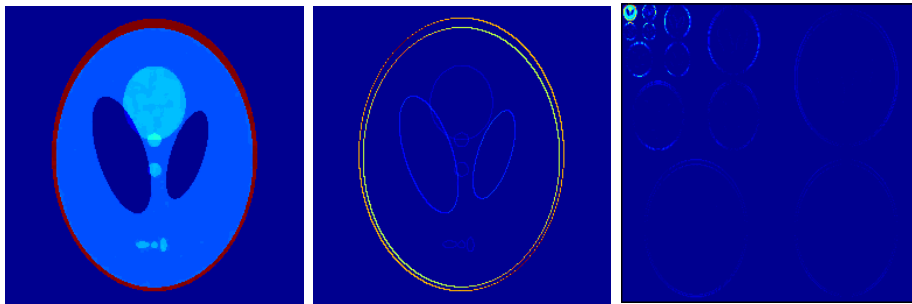
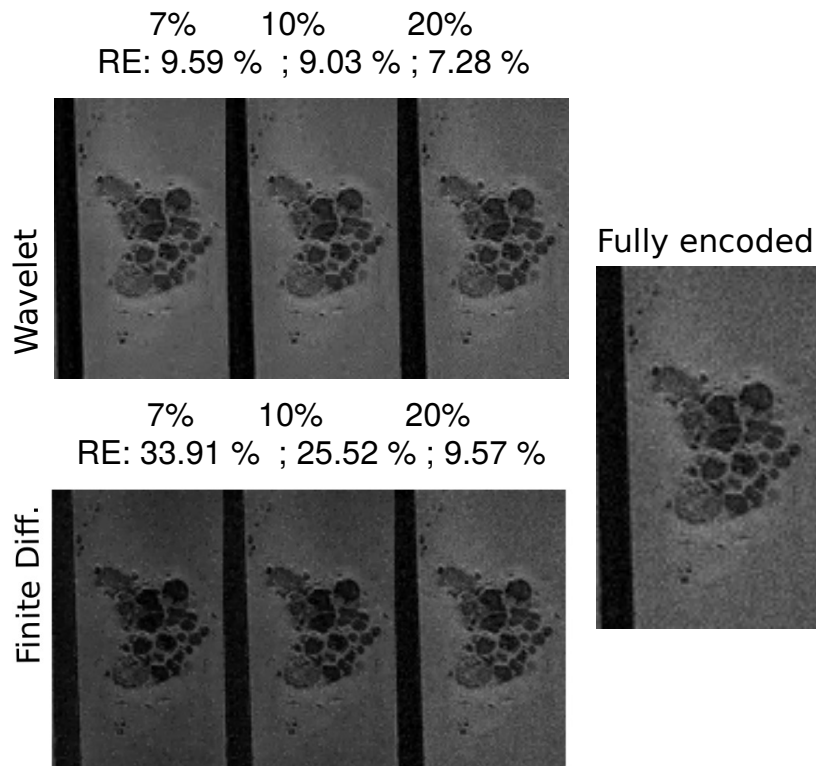


Figure 18 – Shepp-Logan image (left) is sparsely presented under finite difference operator (middle) and Wavelet transform (right).

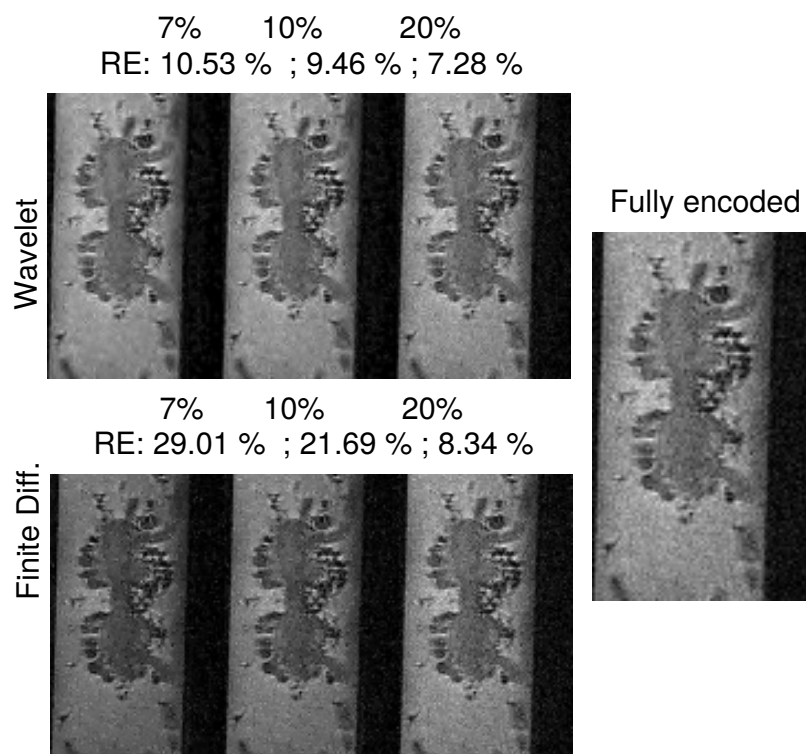
representation of images, the Wavelet transform, becomes an image compression standard in JPEG-2000 image [114]. Almost all images are spare in the Wavelet transform domain.

## 12.1 Sparsity of MR images

The MRI image can be sparsely presented by applying the sparsity transform to the fully encoded image. An approximation image can be reconstructed from a subset of the largest transform coefficients. The sparsity of an image is measured by the percentage of transform coefficients that are sufficient for an acceptable reconstruction. In practice, we can measure the sparsity of image by trying reconstructions from some arbitrary small percentages of transform coefficients and estimations the relative errors between the sparse approximation image and the fully encoded image. For example, in our study, two experimental T2w images of the abdominal ganglia and buccal ganglia of *Aplysia californica* were used. We applied the finite different transform and wavelet transform on these images and then reconstructing from 7%, 10% and 20% of the largest transform coefficients. The results are shown in Figure 19. By investigation the relative error between the sparsity reconstructed images from a subset of the largest sparse transform and the fully encoded image, we found that the Wavelet transform performs better than the finite different transform on the sparsify the abdominal ganglia and buccal ganglia T2w images. The relative error formula will be described in equation (98) in section 13.1 below.



(a)



(b)

Figure 19 – The sparsity of abdominal ganglia (a) and buccal ganglia (b) T2w images of *Aplysia*. The fully encoded image (right column) and the reconstructed images (three left column) from a subset of 7%, 10% and 20% of the largest wavelet transform and finite different transform coefficients.

## 12.2 Incoherence

In practice some undersampling pattern perform better than others. We need a metric to evaluate the incoherence of the aliasing interference to make sure that the choice of sampling is incoherent and evaluate which undersampling pattern is best. The Point Spread Function (PSF) proposed by Lustig et al [81] is a natural tool to measure incoherence. Let  $\mathcal{F}_u = M\mathcal{F}$  is the undersampled Fourier operator, where  $M$  is the undersampling pattern, and denote  $\mathcal{F}_u^H$  is the adjoint operator. The PSF is defined as:

$$PSF(i, j) = \mathcal{F}_u^H \mathcal{F}_u(i, j). \quad (65)$$

The PSF measures the contribution of a unit-intensity pixel at the  $(i, j)$  position. In case fully Nyquist sampling there is no interference between pixels and  $PSF(i, j) = \delta(i, j)$ . Where delta function  $\delta(i, j) = 1$  if and only if  $i = j$  and  $\delta(i, j) = 0$  in otherwise. Undersampling causes aliasing which shows the correlations between different pixels. The MR images are usually sparse in a transform domain rather than in the image domain. Let  $\mathcal{W}$  denote the sparsifying transform and  $\mathcal{W}^H$  is the adjoint operator. The Transform Point Spread Function (TPSF) (see more [107, 115, 81, 112]) is defined as:

$$TPSF(i, j) = \mathcal{W}^H \mathcal{F}_u^H \mathcal{F}_u \mathcal{W}(i, j). \quad (66)$$

The maximum value of  $TPSF(i, j)$  where  $i \neq j$  are used to measure the coherence of a undersampling pattern. The small coherence, that means incoherence, is desirable. Basically, the lower value of  $TPSF$  corresponding with the undersampling pattern  $M$  will gives the small reconstruction error. However, the undersampling patterns with the same incoherent measure, which one higher correlations between all coefficients will lead a large error in reconstruction [107]. Therefore in practice we applied the undersampling patterns which the same small value of TPSF to a data library and calculating the reconstruction error to evaluate the best pattern.

## 12.3 Polynomial undersampling patterns

Lustig et al [81] suggested to make use of quasi-random patterns following a Monte Carlo procedure based on a variable probability density function (pdf) :

$$pdf = \begin{cases} (1 - r)^p & \text{if } |r| \geq rad, \\ 1 & \text{if } |r| < rad, \end{cases} \quad (67)$$

where  $p$  is the arbitrary polynomial degree (usually chosen  $p = 2$ ), and  $rad$  is the maximum distance measured from center of k-space which we always samples. The pdf assigned different sampling probabilities for different region of k-space. There are two parts, in the central of k-space which will be always sampled, and the otherwise which will be sampled under the selected probability decay rate user-selected by polynomial degree  $p$ . By this way, the undersampling less near the k-space boundary and more in the central of k-space. The problem is how many samples should be acquire? By theoretical, the number of Fourier sample points that need be collected with respect to the number of sparse coefficients is derived in references [108] and [110]. In practical, the number of k-space samples should be roughly two to five times the number of

sparse coefficients [116, 117, 81]. On the other hand, the random sampling selected by polynomial scheme described above often gives a good result, incoherent and near-optimal solution. In order to optimal sampling scheme that maximizes the incoherence, Lustig et al suggested the use of TPSF to select appropriate undersampling patterns. Because of the TPSF measures propagation error, the best pattern is the lowest TPSF. The procedure shown as below:

1. Generate pdf function gives the probability of sampling points based on the desired resolution and FOV.
2. Randomly sampling of k-space based on pdf construction gives the sampling pattern S.
3. Measure the peak interference in the PSF or TPSF of the sampling pattern S.
4. Repeat 2-3 several times and choose the pattern with the lowest peak interference.

The sampling pattern generated can be used for future scans.

## 12.4 Image reconstruction: Discrete Fourier Transform

In MRI, the desired image function  $I(\cdot)$  can be encoded in the measured data  $S(\cdot)$ . Note that  $I(\cdot)$  representing spin density distributions weighted by relaxation effects, diffusion effects, etc. Basically, the signal  $S(\cdot)$  is the Fourier transform of  $I(\cdot)$ :

$$S(\mathbf{k}) = \mathcal{F}[I(\mathbf{r})] = \int I(\mathbf{r}) e^{-i2\pi \mathbf{k} \cdot \mathbf{r}} d\mathbf{r}. \quad (68)$$

For simplicity in present, the two dimensional case is considered,  $\mathbf{k} = (k_x, k_y)$ ,  $\mathbf{r} = (x, y)$ , and the imaging equation (68) can be written as

$$S(k_x, k_y) = \int_{-\infty}^{\infty} \int_{-\infty}^{\infty} I(x, y) e^{-i2\pi(k_x x + k_y y)} dx dy. \quad (69)$$

In MRI practice,  $S(k_x, k_y)$  is collected at a discrete set of k-space points. There are many ways to sampling data, the two most popular data collection is *rectilinear sampling* and *polar sampling*, are shown in Figure 20. It is easy to see that

$$\begin{cases} k_x &= m\Delta k_x \\ k_y &= n\Delta k_y \end{cases} \quad (70)$$

for rectilinear sampling, and

$$\begin{cases} k_x &= m\Delta k \cos(n \Delta \Phi) \\ k_y &= m\Delta k \sin(n \Delta \Phi) \end{cases} \quad (71)$$

for polar sampling, where  $m$  and  $n$  take integer numbers.

In this thesis, we focus on rectilinear sampling (Cartesian sampling), thus we following briefly introduce about the reconstruction formula for rectilinear sampling and skip for

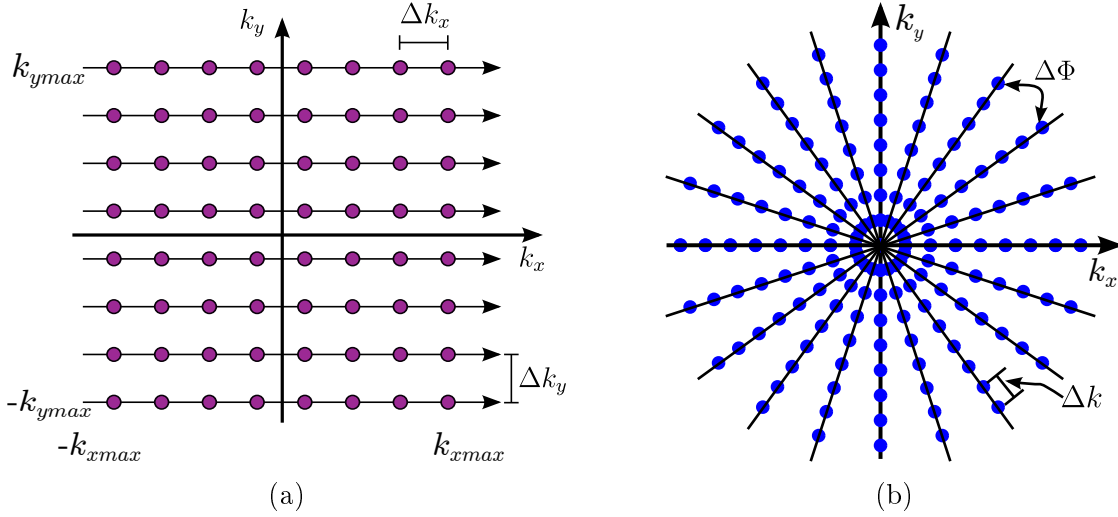


Figure 20 – Two most popular  $k$ -space sampling schemes: (a) rectilinear sampling and (b) polar sampling.

other samplings (non-Cartesian sampling). Readers interested in non-Cartesian sampling is referred to literatures [1, 2, 3, 4, 5, 118].

In MRI experiments, the image usually measured inside an rectangle region (for 2D imaging) or a box region (for 3D imaging). The limit bounded by this rectangle or box is called field-of-view (FOV). The original coordinate usually placed to central FOV region. The image function  $I(x, y)$  satisfy:

$$I(x, y) = 0 \quad \text{for } |x| \geq \frac{\text{FOV}_x}{2} \text{ and } |y| \geq \frac{\text{FOV}_y}{2}.$$

According to the sampling theorem, we have [118],

$$\Delta k_x \leq \frac{1}{\text{FOV}_x}, \quad \Delta k_y \leq \frac{1}{\text{FOV}_y}$$

The image function  $I(x, y)$  reconstructed from collected signal  $S(m\Delta k_x, n\Delta k_y)$  by:

$$I(x, y) = \Delta k_x \Delta k_y \sum_{m=-\frac{N_x}{2}}^{\frac{N_x}{2}-1} \sum_{n=-\frac{N_y}{2}}^{\frac{N_y}{2}-1} S(m\Delta k_x, n\Delta k_y) e^{i2\pi(m\Delta k_x x + n\Delta k_y y)}, \quad (72)$$

where  $|x| \leq \frac{1}{2\Delta k_x}$  and  $|y| \leq \frac{1}{2\Delta k_y}$ . Equation (72) is known as inverse Discrete Fourier transform. And therefore equation (69) can be written as Discrete Fourier transform:

$$S(k_x, k_y) = \sum_{m=-\frac{N_x}{2}}^{\frac{N_x}{2}-1} \sum_{n=-\frac{N_y}{2}}^{\frac{N_y}{2}-1} I(m\Delta x, n\Delta y) e^{i2\pi(mk_x \Delta x + nk_y \Delta y)}. \quad (73)$$

## 12.5 CS image reconstruction

The fully encoded images reconstruction were processed directly in Paravision. For the sparse MRI reconstruction, the general form for the reconstruction problem is presented

in [81, 119, 120, 121]. Briefly, if we denote the undersampled Fourier transform corresponding to the k-space undersampled pattern  $\mathcal{F}_u$ , and  $\mathcal{W}$  the sparse transform, the reconstructed image  $m$  is obtained by solving the following constrained optimization problem:

$$\begin{aligned} \text{minimize} \quad & \|\mathcal{W}m\|_1, \\ \text{s.t.} \quad & \|\mathcal{F}_u m - y\|_2 < \epsilon, \end{aligned} \quad (74)$$

where  $y$  is the measured undersampled k-space data. The norms,  $\ell_1$  and  $\ell_2$ , are defined as  $\|x\|_1 = \sum_i |x_i|$  and  $\|x\|_2 = \sqrt{\sum_i |x_i|^2}$ , respectively. The thresholding parameter  $\epsilon$  is the expected noise level. The undersampling Fourier transform operator  $\mathcal{F}_u$  can be expressed as the product of a full Fourier transform operator  $\mathcal{F}$  and an undersampling matrix  $M$ :  $\mathcal{F}_u = M\mathcal{F}$ . The undersampling matrix  $M$  defines the role of selecting the points of k-space that will be sampled or preserved.

When finite difference is used as a sparse transform,  $\mathcal{W} = \nabla$ , the objective in equation (74) becomes  $\|\nabla m\|_1$  which is called TV penalty and usually written as  $TV(m)$ . The spatial TV can be used as the isotropic TV model [122, 123, 124, 125] which is defined by:

$$TV(m) = \sum_i \sqrt{|\nabla_x m_i|^2 + |\nabla_y m_i|^2 + |\nabla_z m_i|^2}, \quad (75)$$

where  $\nabla_k m_i$  representing the gradient of image  $m$  at voxel index  $i$  in the direction  $k$  ( $k = x, y, z$ ). The gradient (or finite difference) of 3D image  $m$  at index  $(i, j, k)$  is defined by:

$$\begin{aligned} \nabla_x m(i, j, k) &= m(i+1, j, k) - m(i, j, k), \\ \nabla_y m(i, j, k) &= m(i, j+1, k) - m(i, j, k), \\ \nabla_z m(i, j, k) &= m(i, j, k+1) - m(i, j, k). \end{aligned} \quad (76)$$

When using the other sparsifying transform operator in the objective, the TV penalty usually included in the objective as well [117, 81, 122, 126]. In this case, the equation (74) is rewritten as:

$$\begin{aligned} \text{minimize} \quad & \|\mathcal{W}m\|_1 + \alpha TV(m), \\ \text{s.t.} \quad & \|\mathcal{F}_u m - y\|_2 < \epsilon, \end{aligned} \quad (77)$$

where  $\alpha$  trades  $\mathcal{W}$  sparsity with finite differences sparsity. The following nonlinear conjugate-gradient decent method for CS reconstruction problem will be focus on this form.

Some authors write the sparse MRI reconstruction problem in the following form (see [125, 122, 121]):

$$\begin{aligned} \text{minimize} \quad & \|\mathcal{W}m\|_1 + TV(m), \\ \text{s.t.} \quad & \|\mathcal{F}_u m - y\|_2^2 < \sigma^2, \end{aligned} \quad (78)$$

where the  $\sigma$  represents the variance of the signal noise. The Split Bregman method for CS reconstruction problem will be focus on this form.

### 12.5.1 Nonlinear conjugate-gradient descent method: SpareMRI toolbox

In this section, we followed the algorithm provided by Lustig et al. in the SparseMRI toolbox [81], which we extended to a 3D version.

Equation (77) can be rewritten in the unconstrained problem form as following:

$$\arg \min_m J(m), \quad (79)$$

where

$$J(m) = \|\mathcal{F}_u m - y\|_2^2 + \lambda_1 \|\mathcal{W}m\|_1 + \lambda_2 TV(m), \quad (80)$$

and  $\lambda_1, \lambda_2$  are two regularization constants. A large  $\lambda_2$  tends to suppress image gradients and make the reconstructed image smooth, losing point-like features [126]. In this thesis, we suggest to using the TV as a penalty because it was shown that it is efficient in suppressing the noise in the reconstructed image [127]. The optimized choose of regularization parameter  $\lambda_1$  and  $\lambda_2$  will be an interested work, but it will not covered during this thesis.

The iterative algorithm starts with a zero-filling Fourier reconstruction,  $m_0$ . The conjugate gradient requires the computation of the gradient of the cost function,  $\nabla J(m)$ , which is:

$$\nabla J(m) = 2\mathcal{F}_u^H (\mathcal{F}_u m - y) + \lambda_1 \nabla \|\mathcal{W}m\|_1 + \lambda_2 \nabla TV(m). \quad (81)$$

As the  $\ell_1$  norm is the sum of absolute values. However, the absolute values are not smooth functions, then the equation (81) is not well defined. Lustig et al proposed an approximation of the absolute value by a smooth function,  $|x| \approx \sqrt{x^H x + \xi}$ , where  $\xi$  is a positive smoothing parameter. Then the gradient becomes  $\frac{d|x|}{dx} \approx \frac{x}{\sqrt{x^H x + \xi}}$ . In practice, a smoothing factor  $\xi \in [10^{-15}, 10^{-6}]$ . Following we shall describe the algorithm for solving (79) using a nonlinear conjugate-gradient descent with backtracking line search taken from [81].

**Data:** $y$ : undersampled k-space data $\mathcal{F}_u$ : undersampled Fourier transform operator $\mathcal{W}$ : wavelet transform operator $\lambda_1, \lambda_2$ : data consistency tuning constants**Optional parameter:**Tol: stopping criteria by gradient magnitude (default  $10^{-4}$  )

Iter: stopping criteria by number of iterations (default 100)

 $\alpha, \beta$ : line search parameters (defaults  $\alpha = 0.01, \beta = 0.6$ )**Result:**  $m$  the numerical approximation to equation (79)

% Initialization

 $k = 0; m_0; g_0 = \nabla J(m_0); \Delta m_0 = -g_0$ 

% Iterations

**while**  $\|g_k\|_2 > Tol$  **do**

% Backtracking line search

 $t = 1;$     **while**  $J(m_k + t\Delta m_k) > J(m_k) + \alpha t \cdot \text{Real}(g_k^* \Delta m_k)$  **and**  $k < Iter$  **do**         $t = \beta t;$     **end**     $m_{k+1} = m_k + t\Delta m_k$      $g_{k+1} = \nabla J(m_{k+1})$      $\gamma = \frac{\|g_{k+1}\|_2^2}{\|g_k\|_2^2}$      $\nabla m_{k+1} = -g_{k+1} + \gamma \Delta m_k$      $k = k + 1$ **end**

**Algorithm 1:** Nonlinear conjugate-gradient descent with backtracking line search for  $\ell_1$  reconstruction.

We have wrote several C-MEX function files, the function written in C or C++ code that are callable from Matlab, to significantly improve the calculation time.

### 12.5.2 Split Bregman method

Split Bregman method for fast CS image reconstruction provided by Tom Goldstein in 2009 [122] with TV penalty and the Haar wavelet transform. The Split Bregman method is a technique for solving a variety of  $\ell_1$ -regularized optimization problems, and is particularly effective for problems involving TV regularization. Split Bregman is one of the fastest solvers for total variation de-noising, image reconstruction from Fourier coefficients, convex image segmentation, and many other problems. The method is a re-interpretation of the alternating direction method of multipliers that is specially adapted to  $\ell_1$  problems. During this thesis, we keep follow the algorithm proposed by Tom Goldstein in [122] for an isotropic TV model which can be easy extended to 3D version for our studies. The original 2D code can be found in reference [128].

A complete technical explanation of the Split Bregman method can be found in the paper [122]. To apply the Split Bregman method to this problem, first we notation

$w = \mathcal{W}m$ ,  $d_x = \nabla_x m$ ,  $d_y = \nabla_y m$ , and  $d_z = \nabla_z m$ , the Equation (78) is rewritten by:

$$\begin{aligned} \min_m \quad & \|w\|_1 + \|(d_x, d_y, d_z)\|_2, \\ \text{s.t.} \quad & \|\mathcal{F}_u m - y\|_2^2 < \sigma^2, \end{aligned} \quad (82)$$

where

$$\|(d_x, d_y, d_z)\|_2 = \sum_{i,j,k} \sqrt{|d_{x,i,j,k}|^2 + |d_{y,i,j,k}|^2 + |d_{z,i,j,k}|^2}.$$

As shown previously in [122, 129], by applying the Bregman iterations the following unconstrained equations converges iteratively to Equation (82):

$$\begin{aligned} \min_{m, d_x, d_y, d_z, w} \quad & \|w\|_1 + \|(d_x, d_y, d_z)\|_2 + \|w\|_1 + \frac{\mu}{2} \|\mathcal{F}_u m - y^h\|_2^2 \\ & + \frac{\lambda}{2} \|d_x - \nabla_x m - b_x^h\|_2^2 + \frac{\lambda}{2} \|d_y - \nabla_y m - b_y^h\|_2^2 + \frac{\lambda}{2} \|d_z - \nabla_z m - b_z^h\|_2^2 \\ & + \frac{\gamma}{2} \|w - \mathcal{W}m - b_w^h\|_2^2, \end{aligned} \quad (83)$$

$$y^{h+1} = y^h + y - \mathcal{F}_u m^{h+1}, \quad (84)$$

where  $\lambda$ ,  $\mu$ , and  $\gamma$  are three constant penalty weighting parameters, the proper value of  $b_x^h$ ,  $b_y^h$ ,  $b_z^h$ ,  $b_w^h$  and  $y^h$  are chosen through Bregman iteration. At each iteration  $h + 1$ , using split Bregman method, Equation (83) can be split to following equations (see more [122]):

$$\begin{aligned} m^{h+1} = \min_m \quad & \frac{\mu}{2} \|\mathcal{F}_u m - y^h\|_2^2 + \frac{\lambda}{2} \|d_x^h - \nabla_x m - b_x^h\|_2^2 + \frac{\lambda}{2} \|d_y^h - \nabla_y m - b_y^h\|_2^2 \\ & + \frac{\lambda}{2} \|d_z^h - \nabla_z m - b_z^h\|_2^2 + \frac{\gamma}{2} \|w - \mathcal{W}m - b_w^h\|_2^2. \end{aligned} \quad (85)$$

$$d_i^{h+1} = \max \left( s^h - \frac{1}{\lambda}, 0 \right) \frac{\nabla_i m^h + b_i^h}{s^h}, \quad i = x, y, z, \quad (86)$$

$$b_i^{h+1} = b_i^h + (\nabla_i m^{h+1} - d_i^{h+1}), \quad i = x, y, z \quad (87)$$

$$w^{h+1} = \text{shrink} \left( \mathcal{W}m^{h+1} + b_w^h, \frac{1}{\gamma} \right), \quad (88)$$

$$b_w^{h+1} = b_w^h + (\mathcal{W}m^{h+1} - w^{h+1}), \quad (89)$$

$$(90)$$

where the variable  $b_i^h$ ,  $d_i^h$ ,  $b_w^h$  ( $i = x, y, z$ ) are initialized by 0,  $y^0 = y$ , the standard shrinkage formula [130, 122] is

$$\text{shrink}(x, \gamma) = \frac{x}{|x|} \max(|x| - \gamma, 0), \quad (91)$$

and the generalized shrinkage formula [130, 122]:

$$s^h = \sqrt{|\nabla_x m^h + b_x^h|^2 + |\nabla_y m^h + b_y^h|^2 + |\nabla_z m^h + b_z^h|^2}. \quad (92)$$

Because of the Equation (85) is differentiable (see [122, 129, 125]), by differentiating with respect to  $m$  and setting the result equal to zeros, we can obtain the update rule:

$$(\mu \mathcal{F}_u^T \mathcal{F}_u + \lambda \nabla_x^T \nabla_x + \lambda \nabla_y^T \nabla_y + \lambda \nabla_z^T \nabla_z + \gamma \mathcal{W}^T \mathcal{W}) m^{h+1} = r^h, \quad (93)$$

where

$$r^h = \mu \mathcal{F}_u^T y^h + \lambda \nabla_x^T (d_x^h - b_x^h) + \lambda \nabla_y^T (d_y^h - b_y^h) + \lambda \nabla_z^T (d_z^h - b_z^h) + \gamma \mathcal{W}^T (w^k - b_w^h), \quad (94)$$

represent the right hand side in the above equation. Remember that  $\mathcal{F}_u = M\mathcal{F}$ , so the  $\mathcal{F}_u^T = \mathcal{F}^T M^T$ . On the other hand,  $\nabla^T \nabla = -\Delta$ ,  $\mathcal{W}^T \mathcal{W} = I$  and  $\mathcal{F}^T = \mathcal{F}^{-1}$ , so the equation (93) can be simplified by:

$$(\mu \mathcal{F}_u^T \mathcal{F}_u - \lambda \Delta + \gamma I) m^{h+1} = r^h. \quad (95)$$

This equation must be inverted to solve  $m^{h+1}$  in circulant that make costly for computational. To avoid this limited, we can thus write the system as  $\mathcal{F}^{-1} H \mathcal{F}$ , where  $H$  now is the diagonal operator:

$$H = (\mu M^T M - \lambda \mathcal{F} \Delta \mathcal{F}^{-1} + \gamma I). \quad (96)$$

The Equation (95) becomes

$$m^{h+1} = \mathcal{F}^{-1} H^{-1} \mathcal{F} r^h. \quad (97)$$

The full split Bregman algorithm for  $\ell_1$  reconstruction problem (78) is described by following.

**Data:** $y$ : undersampled k-space data $\mathcal{F}$ : Fourier transform operator $M$ : undersampling matrix $\mathcal{W}$ : Haar orthogonal wavelet transform operator $\sigma$ : expected variance of the noise constants $\mu, \lambda, \gamma$ : regularization terms $N$ : stopping criteria by number of iterations**Result:**  $m$  the numerical approximation to equation (78)

% Initialization

 $h = 0$ ;  $y^0 = y$ ;  $m^0 = \mathcal{F}^{-1}y$ ; and  $d_x^0 = d_y^0 = d_z^0 = w^0 = b_x^0 = b_y^0 = b_z^0 = b_w^0 = 0$ ;

% Iterations

**do****for**  $i = 1$  **to**  $N$  **do**

$$r^h := \mu \mathcal{F}^T M^T y^h + \lambda \nabla_x^T (d_x^h - b_x^h) + \lambda \nabla_y^T (d_y^h - b_y^h) + \lambda \nabla_z^T (d_z^h - b_z^h) + \gamma \mathcal{W}^T (w^h - b_w^h)$$

$$m^h := \mathcal{F}^{-1} H^{-1} \mathcal{F} r^h$$

$$s^h := \sqrt{|\nabla_x m^h + b_x^h|^2 + |\nabla_y m^h + b_y^h|^2 + |\nabla_z m^h + b_z^h|^2}$$

$$d_x^h := \max \left( s^h - \frac{1}{\lambda}, 0 \right) \frac{\nabla_x m^h + b_x^h}{s^h}$$

$$d_y^h := \max \left( s^h - \frac{1}{\lambda}, 0 \right) \frac{\nabla_y m^h + b_y^h}{s^h}$$

$$d_z^h := \max \left( s^h - \frac{1}{\lambda}, 0 \right) \frac{\nabla_z m^h + b_z^h}{s^h}$$

$$w^h := \mathit{shrink} \left( \mathcal{W} m^h + b_w^h, \frac{1}{\gamma} \right)$$

$$b_x^h := b_x^h + (\nabla_x m^h - d_x^h)$$

$$b_y^h := b_y^h + (\nabla_y m^h - d_y^h)$$

$$b_z^h := b_z^h + (\nabla_z m^h - d_z^h)$$

$$b_w^h := b_w^h + (\mathcal{W} m^h - w^h)$$

**end**% update variables to next step  $m^{h+1} := m^h$ 

$$d_x^{h+1} := d_x^h$$

$$d_y^{h+1} := d_y^h$$

$$d_z^{h+1} := d_z^h$$

$$b_x^{h+1} := b_x^h$$

$$b_y^{h+1} := b_y^h$$

$$b_z^{h+1} := b_z^h$$

$$w^{h+1} := w^h$$

$$b_w^{h+1} := b_w^h$$

$$y^{k+1} = y^k + y - M \mathcal{F} m^{k+1}$$

$$h := h + 1$$

**while**  $\|M \mathcal{F} m^h - y\|_2^2 > \sigma^2$ ;**Algorithm 2:** Split Bregman algorithm for  $\ell_1$  reconstruction.

## 13 Measuring the quality of accelerated acquisition

In our study, it is important to compare the two fully encoded and CS encoded images. The  $\ell_2$  relative errors (RE) can be used to calculate the relative errors between CS and fully encoded images, beside, the Pearson's Correlation Coefficient (PCC) can be used to measure the strength of a linear relationship between CS and fully encoded images.

### 13.1 Image error

In order to compare the two undersampling strategies we computed the  $\ell_2$  relative error (RE) between the CS and fully encoded images:

$$\text{RE} = \frac{\sqrt{\sum_{i=1}^n (y_i - \hat{y}_i)^2}}{\sqrt{\sum_{i=1}^n y_i^2}}, \quad (98)$$

where  $y_i$  and  $\hat{y}_i$  are the signal intensities corresponding to voxel  $i$  in the fully encoded image and the undersampled image, respectively.  $n$  is the number of voxels.

Moreover, root mean square error (RMSE) can be used for measured the different between two images:

$$\text{RMSE} = \sqrt{\frac{1}{n} \sum_{i=1}^n (y_i - \hat{y}_i)^2}. \quad (99)$$

### 13.2 Pearson's Correlation Coefficient

The PCC is a statistical measure of the strength of a linear relationship between two paired data. It is described as [131, 132]:

$$\text{PCC} = \frac{\sum_{i=1}^n (y_i - y_{\text{mean}}) (\hat{y}_i - \hat{y}_{\text{mean}})}{\sqrt{\sum_{i=1}^n (y_i - y_{\text{mean}})^2} \sqrt{\sum_{i=1}^n (\hat{y}_i - \hat{y}_{\text{mean}})^2}}, \quad (100)$$

where  $\{y_i : i = 1, \dots, n\}$  and  $\{\hat{y}_i : i = 1, \dots, n\}$  are two sample datasets with the mean sample are  $y_{\text{mean}}$  and  $\hat{y}_{\text{mean}}$ , respectively. In this thesis,  $y_i$  and  $\hat{y}_i$  represent signal intensities of voxel  $i$  in the fully encoded image and the undersampled image, respectively, and  $y_{\text{mean}}$  and  $\hat{y}_{\text{mean}}$  are the corresponding mean signal intensity values over all voxels.  $n$  is the number of voxels.

## Part IV

# Compressed sensing for high resolution MRI

## Summary

---

<b>14</b>	<b><i>k</i>-space undersampling patterns</b>	<b>69</b>
14.1	DLA undersampling patterns . . . . .	69
14.2	DLA vs polynomial undersampling . . . . .	70
<b>15</b>	<b>The implementation of CS on T2w and T1w pulse sequences</b>	<b>72</b>
<b>16</b>	<b>Image reconstruction</b>	<b>73</b>
<b>17</b>	<b>Cell segmentation algorithm</b>	<b>74</b>
<b>18</b>	<b>CS in T2-weighted imaging: CS-RARE</b>	<b>76</b>
18.1	The choice of undersampling ratio for generating undersampling patterns	76
18.2	Sample preparation and data acquisition . . . . .	76
18.3	Signal to noise ratio and spatial resolution . . . . .	76
<b>19</b>	<b>CS in T1-weighted imaging: CS-FLASH</b>	<b>78</b>
19.1	Undersampling pattern generation . . . . .	80
19.2	Data acquisition . . . . .	80
19.3	Sample preparation . . . . .	81
19.4	Image analysis . . . . .	81
19.5	Results . . . . .	82
<b>20</b>	<b>Conclusion and discussion</b>	<b>85</b>

---

CS produces images from significantly fewer data points than what is required by the Nyquist criterion using a non-linear reconstruction which enforces both sparsity of the image representation and consistency with the acquired data. The main requirement for undersampled k-space CS data is incoherence. Starting from this and considering the MR hardware constrains several ways of generating undersampling patterns have been proposed. The most commonly used undersampling schemes, either Cartesian or non-Cartesian, consist of variable-density random trajectories [81] based on a probability density function. Here we introduce a new method to generate the undersampling pattern based on the diffusion limited aggregation (DLA) random growth model [133] and present its application to the undersampling of T2w and T1w high resolution images.

## 14 $k$ -space undersampling patterns

CS undersampling patterns are subsets of frequency domain points which are incoherent with respect to the sparsifying transform and satisfy hardware constraints. The most commonly used CS designs are obtained by generating quasi-random patterns following a Monte Carlo procedure based on a variable probability density function [81, 125, 134] (called polynomial undersampling). Here we will briefly describe the polynomial undersampling and compare it with the method we called DLA undersampling method [135]. The description of polynomial undersampling scheme presented below is taken from Lustig et al [81]. The DLA undersampling method is adapted from our paper [135].

### 14.1 DLA undersampling patterns

We propose a new way of producing undersampling patterns employing the DLA random growth model. The DLA was proposed, for the first time, by T.A. Witten and L.M. Sander in 1981 [133]. The basic DLA growth process in two dimensions is relatively simple. An initial particle, the "seed", is placed at the origin of the lattice. A second particle, the "walker", is added at a random position far away from the seed and undergoes random walk in the plane until it reaches a site neighboring the seed when it becomes part of the cluster. Subsequently, other walkers are introduced, one by one, at different random locations and allowed to walk randomly until they join the cluster. The basic DLA undersampling process consists in the following steps:

1. An initial particle, the seed, is placed at the origin of a 2-dimensional lattice containing  $M \times N$  points.
2. A kill circle, whose radius is much larger than the linear size of the lattice and centered on the seed, is defined.
3. A walker is launched at a random position on a birth circle with radius  $R_i$  defined by:

$$R_i = \frac{1}{100} \times \max(M, N) \times \left( 1 + 49 \times \frac{i-1}{P} \right), \quad (101)$$

with  $i = 1$  to  $P$ , where  $P$  is the desired final number of particles in the cluster, dictated by the undersampling ratio. If the radius of the birth circle is smaller than a predefined  $R_{min}$  (here we chose  $R_{min} = 2$ ) then  $R_i = R_{min}$ .

4. The walker walk randomly until one of three outcomes is reached:
  - (a) The walker escapes the kill circle. A new walker is placed on the same birth circle and the random walk is restarted.
  - (b) The walker hits a lattice point which is a nearest neighbor to one member of the cluster. The walker then becomes part of the cluster and the index  $i$  is incremented to  $i + 1$ .
  - (c) The walker diffuses a long time without neither joining the cluster nor leaving the kill circle. The index  $i$  is incremented to  $i + 1$ , and there will be no contribution to the cluster from this walker. NOTE: If  $i$  reaches  $P$  while the number of particles in the cluster is smaller than  $P$ , the counter is reset to  $i = 1$  (i.e. restart from the smallest birth circle).
5. Steps 3 and 4 are repeated until the desired cluster size is reached.

As in Lustig et al we also use PSF (or TPSF) to select the appropriate undersampling patterns. However, we propose to use many undersampling patterns with lower enough PSF (or TPSF, respectively) and apply them to a library of a priori acquired fully sampled data sets in order to choose which ones gives the lowest relative error between the CS and fully encoded images. The procedure is briefly described below:

1. Generate DLA undersampling patterns.
2. Measure the peak interference in the PSF (or TPSF) of the DLA undersampling patterns. Select the DLA undersampling pattern with lowest PSF (or TPSF, respectively).
3. Repeat step 1-2 many times, to produce a set of DLA undersampling pattern candidates.
4. Apply each undersampling pattern in *candidate set* to the library of priori acquired fully sampled data. Choose the undersampling pattern with the lowest relative error between CS and fully encoded images.

## 14.2 DLA vs polynomial undersampling

In our case the 2D lattices sampled belong to a 3D Cartesian k-space grid, predefined for a given field-of-view ( $10 \times 2.2 \times 2.2 \text{ mm}^3$ ) and spatial resolution ( $25\mu\text{m}$  isotropic), with the undersampling being done along the two phase encoding directions. Figure 21a shows the proposed undersampling for one phase encoding plane. Such undersampling can be applied to a RARE acquisition with an acceleration factor  $A_F = 4$  by generating subsampling patterns for k-space points subsets corresponding to one echo time, and repeating this sampling patterns  $A_F$  times to cover the entire k-space, resulting therefore in repeating the pattern in Figure 21a four times (Figure 21b). The 2D patterns obtained

are repeated for each point in the read direction to generate the 3D undersampling pattern (Figure 21c). Eleven undersampling ratios were chosen between 80% and 30%. For each undersampling ratio 300 sets consisting of 100 undersampling masks were generated and from each set the mask with the lowest PSF was selected [81]. The  $300 \times 11 = 3300$  masks produced were then applied to a library of a priori acquired fully sampled data sets consisting of six images of abdominal and buccal ganglia of *Aplysia californica* (three of each). Undersampling patterns based on the polynomial probability density function, with  $A_F = 1$  (Figure 21d),  $A_F = 4$  (Figure 21e) and extended to a 3D RARE acquisition with  $A_F = 4$  (Figure 21f), were also generated as in [81] and were applied to the same library of images. In order to compare the two undersampling strategies we computed the RE between the CS and fully encoded images (see Equation (98)). In addition, the performances of DLA and polynomial schemes when applied to RARE acquisitions with  $A_F = 1$  were similarly evaluated this time applying the generated masks to a fully encoded image of the buccal ganglia acquired without acceleration.

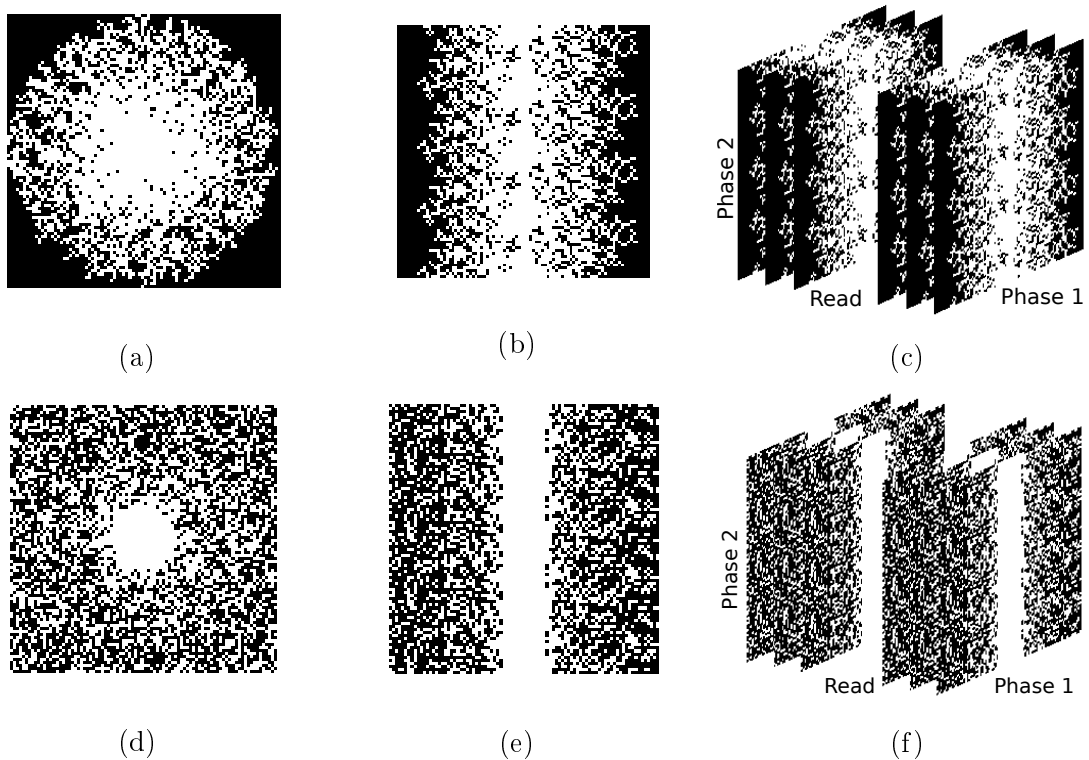


Figure 21 – Undersampling patterns (50 %) for a RARE acquisition: DLA (a) and polynomial (d) undersampled phase encoding plane for  $A_F = 1$ ; DLA (b) and polynomial (e) undersampled phase encoding plane for  $A_F = 4$ . The undersampling patterns was applied for one group of k-space points corresponding to the first echo time, the results was then repeated  $A_F = 4$  times corresponding to all echo time; (c) 3D DLA undersampling and (f) 3D polynomial undersampling generated by repeat 2D undersampling pattern in read direction.

The DLA sampling pattern with the minimum relative error was implemented in Paravision 5.1 (Bruker BioSpin, Ettlingen, Germany).

As seen in Figure 22, in the case of RARE acquisitions with  $A_F = 4$ , and Figure 23

in the case of RARE acquisitions with  $A_F = 1$  the mean relative errors between the CS and the fully encoded images are smaller for DLA than for polynomial patterns for both the buccal and the abdominal ganglia. Moreover, the DLA method is more stable as the standard deviation of the relative error is smaller than for the polynomial scheme. The difference in performance between the two undersampling schemes is even larger for  $A_F = 1$  than for  $A_F = 4$ .

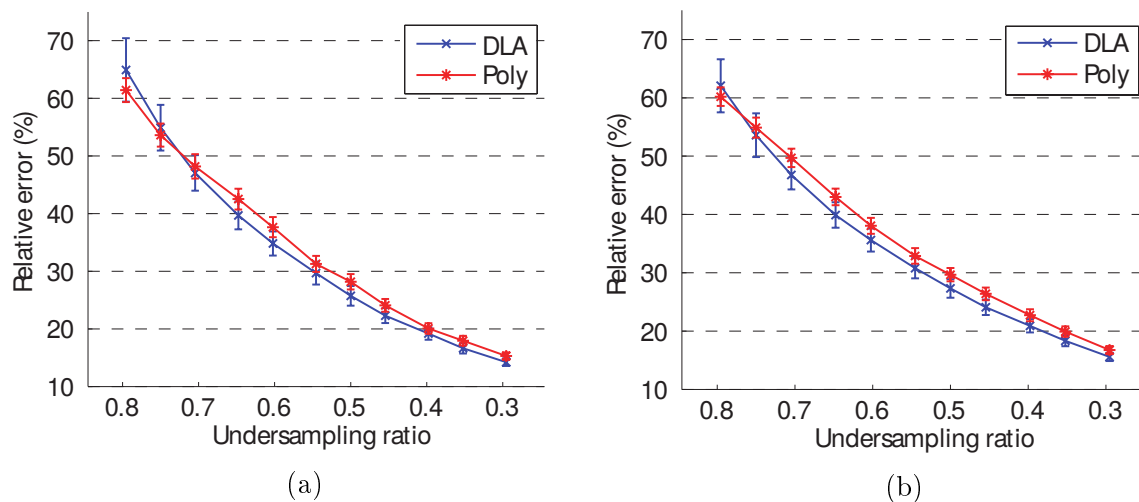


Figure 22 – The relative errors between the fully encoded and CS images obtained by applying DLA and polynomial undersampling schemes to abdominal (a) and buccal ganglia image libraries (b) as a function of the undersampling ratio. The fully encoded images were acquired using a standard RARE acquisition with  $A_F = 4$ . The error bars represent standard deviations ( $n=300$ ).

## 15 The implementation of CS on T2w and T1w pulse sequences

Programming of ParaVision method is was performed in order to realize actual undersampling on the MRI scanner. The structure of programming in ParaVision 5.1 is very similar for all sequences. As an example we will briefly show here the way to implement the CS version starting from the Bruker standard RARE sequence (T2w imaging). The procedure presented here can be easily to extended to any sequence (including the FLASH sequence).

The compressed sensing-RARE (CS-RARE) sequence was programmed starting from the existing RARE sequence distributed by Bruker Biospin. In Paravision, the files necessary for generating pulse sequences are divided in two parts: the core method written in C++ language pre-defines all the necessary components and defines user interface; and the Pulse program which sends commands to the scanner. It is recommended that the core method utilizes the internal PVM code structure shown in Figure 24 (taken from the ParaVision Manual part D, section 8.3.15). The CS-RARE sequence is initially copied from the standard Bruker RARE sequence using the *copyMethod* script

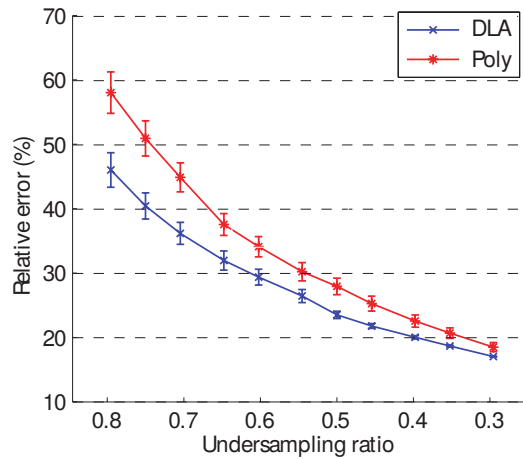


Figure 23 – The relative errors between the fully encoded and CS images obtained by applying DLA and polynomial undersampling schemes to a fully encoded (RARE acquisition with  $A_F = 1$ ) image of buccal ganglia. The error bars represent standard deviations ( $n=300$ ).

in a terminal. Several files are created and modified according to Figure 24 where the name of function highlighted by blue color mean created and/or reprogrammed. First of all, the variables needed for CS mode are defined in three header files: *parsDefination.h*, *parsRelation.h*, *parsLayout.h* and their relation to new functions are defined in the backbone() function. Second, a new function named *my\_set\_gradient()* for converting the generated undersampling  $k$ -space pattern in gradient parameters is defined in a new header file called *myLib.h*. This function is then incorporated in the function *SetGradientParameters()*. Third, the new option for CS mode and the corresponding graphics user interface are defined in *parsRelation.c* file. The successful compilation of the source code generates object files and clones the pulse program (.ppg in extension) from the original sequence. We also needed to modify the pulse program file *csRARE.ppg* to match the encoding steps with the undersampling ratio. The image reconstruction is done in Matlab.

The compressed sensing-FLASH sequence (CS-FLASH) is created using the same procedure but a different undersampling pattern was implemented.

We successful implemented the CS version of RARE and FLASH pulse sequences in Paravision 5.1, Bruker Biospin.

## 16 Image reconstruction

The fully encoded images were processed directly in Paravision. For the T2w, CS undersampled data we followed the algorithm provided by Lusting et al. [81], which we extended to 3D version (see section 12.5.1). For the T1w, CS undersampled data were reconstructed following the Split-Bregman algorithm provided by Goldstein and Osher in 2009 [122], which was extended for this study to a 3D version with total variation (TV) penalty and Haar wavelet transform (see section 12.5.2). The comparison of two reconstruction method is interesting works, but during this thesis we did not

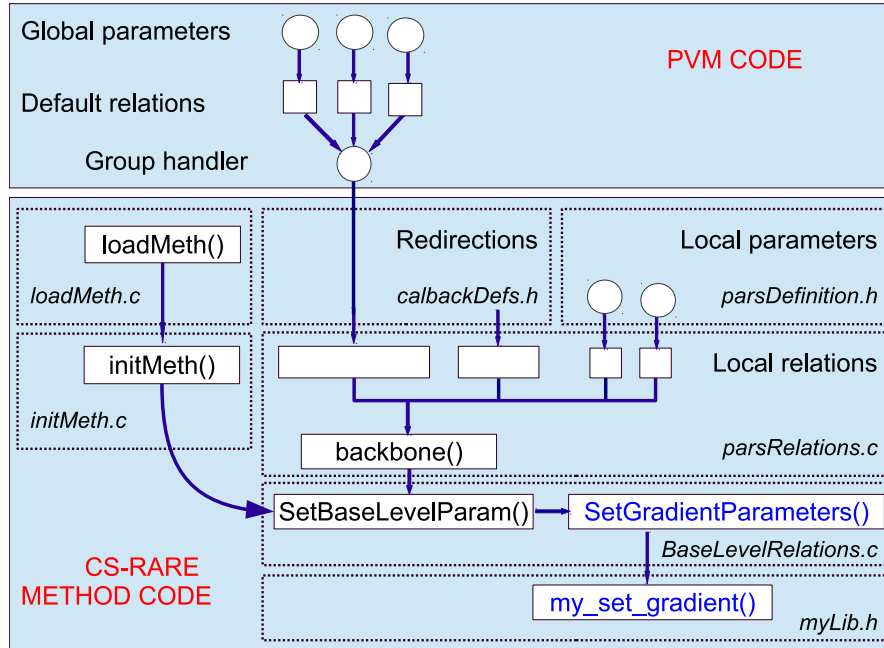


Figure 24 – Flow diagram illustrating the outline of created and modified ParaVision files.

compare two methods. For our experience, the Split-Bregman method running faster than the nonlinear conjugate-gradient descend method. Both Split-Bregman and nonlinear conjugate-gradient descend methods can be used for T2w and T1w CS.

The following sections will summarize some results of DLA-CS strategy for high resolution T2w and T1w imaging.

## 17 Cell segmentation algorithm

Due to failure when using some cell segmentation packages for T2w images, in this section we introduce a simple algorithm for automatic cell segmentation on MR  $T_2$  weighted images, which will be used to quantify the spatial resolution of CS and fully encoded RARE image. The main steps are as follows:

1. Different signal intensity levels ( $C_1, C_2, C_3$ , etc) contour maps are created from a given image data,  $C_0$ .
2. The area for each contour map is computed and maps with areas larger than a predefined maximum are removed. This step removes the water region around the ganglia and the inner part of the ganglia not containing cells.
3. The contour maps are then thresholded several times in order to separate isolated cells or cell clusters. The thresholding stops when repeating the algorithm will lead to unwanted cell elimination.
4. The cells within the clusters are further separated (Figure 25):

- (a) 1s are assigned to pixels corresponding to cell regions and 0s to all the others. The 1s located on the cluster boundary are removed. (One pixel is considered as part of the boundary if connected with at least two 0 pixels.)
- (b) 1s and 0s are inverted.
- (c) The boundary pixels are removed again.
- (d) The 1s and 0s are inverted.
- (e) Steps 4a-4d are repeated two or three times.

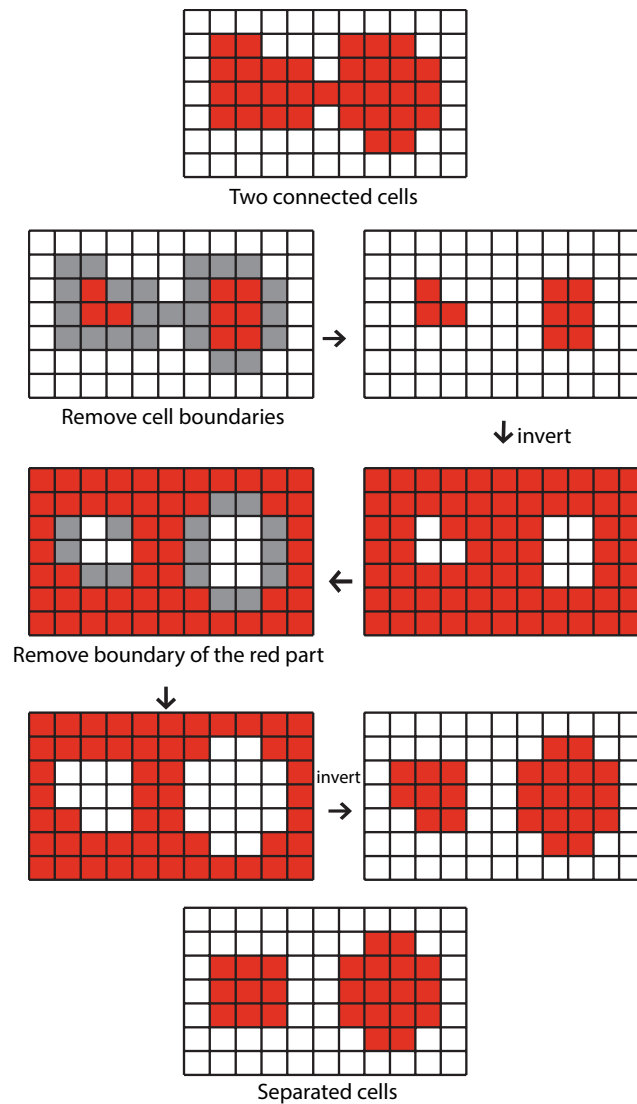


Figure 25 – Flow diagram illustrating the proposed algorithm for separating cells within clusters.

5. The cells detected in all the contour maps are combined. To avoid false detection one cell is considered "true" if it is detected in at least two maps.

This cell segmentation algorithm was implemented in Matlab.

## 18 CS in T2-weighted imaging: CS-RARE

In this section we will present results obtained using the CS-RARE pulse sequence.

### 18.1 The choice of undersampling ratio for generating undersampling patterns

By results from section 14.2, as seen in Figure 22, the DLA method performs better than the polynomial undersampling method. In addition, asking for an upper limit of 25% for the relative error we find a maximum undersampling ratio of 0.5 which was therefore used for the rest of this study.

### 18.2 Sample preparation and data acquisition

All experiments were performed at 19°C on a 17.2 T system (Bruker BioSpin, Ettlingen, Germany) equipped with 1 T/m gradients. The RF transceiver was home-built solenoidal single-microcoil with an inner diameters of 2.4 mm, the design of which has been described elsewhere ([136, 137]). Two acquisitions were acquired for each sample. A standard, fully encoded RARE acquisition with a matrix size of  $400 \times 88 \times 88$  and a CS undersampling RARE acquisition CS-RARE with a total acquired data points reduced to 50%. All the other parameters were identical for the two acquisitions: TR = 3500 ms, TE = 20 ms, RARE acceleration factor  $A_F = 4$ , FOV =  $10 \times 2.2 \times 2.2$  mm<sup>3</sup>. The acquisition times is 1 hour 52 minutes and 56 minutes for fully encoded RARE and CS-RARE encoded, respectively.

*Phantom samples:* SNR measurements were performed on images obtained using CS and fully encoded RARE acquisitions on phantom samples. The latter were 2 mm ID glass capillaries (VitroCom, Mountain Lakes, NJ, USA) filled with artificial sea water (ASW) (NaCl, 450 mM; KCl, 10 mM; MgCl<sub>2</sub>, 30 mM; MgSO<sub>4</sub>, 20 mM). All chemicals were purchased from Sigma-Aldrich (Saint Luis, MO, USA).

*Neuronal tissue:* Four *Aplysia californica* (National Resource for Aplysia, Miami, FL, USA) were used for this study. Three animals were used for generating the library necessary to optimize the undersampling trajectories, and one was used to acquire the fully encoded and CS encoded images. The animals were anaesthetized by injection of an isotonic magnesium chloride solution (MgCl<sub>2</sub>, 360 mM; HEPES, 10 mM; pH = 7.5). The buccal and abdominal ganglia were resected and inserted into a 2.0 mm ID glass capillary filled with ASW and then slid inside the transceiver for imaging.

### 18.3 Signal to noise ratio and spatial resolution

The reconstructed MR image of an ASW phantom acquired with the newly modified CS-RARE sequence was compared to the fully sampled MR image acquired with the conventional RARE sequence (Fig. 26). The signal to noise ratios obtained, calculated by dividing the mean signal value from a water region to the standard deviation of the noise in an ROI outside the sample, were found 19.9 and 14.6 for the CS and

fully encoded data sets, respectively. The CS data set presents higher SNR than the fully encoded acquisition due to the reduction of noise in the CS reconstructed image. Specifically, the standard deviation of the noise (measured in the blue ROI in Fig. 26) was found to be 165 and 120, respectively, for the two data sets, while the mean signal levels were similar ( $\sim 2400$ ).

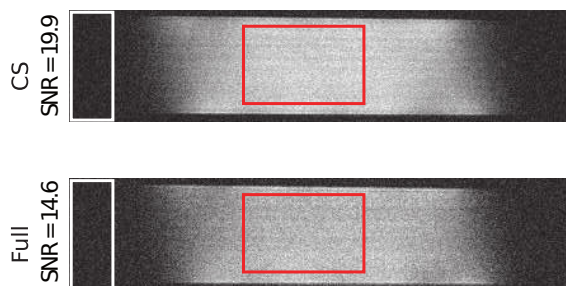


Figure 26 – CS (top) and fully encoded (bottom) images of a water phantom. The SNR was calculated as the mean of signal intensity (red ROI) divided by the standard deviation of the noise (white ROI).

To test the effect of CS undersampling on the spatial resolution we compared fully encoded and undersampled images of buccal and abdominal ganglia. For this particular comparison the undersampling was performed starting from the same fully sampled data set in order to avoid possible confounds such as coil instability or sample deterioration. Signal intensity profiles drawn across the sample (Fig. 27) demonstrate that no spatial or intensity information is lost. This was further confirmed by the Pearson correlation coefficients [138] between the fully and CS encoded images, calculated within a region containing the ganglia and consisting of approximately 180 000 voxels, which were found to be 0.90 and 0.91 for the buccal and abdominal samples, respectively.

To complete the CS performance assessment the automatic cell segmentation algorithm described in the Methods section was applied in each slice of the 3D fully encoded and CS images. The segmentation produced similar results for CS and fully encoded images, with an identical number of cells detected for abdominal ganglia and one false positive for the CS image (out of 31 cells) of the buccal ganglia (Figure 28).

To conclude, the new acquisition schemes CS-RARE cuts back the experimental time by a factor of two (50%) while preserving the signal to noise ratio, spatial resolution, and image contrast. The CS-RARE image quality is assessed by comparing fully encoded and undersampled images of water phantoms and biological tissues. An automatic cell segmentation algorithm applied to 3D images of buccal and abdominal ganglia of *Aplysia californica* ( $25\mu\text{m}$  isotropic resolution) allowed us to further evaluate the performance of the CS-RARE acquisition. We find that DLA based compressed sensing is applicable to imaging live neuronal tissues, allowing significantly shorter acquisition times while providing the image quality necessary for identifying the majority of neurons.

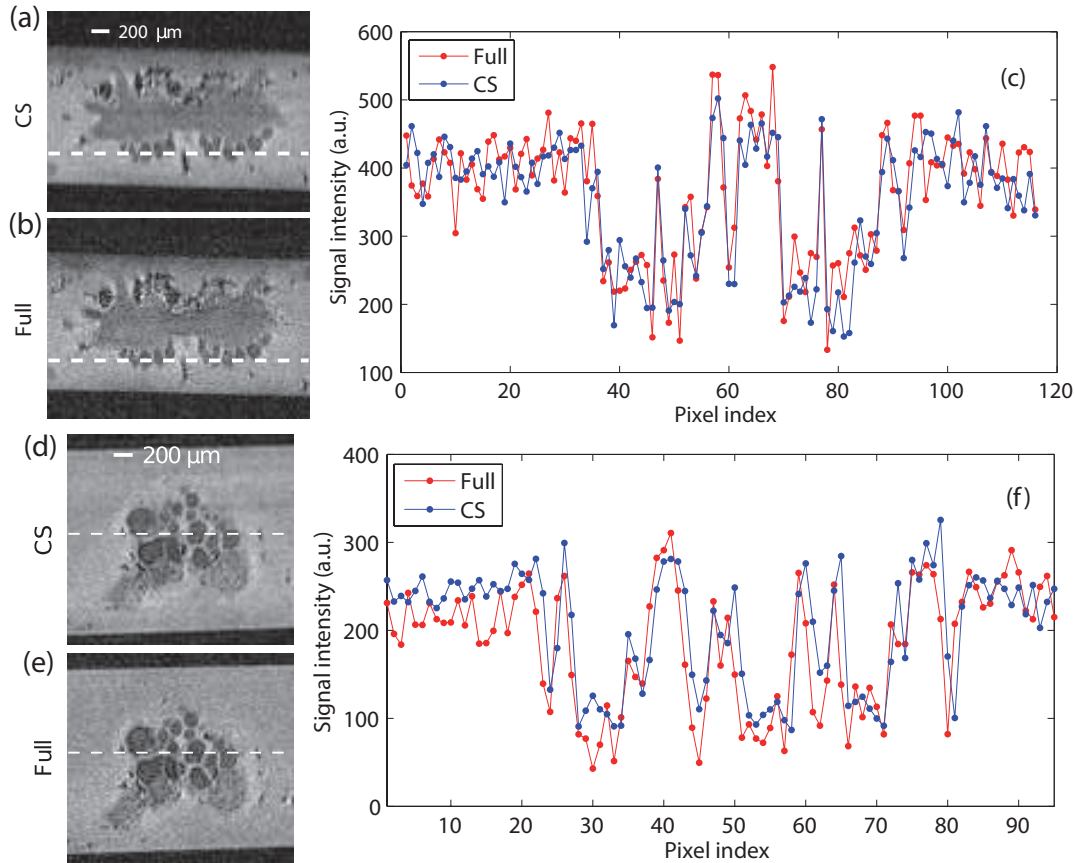


Figure 27 – Buccal (a , b) and abdominal (d, e) ganglia images acquired with a CS-RARE (a, d) and a standard RARE sequence (b, e), along with the signal intensity profiles (c,f) at locations indicated by the white lines across the images. The hypointense regions seen in the images correspond to cell bodies.

## 19 CS in T1-weighted imaging: CS-FLASH

The use of manganese ions ( $Mn^{2+}$ ) as an MRI contrast agent was introduced in studies of  $Mn^{2+}$  toxicity in anesthetized rats [139]. Manganese Enhanced Magnetic Resonance Imaging (MEMRI) works based on three main properties of  $Mn^{2+}$  (see more in [140]): (1) it is a paramagnetic ion that shortens the  $T_1$  (spin lattice relaxation time constant) of tissues, where it accumulates and hence functions as an  $T_1$  contrast agent; (2) it is a calcium ( $Ca^{2+}$ ) analog that can enter excitable cells, such as neurons and cardiac cells via voltage-gated  $Ca^{2+}$  channels; and (3) once in the cells  $Mn^{2+}$  can be transported along axons by microtubule-dependent axonal transport and can also cross synapses trans-synaptically to neighboring neurons. Because of chronic exposure to manganese can lead to a toxic condition referred to as “manganism”,  $Mn^{2+}$  is not used as an MR contrast agent in humans.

High resolution MEMRI has great potential for functional imaging of live neuronal tissue at single neuron scale. However, reaching high resolutions often requires long acquisition times which can lead to reduced image quality due to sample deterioration and hardware instability. CS techniques offer the opportunity to significantly reduce the imaging time.

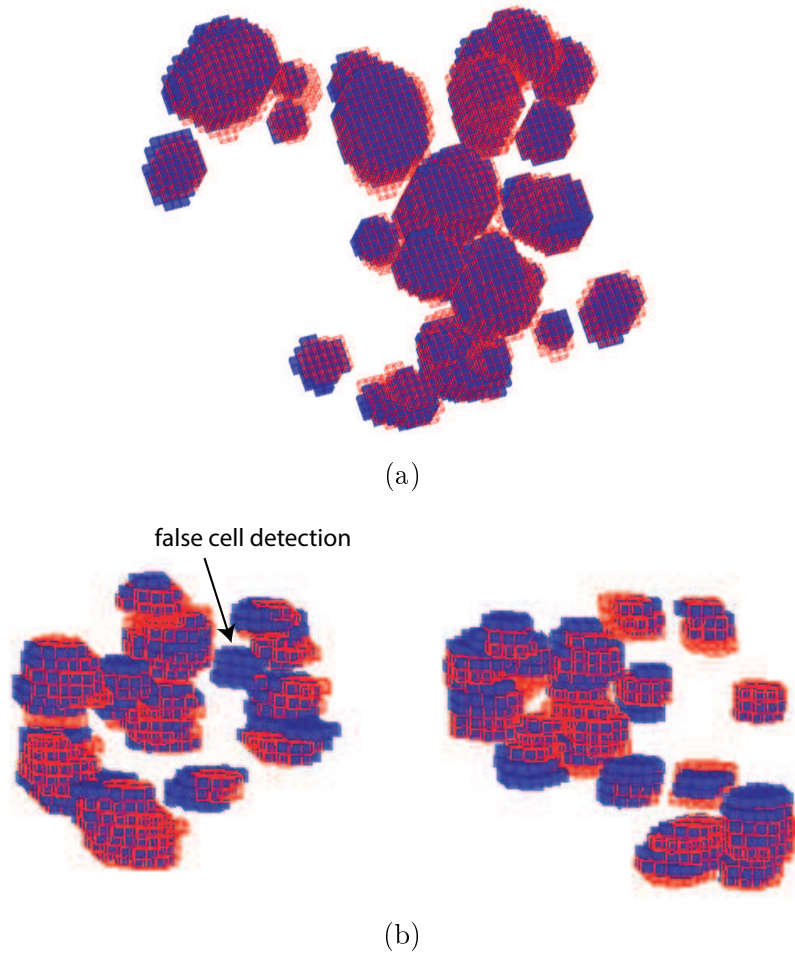


Figure 28 – Comparison between the cells detected on the fully encoded (red wire-frame) and CS (solid blue) images of abdominal (a) and buccal ganglia (b). An identical number of cells was detected on the abdominal ganglion with both acquisitions, while on the buccal ganglia one false positive was detected on the CS data set.

Recent advances in the static magnetic field strength of magnetic resonance scanners and in the radio-frequency (RF) detector designs has allowed magnetic resonance microscopy (MRM) to reach spatial resolutions suitable for functional imaging of single cells [136, 137, 141]. However, in order to reach the full potential of functional MRM it is necessary to reduce the currently long acquisition times required for obtaining high resolution images. The CS method has been previously utilized for the acceleration of T1 weighted acquisitions for knee cartilage quantification [142] as well as for MEMRI [143]. In case of the MEMRI study, CS with random k-space undersampling patterns was employed for fast cardiac T1 mapping in mice [143], demonstrating the feasibility and performance of this approach. Both studies used random undersampling schemes in the high frequency domain while fully sampling the low frequency domain, which has been shown to reach a similar performance to that of the polynomial undersampling algorithms [143]. In this section we present the implementation of DLA-CS for T1 weighted acquisitions in order to perform high-resolution quantitative functional MEMRI and we evaluate its performance.

## 19.1 Undersampling pattern generation

The undersampling pattern generation followed the description in section 14.1. Briefly, the two phase encoding directions in a Cartesian 3D trajectory were undersampled using an acquisition pattern based on the diffusion limited aggregation random growth model [133] with the k-space points in the resulting patterns always being restricted to be a subset of the fully sampled Cartesian k-space points. In this study, following the same procedure, acquisition patterns were generated for seven undersampling ratios ranging from 30% to 90% for a T1 weighted FLASH (Fast Low Angle Shot) acquisition. For each undersampling ratio, 300 sets of undersampling patterns, each consisting of 100 candidates, were created. From each set, the one pattern (out of 100) with the lowest Point Spread Function was selected. Hence, 300 patterns were produced for each undersampling ratio, making a total of  $300 \times 7 = 2100$  patterns. The 2100 patterns were applied to a library of six fully sampled T1 weighted images of *Aplysia californica* buccal ganglia. In order to compare the CS and fully sampled images, the RMSE between the voxels signal intensities of fully encoded image and the undersampled image were calculated. In order to compare the CS and fully sampled images, the RMSE were calculated (see equation (98)). For each undersampling ratio, the averaged RMSE over the six images in the library was computed. The DLA undersampling pattern with the lowest average RMSE was selected for each of the seven undersampling ratios (Table 2) and implemented in Paravision 5.1 starting from the standard FLASH pulse sequence.

Dataset	Undersampling ratios						
	30.0%	40.0%	50.0%	60.0%	70.0%	80.0%	90.0%
1	0.053	0.067	0.067	0.085	0.091	0.108	0.122
2	0.061	0.07	0.068	0.084	0.092	0.1	0.118
3	0.054	0.063	0.074	0.082	0.086	0.099	0.108
4	0.051	0.061	0.08	0.081	0.089	0.098	0.111
5	0.045	0.057	0.066	0.069	0.076	0.089	0.103
6	0.046	0.055	0.069	0.071	0.077	0.087	0.098

Table 2 – The RMSE of each winning DLA pattern for the library data.

Examples of k-space undersampling patterns are shown in Figure 29. The k-space was undersampled along the two phase encoding directions and the pattern was repeated for every point in read direction.

## 19.2 Data acquisition

All MRI acquisitions were performed at 19°C on the 17.2 T system using RF transceiver with an ID (inner diameter) of 2.4 mm. The RF transceiver was home-built solenoidal single-microcoil with an inner diameters of 2.4 mm. Two types of acquisitions were performed for each sample: a RARE acquisition, providing T2 contrast (TR = 3000 ms, TE = 20 ms, AF = 4, 25  $\mu\text{m}$  isotropic resolution) and a FLASH acquisition providing T1 contrast (TR = 150 ms, TE = 2.441 ms, 3 averages, 2 repetitions, 25  $\mu\text{m}$  isotropic resolution) in fully encoded and CS variants. The FOV was either  $10 \times 2.2 \times 2.2 \text{ mm}^3$  or  $10 \times 2.0 \times 2.0 \text{ mm}^3$  corresponding to matrix sizes of  $400 \times 88 \times 88$  and  $400 \times 80 \times 80$  and fully encoded FLASH acquisition times, per repetition, of 58 and 48 minutes, respectively.

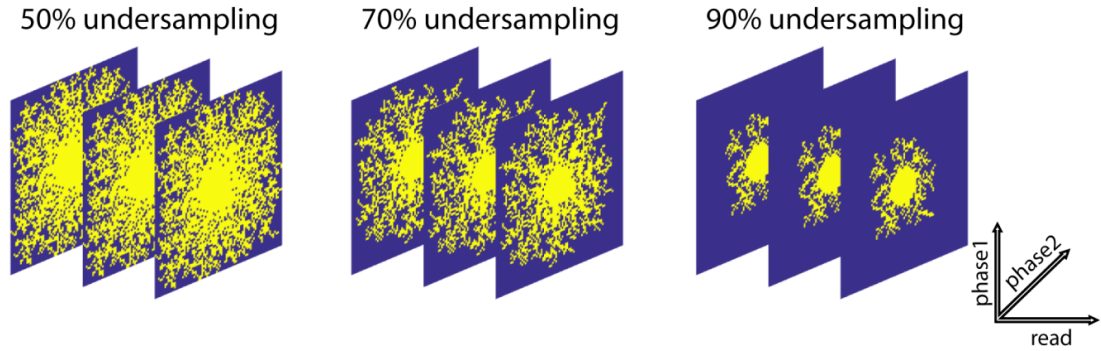


Figure 29 – DLA acquisition patterns for 50%, 70% and 90% undersampling ratios. The horizontal axis represents the read direction, and the other two axes represent the phase encoding directions, as shown in the lower right corner.

Since the FOV size was not found to influence the DLA performance, the two groups were pooled together.

### 19.3 Sample preparation

A total of fourteen *Aplysia californica* were used in this study. Images acquired on ganglia from six animals were used for generating the library necessary to optimize the DLA based CS trajectories. Six other animals were used for acquiring fully sampled data sets. Besides providing reference images, these data sets were retrospectively undersampled in order to determine the optimal undersampling ratio. Finally, two animals were used to acquire both fully encoded and CS images. These data were also retrospectively undersampled. For all experiments the animals were food deprived for 48h prior to the beginning of the experiment in order to increase their food seeking behavior and maximize the intracellular  $Mn^{2+}$  accumulation as described previously [137]. On the day of the experiment, the animals were injected with 100 mM  $MnCl_2$  solution ( $500\mu l$  per 100g body weight; NaCl 345 mM, KCl 10mM,  $MgCl_2$  25mM,  $MnCl_2$  100mM, pH = 7.5) and were left in the aquarium for 45 minutes with unrestricted access to food (seaweed). The animals were then anesthetized with isotonic  $MgCl_2$  solution. Buccal ganglia were resected and inserted in 1.5 mm ID borosilicate glass capillaries containing ASW and then slid inside the transceiver for MRI. The *Aplysia* buccal ganglia contain large neurons, some of which are up to 200  $\mu m$  in diameter [67, 66] and can therefore be resolved with the spatial resolution employed here.

### 19.4 Image analysis

In order to evaluate the extent of resolution loss between the fully encoded and undersampled images, we computed the Pearson's Correlation Coefficient (PCC, see equation 100) [132] between the mean signal intensity values over all voxels of the fully encoded and CS encoded. The PCC was calculated in manually drawn ROIs containing the ganglia and encompassing approximately 50 000 voxels.

The performance of the DLA-CS strategy was further evaluated by comparing signal intensities measured in individual neurons and in water in both fully encoded and un-

undersampled images. Five biggest neurons in the Aplysia’s buccal ganglia (B1, B2, B3, B6 and B9) were identified and manually segmented on RARE (T2 weighted) images (Figure 30 a). (Note that as the buccal ganglia are bilaterally symmetric, one sample contains two neurons of each type). The corresponding ROIs were co-registered to the FLASH (T1 weighted) images and the mean signal intensity for each of them was calculated (Figure 30 b).

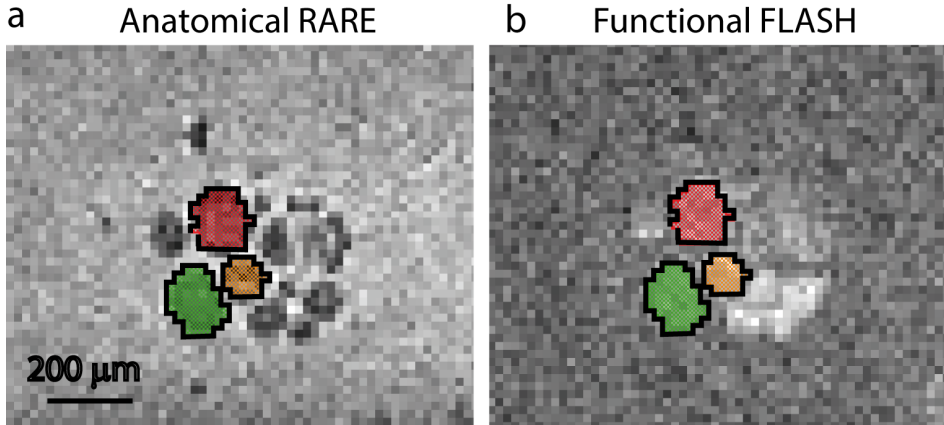


Figure 30 – Schematic representation of the ROI selection for signal intensity quantification. Two acquisitions were performed for each sample: a T2 weighted RARE (a), providing information about the sample anatomy and a T1 weighted FLASH (b) reflecting the intracellularly accumulated  $Mn^{2+}$  ions. Neurons were manually segmented on the RARE image and the corresponding ROIs were co-registered with the FLASH image. The drawn ROIs correspond to neurons B9 (red), B6 (orange) and B3 (green). Spatial resolution:  $25 \mu m$  isotropic.

The signal intensity quantification was performed by normalization against the water signal. To correct for possible RF inhomogeneities, the images were normalized in a position-dependent manner: the signal intensity of each voxel in the transverse plane (perpendicular to the longitudinal axis of the receiver coil) was normalized against the mean signal intensity of all voxels corresponding to ASW in this plane [137].

## 19.5 Results

Examples of fully encoded and retrospectively DLA-CS undersampled T1 weighted images of the buccal ganglia are shown in Figure 31. In a first step we estimated the performance of the DLA-CS approach for seven different undersampling ratios both in terms of image resolution (characterized by PCC expressing relative resolution loss between the two image sets) and relative signal intensity error (Figure 32). As can be seen in Figure 32a, the PCC between the CS and fully encoded images for undersampling ratios higher than 50% drops to values below 0.8, generally considered as the threshold for a strong correlation [144]. We observe an increase in PCC when averaging the signal over two repetitions. The relative signal intensity error was calculated according to:

$$SI_{diff} = 100 \times \frac{S_{mean} - S'_{mean}}{S_{mean}}, \quad (102)$$

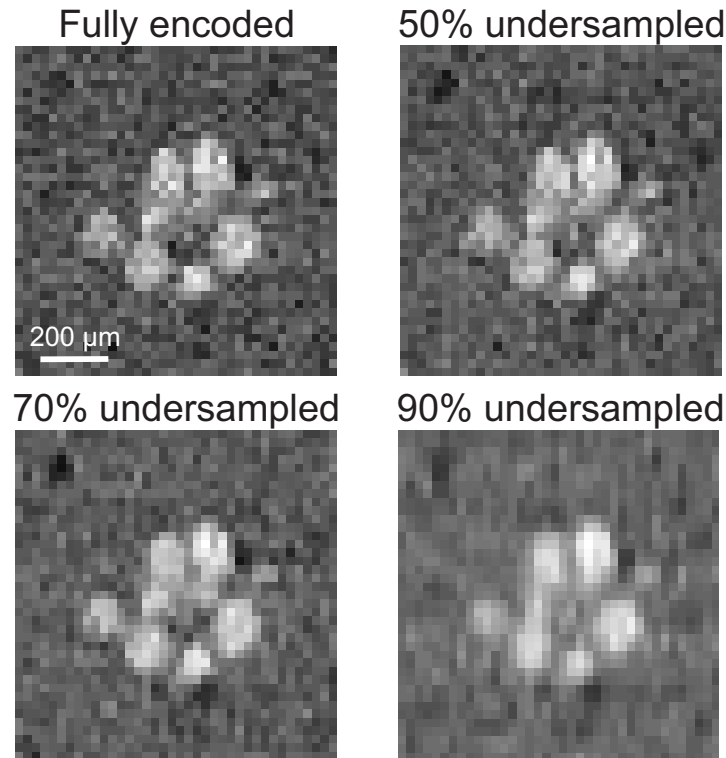


Figure 31 – Fully encoded FLASH image (top left) and corresponding undersampled images after CS reconstruction (50%, 70% and 90% undersampling ratios). The CS images shown here were obtained by retrospectively undersampling the fully encoded k-space data.

where  $S_{mean}$  and  $S'_{mean}$  are average signal intensities, for a given ROI, in the non-normalized fully encoded images and CS images retrospectively undersampled from the same raw data set, respectively. Measurements were performed in water (water ROI) and neuron bodies (cells ROI). For the latter the signal intensities were measured in the five biggest cells (B1, B2, B3, B6 and B9) and averaged. The relative error between the average signal intensities of fully encoded and CS images, for all the undersampling ratios considered, are displayed in Figure 32b. We notice that this error is inferior to 6% for all undersampling ratios considered. However, for undersampling ratios larger than 60% the error corresponding to the cells ROI and the water ROIs diverge, which could introduce a bias in the signal intensity quantification. The different behavior of the signal intensity error in water versus cell bodies at large undersampling ratios is most likely due to the loss in spatial resolution (increased blurring) as indicated by the PCC results. Surprisingly, the signal intensity error did not show SNR dependence (no difference between one and two repetitions). However, not only does the standard deviation of the error for the cell ROIs increase with the undersampling ratio (Figure 32b) but we also found it to be significantly higher for one repetition when compared to two repetitions (see Table 3). Specifically, a student t-test showed a statistical significance ( $p = 0.0005$ ) while for the water ROI no difference was found ( $p = 0.26$ ).

Based on the results presented above we chose an undersampling of 50% (determined by signal intensity error divergence and above-threshold PCC value) for our next experiments which aimed at evaluating the performance of DLA-CS acquisitions for single neuron signal intensity quantification. The difference in the normalized signal intensity

Undersampling ratio (%)	Cells ROI				Water ROI			
	One repetition		Two repetitions		One repetition		Two repetitions	
	$SI_{\text{diff}}(\%)$	SD	$SI_{\text{diff}}(\%)$	SD	$SI_{\text{diff}}(\%)$	SD	$SI_{\text{diff}}(\%)$	SD
30	1.6	0.34	1.6	0.26	1.84	0.07	1.84	0.08
40	1.88	0.52	1.87	0.42	2.12	0.11	2.12	0.11
50	2.4	0.71	2.4	0.56	2.45	0.15	2.45	0.14
60	2.87	0.7	2.87	0.61	2.78	0.12	2.78	0.12
70	3.48	0.84	3.48	0.73	3.11	0.22	3.1	0.21
80	4.25	1.17	4.25	1.07	3.51	0.26	3.51	0.26
90	5.18	1.64	5.19	1.42	3.91	0.25	3.91	0.25

Table 3 – Signal intensity errors ( $SI_{\text{diff}}$ ) and corresponding standard deviations (SD) between fully encoded and compressed sensing acquisitions for one and two repetitions calculated in cells and water ROIs.

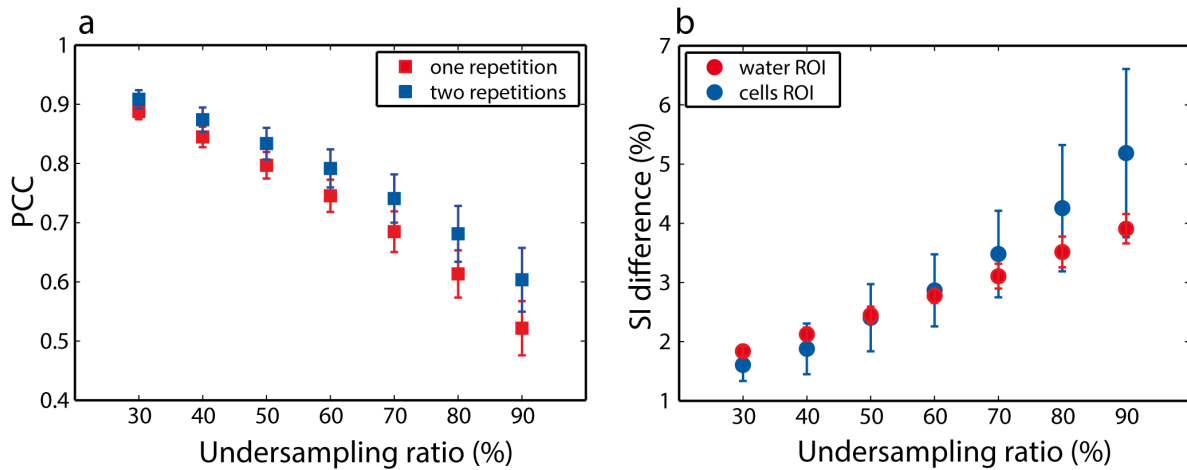


Figure 32 – Evaluation of the performance of DLA-CS for different undersampling ratios. (a). PCC between fully and CS encoded images as a function of undersampling ratio for one (red) and two (blue) repetitions. The PCC was calculated according to equation 100, over the ganglia region containing approximately 50 000 voxels. Error bars represent standard deviations. (b) Percentage signal intensity difference between the fully encoded and CS images (the data represented is the average over two repetitions). Blue and red marks correspond to cell bodies and water regions, respectively. Error bars represent standard deviations. The data was obtained from 6 samples.

between fully encoded and compressed images was calculated for 20 neurons in two different *Aplysia* buccal ganglia (10 neurons per ganglia) according to:  $S_{mean}^* - S_{mean}'$ , with  $S_{mean}^*$  and  $S_{mean}'$  being the average signal intensities calculated for a given ROI for fully encoded and CS images, respectively, after performing image normalization against water as described in section 19.4. The results for 50% prospectively and retrospectively undersampled datasets are shown in Figure 33. The average difference in the normalized signal intensity values was 1.37% and 0.50% for the prospectively and retrospectively undersampled data sets, respectively.

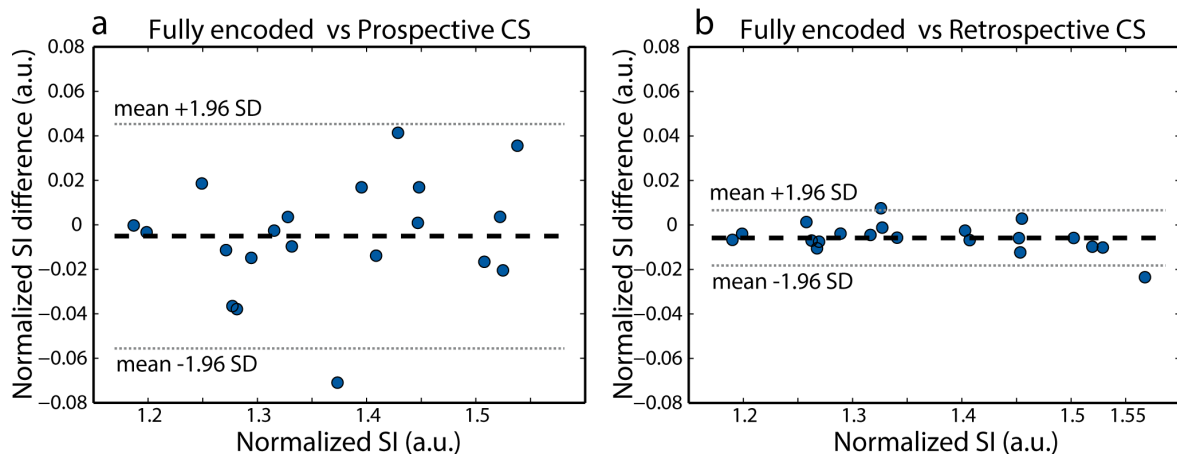


Figure 33 – Bland–Altman plots showing the difference in the normalized signal intensity values estimated from the fully sampled dataset and the 50% prospectively undersampled dataset (a) and the 50% retrospectively undersampled dataset (b). Each point corresponds to the signal intensity measured in one single neuron (2 samples, 10 neurons per sample).

## 20 Conclusion and discussion

We introduced a new way of generating CS undersampling trajectories based on the DLA pattern and applied it to the undersampling of RARE and FLASH encoding acquisition schemes. Our results demonstrate that the DLA pattern performs better than the standard polynomial pattern for undersampling superior to 25%. In addition, we show that when applied to imaging live neuronal tissue the proposed CS acquisitions maintain the spatial resolution and contrast to noise ratio necessary to the identification of the majority of neurons within *Aplysia* ganglia while reducing the acquisition time to 50%. For the RARE we applied the DLA undersampling for an acceleration factor 4, however, the implementation to acquisitions with different acceleration factors, or without acceleration for species with short  $T_2$  relaxation times, is straightforward. Moreover, this undersampling is not limited to RARE acquisitions and can be easily extended to other types of sequences.

The performance of the DLA-CS FLASH acquisitions was also evaluated at various undersampling ratios. We found an undersampling ratio of 50% acceptable both in terms of image resolution and signal intensity quantification. Regarding single neuron signal intensity quantification we found, on average, a 1.37% percentage error between

the fully sampled and prospectively undersampled data. This error was observed to be higher than the error measured using retrospective undersampling of the fully encoded data, which was found to be 0.50%. The difference between the two undersampling scenarios can be due to experimental errors such as hardware instability, subtle changes in the sample position in the  $B_0$  field (resulting from vibrations associated with the strong encoding gradients), or slight sample modification.

It should be also noted that one of the reasons the retrospective CS outperforms prospective CS is that the retrospective datasets share the noise realization with the full encoded dataset. When evaluating the Pearson Correlation Coefficient between the fully encoded and the undersampled images we notice that the performance of the DLA-CS technique is influenced by the image signal to noise ratio, in agreement with earlier studies [145], suggesting that higher accelerations are possible for higher SNR data. The spatial resolution employed in this study was  $25 \mu\text{m}$  isotropic. The impact of using DLA-CS approach at different spatial resolutions will likely show strong SNR dependence: decreasing the resolution will result in higher SNR, therefore allowing for greater accelerations and vice versa[143].

In conclusion, the results presented here suggest that DLA pattern is a promising alternative to the standard polynomial CS undersampling pattern and may be beneficial to magnetic resonance microscopy studies by reducing the notoriously long acquisitions to more reasonable times, thus enabling the expansion of the technique to the study of living specimens and eventually to dynamic investigations. Even though the acquisitions times remain long when compared to fast techniques, such as EPI or spiral imaging, the DLA-CS appears to be a promising approach at high magnetic fields and high spatial resolutions, where single shot acquisitions are not feasible. Moreover, the DLA-CS is not limited to magnetic resonance microscopy and could be also applied to preclinical and clinical studies, where shortening the acquisition time is equally desirable.

---

## Part V

# Diffusion magnetic resonance imaging in the *Aplysia*

## Summary

---

<b>21 Introduction</b>	<b>88</b>
<b>22 Materials and methods</b>	<b>89</b>
22.1 Sample preparation . . . . .	89
22.2 Image acquisition . . . . .	89
22.3 Image analysis . . . . .	90
22.4 Simulations . . . . .	92
22.4.1 Large cell neurons . . . . .	94
22.4.2 Bag cell neurons . . . . .	95
22.4.3 Nerve: group of axons . . . . .	96
<b>23 Results</b>	<b>97</b>
23.1 Experimental time-dependent ADC . . . . .	97
23.2 Estimating cell size using short time ADC formula . . . . .	100
23.3 Simulation of a two compartments model of large cell neurons . . . . .	103
23.4 Simulations of the ADC in bag cell neurons and nerves . . . . .	104
<b>24 Conclusion</b>	<b>107</b>

---

The nerve cells of the *Aplysia* are much larger than mammalian neurons. Using the *Aplysia* ganglia to study the relationship between the cellular structure and the diffusion MRI signal can potentially shed light on this relationship for more complex organisms. We measured the dMRI signal of chemically-fixed abdominal ganglia of the *Aplysia* at several diffusion times. At the diffusion times measured, the dMRI signal is mono-exponential and can be accurately represented by the parameter ADC.

We analyzed the diffusion time-dependent ADC using a well-known analytical formula that is valid in the short diffusion time regime. We performed this analysis for the largest sized cells of the ganglia to satisfy the short diffusion time requirement. We noted that a naive application of the short time formula is not adequate because of the presence of the cell nucleus, making the effective cell size much smaller than the actual cell size.

We went on to perform numerical simulation of the ADC for several cell types of the abdominal ganglia. To create the simulation geometries, for the largest cells, we segmented a high resolution T2-weighted images and incorporated a manually generated nucleus. For small cells and nerve cells, we created spherical and cylindrical geometrical domains that are consistent with known information about the cellular structures from the literature. Using the library of simulation results, we fitted for the intrinsic diffusivities of the small cells and the nerve cells.

The results presented here are used for the preparation of a manuscript which we plan to submit.

## 21 Introduction

To adequately study diffusion time dependence of the dMRI signal and discover if the additional information the measurements at multiple diffusion times provides can give worthwhile information about the tissue microstructure, we image the *Aplysia* abdominal ganglia at high resolution and multiple diffusion times. Given that this requires very long experimental times, we decided not to image living *Aplysia* neurons, which deteriorates rather quickly. Instead, we used chemically-fixed nervous tissues which are well suited for high resolution, time-intensive MRI acquisitions. However, one should keep in mind that the aldehyde fixatives used may significantly alter tissue MRI properties. Shepherd and colleagues reported in [146] that the rat cortical slices fixed by immersion in 4% formaldehyde solution demonstrated 21% and 81% reductions in tissue  $T_1$  and  $T_2$ , respectively. By washing fixed tissues with phosphate-buffered saline (PBS) to remove free formaldehyde solution  $T_2$  can be recovered. In addition, the membrane permeability was increased after fixation with 4% formaldehyde [146]. In this study, we followed the protocol in reference [59] and we fixed abdominal ganglia in 4% formaldehyde.

In dMRI, the incoherent motion of water molecules during the diffusion encoding time causes a signal attenuation from which the ADC can be calculated [21, 28, 32]. For unrestricted diffusion, the mean squared displacements of molecules is given by  $\bar{x} = \sqrt{2dD_0t}$  [147, 148] where  $d = 1, 2, 3$  for one, two and three dimension,  $D_0$  is the intrinsic diffusion coefficient, and  $t$  is the diffusion time.

In biological tissue, the diffusion is usually hindered or restricted (e.g. by cell mem-

branes) and the mean squared displacement is smaller than in the case of unrestricted diffusion. Intuitively, more hinderance or restriction will occur for more molecules as the diffusion time increases, so we expect the experimentally determined ADC will decrease with increasing diffusion time [28, 149, 150]. As a result, the extent of the ADC decrease potentially can be used to gather information about the tissue micro-structure, for example, by acquiring several diffusion weighted images with different diffusion times and fitting the data to a model [40, 151]. Numerous biophysical models have been proposed, usually subdividing the tissue into compartments described by spheres, ellipsoids, cylinders, and the extra-cellular space [34, 35, 36, 37, 38, 39]. However, it is difficult to connect the geometrical parameters contained in these models to the ground truth values due to the complexity of brain tissue.

In this work, we use much larger neural cells of the *Aplysia californica* as the animal model. The advantages of this animal model is that the cellular structure is relatively simple, some of the largest cells even can be visualized in the T2w images we acquire along with the diffusion images. This animal model exhibits simpler and more direct links between the geometrical structure, intrinsic diffusivity in the cell components, and the ADC, making this a good model problem and eases a lot of the experimental and modeling challenges. For example, the large size of the biggest *Aplysia* neural cells can be used to test short time diffusion models while keeping the PGSE [28] sequence, instead of resorting to more specialized sequences such as Oscillating-Gradient Spin Echo (OGSE) [53] sequences.

## 22 Materials and methods

### 22.1 Sample preparation

Six *Aplysia californica* (National Resource for Aplysia, Miami, FL, USA) were used in this study. The animals were anesthetized by injection of an isotonic magnesium chloride solution ( $\text{MgCl}_2$ , 360 mM; HEPES, 10 mM; pH = 7.5). All chemicals were purchased from Sigma-Aldrich (Saint Luis, MO, USA). The abdominal ganglion was resected and fixed by PFA 4% by immersion for 10 minutes and then washed three times in PBS pH = 7.4. For imaging, the abdominal ganglion was inserted into a 2.0 mm ID glass capillary filled with fluorinert and then slid inside the transceiver.

### 22.2 Image acquisition

All experiments were performed at 19°C on a 17.2 T system (Bruker BioSpin, Ettlingen, Germany) equipped with 1.0 T/m gradients. RF transceivers were home-built micro-coils with inner diameters of 2.4 mm, the design of which has been described in [136, 137]. Typically, a T2 weighted image and five to seven diffusion weighted images were acquired for each sample. The T2 weighted image was acquired with the following parameters TR = 1500 ms, TE = 20 ms, acceleration factor  $A_F = 8$ , isotropic spatial resolution 26  $\mu\text{m}$ , matrix size of  $400 \times 88 \times 88$ , 8 averages for the a acquisition time of 3 hours 14 minutes. The acquisition parameters for the diffusion-weighted images (DP-FISP pulse sequence [69]) were TE/TR=1.63/1000 ms, 2 averages, isotropic spatial resolution 52 $\mu\text{m}$ ,

3 directions ( $x, y, z$ ), four samples acquired with seven diffusion encoding times ( $\delta = 2.5$  ms,  $\Delta = [5, 7.5, 10, 12, 15, 20, 25]$  ms), one sample acquired with six diffusion encoding times ( $\delta = 2.5$  ms,  $\Delta = [5, 10, 12, 15, 20, 25]$  ms) and one sample acquired with five diffusion encoding times ( $\delta = 2.5$  ms,  $\Delta = [5, 10, 15, 20, 25]$  ms). All diffusion weighted images were acquired with 8 b-values ( $[70, 100, 200, \dots, 700]$  s/mm<sup>2</sup>), and matrix size  $200 \times 44 \times 44$ . The diffusion acquisition time was 2 hours 05 minutes for one diffusion time, 3 directions, 8 b-values. All acquisition were acquired with a FOV of  $10.4 \times 2.3 \times 2.3$  mm<sup>3</sup>.

## 22.3 Image analysis

The T2w images were manually co-registered with the diffusion-weighted images. We are interested in studying three types of cells in the abdominal ganglia: 1) large cell neurons; 2) bag cell neurons; 3) nerves. For each of the six imaged ganglia, several three dimensional ROIs of these three types of cells were manually segmented slice by slice from the T2w image. We show in Figure 34 the T2w image and the physical locations of 5 ROIs from ganglion number 2. In total, we have selected for further analysis 22 ROIs of large cell neurons; 11 ROIs of bag cell neurons; 13 ROIs of nerves.

### 1) Large cell neurons:

For large cell neurons, the ROIs were manually segmented so that each ROI contains only the voxels associated with one large cell neuron. There are many large cell neurons in each abdominal ganglia, we usually, however, select the cells which are clearly visualized in T2w image based on the signal intensity, contrast, and the position within the ganglion (see diagram in Figure 12). In Table 4 we listed the information about the ROIs, including the number of voxels in each ROI. To define an effective size for each large cell neuron, we computed an effective radius  $R_{\text{eff}}$  in the following way. Assuming a spherical shape and knowing the total volume, we define

$$R_{\text{eff}} = \sqrt[3]{\Delta x \times \Delta y \times \Delta z \times \frac{3 \times (\#\text{voxels})}{4\pi}},$$

where  $\Delta x \times \Delta y \times \Delta z = 26\mu\text{m} \times 26\mu\text{m} \times 26\mu\text{m}$  is the resolution of T2w images.

### 2) Bag cell neurons:

For bag cell neurons, we made sure to draw the ROI within the bag cell region, but we did not try to cover all the bag cell neurons inside the ROI (Figure 34). There are two bag cell neurons in each abdominal ganglia (see diagram in Figure 12), one on the left side (Bag L) and one on the right side (Bag R). However, often not both are clearly visible in the T2w image and we only included which one visible in the T2w image in the ROI. There are 11 ROIs of the bag cell neurons (see Table 5) selected for analysis.

### 3) Nerve - A group of axons:

There are 13 ROIs of the nerve (see Table 6) selected for analysis. For each nerve, the ROI of the nerve was selected where the nerve is approximately straight. The nerve's ROI direction (parallel direction) shown in Table 6 was estimated by selecting two points inside the nerve's ROI and calculating the unit vector direction via these two points.

The dMRI signals corresponding to the ROIs were processed to compute the experimental ADC using a linear fit of the log of the signal versus the b-value. For the

ROI#	Aplysia#	#voxels	$R_{\text{eff}}$ ( $\mu\text{m}$ )
1	1	1070	164.97
2	1	539	131.26
3	2	370	115.79
4	2	576	134.20
5	2	314	109.63
6	2	833	151.76
7	2	477	126.02
8	3	424	121.17
9	3	519	129.62
10	3	248	101.34
11	3	800	149.73
12	4	480	126.29
13	4	810	150.35
14	4	985	160.48
15	4	985	160.48
16	5	352	113.88
17	5	366	115.37
18	5	528	130.36
19	5	2138	207.78
20	6	1024	162.57
21	6	900	155.72
22	6	664	140.71

Table 4 – The 22 ROIs of large cell neurons selected for analysis. The effective radius ( $R_{\text{eff}}$ ) estimated from the number of voxels ( $\#$ voxels) in each ROI.

ROI#	Aplysia#	Type	#voxels
1	1	Bag L	1619
2	1	Bag R	1785
3	2	Bag L	2371
4	2	Bag R	938
5	3	Bag L	2368
6	4	Bag L	1880
7	4	Bag R	680
8	5	Bag L	1744
9	5	Bag R	1659
10	6	Bag L	571
11	6	Bag R	771

Table 5 – The 11 ROIs of bag cell neurons selected for analysis.

ROI#	Aplysia#	#voxels	Parallel direction
1	1	884	(-0.997, 0.061, 0.045)
2	1	749	(-0.994, 0.047, -0.102)
3	2	865	( -0.915, -0.346, 0.210)
4	2	524	(-0.965, -0.253, 0.070)
5	2	1106	(-0.993, 0.092, -0.075)
6	2	864	(-0.983, -0.128, 0.128)
7	3	565	( -0.887, 0.105, -0.450)
8	3	742	(-0.681, -0.515, -0.521)
9	4	2696	(-0.964, -0.039, 0.265)
10	4	1896	(-0.744, -0.329, 0.581)
11	5	1864	(-0.873, 0.442, -0.207)
12	5	1958	(-0.625, 0.743, 0.239)
13	6	2296	(-0.998, 0.004, 0.059)

Table 6 – The selected 13 ROIs of the nerve with the approximate unit vector of the nerve direction (parallel direction) from visualization on the T2w image.

nerve, the diffusion is anisotropic due to the cylindrical shape of the axons. Because in this study only three diffusion directions were measured, it is not possible to compute the effective diffusion tensor for the nerve regions. Besides, the nerve ROI direction estimated above could be slightly off from the real direction due to errors in the visualization. Even for large cell neurons and bag cell neurons, there might be, although less pronounced, some anisotropy due to the shape of the cells as well as the shape and position of the nucleus. For these reasons we decided to average the ADC's in the three directions  $x$ ,  $y$ , and  $z$  to obtain the mean diffusivity, MD [152, 153, 154, 155]:

$$\text{MD} = \frac{\text{ADC}_x + \text{ADC}_y + \text{ADC}_z}{3}.$$

## 22.4 Simulations

In diffusion MRI, the complex transverse water proton magnetization  $M(\mathbf{x}, t)$  is a function of position  $\mathbf{x}$  and time  $t$ , and depends on the diffusion-encoding gradient magnetic field  $\mathbf{G}(t) = \mathbf{g}f(t)$ . The amplitude and direction information of the diffusion-encoding gradient is contained in the vector  $\mathbf{g} \in \mathbb{R}^3$ , the time profile of the effective gradient magnetic field is  $f(t)$ . For the PGSE sequence, the effective time profile is defined by:

$$f(t) = \begin{cases} 1 & 0 < t \leq \delta, \\ -1 & \Delta < t \leq \Delta + \delta, \\ 0 & \text{otherwise,} \end{cases}$$

where  $\delta$  is the duration of the pulses and  $\Delta$  the delay between the start of the pulses. The signal is measured at the echo time TE,  $2\delta \leq \text{TE} < 2\Delta$ . In this study, we use  $\delta = 2.5$  ms and  $\Delta = [5, 7.5, 10, 12, 15, 20, 25]$  ms.

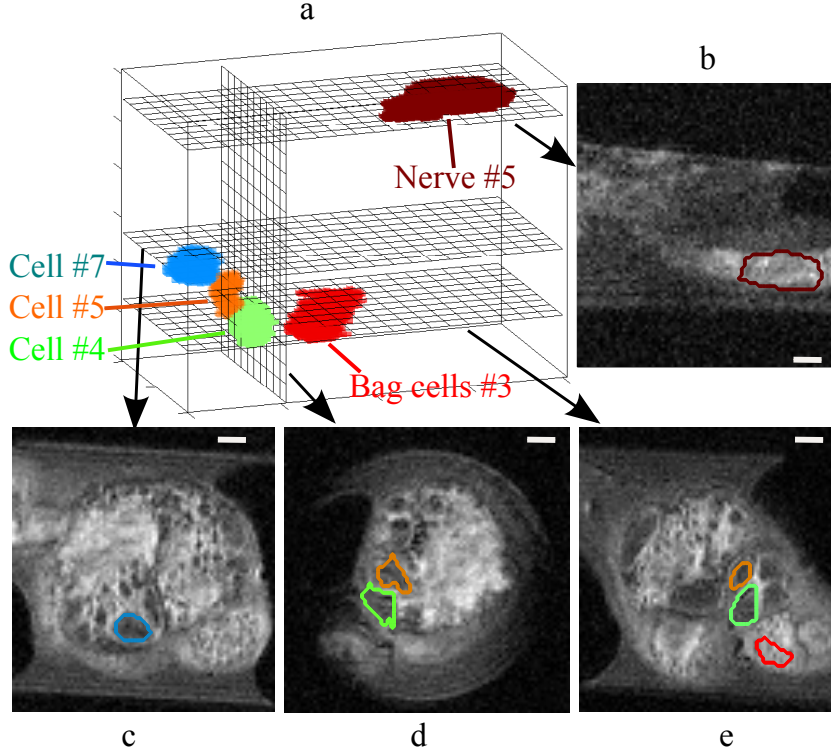


Figure 34 – Abdominal ganglion T2w image (*Aplysia* # 2) and ROIs: (a) the 3D representation showing the selected ROIs; (b)-(e) four slices from the T2w image; The information of the ROIs is shown in Tables 4, 5, and 6. The direction of the nerve (# 5) is  $(-0.993, 0.092, -0.075)$ . The scale bar represents  $260 \mu\text{m}$ .

The complex transverse magnetization is governed by Bloch-Torrey equation [31]

$$\frac{\partial}{\partial t} M(\mathbf{x}, t) = -i\gamma f(t) \mathbf{g} \cdot \mathbf{x} M(\mathbf{x}, t) + \nabla \cdot (D^l \nabla M(\mathbf{x}, t)), \quad \mathbf{x} \in \cup \Omega^l, \quad (103)$$

where  $i$  is the imaginary unit,  $D^l$  is the intrinsic diffusion coefficient in the geometrical compartment  $\Omega^l$ , and  $\gamma$  is the gyromagnetic ratio of the water proton. We solve the above equation subject to impermeable boundary conditions on  $\partial\Omega^l$ :

$$D^l \nabla M(\mathbf{x}, t) \cdot \nu = 0, \quad \mathbf{x} \in \partial\Omega^l, \quad (104)$$

where  $\nu$  is the outward normal vector. We impose the initial condition

$$M(\mathbf{x}, 0) = 1, \quad \mathbf{x} \in \Omega^l, \quad (105)$$

meaning uniform spin density in all  $\Omega^l$ . There are many numerical methods can be used to solving equations (103)-(105) such as spatial finite elements method coupled to the adaptive explicit Runge-Kutta-Chebyshev time-stepping method under the assumption of periodic for boundary domain condition [156]; a parametric finite element method for arbitrary domains [157], etc. In this thesis, we use the finite volume method coupled to the explicit Runge-Kutta-Chebyshev time-stepping method for solving equations (103)-(105). This method is adapted from [158].

The diffusion MRI signal is the integral of magnetization at TE:

$$S = \sum_l \int_{\mathbf{x} \in \Omega^l} M(\mathbf{x}, \text{TE}) d\mathbf{x}. \quad (106)$$

Under the assumption that there is no exchange (or *impermeable* boundaries) between the compartments, the total signal,  $S_{\text{total}}$ , can be determined by the summation of the signal weighted by the volume fraction of each compartment [39]:

$$S_{\text{total}} = \sum_l V_l S_l, \quad (107)$$

where  $V_l$  and  $S_l$  is the volume fraction and the signal of compartment  $\Omega^l$ , respectively. The  $b$ -value [32], in case of the PGSE sequence is

$$b(\mathbf{g}, \delta, \Delta) = \gamma^2 \|\mathbf{g}\|^2 \delta^2 (\Delta - \delta/3).$$

The apparent diffusion coefficient ( $ADC$ ) is

$$ADC = - \left. \frac{\partial}{\partial b} \log \frac{S(b)}{S(0)} \right|_{b=0}. \quad (108)$$

Note that, during this thesis, the relationship between the logarithm of dMRI signals and  $b$ -values (in the observed range of  $b$ -value from 0 to 700 s/mm<sup>2</sup>) is a linear relationship. So the equation (108) can be rewritten by select  $b_1 = 10$  s/mm<sup>2</sup>:

$$ADC = - \frac{\log S(b_1) - \log S(b=0)}{b_1}.$$

Moreover, in order to avoid the numerical truncated error, the  $b_1$  value should not be so small. Due to these reasons, the  $ADC$  obtained from the numerically simulated dMRI signal was computed by

$$ADC_{\text{simul}} = - \frac{\log S(b=10) - \log S(b=0)}{10}, \quad (109)$$

and compared to the  $ADC$  values found from the experimental data.

Following we will describe the simulations performed for the three geometry domains considered: large cell neurons, bag cell neurons, and nerve.

### 22.4.1 Large cell neurons

To create a computational domain to perform numerical simulations of Large cell neurons, we segmented the cell outline of only one particular large cell neuron. The cell outline geometry (denoted by  $\Omega_{\text{cell}}$ ) used for all later simulations of large cell neurons was segmented from the anatomical T2w image of large cell neuron ROI#7 (*Aplysia* number 2) (see Table 4, Figure 35a). We note  $\Omega_{\text{cell}}$  is a slightly elongated ellipsoid. Inside  $\Omega_{\text{cell}}$ , an irregularly shaped nucleus,  $\Omega_n$ , was manually generated (approximately 25-30% volume fraction) (Figure 35b). The shape of the nucleus was inspired by the high resolution images in [59]. Even though not visible in the T2w images, there may be a small volume (up to 5%) of satellite cells (very small cells, 6 $\mu$ m maximum diameter, without nucleus [55, 56, 59]) surrounding the single cell neurons (Figure 35f). Since the volume of the satellite cells are small and to simplify the study, we did not include the satellite cells in the simulations.

The generated geometries  $\Omega_{\text{cell}}$  and  $\Omega_{\text{cell}}$  are considered our reference geometries. To consider the effect of the size of the cells on the  $ADC$ , we simply scaled the reference

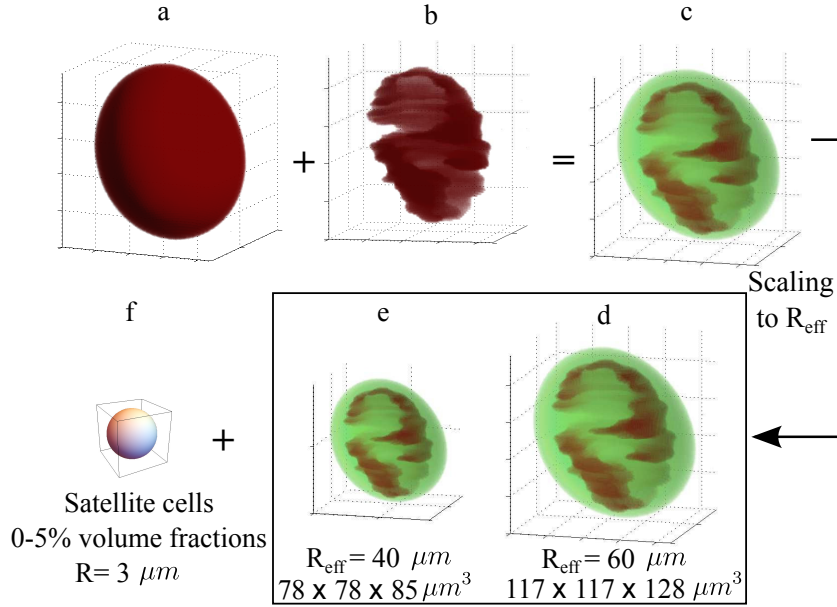


Figure 35 – Large single cell neuron geometry. The cell outline was estimated from cell ROI#7 (see Table 4) (a). A nucleus with irregular shape was manually generated (b). The nucleus was manually placed inside the cell outline (c): cell nucleus is displayed in red while cytoplasm is displayed in green. Different cell sizes were generated by scaling the size of the nucleus to  $R_{\text{eff}}$  for the simulations (e.g  $R_{\text{eff}} = 60 \mu\text{m}$  (d) and  $R_{\text{eff}} = 40 \mu\text{m}$  (e) ). The satellite cell ( $R=3 \mu\text{m}$ ) (no nucleus) (f) with volume fraction of 0-5% surrounding the cell neurons (not accounted for in the simulations).

geometries so that  $\Omega_{\text{cell}}$  has the desired total volume. In particular, the shape in Figure 35c was scaled so that the effective cell diameter ranging from  $160 \mu\text{m}$  to  $420 \mu\text{m}$  (e.g Figure 35d-e) for the numerical simulations that follow.

The simulated dMRI signal for large cell neurons can be generated by solving the Bloch-Torrey equations in  $\Omega_{\text{cell}}$  with two compartments: the nucleus  $\Omega_n$  and the cytoplasm  $\Omega_c = \Omega_{\text{cell}} - \Omega_n$ . The intrinsic diffusivities in the cytoplasm and nucleus,  $D_c$  and  $D_n$ , respectively, were chosen from a range described in the literature [59]. The total signal in a large cell neuron is:

$$S_{\text{cell}} = (1 - v_n)S_c + v_n S_n, \quad (110)$$

where  $v_n$  is the volume fraction of the nucleus,  $S_c$  and  $S_n$  are the signals in the cytoplasm and the nucleus, respectively.

### 22.4.2 Bag cell neurons

In order to match the dMRI signal of the bag cell neurons, the small cells were modeled as small spheres,  $\Omega_{\text{cell\_small}}$ , with a smaller concentric spherical nucleus,  $\Omega_{n\_small}$ , (approximately 25% volume fraction). The cytoplasm compartment is  $\Omega_{c\_small} = \Omega_{\text{cell\_small}} - \Omega_{n\_small}$ . As all *Aplysia* used in this study are approximately the same age (late juvenile period), therefore we modeled the small cells as spheres with diameters that varied between 20 and  $60 \mu\text{m}$ , following a normal distribution with mean =  $46 \mu\text{m}$  and  $\text{std} = 6$  (see Figure 36) (equivalent with cell radius varied between 10 and

30  $\mu\text{m}$ , following a normal distribution with mean = 23  $\mu\text{m}$  and std = 3). The mean and std here were chosen so that 99% of cell diameter is between 20 and 60  $\mu\text{m}$ . For

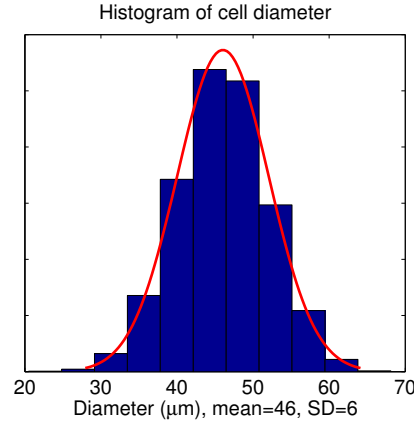


Figure 36 – The bag cell neurons diameter histogram.

simplicity of the simulations, we did not account for the extra-cellular space between the small cells in bag cell neurons ROI. Thus, the simulated dMRI signal in bag cell ROI,  $S_{bag}$ , is generated by solving the Bloch-Torrey equation in small cells of various diameters  $d_i$  to obtain the signal due to that cell,  $S_{cell}(d_i)$ , and combining the resulting signals together weighted by normal distribution as described above:

$$S_{bag} = \sum_i v(d_i) S_{cell}(d_i),$$

where  $v(d_i)$  is the fraction of cells with diameter  $d_i$  determined by the normal distribution with mean = 23 and std = 3, where  $d_i$  from 20 to 60  $\mu\text{m}$ . Note that the signal in each small cell  $S_{cell}(d_i)$  is the total signal of the cytoplasm and the nucleus compartments weighted by volume fraction of the nucleus as described in equation (110). The intrinsic diffusivities in the cytoplasm and nucleus,  $D_c$  and  $D_n$ , respectively, were chosen from a range described in the literature [59], and are the same for all cell diameter  $d_i$ .

### 22.4.3 Nerve: group of axons

We model the nerve by combining axons (cylindrical shapes) of different diameters, and again, for simplicity, without the extra-cellular space. The groups of axons range from small (modeled by cylindrical shapes as small as 1  $\mu\text{m}$  in diameter) to large (modeled by cylindrical shapes as large as 25  $\mu\text{m}$  in diameter), consistent with the literature [56]. In Table 7 shown the volume fraction of each axon type in different buccal nerves mentioned previously in Table 1 with particular choices of diameters in the range mentioned in Section 8:  $2R_I = 26 \mu\text{m}$ ,  $2R_{II} = 18 \mu\text{m}$ ,  $2R_{III} = 6 \mu\text{m}$ , and  $2R_{IV} = 1 \mu\text{m}$  for axon type I, II, III, and IV, respectively. For each nerve, the volume fraction of each axon type  $V(R_i)$ ,  $i=I, II, III, IV$ , can be calculated according to:

$$V(R_i) = \frac{N(i) \times \pi \times R^2(i)}{\sum_i N(i) \times \pi \times R^2(i)}, \quad (111)$$

where  $N(i)$  is the number of axons of type  $i=I, II, III, IV$ , and  $R(i)$  is the choice of radius in the range mentioned in the section 8.

Nerve	I ( $2R = 26\mu\text{m}$ )	II ( $2R = 18\mu\text{m}$ )	III ( $2R = 6\mu\text{m}$ )	IV ( $2R = 1\mu\text{m}$ )
1b	0.0000	0.0892	0.5174	0.3934
2b	0.0612	0.2443	0.3287	0.3658
3b	0.0000	0.5136	0.2549	0.2315
ON	0.0290	0.0721	0.6296	0.2692
RN	0.0000	0.0801	0.8783	0.0416
CBC	0.0974	0.2800	0.5081	0.1146

Table 7 – The distribution of volume fraction for each axon type in different buccal nerves (note that we assumed the same distribution for the abdominal ganglion) estimated from the literature [56] with particular choice of diameter in range mentioned before:  $2R_I = 26 \mu\text{m}$ ,  $2R_{II} = 18 \mu\text{m}$ ,  $2R_{III} = 6 \mu\text{m}$ , and  $2R_{IV} = 1 \mu\text{m}$  for axon type I, II, III, and IV, respectively. See more in Table 1 regarding the distribution of number of axons of each type within each nerve.

The numerical simulations were performed in one direction perpendicular to the nerve. The simulations were performed in 2D, there is no need to simulate two orthogonal directions perpendicular to the nerve due to the circular shape of the axons. We solved the Bloch-Torrey equation in single disks with the diameter determined by four type of axons (I, II, III, IV). The simulated dMRI signal in the perpendicular direction to the nerve,  $S_{perp}$ , is determined after weighing by the diameter distribution:

$$S_{perp} = \sum_i V(R_i) S_{2D}(R_i),$$

where  $i = \text{I, II, III, IV}$  four types of axons,  $S_{2D}(R_i)$  is the signal in perpendicular direction of the axons with diameter  $2R_i$  (disk radius  $R_i$ ).

The ADC in the perpendicular direction to the nerve (the transverse ADC),  $ADC_T$ , is linearly fitted from  $\log S_{perp}(b)$  and the  $b$ -value. Knowing that the ADC in the direction parallel to the nerve is close to unrestricted we make the approximation that the parallel ADC is equal to the intrinsic diffusivity inside the axons  $Da$ . Hence the simulated mean diffusivity is obtained using the following formula:

$$\overline{\text{MD}} = \frac{Da + 2 \times ADC_T}{3}, \quad (112)$$

## 23 Results

### 23.1 Experimental time-dependent ADC

The experimental dMRI signals acquired for multiple diffusion times on the large cell neurons ROIs, the bag cell neurons ROI and on the nerve ROIs are shown in Figure 37, Figure 38 and Figure 39, respectively. Within the range of  $b$ -values where the signals are acquired, from 70 to 700  $\text{s}/\text{mm}^2$ , the logarithm of the signal acquired showed a clear linear dependence with  $b$ -value, meaning that the ADC is sufficient to describe the signal in this range. Higher order effects such as a Kurtosis [159, 160, 161, 162] term need not to be considered. Moreover, the signals in the  $x$ ,  $y$ , and  $z$  directions do

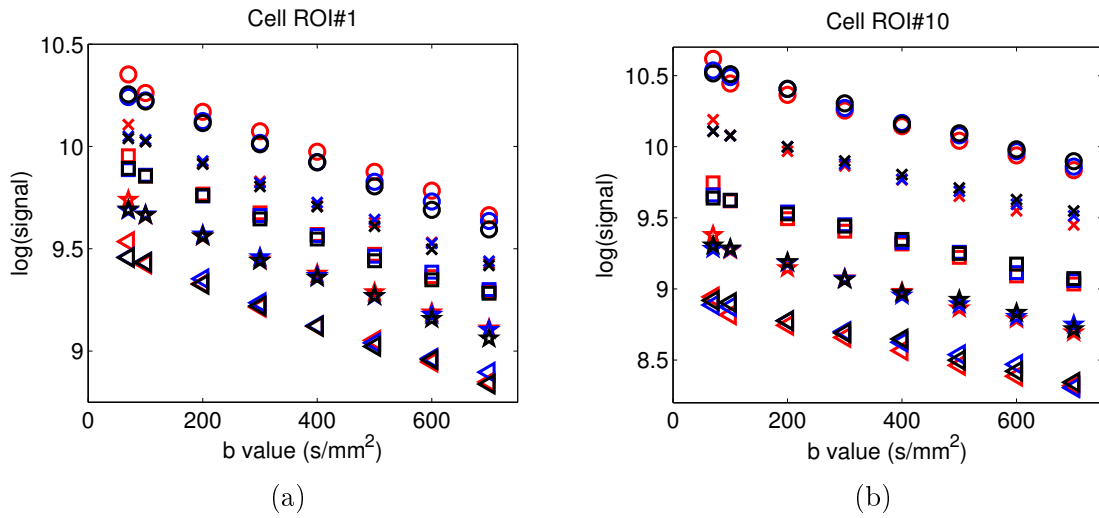


Figure 37 – The dMRI signals for multiple diffusion times in: large cell neurons ROI # 1  $R_{\text{eff}} \approx 164.97 \mu\text{m}$  (a), large cell neurons ROI # 10  $R_{\text{eff}} \approx 101.34 \mu\text{m}$  (b). In each sub figure, from top to bottom we represent the scaled signals for  $\Delta$  from 5 ms to 25 ms. The different colors represent the different gradient directions, red, blue, and black for  $x$ ,  $y$ , and  $z$  directions, respectively.

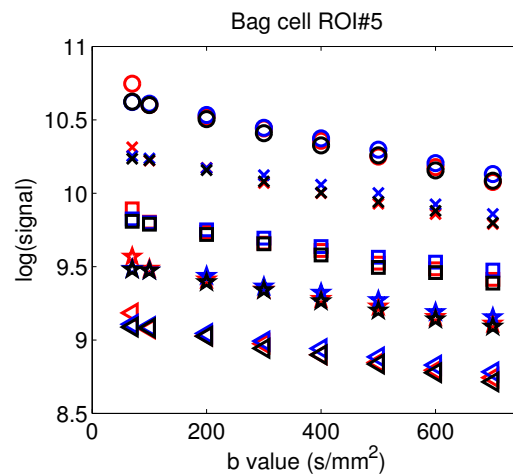


Figure 38 – The dMRI signals for multiple diffusion times in bag cell neurons ROI # 5. From top to bottom we represent the scaled signals for  $\Delta$  from 5 ms to 25 ms. The different colors represent the different gradient directions, red, blue, and black for  $x$ ,  $y$ , and  $z$  directions, respectively.

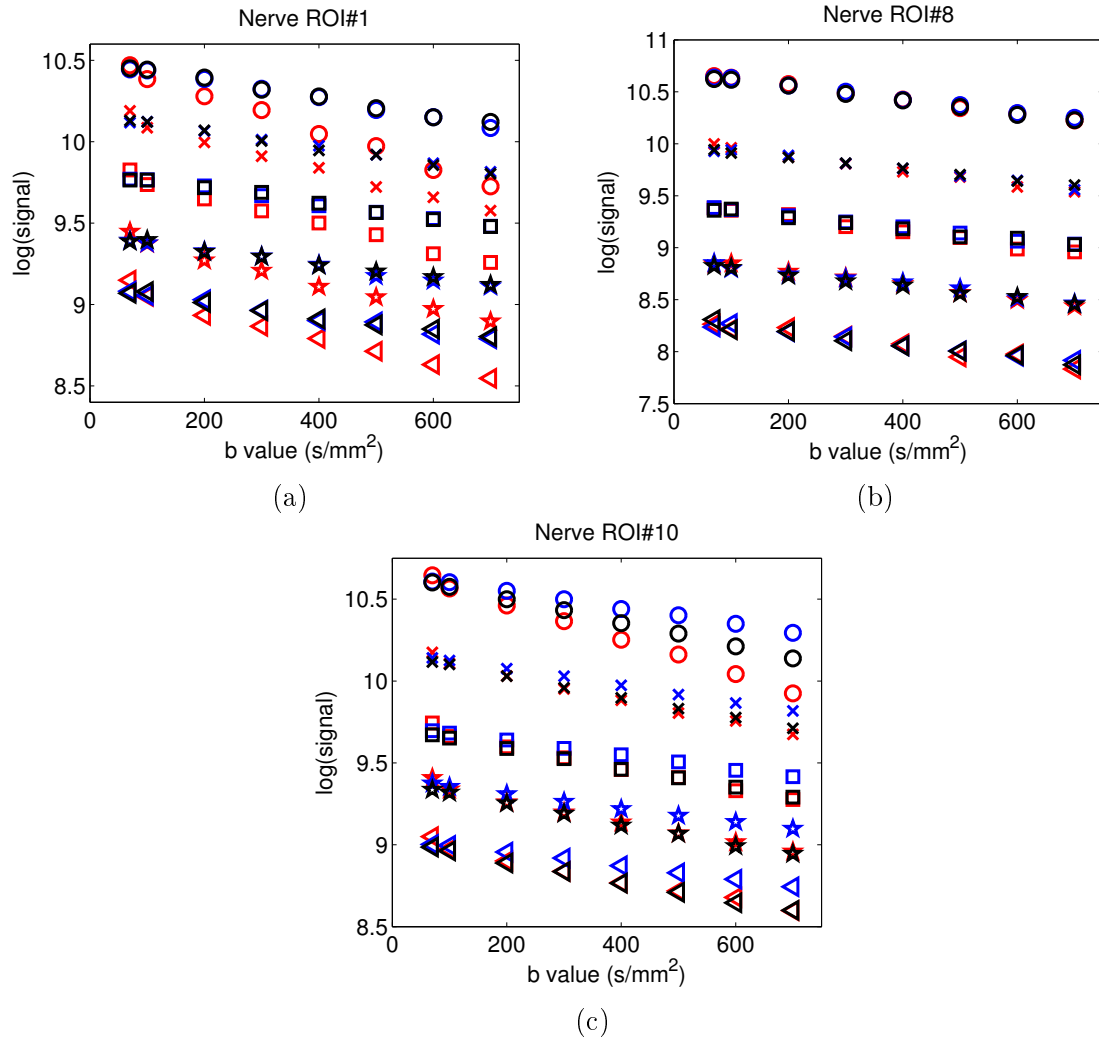


Figure 39 – The dMRI signals for multiple diffusion times in nerve neurons with different direction. (a) the nerve ROI # 1: the nerve direction is mainly orientated in the  $x$  direction, and the  $y$  and  $z$  component are similar; (b) the nerve ROI # 8: the nerve direction has the same component in  $x$ ,  $y$ , and  $z$  directions; (c) the nerve ROI # 10: the nerve direction has a larger component in  $x$  and  $z$  directions, smaller in  $y$  component; In each sub-figure, from top to bottom we represent the signals for  $\Delta$  from 5 to 25 ms. The different colors represent the different gradient directions, red, blue, and black for  $x$ ,  $y$ , and  $z$  directions, respectively.

not show significant anisotropy in large cell neurons and bag cell neurons. The time-dependent ADC measured over the ROIs of the three cell types are shown in Table 8. We found that, when the diffusion time is increased from  $\delta = 2.5$  ms,  $\Delta = 5$  ms to  $\delta = 2.5$  ms,  $\Delta = 25$  ms, the average experimental ADC drops by 9.45% in large cell neurons; by 20.8% in bag cell neurons; and the MD in nerves drops by 14.98%.

$\Delta$ (ms)	Bag cells (N=11)		Large cells (N=22)		Nerve (N=13)	
	Mean	SD	Mean	SD	Mean	SD
5	0.779	0.060	0.974	0.096	0.821	0.083
7.5	0.755	0.054	0.957	0.085	0.812	0.095
10	0.705	0.054	0.938	0.087	0.749	0.085
12	0.687	0.067	0.915	0.080	0.741	0.089
15	0.660	0.051	0.914	0.080	0.724	0.09
20	0.632	0.056	0.897	0.081	0.708	0.087
25	0.617	0.055	0.882	0.087	0.698	0.086
Drop	20.80%		9.45%		14.98%	

Table 8 – Mean and standard deviation (SD) of average ADC in bag cell neurons, large cell neurons, and nerve ROIs. The average ADC were observed drop by 20.8%, 9.45% and 14.98% for bag cell neurons, large cell neurons and nerve, respectively.

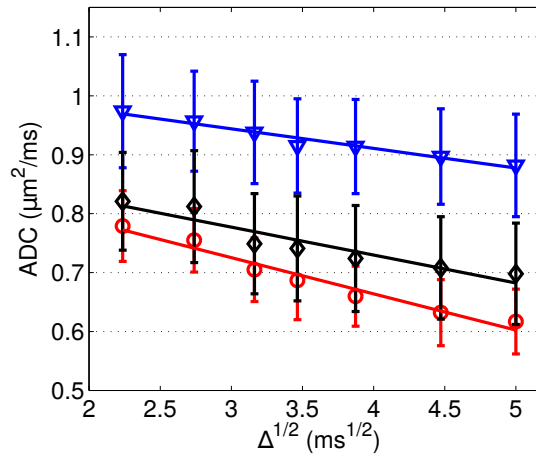


Figure 40 – The measured ADC values are shown as colored markers (mean) with error bars (standard deviation) for the bag cell neurons (circle, N=11 ROIs), for the large cell neurons (triangle, N=22 ROIs) and for the nerves (diamond, N=13 ROIs). The solid lines represent linear fits of the measured data. The experimental ADC drops by 20.8%, 9.45% for bag cell neurons and large cell neurons, respectively, and the MD drops by 14.98% in the nerves.

## 23.2 Estimating cell size using short time ADC formula

Assuming a free diffusivity of  $2 \mu\text{m}^2/\text{ms}$ , the average diffusion displacement is between 7.7 and 17.3  $\mu\text{m}$  for the diffusion times between 5 and 25 ms. Thus from the point of view of diffusing water molecules, their diffusion displacement is large with respect to

some cell features in the bag cell neurons and the nerve but not with respect to the large cell neurons. So, from a theoretical point of view we can use the mathematical models for the ADC in the short diffusion time regime proposed by Mitra et al. [50, 51] (equation (63)) and the updated version proposed by Schiavi et al. [52] (equation (64)) and apply them to large cell neurons to estimate the surface to volume ratio, which when assuming spherical cell shape, can give the estimated cell diameter.

We proceed in the following way. From the experimental ADC, by fitting  $ADC = A\sqrt{\Delta} + B$  (corresponding with formula (63)) or  $ADC = AC_{\delta,\Delta} + B$  (corresponding with formula (64)), we can find the coefficients A and B. By comparing with the short time ADC formula for  $\frac{S}{V}$  from both equation (63) and (64), we found that  $A = -D_0 \frac{4\sqrt{D_0}}{3\sqrt{\pi}} \frac{1}{R}$ , and  $B = D_0$ , implying that,

$$R_{est} = -D_0 \frac{4\sqrt{D_0}}{3\sqrt{\pi}} \frac{1}{A}. \quad (113)$$

We denote by  $R_{est}$  the estimated cell radius determined by applying the mathematical formula to the experimental ADC. The  $R_{est}$  will be compared to the visually obtained effective radius  $R_{eff}$  of the 22 large cell ROIs. The results are shown in 9.

In Figure 41, we plot the effective radius  $R_{eff}$  against the estimated radius  $R_{est}$  from applying the mathematical ADC model. There is a positive correlation between  $R_{eff}$  of the 22 large cell neuron ROIs and the reference value  $R_{est}$ . We show the positive correlation between  $R_{est}$  and the fitting quantity  $-A$  in Figure 41 as well.

However, it is clear that cell size is severely underestimated,  $R_{est}$  is on average only 25% of  $R_{eff}$ . This suggests that a one compartment model is not sufficient to model diffusion in large cell neurons of the *Aplysia*.

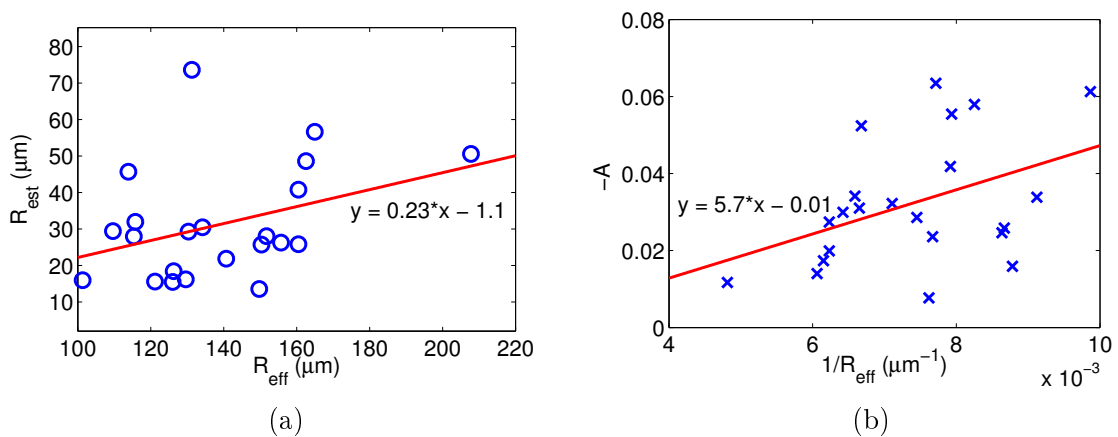


Figure 41 – (a) The positive correlation between effective radius ( $R_{eff}$ ) and estimated radius ( $R_{est}$ ) from 22 large cell neuron ROIs using the formula (63). (b) The relation between slope value  $A$  and  $R_{eff}$ . The cell size is severely underestimated,  $R_{est}$  is on average only 25% of  $R_{eff}$ .

ROI#	$R_{\text{eff}}$	Fitting by formula (63)				Fitting by formula (64)			
		A	B	$R_{\text{est}}$	Err	A	B	$R_{\text{est}}$	Err
1	101.3	-0.0613	1.191	16.0	1.79%	-0.0634	1.212	15.8	2.23%
2	109.6	-0.0339	1.206	29.4	1.89%	-0.0351	1.218	28.8	2.00%
3	113.9	-0.0159	0.978	45.7	1.86%	-0.0165	0.983	44.6	1.90%
4	115.4	-0.0258	0.973	28.0	1.99%	-0.0267	0.982	27.4	2.08%
5	115.8	-0.0246	1.031	32.0	0.94%	-0.0255	1.039	31.3	1.09%
6	121.2	-0.0579	1.131	15.6	1.91%	-0.0600	1.150	15.5	2.33%
7	126.0	-0.0554	1.092	15.5	2.59%	-0.0574	1.111	15.3	2.90%
8	126.3	-0.0418	1.018	18.5	1.14%	-0.0433	1.032	18.2	1.53%
9	129.6	-0.0635	1.232	16.2	2.76%	-0.0657	1.253	16.1	3.07%
10	130.4	-0.0236	0.946	29.3	1.62%	-0.0244	0.953	28.7	1.72%
11	131.3	-0.0077	0.829	73.6	1.16%	-0.0080	0.831	71.5	1.17%
12	134.2	-0.0286	1.103	30.5	1.73%	-0.0296	1.113	29.8	1.83%
13	140.7	-0.0322	0.957	21.9	1.52%	-0.0333	0.967	21.5	1.71%
14	149.7	-0.0524	0.962	13.6	1.69%	-0.0543	0.980	13.5	2.21%
15	150.4	-0.0310	1.041	25.7	0.59%	-0.0321	1.051	25.2	0.92%
16	151.8	-0.0341	1.175	28.1	2.69%	-0.0354	1.186	27.5	2.78%
17	155.7	-0.0299	1.030	26.3	1.41%	-0.0310	1.040	25.8	1.56%
18	160.5	-0.0199	1.052	40.8	1.37%	-0.0206	1.059	39.8	1.44%
19	160.5	-0.0274	0.961	25.8	1.60%	-0.0284	0.970	25.3	1.74%
20	162.6	-0.0173	1.079	48.6	1.59%	-0.0179	1.085	47.4	1.63%
21	165.0	-0.0140	1.037	56.6	1.18%	-0.0145	1.042	55.1	1.21%
22	207.8	-0.0117	0.853	50.6	0.83%	-0.0121	0.857	49.2	0.88%

Table 9 – Fitting experimental  $ADC(\Delta)$  by using the equation (63) ( $ADC = A\sqrt{\Delta} + B$ ) and using the equation (64) ( $ADC = AC_{\delta,\Delta} + B$ ) for 22 large cell neuron ROIs (ROI#). The effective radius ( $R_{\text{eff}}$ ) of each cell were estimated from T2w image. The cell radius estimated ( $R_{\text{est}}$ ) by using the equation (113). The error between fitting and data are shown in Err columns. There is not much difference on cell radius estimated between two prediction models.

### 23.3 Simulation of a two compartments model of large cell neurons

In this part, we simulate a two compartments model of large cell neurons, namely, a nucleus and surrounding cytoplasm, with a limited exchange between them. First, we generated four computational domains based on three types of nucleus shapes and the position of the nucleus inside the cell, as shown in Figure 42.

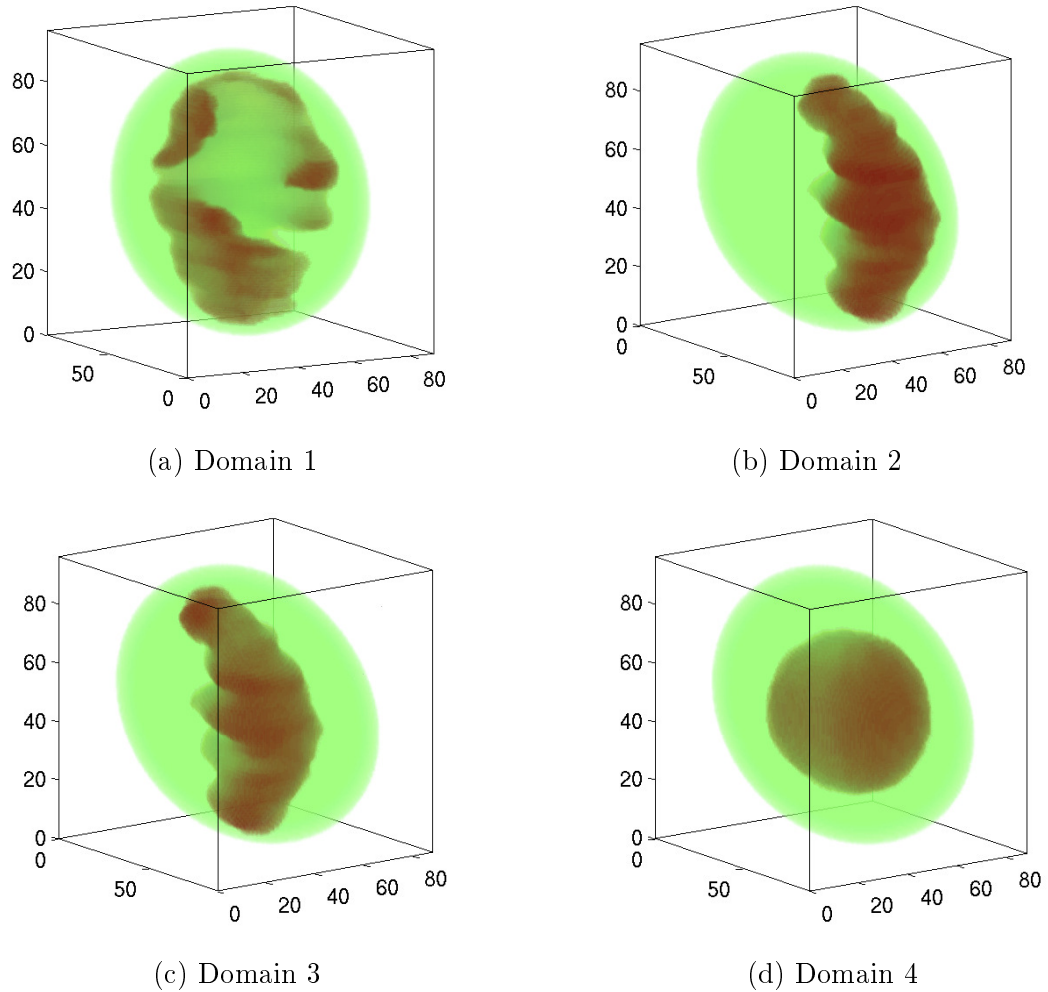


Figure 42 – Four generated domains of the same cell size and cell outline, based on three different shapes of nucleus (red) (a, b-c, and d) and different position of nucleus inside the cell neurons (b and c). The cell outlines are the same for the four geometries, which is generated from T2w image (large cell ROI#7). The volume fraction of the nucleus in all four domains is approximate 25%.

We studied the dependence of the ADC on the nucleus shape and on the nucleus volume fraction by simulating  $ADC(\Delta, R)$  for an intrinsic diffusivity in the cytoplasm of  $D_c = 1.0 \mu\text{m}^2/\text{ms}$  and an intrinsic diffusivity in the nucleus of  $D_n = 2.0 \mu\text{m}^2/\text{ms}$ , ( $\Delta$  varied between 5 and 25 ms). By fitting the obtained simulated ADC values using the model  $ADC(\Delta, R) = A(R) \times \sqrt{\Delta} + B(R)$ , we find the slope  $A(R)$  which represents how the  $ADC(\Delta, R)$  value drops (when the diffusion time  $\Delta$  increases) as a function of the cell radius  $R$ .

As shown in Figure 43 the slope  $A(R)$  depends more on the nucleus shape than on the position of the nucleus inside the cell neurons. Moreover, a more irregular shape of the nucleus gives a larger value of  $A(R)$ , meaning that the drop of ADC (when increasing  $\Delta$  from 5 to 15 ms) is much larger in the case of an irregular shape of the nucleus (Domain 1,2,3) than in a (almost) spherical shape of the nucleus (Domain 4). On the other hand, the coefficient  $B(R)$  seem not to depend on the radius of the cells and the shape of the nucleus as shown in Figure 43b. The freedom coefficient  $B(R)$  represents the effective intrinsic diffusivity in the cells (see Equation (63)).

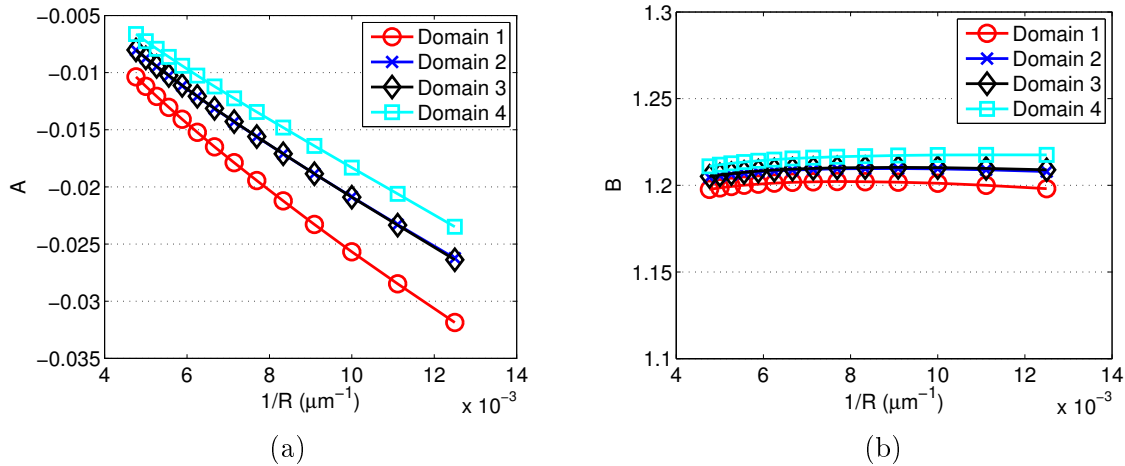


Figure 43 – Slope  $A(R)$  as a function of the cell radius  $R$  (a); and the freedom coefficient  $B$  as a function of the cell radius  $R$  (b) for four identical domains with the same nucleus volume fraction (25%). The slope  $A$  depends stronger on the shape of the nucleus (Domain 1, 2-3, and 4) than the position of the nucleus inside the cell neurons (Domain 2, 3) while the coefficient  $B$  seems not to depend on the cell radius and the shape of the nucleus.

As shown in Figure 44a, the slope  $A(R)$  also depends on the volume fraction of the nucleus,  $\text{VF}_N$ . The nucleus shape in domain 5 (Figure 44b) is similar with the nucleus shape in domain 1 (Figure 42a), the volume fraction, however, of the nucleus is around 29% for domain 5 and is around 25% for domain 1. A larger nucleus volume fraction results in a larger drop in the ADC for a given cell size.

Therefore, we can predict that with detailed information regarding the size and shape of the nucleus one can obtain more precise results by combining simulations and experimentation in the *Aplysia*.

### 23.4 Simulations of the ADC in bag cell neurons and nerves

Because it is not possible to visualize the individual neurons of the bag cell ROIs or the axons in the nerves from the T2w images, we relied on information about the cell structures from the literature to construct the simulation domains, as described in the previous sections. By comparing the time-dependent simulated ADC with the experimental ADC, we extracted the parameters  $D_c, D_n$  for the cytoplasm and the nucleus intrinsic diffusivities, respectively, and  $D_a$  for the axons intrinsic diffusivity.

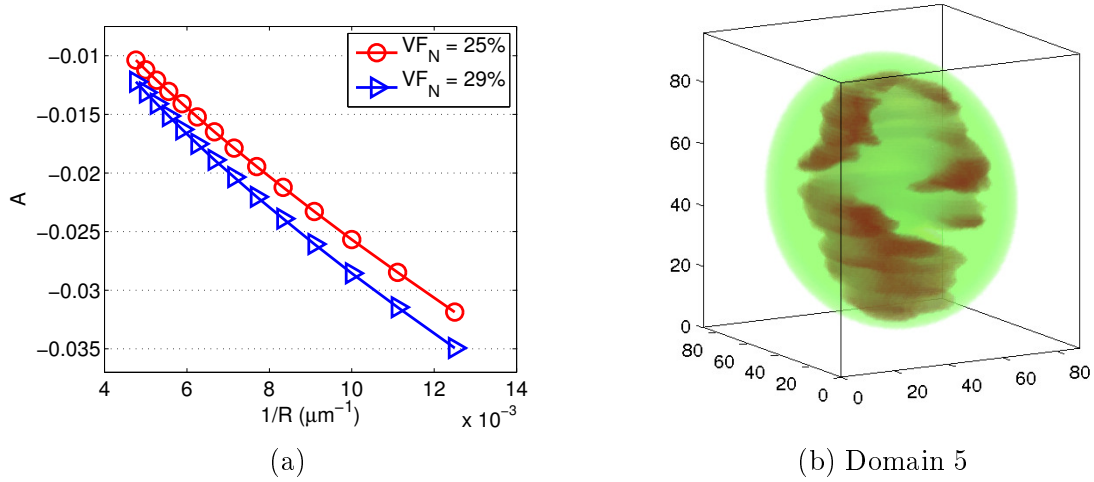


Figure 44 – (a) Slope  $A(R)$  as a function of the cell radius  $R$  for different nucleus volume fraction,  $\text{VF}_N$ . (b) The geometry domain in which the volume fraction of the nucleus is about 29% and the nucleus shape in this domain is similar with the nucleus shape in domain 1.

#### **Bag cell neurons:**

We simulated the ADC for  $Dc$  varied between 0.50 and 2.00  $\mu\text{m}^2/\text{ms}$  and for  $Dn$  varied between 1.25 and 2.00  $\mu\text{m}^2/\text{ms}$ . Let us denote

$$\text{ErrFit} = \frac{\sqrt{\sum_{\Delta} |ADC_{\text{fit}}(\Delta) - ADC(\Delta)|^2}}{\sqrt{\sum_{\Delta} |ADC(\Delta)|^2}},$$

the error when fitting the experimental ADC values for each ROI of bag cell neurons, where  $ADC_{\text{fit}} = A_{\text{fit}}\sqrt{\Delta} + B_{\text{fit}}$ . The simulated ADC values,  $ADC_{\text{simul}}(Dc, Dn)$ , are compared with the experimental ADC values to extract the information of  $(Dc, Dn)$  which will satisfy the following condition:

$$\frac{\sqrt{\sum_{\Delta} |ADC_{\text{simul}}(Dc, Dn, \Delta) - ADC(\Delta)|^2}}{\sqrt{|ADC(\Delta)|^2}} \leq 2 \times \text{ErrFit}. \quad (114)$$

Figure 45b displays the range of pairs  $(Dc, Dn)$  which satisfy the condition (114) (called solution  $(Dc, Dn)$ ). The colored dash-lines in Figure 45a represent the simulated ADC curves generated for each pair of the solutions  $(Dc, Dn)$  shown in Figure 45b (same color code).

#### **Nerve - group of axons:**

The simulation was ran over the range of  $Da = [0.85 : 0.05 : 2.00]$   $\mu\text{m}^2/\text{ms}$  for six different distribution of the axons (corresponding with six nerves mentioned before). As shown in Table 1 the number of axons varies, the maximum error of 5% between simulated mean diffusivities,  $\text{MD}_{\text{simul}}(Da)$ , and experimental mean diffusivity,  $\text{MD}$ , will be used to select the acceptable solutions instead of using  $2 \times \text{ErrFit}$  as an upper limit (like for bag cell neurons). It means that, for each nerve distribution, we find all  $Da$  such that:

$$\frac{\sqrt{\sum_{\Delta} |\text{MD}_{\text{simul}}(Da, \Delta) - \text{MD}(\Delta)|^2}}{\sqrt{\sum_{\Delta} |\text{MD}(\Delta)|^2}} \leq 0.05. \quad (115)$$

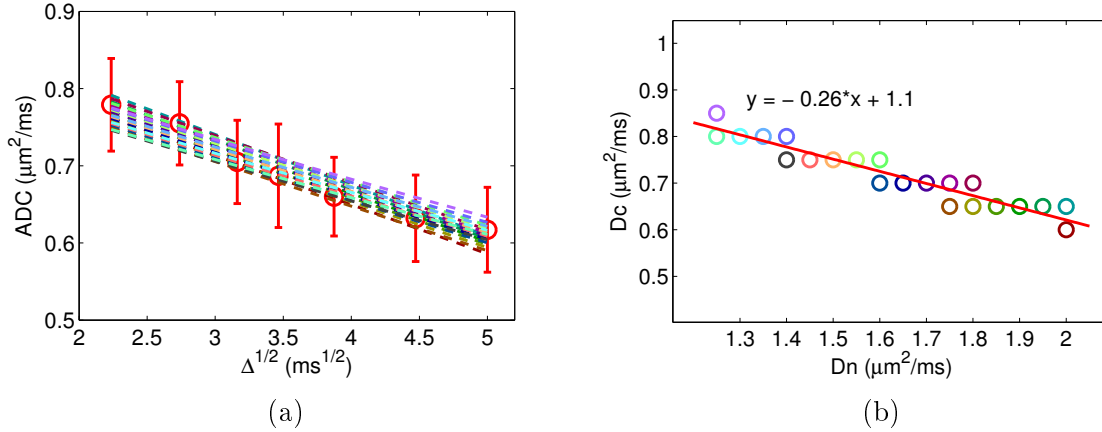


Figure 45 – Averaged experimental ADC values (marker) with error bars representing the standard deviations (N=11 ROIs), and the optimal obtained simulated ADC (dashed lines) (a). The range of paired solutions ( $D_c, D_n$ ) are represented as circle in (b), the intrinsic diffusivity  $D_c$  and  $D_n$  are correlated by the formula  $D_c + 0.26 \times D_n = 1.1$ . The colored line in (a) corresponds to the colored marker represented in (b).

The best fits between the simulated mean diffusivities and those from experimental data are shown in Figure 46. In Table 10, we shown the range of intrinsic diffusivities which yields good fitting results for particular types of the nerves. In Figure 46 presents

Nerve	$D_a$ range
1b	1.85-2.00
2b	1.55-1.65
3b	1.30-1.40
ON	1.80-1.95
RN	1.75-1.90
CBC	1.40-1.50

Table 10 – The ranges of intrinsic diffusivity  $D_a$  ( $\mu\text{m}^2/\text{ms}$ ) which yield good fitting between the simulated mean diffusivity ( $\text{MD}_{\text{simul}}(D_a)$ ) and the experimental mean diffusivity MD corresponds to six axons distributions of buccal ganglia nerves (1b, 2b, 3b, ON, RN, CBC).

the experimental mean diffusivity (MD) (marker) and standard deviation over 13 nerve ROIs and the good fitting simulated mean diffusivity for the nerve 1b and the nerve ON (dashed line).

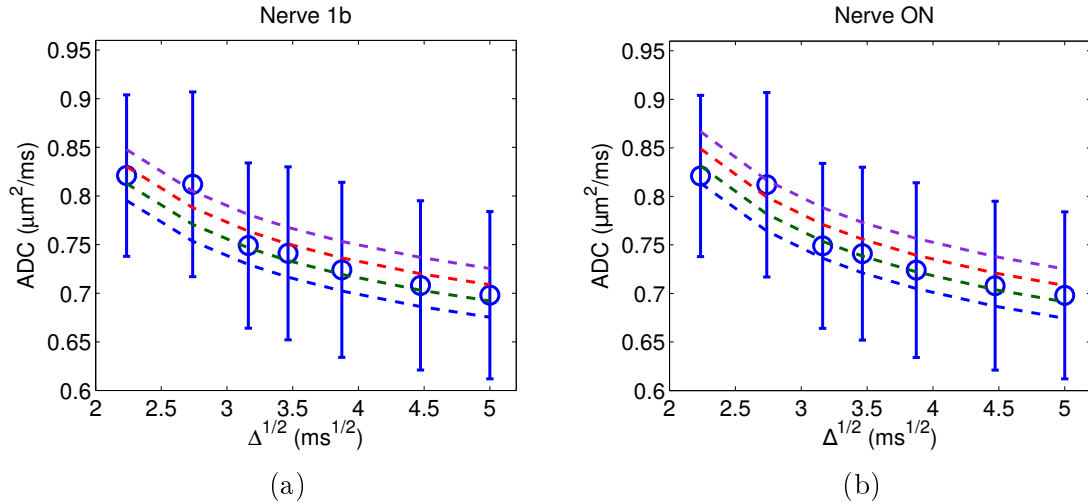


Figure 46 – Assumed the axons distribution in the abdominal nerves are the same with the axons distribution in the buccal nerve 1b (a) and the buccal nerve ON (b). For both sub figures, the marker (with errors bar as the standard deviation) represent the averaged experimental MD of the 13 nerve ROIs; while the solid lines represent the good fits simulated mean diffusivities. The extracted intrinsic diffusivity of these solid lines are presented in table 10.

## 24 Conclusion

We have acquired and analyzed the time-dependent dMRI data in the *Aplysia* neuronal network for large cell neurons, bag cell neurons, and nerves. We found that given the large drop of the experimental ADC with increasing diffusion time in the large cell neurons, it is not sufficient to approximate these cells by a one compartment model. Using the one compartment model and fitting with the short time ADC formula, we found a serious under-estimation of the cell size. In the bag cell neurons, we found that good ADC fit can be obtained by a range of solutions of the intrinsic diffusivities in the nucleus and the cytoplasm,  $D_n$  and  $D_c$ , respectively. And the solutions all exhibit a certain linear relationship between  $D_n$  and  $D_c$ . Base on the simulation results we obtained for large cells, we predict that an irregular nucleus shape of the cells in bag cell neurons will also influence the range of intrinsic diffusivities ( $D_c, D_n$ ) found. In the nerves, we found that a range of solutions for the intrinsic diffusivity of the axons,  $D_a$ , depends significantly on the axon diameter distribution we chose. Further work combining simulations and experimentation in the *Aplysia* is needed to make the relationship between the geometry and the dMRI signal more precise.

## Part VI

# Summary and future directions

## Summary

---

<b>25</b>	<b>Summary</b>	<b>109</b>
<b>26</b>	<b>Future directions</b>	<b>110</b>
26.1	Future work on DLA-CS strategy applications . . . . .	110
26.2	Future work on optimizing the CS image reconstruction and dMRI simulation codes . . . . .	110
26.3	Future work on combining dMRI experiment, simulation and histology imaging . . . . .	111

---

## 25 Summary

One of the goals of this thesis was to implement compressed sensing for magnetic resonance microscopy studies. We proposed a new undersampling model based on the diffusion limited aggregation (DLA) which performed better than the commonly used random variable undersampling method [135]. We successfully implemented the DLA-CS strategies for undersampling T2-weighted (starting from RARE sequence) and T1-weighted images (starting from FLASH sequence). We found 50% undersampling ratio satisfactory not only in terms of image quality (contrast to noise ratio, spatial resolution) but also in terms of intensity quantification (in MEMRI images) [135]. In addition, we proposed a simple cell segmentation algorithm as a tool for image analysis in MR microscopy.

We acknowledge the even when using CS the acquisitions times remain relatively long when compared to fast techniques, such as EPI or spiral imaging, the DLA-CS appears to be a promising approach at high magnetic fields and high spatial resolutions, where single shot acquisitions are not feasible. The results presented in this thesis suggest that the DLA-CS is beneficial to magnetic resonance microscopy studies, thus enabling the expansion of the technique to the study of living specimens and eventually to dynamic investigations. Moreover, the DLA-CS is not limited to magnetic resonance microscopy and could be also applied to preclinical and clinical studies, where shortening the acquisition time is equally desirable.

The second objective of this thesis was to adequately study diffusion time dependence of the dMRI signal and discover if the additional information the measurements at multiple diffusion times provides can give worthwhile information about the tissue micro structure, we image the *Aplysia* abdominal ganglia at high resolution and multiple diffusion times.

We investigated dependence of the ADC on the diffusion time in three different structures within the abdominal ganglia of the *Aplysia*. We found that by increasing the diffusion time from 5 to 25 ms the ADC dropped by 20.8%, 9.35%, and 14.98% for bag cell neurons, large single cell neurons and the nerve ROI, respectively. The different behavior in the three different regions can be explained by the different sizes and shapes of the cellular components. We found that it is not sufficient to approximate the large cell size by using the predicted one compartment model. Based on the results from numerical simulation and evidence from experimental data, we established that it is necessary to include a nucleus region embedded in a cytoplasmic region in order to fit the large drop in ADC observed when varying the diffusion time from 5 ms to 25 ms. In agreement to the literature we find that the intrinsic diffusivity in the nucleus is higher than in the cytoplasm. One possibility is that the protons are more “bound” in the cytoplasm than in the nucleus, as shown in the reference [163] (page 128-129) the cytoplasm region appears darker than the nucleus region in the magnetization transfer images. Moreover, both the shape and the volume fraction of nucleus were found to significantly influence the ADC behavior, while the position of the nucleus did not seem to be important. This results suggests that dMRI can be used as a diagnostic tool as the shape and size of cell nuclei can signify cellular abnormalities [164]. Regarding the bag cell neurons, we found the linear relationship between the intrinsic diffusivities in the cytoplasm and the nucleus for which the fitting ADC was successful. Moreover, we found regarding

the nerve that the extracted intrinsic diffusivity of axons depends significantly on the axons diameter distribution we chose. In addition, by combining dMRI experiment, the numerical simulation and the histology imaging it will be possible to extract the intrinsic diffusivity in the nucleus, the cytoplasm and the axons components.

## 26 Future directions

### 26.1 Future work on DLA-CS strategy applications

One of my next projects is to use the DLA-CS method to accelerate DTI acquisitions. Such acquisitions are notoriously time consuming as data for several  $b$  values and at least six different encoding directions has to be collected. For this reason in vivo acquisitions are usually performed using EPI techniques which have, however, the disadvantages of presenting limited spatial resolution, high sensitivity to field inhomogeneity, and low signal-to-noise ratio. Our plan is to use DLA-CS to under-sample other types of acquisitions such as diffusion prepared FISP (DP-FISP). By using different undersampling patterns for different  $b$  values we anticipate to be able to obtain much higher acceleration factors than those reported in our previous studies, and render these acquisitions applicable to in vivo studies. In addition, since most modern MR systems incorporate multiple receivers, the combination of CS and parallel imaging to shorten even more the acquisition time is foreseeable. While parallel imaging can be difficult to implement in MR microscopy due to the limited space available for placing multiple coil elements, it should be feasible for preclinical and clinical scanners. The reconstruction of combined CS and parallel imaging should be straightforward.

The successful implementation of this DLA-CS-DTI acquisition strategy will allow in vivo DTI investigations with high spatial resolution and free of susceptibility artifacts at high magnetic fields.

### 26.2 Future work on optimizing the CS image reconstruction and dMRI simulation codes

There are two paradigms for parallel computing based on CPU (Central Processor Unit) and GPU (Graphics Processing Unit). Based on CPU, we can use OpenMP (Open Multi-Processing) for multi-threaded and shared memory machines [165] for acceleration. OpenMP consists of a set of compiler directives, library routines and environment variables that influence run-time behavior [166]. The advantage of OpenMP is that is free-usable and portable. The performance of OpenMP parallel programming depends on the number of “core” existent in the computer. However, it is not the limitation because nowadays almost all computers are “multi-core”. Another strategy is to use GPU-accelerated computing. The advantage of this approach is using GPU together with a CPU for processing. As known, the GPU computing performs faster than CPU computing due to the fact that the GPU has a massively parallel architecture consisting of thousands of smaller, more efficient cores designed for handling multiple tasks simultaneously while a CPU consists of a few cores optimized for sequential serial processing (Figure 47). However, GPU-accelerated approach is disadvantage in term of cost for

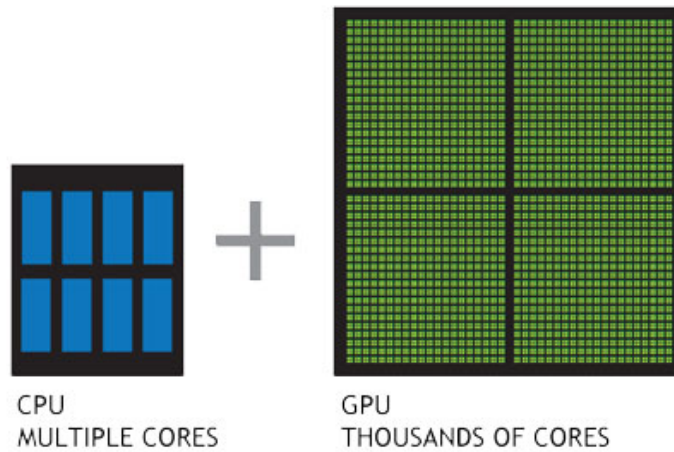


Figure 47 – GPUs have thousands of cores to process parallel workloads efficiently. Source: <http://www.nvidia.com/object/what-is-gpu-computing.html>

hardware.

The application of parallelized code can be used to implement the CS image reconstruction directly in ParaVision commercial software. For the dMRI simulation finite volume codes, fortunately, since this method coupled the explicit time stepping method, so each compartment can be managed separately and need to be synchronized only once at the beginning of each time-step.

### 26.3 Future work on combining dMRI experiment, simulation and histology imaging

As mentioned before, the closer the geometry domain used in simulations to the true geometry of the tissue leads to more accurate results. As a next step we plan to use histology imaging to extract the exact information of the cell size as well as the shape of the nucleus in specific tissues. Using this information we will generate the geometry domain for simulations. By comparing the numerical simulated time-dependent ADC and with results from experiments we aim to extract the intrinsic diffusivity. These results will then be used back to predict the shape of nucleus as well as cell size in other samples.

## List of publications

### In preparation

3. **Khieu V. Nguyen**, Denis Le Bihan, Luisa Ciobanu, Jing-Rebecca Li, *The time-dependent diffusivity in the abdominal ganglion of Aplysia californica, comparing experiments and simulations*, in preparation, 2017.
2. Pavel Svehla, **Khieu V. Nguyen**<sup>1</sup>, Jing-Rebecca Li, Luisa Ciobanu, *Quantitative DLA-based Compressed sensing for MEMRI acquisitions*, submitted, 2017.
1. Y. Abe, **Khieu V. Nguyen**, T. Tsurugizawa, L. Ciobanu, D. Le Bihan, *MR microscopy of Aplysia californica reveals that the DfMRI signal is linked with activation-induced neural cell swelling*, submitted, 2016.

### Peer-reviewed journals

1. **K.-V. Nguyen**, J.-R. Li, G. Radecki, L. Ciobanu, *DLA based compressed sensing for high resolution MR microscopy of neuronal tissue*, Journal of Magnetic Resonance, vol. 259, pp. 186-191, 2015.

### Conferences

5. **Khieu V. Nguyen**, Denis Le Bihan, Luisa Ciobanu, Jing-Rebecca Li, *Diffusion MRI in the Aplysia Neuronal Network: Experiments & Numerical Simulations*, Poster section, SIAM CSE conference, 2017.
4. **Khieu V. Nguyen**, Denis Le Bihan, Luisa Ciobanu, Jing-Rebecca Li, *Diffusion MRI in the Aplysia Neuronal Network: Experiments & Numerical Simulations*, Poster section, ISMRM Workshop, 2016.
3. **Khieu V. Nguyen**, Jing-Rebecca Li, Luisa Ciobanu, *DLA-based compressed sensing for high resolution MR of neuronal tissue*, Poster section, ICMRM, 2015.
2. **Khieu V. Nguyen**, Jing-Rebecca Li, Luisa Ciobanu, *Numerical simulation of diffusion MRI in Aplysia neuronal network*, Oral presentation, SMAI, 2015.
1. **Khieu V. Nguyen**, Jing-Rebecca LI, Luisa CIOBANU, *Compressed sensing for high resolution MR microscopy of neuronal tissue*, Poster section, NEuroscience Workshop, 2014.

---

<sup>1</sup>co-first author

## List of Figures

1	In presence of a static magnetic field, the spin magnetic moments and the resulting bulk magnetization precesses at the Larmor frequency. . . . .	22
2	Effects of relaxation on the magnetization vector after a 90 degree excitation pulse. (a) The magnetization vector precesses around the $z$ -axis. (b) The measured net magnetization in the $x - y$ plane ( $M_{xy}$ ) and the $z$ -component of the relaxing magnetization. In both subfigures, $T_2 = 200$ ms, $T_1 = 500$ ms. . . . .	26
3	Diagram of gradient field effects on the main magnetic field $\mathbf{B}_0$ . . . . .	27
4	Diagram of the slice selection when applying an excitation pulse. A gradient $G_z$ imposes a space dependence on the main magnetic field. An RF pulse with the single frequency $\omega$ will excite only the spins at the appropriate position. Thus, the slice position depends on the strength of the gradient and the pulse frequency. . . . .	31
5	Diagram of the k-space and the relationships between k-space FOV and resolution. The sampled k-space points are plotted as dots; the arrows show the trajectories during one frequency encoding scan corresponding to one phase encoding step. . . . .	34
6	Spin echo pulse diagram. . . . .	37
7	RARE pulse diagram. . . . .	37
8	Gradient echo pulse diagram. . . . .	38
9	FLASH pulse diagram. . . . .	39
10	FISP pulse diagram. . . . .	40
11	The PGSE time profile for $t_s = 0$ , consisting of two rectangular pulses (duration $\delta$ , separated by a time interval $\Delta$ . . . . .	42
12	The <i>Aplysia</i> abdominal ganglion diagram. . . . .	45
13	The ADC in the nucleus (N) is larger than it in the cytoplasm (C) of L7 <i>Aplysia</i> neuron. ( $7.8\mu\text{m}$ in-plane resolution, source: Lee et al. [59]: <a href="http://www.nature.com/articles/srep11147">www.nature.com/articles/srep11147</a> ) . . . . .	46
14	The <i>Aplysia</i> buccal ganglion diagram realized by R. Nargeot. . . . .	48
15	Echo planar imaging pulse sequence timing diagram. A spin echo excitation scheme and an echo train length of 8 are illustrated. . . . .	49
16	DP-FISP pulse sequence timing diagram. . . . .	50
17	Non-Cartesian sampling: a) Spiral k-space trajectory and b) Radial trajectory. . . . .	54
18	Shepp-Logan image (left) is sparsely presented under finite difference operator (middle) and Wavelet transform (right). . . . .	56

19	The sparsity of abdominal ganglia (a) and buccal ganglia (b) T2w images of <i>Aplysia</i> . The fully encoded image (right column) and the reconstructed images (three left column) from a subset of 7%, 10% and 20% of the largest wavelet transform and finite different transform coefficients. . . . .	57
20	Two most popular $k$ -space sampling schemes: (a) rectilinear sampling and (b) polar sampling. . . . .	60
21	Undersampling patterns (50 %) for a RARE acquisition: DLA (a) and polynomial (d) undersampled phase encoding plane for $A_F = 1$ ; DLA (b) and polynomial (e) undersampled phase encoding plane for $A_F = 4$ . The undersampling patterns was applied for one group of $k$ -space points corresponding to the first echo time, the results was then repeated $A_F = 4$ times corresponding to all echo time; (c) 3D DLA undersampling and (f) 3D polynomial undersampling generated by repeat 2D undersampling pattern in read direction. . . . .	71
22	The relative errors between the fully encoded and CS images obtained by applying DLA and polynomial undersampling schemes to abdominal (a) and buccal ganglia image libraries (b) as a function of the undersampling ratio. The fully encoded images were acquired using a standard RARE acquisition with $A_F = 4$ . The error bars represent standard deviations (n=300). . . . .	72
23	The relative errors between the fully encoded and CS images obtained by applying DLA and polynomial undersampling schemes to a fully encoded (RARE acquisition with $A_F = 1$ ) image of buccal ganglia. The error bars represent standard deviations (n=300). . . . .	73
24	Flow diagram illustrating the outline of created and modified ParaVision files. . . . .	74
25	Flow diagram illustrating the proposed algorithm for separating cells within clusters. . . . .	75
26	CS (top) and fully encoded (bottom) images of a water phantom. The SNR was calculated as the mean of signal intensity (red ROI) divided by the standard deviation of the noise (white ROI). . . . .	77
27	Buccal (a , b) and abdominal (d, e) ganglia images acquired with a CS-RARE (a, d) and a standard RARE sequence (b, e), along with the signal intensity profiles (c,f) at locations indicated by the white lines across the images. The hypointense regions seen in the images correspond to cell bodies. . . . .	78
28	Comparison between the cells detected on the fully encoded (red wire-frame) and CS (solid blue) images of abdominal (a) and buccal ganglia (b). An identical number of cells was detected on the abdominal ganglion with both acquisitions, while on the buccal ganglia one false positive was detected on the CS data set. . . . .	79

- 29 DLA acquisition patterns for 50%, 70% and 90% undersampling ratios. The horizontal axis represents the read direction, and the other two axes represent the phase encoding directions, as shown in the lower right corner. 81
- 30 Schematic representation of the ROI selection for signal intensity quantification. Two acquisitions were performed for each sample: a T2 weighted RARE (a), providing information about the sample anatomy and a T1 weighted FLASH (b) reflecting the intracellularly accumulated Mn<sup>2+</sup> ions. Neurons were manually segmented on the RARE image and the corresponding ROIs were co-registered with the FLASH image. The drawn ROIs correspond to neurons B9 (red), B6 (orange) and B3 (green). Spatial resolution: 25  $\mu\text{m}$  isotropic. . . . . 82
- 31 Fully encoded FLASH image (top left) and corresponding undersampled images after CS reconstruction (50%, 70% and 90% undersampling ratios). The CS images shown here were obtained by retrospectively undersampling the fully encoded k-space data. . . . . 83
- 32 Evaluation of the performance of DLA-CS for different undersampling ratios. (a). PCC between fully and CS encoded images as a function of undersampling ratio for one (red) and two (blue) repetitions. The PCC was calculated according to equation 100, over the ganglia region containing approximately 50 000 voxels. Error bars represent standard deviations. (b) Percentage signal intensity difference between the fully encoded and CS images (the data represented is the average over two repetitions). Blue and red marks correspond to cell bodies and water regions, respectively. Error bars represent standard deviations. The data was obtained from 6 samples. . . . . 84
- 33 Bland–Altman plots showing the difference in the normalized signal intensity values estimated from the fully sampled dataset and the 50% prospectively undersampled dataset (a) and the 50% retrospectively undersampled dataset (b). Each point corresponds to the signal intensity measured in one single neuron (2 samples, 10 neurons per sample). . . . . 85
- 34 Abdominal ganglion T2w image (*Aplysia* # 2) and ROIs: (a) the 3D representation showing the selected ROIs; (b)-(e) four slices from the T2w image; The information of the ROIs is shown in Tables 4, 5, and 6. The direction of the nerve (# 5) is (-0.993, 0.092, -0.075). The scale bar represents 260  $\mu\text{m}$ . . . . . 93
- 35 Large single cell neuron geometry. The cell outline was estimated from cell ROI#7 (see Table 4) (a). A nucleus with irregular shape was manually generated (b). The nucleus was manually placed inside the cell outline (c): cell nucleus is displayed in red while cytoplasm is displayed in green. Different cell sizes were generated by scaling the size of the nucleus to  $R_{\text{eff}}$  for the simulations (e.g  $R_{\text{eff}} = 60 \mu\text{m}$  (d) and  $R_{\text{eff}} = 40 \mu\text{m}$  (e) ). The satellite cell ( $R=3 \mu\text{m}$ ) (no nucleus) (f) with volume fraction of 0-5% surrounding the cell neurons (not accounted for in the simulations). . . . . 95
- 36 The bag cell neurons diameter histogram. . . . . 96

- 37 The dMRI signals for multiple diffusion times in: large cell neurons ROI # 1  $R_{\text{eff}} \approx 164.97 \mu\text{m}$  (a), large cell neurons ROI # 10  $R_{\text{eff}} \approx 101.34 \mu\text{m}$  (b). In each sub figure, from top to bottom we represent the scaled signals for  $\Delta$  from 5 ms to 25 ms. The different colors represent the different gradient directions, red, blue, and black for  $x$ ,  $y$ , and  $z$  directions, respectively. . . . . 98
- 38 The dMRI signals for multiple diffusion times in bag cell neurons ROI # 5. From top to bottom we represent the scaled signals for  $\Delta$  from 5 ms to 25 ms. The different colors represent the different gradient directions, red, blue, and black for  $x$ ,  $y$ , and  $z$  directions, respectively. . . . . 98
- 39 The dMRI signals for multiple diffusion times in nerve neurons with different direction. (a) the nerve ROI # 1: the nerve direction is mainly orientated in the  $x$  direction, and the  $y$  and  $z$  component are similar; (b) the nerve ROI # 8: the nerve direction has the same component in  $x$ ,  $y$ , and  $z$  directions; (c) the nerve ROI # 10: the nerve direction has a larger component in  $x$  and  $z$  directions, smaller in  $y$  component; In each sub-figure, from top to bottom we represent the signals for  $\Delta$  from 5 to 25 ms. The different colors represent the different gradient directions, red, blue, and black for  $x$ ,  $y$ , and  $z$  directions, respectively. . . . . 99
- 40 The measured ADC values are shown as colored markers (mean) with error bars (standard deviation) for the bag cell neurons (circle, N=11 ROIs), for the large cell neurons (triangle, N=22 ROIs) and for the nerves (diamond, N=13 ROIs). The solid lines represent linear fits of the measured data. The experimental ADC drops by 20.8%, 9.45% for bag cell neurons and large cell neurons, respectively, and the MD drops by 14.98% in the nerves. . . . . 100
- 41 (a) The positive correlation between effective radius ( $R_{\text{eff}}$ ) and estimated radius ( $R_{\text{est}}$ ) from 22 large cell neuron ROIs using the formula (63). (b) The relation between slope value  $A$  and  $R_{\text{eff}}$ . The cell size is severely underestimated,  $R_{\text{est}}$  is on average only 25% of  $R_{\text{eff}}$ . . . . . 101
- 42 Four generated domains of the same cell size and cell outline, based on three different shapes of nucleus (red) (a, b-c, and d) and different position of nucleus inside the cell neurons (b and c). The cell outlines are the same for the four geometries, which is generated from T2w image (large cell ROI#7). The volume fraction of the nucleus in all four domains is approximate 25%. . . . . 103
- 43 Slope  $A(R)$  as a function of the cell radius  $R$  (a); and the freedom coefficient  $B$  as a function of the cell radius  $R$  (b) for four identical domains with the same nucleus volume fraction (25%). The slope  $A$  depends stronger on the shape of the nucleus (Domain 1, 2-3, and 4) than the position of the nucleus inside the cell neurons (Domain 2, 3) while the coefficient  $B$  seems not to depend on the cell radius and the shape of the nucleus. . . . . 104

- 
- 44 (a) Slope  $A(R)$  as a function of the cell radius  $R$  for different nucleus volume fraction,  $VF_N$ . (b) The geometry domain in which the volume fraction of the nucleus is about 29% and the nucleus shape in this domain is similar with the nucleus shape in domain 1. . . . . 105
- 45 Averaged experimental ADC values (marker) with error bars representing the standard deviations (N=11 ROIs), and the optimal obtained simulated ADC (dashed lines) (a). The range of paired solutions ( $Dc, Dn$ ) are represented as circle in (b), the intrinsic diffusivity  $Dc$  and  $Dn$  are correlated by the formula  $Dc + 0.26 \times Dn = 1.1$ . The colored line in (a) corresponds to the colored marker represented in (b). . . . . 106
- 46 Assumed the axons distribution in the abdominal nerves are the same with the axons distribution in the buccal nerve 1b (a) and the buccal nerve ON (b). For both sub figures, the marker (with errors bar as the standard deviation) represent the averaged experimental MD of the 13 nerve ROIs; while the solid lines represent the good fits simulated mean diffusivities. The extracted intrinsic diffusivity of these solid lines are presented in table 10. . . . . 107
- 47 GPUs have thousands of cores to process parallel workloads efficiently. Source: <http://www.nvidia.com/object/what-is-gpu-computing.html> . . . 111

## List of Tables

1	The nerves (1b, 2b, 3b, ON, RN, CBC) of buccal ganglia. There are four type of axons with different range of axons diameter: type I , II , III and IV. The distribution of axons type of each nerve [56] were shown. . . . .	47
2	The RMSE of each winning DLA pattern for the library data. . . . .	80
3	Signal intensity errors ( $SI_{diff}$ ) and corresponding standard deviations (SD) between fully encoded and compressed sensing acquisitions for one and two repetitions calculated in cells and water ROIs. . . . .	84
4	The 22 ROIs of large cell neurons selected for analysis. The effective radius ( $R_{eff}$ ) estimated from the number of voxels ( $\#voxels$ ) in each ROI. . . . .	91
5	The 11 ROIs of bag cell neurons selected for analysis. . . . .	91
6	The selected 13 ROIs of the nerve with the approximate unit vector of the nerve direction (parallel direction) from visualization on the T2w image. . . . .	92
7	The distribution of volume fraction for each axon type in different buccal nerves (note that we assumed the same distribution for the abdominal ganglion) estimated from the literature [56] with particular choice of diameter in range mentioned before: $2R_I = 26 \mu m$ , $2R_{II} = 18 \mu m$ , $2R_{III} = 6 \mu m$ , and $2R_{IV} = 1 \mu m$ for axon type I, II, III, and IV, respectively. See more in Table 1 regarding the distribution of number of axons of each type within each nerve. . . . .	97
8	Mean and standard deviation (SD) of average ADC in bag cell neurons, large cell neurons, and nerve ROIs. The average ADC were observed drop by 20.8%, 9.45% and 14.98% for bag cell neurons, large cell neurons and nerve, respectively. . . . .	100
9	Fitting experimental $ADC(\Delta)$ by using the equation (63) ( $ADC = A\sqrt{\Delta} + B$ ) and using the equation (64) ( $ADC = AC_{\delta,\Delta} + B$ ) for 22 large cell neuron ROIs (ROI#). The effective radius ( $R_{eff}$ ) of each cell were estimated from T2w image. The cell radius estimated ( $R_{est}$ ) by using the equation (113). The error between fitting and data are shown in Err columns. There is not much difference on cell radius estimated between two prediction models. . . . .	102
10	The ranges of intrinsic diffusivity $Da$ ( $\mu m^2/ms$ ) which yield good fitting between the simulated mean diffusivity ( $MD_{simul}(Da)$ ) and the experimental mean diffusivity MD corresponds to six axons distributions of buccal ganglia nerves (1b, 2b, 3b, ON, RN, CBC). . . . .	106

## List of Algorithms

- 1 Nonlinear conjugate-gradient descent with backtracking line search for  $\ell_1$  reconstruction. . . . . 63
- 2 Split Bregman algorithm for  $\ell_1$  reconstruction. . . . . 66

## Index

Symbols			
2D		28, 70	
Fourier transform		29	
image reconstruction		29, 31	
imaging		30	
3D		28	
Fourier transform		29	
image reconstruction		29, 33	
3D DP-FISP		49	
<b>A</b>			
Acquisition time		35	
ADC	43, 46, 88, 94		
experimental		90	
Analog complex signal		26	
Anti-Parallel state		20	
Apparent Diffusion Coefficient		43	
ASW		76, 81	
<b>B</b>			
b-value		49, 90	
Bag cell neurons		90	
Bloch equation		21	
Bloch-Torrey equation		43	
Boltzmann (constant)		21	
Bulk magnetization		22	
<b>C</b>			
Cell segmentation		74	
algorithm		74	
Complex transverse component		24	
Compressed sensing		55	
reconstruction		60	
CS-FLASH		73, 78	
CS-RARE		76, 77	
pulse sequence		76	
<b>D</b>			
Diffusion encoding		42	
Diffusion limited aggregation		69	
Diffusion MRI		44	
diffusion tensor imaging		110	
Diffusion weighted		89	
Digital signal		26	
DLA		69, 85	
undersampling		69	
undersampling		69, 85	
undersampling pattern		70	
DLA-CS	74, 79, 81, 83, 84, 86		
FLASH		85	
undersampled		82	
dMRI	44, 45, 88, 90		
DP-FISP		49	
DTI		44	
DW-SE		49	
<b>E</b>			
Echo planar imaging		48	
Equilibrium magnetization		21, 22	
External magnetic field		21, 23	
<b>F</b>			
Fast Spin Echo		37	
Field-of-view		33	
FISP	40, 49		
sequence		40	
FLASH	39, 80, 82, 85		
pulse sequence		80	
pulse diagram		39	
sequence		39, 40	
Fourier transform		29, 61	
FOV		33, 81	
Free diffusion coefficient		43	
Frequency encoding		30	
gradient		30	
<b>G</b>			
Gradient		27	
-echo		39	
encoding		27	
fields		27	
Gradient Echo		38	
pulse diagram		38	
sequence		38	
Gradient Echo (GRE)		38	
GRE		38	
imaging		38	
Gyromagnetic ratio		20	
water proton		26	
<b>I</b>			
Image reconstruction		29	
Imaginary signal		25	
Incoherence	55, 58		
Intrinsic quantum property		20	
<b>K</b>			
k-space	28, 35, 73		

<b>L</b>		PSF	58, 59, 70
Larmor angular frequency	21, 22	Pulse program	72, 73
Larmor frequency	22, 25, 30, 32	Pulse sequence	20, 36, 72
Longitudinal magnetization	23	<b>R</b>	
Low pass filtering	25	Radial trajectory	53
<b>M</b>		Random walk	69
Magnetic	20	Rapid Spin Echo	37
field	20	RARE	37, 82, 85
moment	20	factor	37
Magnetic field gradients	27	sequence	37, 72
Magnetic quantum number	20	RE	67
Magnetic resonance microscopy	79	Read gradient	30
Magnetization	21, 23	Real signal	25
MEMRI	78, 79	Receiver coil	24
Monte Carlo	69	Resolution (of image)	33
MR	24	RF	22
imaging	30	channel	53
signal	24	coil	24
MRI	26	excitation (pulse)	30
pulse sequence	36	field	23
signal	29	pulse	22, 23, 36
Parallel imaging	110	RMSE	67, 80
MRM	45, 79	Rosette trajectory	53
<b>N</b>		<b>S</b>	
Nerve	90	Sample period	54
Net magnetization	21, 27	Sampling interval	54
Neutron	20	SE	36
NMR	20	Shannon sampling theorem	54
Non-Cartesian trajectory	53	Signal detection	24
Nuclear magnetic moment	21	Slice selection	30
Nyquist frequency	54	SNR	34, 86
Nyquist rate	54	Spare MRI	60
<b>O</b>		Spare MRI toolbox	62
OGSE	45	3D version	62
<b>P</b>		Sparse representation	55
Parallel imaging	52, 110	Sparse transform	61
Parallel state	20	Spin	20
Partial Fourier Imaging	52	-lattice relaxation	23, 27
PBS	88	-spin relaxation	23, 27, 28
pdf	58	angular momentum	20
PGSE	42, 92	down	20
sequence	45	echo sequence	27
time profile	42	quantum number	20
Phase 2 encoding	32	states	20
Phase encoding	30	up	20
Polynomial undersampling	58	Spin Echo	36
Proton	20	pulse diagram	37
		sequence	36
		Spin Echo (SE)	36

Spiral trajectory	53
Steady-state	38
Stochastic trajectory	53

### T

T <sub>1</sub> relaxation	49
T <sub>2</sub> relaxation	27
T2-weighted image	18, 37, 88, 89
Thermal equilibrium	20
TPSF	58, 59, 70
Transverse magnetization	23
Transverse relaxation time	24
Turbo Spin Echo	37

### U

Undersampled Fourier transform	58
--------------------------------	----

### W

Wavelet transform	56
-------------------	----

### X

x-gradient	27
------------	----

### Y

y-gradient	27
------------	----

### Z

z-gradient	27
Zeeman levels	21

## References

- [1] R. Brown, E. Haacke, Y. Cheng, M. Thompson, and R. Venkatesan, *Magnetic Resonance Imaging: Physical Principles and Sequence Design*. Wiley, 2014.
- [2] M. Bernstein, K. King, and X. Zhou, *Handbook of MRI Pulse Sequences*. Elsevier Science, 2004.
- [3] C. Westbrook, C. Roth, and J. Talbot, *MRI in Practice*. Wiley, 2011.
- [4] B. Dale, M. Brown, and R. Semelka, *MRI: Basic Principles and Applications*. Wiley, 2015.
- [5] J. Prince and J. Links, *Medical Imaging Signals and Systems*. Pearson Education, 2014.
- [6] R. Eisberg and R. Resnick, *Quantum physics of atoms, molecules, solids, nuclei, and particles*. Quantum Physics of Atoms, Molecules, Solids, Nuclei and Particles, Wiley, 1985.
- [7] W. S. Hinshaw and A. H. Lent, “An introduction to NMR imaging: From the Bloch equation to the imaging equation,” *Proceedings of The IEEE*, vol. 71, pp. 338–350, 1983.
- [8] R. Likes, “Moving gradient zeugmatography,” Dec. 22 1981. US Patent 4,307,343.
- [9] S. Ljunggren, “A simple graphical representation of fourier-based imaging methods,” *Journal of Magnetic Resonance (1969)*, vol. 54, no. 2, pp. 338 – 343, 1983.
- [10] D. B. Twieg, “The k-trajectory formulation of the NMR imaging process with applications in analysis and synthesis of imaging methods,” *Med Phys*, vol. 10, no. 5, pp. 610–621, 1983.
- [11] R. Ernst, G. Bodenhausen, and A. Wokaun, *Principles of Nuclear Magnetic Resonance in One and Two Dimensions*. International series of monographs on chemistry, Clarendon Press, 1987.
- [12] E. Brigham, *The fast Fourier transform*. Prentice-Hall signal processing series, Prentice-Hall, 1974.
- [13] E. Brigham, *The Fast Fourier Transform and Its Applications*. Prentice-Hall Signal Processing Series: Advanced monographs, Prentice Hall, 1988.
- [14] T. Körner, *Fourier Analysis*. Cambridge University Press, 1989.
- [15] L. Schröder and C. Faber, *In vivo NMR Imaging: Methods and Protocols*. Methods in Molecular Biology, Humana Press, 2011.
- [16] W. A. Edelstein, G. H. Glover, C. J. Hardy, and R. W. Redington, “The intrinsic signal-to-noise ratio in NMR imaging,” *Magn Reson Med*, vol. 3, pp. 604–618, Aug 1986.

- [17] D. Hoult and R. Richards, "The signal-to-noise ratio of the nuclear magnetic resonance experiment," *Journal of Magnetic Resonance*, vol. 24, no. 2, pp. 71–85, 1976. Magnetic Moments Groundbreaking papers from the pages of the Journal Magnetic Resonance - and recollections from the scientists behind them.
- [18] K. Ocegueda and A. Rodriguez, "A simple method to calculate the signal-to-noise ratio of a circular-shaped coil for MRI," *Concepts in Magnetic Resonance Part A*, vol. 28A, no. 6, pp. 422–429, 2006.
- [19] G. Johnson, Y. Z. Wadghiri, and D. H. Turnbull, "2D multislice and 3D MRI sequences are often equally sensitive," *Magnetic Resonance in Medicine*, vol. 41, no. 4, pp. 824–828, 1999.
- [20] N. Balu, B. Chu, T. S. Hatsukami, C. Yuan, and V. L. Yarnykh, "Comparison between 2D and 3D high-resolution black-blood techniques for carotid artery wall imaging in clinically significant atherosclerosis," *Journal of Magnetic Resonance Imaging*, vol. 27, no. 4, pp. 918–924, 2008.
- [21] E. L. Hahn, "Spin echoes," *Phys. Rev.*, vol. 80, pp. 580–594, Nov 1950.
- [22] H. Y. Carr and E. M. Purcell, "Effects of diffusion on free precession in nuclear magnetic resonance experiments," *Phys. Rev.*, vol. 94, pp. 630–638, May 1954.
- [23] J. Hennig, A. Nauerth, and H. Friedburg, "RARE imaging: a fast imaging method for clinical MR," *Magn Reson Med*, vol. 3, pp. 823–833, Dec 1986.
- [24] R. R. Ernst and W. A. Anderson, "Application of fourier transform spectroscopy to magnetic resonance," *Review of Scientific Instruments*, vol. 37, no. 1, pp. 93–102, 1966.
- [25] J. Frahm, A. Haase, and D. Matthaei, "Rapid three-dimensional MR imaging using the FLASH technique," *J Comput Assist Tomogr*, vol. 10, no. 2, pp. 363–368, 1986.
- [26] B. A. Hargreaves, "Rapid gradient-echo imaging," *J Magn Reson Imaging*, vol. 36, pp. 1300–1313, Dec 2012.
- [27] A. Oppelt, R. Graumann, H. Barfuss, H. Fischer, W. Hartl, and W. Shajor, "FISP – a new fast MRI sequence," *Electromedica*, no. 54, pp. 15–58, 1986.
- [28] E. O. Stejskal and J. E. Tanner, "Spin Diffusion Measurements: Spin Echoes in the Presence of a Time-Dependent Field Gradient," *The Journal of Chemical Physics*, vol. 42, no. 1, pp. 288–292, 1965.
- [29] P. T. Callaghan, *Principles of Nuclear Magnetic Resonance Microscopy*. Oxford science publications, Clarendon Press, 1993.
- [30] W. Price, *NMR Studies of Translational Motion: Principles and Applications*. Cambridge Molecular Science, Cambridge University Press, 2009.
- [31] H. C. Torrey, "Bloch equations with diffusion terms," *Phys. Rev.*, vol. 104, pp. 563–565, Nov 1956.

- [32] D. L. Bihan, E. Breton, D. Lallemand, P. Grenier, E. Cabanis, and M. Laval-Jeantet, "MR imaging of intravoxel incoherent motions: application to diffusion and perfusion in neurologic disorders.," *Radiology*, vol. 161, no. 2, pp. 401–407, 1986. PMID: 3763909.
- [33] Y. Assaf and P. J. Basser, "Composite hindered and restricted model of diffusion (charmed) MR imaging of the human brain," *NeuroImage*, vol. 27, no. 1, pp. 48 – 58, 2005.
- [34] Y. Assaf, T. Blumenfeld-Katzir, Y. Yovel, and P. J. Basser, "Axciliber: A method for measuring axon diameter distribution from diffusion MRI," *Magnetic Resonance in Medicine*, vol. 59, no. 6, pp. 1347–1354, 2008.
- [35] H. Zhang, P. L. Hubbard, G. J. Parker, and D. C. Alexander, "Axon diameter mapping in the presence of orientation dispersion with diffusion MRI," *NeuroImage*, vol. 56, no. 3, pp. 1301 – 1315, 2011.
- [36] D. C. Alexander, P. L. Hubbard, M. G. Hall, E. A. Moore, M. Ptito, G. J. Parker, and T. B. Dyrby, "Orientationally invariant indices of axon diameter and density from diffusion MRI," *NeuroImage*, vol. 52, no. 4, pp. 1374 – 1389, 2010.
- [37] E. Fieremans, J. H. Jensen, and J. A. Helpert, "White matter characterization with diffusional kurtosis imaging," *NeuroImage*, vol. 58, no. 1, pp. 177 – 188, 2011.
- [38] E. Panagiotaki, T. Schneider, B. Siow, M. G. Hall, M. F. Lythgoe, and D. C. Alexander, "Compartment models of the diffusion MR signal in brain white matter: A taxonomy and comparison," *NeuroImage*, vol. 59, no. 3, pp. 2241 – 2254, 2012.
- [39] S. N. Jespersen, C. D. Kroenke, L. Østergaard, J. J. Ackerman, and D. A. Yablonskiy, "Modeling dendrite density from magnetic resonance diffusion measurements," *NeuroImage*, vol. 34, no. 4, pp. 1473 – 1486, 2007.
- [40] O. Dietrich, A. Hubert, and S. Heiland, "Imaging cell size and permeability in biological tissue using the diffusion-time dependence of the apparent diffusion coefficient," *Physics in Medicine and Biology*, vol. 59, no. 12, p. 3081, 2014.
- [41] I. Lavdas, K. C. Behan, A. Papadaki, D. W. McRobbie, and E. O. Aboagye, "A phantom for diffusion-weighted MRI (DW-MRI)," *Journal of Magnetic Resonance Imaging*, vol. 38, no. 1, pp. 173–179, 2013.
- [42] J. S. Campbell, K. Siddiqi, V. V. Rymar, A. F. Sadikot, and G. B. Pike, "Flow-based fiber tracking with diffusion tensor and q-ball data: Validation and comparison to principal diffusion direction techniques," *NeuroImage*, vol. 27, no. 4, pp. 725 – 736, 2005.
- [43] A. Moussavi-Biugui, B. Stieltjes, K. Fritzsche, W. Semmler, and F. B. Laun, "Novel spherical phantoms for q-ball imaging under in vivo conditions," *Magnetic Resonance in Medicine*, vol. 65, no. 1, pp. 190–194, 2011.
- [44] P. Pullens, A. Roebroek, and R. Goebel, "Ground truth hardware phantoms for validation of diffusion-weighted MRI applications," *Journal of Magnetic Resonance Imaging*, vol. 32, no. 2, pp. 482–488, 2010.

- [45] A. R. Khan, A. Cornea, L. A. Leigland, S. G. Kohama, S. N. Jespersen, and C. D. Kroenke, “3D structure tensor analysis of light microscopy data for validating diffusion MRI,” *NeuroImage*, vol. 111, pp. 192 – 203, 2015.
- [46] S. N. Jespersen, L. A. Leigland, A. Cornea, and C. D. Kroenke, “Determination of axonal and dendritic orientation distributions within the developing cerebral cortex by diffusion tensor imaging,” *IEEE Trans Med Imaging*, vol. 31, pp. 16–32, Jan 2012.
- [47] K. Schilling, V. Janve, Y. Gao, I. Stepniewska, B. A. Landman, and A. W. Anderson, “Comparison of 3D orientation distribution functions measured with confocal microscopy and diffusion MRI,” *NeuroImage*, vol. 129, pp. 185 – 197, 2016.
- [48] I. O. Jelescu, M. Zurek, K. V. Winters, J. Veraart, A. Rajaratnam, N. S. Kim, J. S. Babb, T. M. Shepherd, D. S. Novikov, S. G. Kim, and E. Fieremans, “In vivo quantification of demyelination and recovery using compartment-specific diffusion MRI metrics validated by electron microscopy,” *NeuroImage*, vol. 132, pp. 104 – 114, 2016.
- [49] H. Wang, C. Lenglet, and T. Akkin, “Structure tensor analysis of serial optical coherence scanner images for mapping fiber orientations and tractography in the brain,” *Journal of Biomedical Optics*, vol. 20, no. 3, p. 036003, 2015.
- [50] P. P. Mitra, P. N. Sen, L. M. Schwartz, and P. Le Doussal, “Diffusion propagator as a probe of the structure of porous media,” *Phys. Rev. Lett.*, vol. 68, pp. 3555–3558, Jun 1992.
- [51] P. P. Mitra, P. N. Sen, and L. M. Schwartz, “Short-time behavior of the diffusion coefficient as a geometrical probe of porous media,” *Phys. Rev. B*, vol. 47, pp. 8565–8574, Apr 1993.
- [52] S. Schiavi, H. Haddar, and J.-R. Li, “Correcting the short time ADC formula to account for finite pulses,” ISMRM Workshop, 09 2016.
- [53] M. D. Does, E. C. Parsons, and J. C. Gore, “Oscillating gradient measurements of water diffusion in normal and globally ischemic rat brain,” *Magnetic Resonance in Medicine*, vol. 49, no. 2, pp. 206–215, 2003.
- [54] E. R. Kandel, , and I. Kupfermann, “The functional organization of invertebrate ganglia,” *Annual Review of Physiology*, vol. 32, no. 1, pp. 193–258, 1970. PMID: 4906119.
- [55] P. Conn and L. Kaczmarek, “The bag cell neurons of aplysia. a model for the study of the molecular mechanisms involved in the control of prolonged animal behaviors,” *Molecular neurobiology*, vol. 3, no. 4, p. 237–273, 1989.
- [56] C. Musio and C. Bedini, “Fine structure and axonal organization in the buccal ganglia nerves of aplysia (mollusca, gastropoda),” *Zoomorphology*, vol. 110, no. 1, pp. 17–26, 1990.
- [57] S. Grant, D. Buckley, S. Gibbs, A. Webb, and S. Blackband, “MR microscopy of multicomponent diffusion in single neurons,” *Magnetic Resonance in Medicine*, vol. 46, no. 6, pp. 1107–1112, 2001.

- [58] J. S. Schoeniger, N. Aiken, E. Hsu, and S. J. Blackband, "Relaxation-time and diffusion NMR microscopy of single neurons," *J Magn Reson B*, vol. 103, pp. 261–273, Mar 1994.
- [59] C. H. Lee, J. J. Flint, B. Hansen, and S. J. Blackband, "Investigation of the sub-cellular architecture of L7 neurons of *aplysia californica* using magnetic resonance microscopy (MRM) at 7.8 microns," *Scientific Reports*, vol. 5, pp. 11147 EP –, Jun 2015. Article.
- [60] E. W. Hsu, N. R. Aiken, and S. J. Blackband, "A study of diffusion isotropy in single neurons by using NMR microscopy," *Magn Reson Med*, vol. 37, pp. 624–627, Apr 1997.
- [61] I. Kupfermann, T. J. Carew, and E. R. Kandel, "Local, reflex, and central commands controlling gill and siphon movements in *aplysia*," *Journal of Neurophysiology*, vol. 37, no. 5, pp. 996–1019, 1974.
- [62] J. E. Blankenship and R. E. Coggeshall, "The abdominal ganglion of *aplysia brasiliana*: A comparative morphological and electrophysiological study, with notes on *a. dactylomela*," *Journal of Neurobiology*, vol. 7, no. 5, pp. 383–405, 1976.
- [63] R. E. Coggeshall, "A light and electron microscope study of the abdominal ganglion of *Aplysia californica*," *J. Neurophysiol.*, vol. 30, pp. 1263–1287, Nov 1967.
- [64] W. T. Frazier, E. R. Kandel, I. Kupfermann, R. Waziri, and R. E. Coggeshall, "Morphological and functional properties of identified neurons in the abdominal ganglion of *Aplysia californica*," *Journal of Neurophysiology*, vol. 30, no. 6, pp. 1288–1351, 1967.
- [65] J. T. Haskins, C. H. Price, and J. E. Blankenship, "A light and electron microscopic investigation of the neurosecretory bag cells of *Aplysia*," *J. Neurocytol.*, vol. 10, pp. 729–747, Oct 1981.
- [66] D. Gardner and E. R. Kandel, "Diphasic postsynaptic potential: A chemical synapse capable of mediating conjoint excitation and inhibition," *Science*, vol. 176, no. 4035, pp. 675–678, 1972.
- [67] D. Gardner, "Bilateral symmetry and interneuronal organization in the buccal ganglia of *aplysia*," *Science*, vol. 173, no. 3996, pp. 550–553, 1971.
- [68] J. Ono, "Localization and identification of neurons with cholecystokinin and gastrin-like immunoreactivity in wholemounts of *aplysia* ganglia," *Neuroscience*, vol. 18, p. 957–974, August 1986.
- [69] L. Lu, B. Erokwu, G. Lee, V. Gulani, M. A. Griswold, K. M. Dell, and C. A. Flask, "Diffusion-prepared fast imaging with steady-state free precession (DP-FISP): A rapid diffusion mri technique at 7 T," *Magnetic Resonance in Medicine*, vol. 68, no. 3, pp. 868–873, 2012.
- [70] I. O. Jelescu, D. L. Bihan, and L. Ciobanu, "3D DP-FISP for diffusion measurements in MR microscopy at ultra-high field," in *Proc. Intl. Soc. Mag. Reson. Med.*, vol. 21, 2013.

- [71] I. O. Jelescu, *Magnetic resonance microscopy of Aplysia neurons : studying neurotransmitter-modulated transport and response to stress*. PhD thesis, 2013. Thèse de doctorat dirigée par Le Bihan, Denis Physique Paris 11 2013.
- [72] G. Marseille, R. de Beer, M. Fuderer, A. Mehlkopf, and D. van Ormondt, “Nonuniform phase-encode distributions for MRI scan time reduction,” *Journal of Magnetic Resonance, Series B*, vol. 111, no. 1, pp. 70 – 75, 1996.
- [73] K. Scheffler and J. Hennig, “Reduced circular field-of-view imaging,” *Magnetic Resonance in Medicine*, vol. 40, no. 3, pp. 474–480, 1998.
- [74] C.-M. Tsai and D. G. Nishimura, “Reduced aliasing artifacts using variable-density k-space sampling trajectories,” *Magnetic Resonance in Medicine*, vol. 43, no. 3, pp. 452–458, 2000.
- [75] D. C. Peters, F. R. Korosec, T. M. Grist, W. F. Block, J. E. Holden, K. K. Vigen, and C. A. Mistretta, “Undersampled projection reconstruction applied to MR angiography,” *Magnetic Resonance in Medicine*, vol. 43, no. 1, pp. 91–101, 2000.
- [76] A. Greiser and M. von Kienlin, “Efficient k-space sampling by density-weighted phase-encoding,” *Magnetic Resonance in Medicine*, vol. 50, no. 6, pp. 1266–1275, 2003.
- [77] M. A. Griswold, P. M. Jakob, R. M. Heidemann, M. Nittka, V. Jellus, J. Wang, B. Kiefer, and A. Haase, “Generalized autocalibrating partially parallel acquisitions (GRAPPA),” *Magnetic Resonance in Medicine*, vol. 47, no. 6, pp. 1202–1210, 2002.
- [78] K. P. Pruessmann, M. Weiger, M. B. Scheidegger, and P. Boesiger, “SENSE: Sensitivity encoding for fast MRI,” *Magnetic Resonance in Medicine*, vol. 42, no. 5, pp. 952–962, 1999.
- [79] O. G. Gruschke, N. Baxan, L. Clad, K. Kratt, D. von Elverfeldt, A. Peter, J. Hennig, V. Badilita, U. Wallrabe, and J. G. Korvink, “Lab on a chip phased-array MR multi-platform analysis system,” *Lab Chip*, vol. 12, pp. 495–502, 2012.
- [80] K. Göbel, O. G. Gruschke, J. Leupold, J. S. Kern, C. Has, L. Bruckner-Tuderman, J. Hennig, D. von Elverfeldt, N. Baxan, and J. G. Korvink, “Phased-array of microcoils allows MR microscopy of ex vivo human skin samples at 9.4 T,” *Skin Research and Technology*, vol. 21, no. 1, pp. 61–68, 2015.
- [81] M. Lustig, D. Donoho, and J. M. Pauly, “Sparse MRI: The application of compressed sensing for rapid MR imaging,” *Magn. Reson. Med.*, vol. 58, no. 6, pp. 1182–1195, 2007.
- [82] T. Wech, A. Lemke, D. Medway, L.-A. Stork, C. A. Lygate, S. Neubauer, H. Köstler, and J. E. Schneider, “Accelerating cine-MR imaging in mouse hearts using compressed sensing,” *Journal of Magnetic Resonance Imaging*, vol. 34, no. 5, pp. 1072–1079, 2011.

- [83] T. Wech, D. Medway, C. Lygate, S. Neubauer, H. Kostler, and J. Schneider, "Accurate infarct-size measurements from accelerated, compressed sensing reconstructed cine-MRI images in mouse hearts," *Journal of Cardiovascular Magnetic Resonance*, vol. 14, no. Suppl 1, p. P57, 2012.
- [84] T. Wech, C. Lygate, S. Neubauer, H. Kostler, and J. Schneider, "Highly accelerated cardiac functional MRI in rodent hearts using compressed sensing and parallel imaging at 9.4T," *Journal of Cardiovascular Magnetic Resonance*, vol. 14, no. Suppl 1, p. P65, 2012.
- [85] S. Hu, M. Lustig, A. Balakrishnan, P. E. Z. Larson, R. Bok, J. Kurhanewicz, S. J. Nelson, A. Goga, J. M. Pauly, and D. B. Vigneron, "3D compressed sensing for highly accelerated hyperpolarized  $^{13}\text{C}$  MRSI with in vivo applications to transgenic mouse models of cancer," *Magnetic Resonance in Medicine*, vol. 63, no. 2, pp. 312–321, 2010.
- [86] Y. Wu, Y.-J. Zhu, Q.-Y. Tang, C. Zou, W. Liu, R.-B. Dai, X. Liu, E. X. Wu, L. Ying, and D. Liang, "Accelerated MR diffusion tensor imaging using distributed compressed sensing," *Magnetic Resonance in Medicine*, vol. 71, no. 2, pp. 763–772, 2014.
- [87] J. Paulsen, V. S. Bajaj, and A. Pines, "Compressed sensing of remotely detected MRI velocimetry in microfluidics," *Journal of Magnetic Resonance*, vol. 205, no. 2, pp. 196 – 201, 2010.
- [88] D. A. Feinberg, J. D. Hale, J. C. Watts, L. Kaufman, and A. Mark, "Halving MR imaging time by conjugation: demonstration at 3.5 kG.," *Radiology*, vol. 161, no. 2, pp. 527–531, 1986. PMID: 3763926.
- [89] C. Constantinides, *Magnetic Resonance Imaging: The Basics*. CRC Press, 2016.
- [90] K. G. Hollingsworth, "Reducing acquisition time in clinical MRI by data undersampling and compressed sensing reconstruction," *Physics in Medicine and Biology*, vol. 60, no. 21, p. R297, 2015.
- [91] A. M. BLAMIRE, "The technology of MRI — the next 10 years?," *The British Journal of Radiology*, vol. 81, no. 968, pp. 601–617, 2008. PMID: 18628329.
- [92] B. Keil, J. N. Blau, S. Biber, P. Hoecht, V. Tountcheva, K. Setsompop, C. Triantafyllou, and L. L. Wald, "A 64-channel 3T array coil for accelerated brain MRI," *Magnetic Resonance in Medicine*, vol. 70, no. 1, pp. 248–258, 2013.
- [93] M. Schmitt, A. Potthast, D. E. Sosnovik, J. R. Polimeni, G. C. Wiggins, C. Triantafyllou, and L. L. Wald, "A 128-channel receive-only cardiac coil for highly accelerated cardiac MRI at 3 tesla," *Magnetic Resonance in Medicine*, vol. 59, no. 6, pp. 1431–1439, 2008.
- [94] D. Weishaupt, J. Froehlich, D. Nanz, V. Köchli, K. Pruessmann, and B. Marincek, *How does MRI work?: An Introduction to the Physics and Function of Magnetic Resonance Imaging*. Lecture notes in mathematics, Springer Berlin Heidelberg, 2008.

- [95] J. F. Glockner, H. H. Hu, D. W. Stanley, L. Angelos, and K. King, "Parallel MR imaging: A user's guide," *RadioGraphics*, vol. 25, no. 5, pp. 1279–1297, 2005. PMID: 16160112.
- [96] D. K. Sodickson and W. J. Manning, "Simultaneous acquisition of spatial harmonics (SMASH): Fast imaging with radiofrequency coil arrays," *Magnetic Resonance in Medicine*, vol. 38, no. 4, pp. 591–603, 1997.
- [97] K. L. Wright, J. I. Hamilton, M. A. Griswold, V. Gulani, and N. Seiberlich, "Non-cartesian parallel imaging reconstruction," *Journal of Magnetic Resonance Imaging*, vol. 40, no. 5, pp. 1022–1040, 2014.
- [98] G. H. Glover and J. M. Pauly, "Projection reconstruction techniques for reduction of motion effects in MRI," *Magn Reson Med*, vol. 28, pp. 275–289, Dec 1992.
- [99] P. C. Lauterbur and P. C. Lauterbur, "Image formation by induced local interactions. Examples employing nuclear magnetic resonance. 1973," *Clin. Orthop. Relat. Res.*, pp. 3–6, Jul 1989.
- [100] C. H. Meyer, B. S. Hu, D. G. Nishimura, and A. Macovski, "Fast spiral coronary artery imaging," *Magn Reson Med*, vol. 28, pp. 202–213, Dec 1992.
- [101] C. B. Ahn, J. H. Kim, and Z. H. Cho, "High-speed spiral-scan echo planar NMR imaging-I," *IEEE Trans Med Imaging*, vol. 5, no. 1, pp. 2–7, 1986.
- [102] D. C. Noll, "Multishot rosette trajectories for spectrally selective MR imaging," *IEEE Transactions on Medical Imaging*, vol. 16, pp. 372–377, Aug 1997.
- [103] K. Scheffler and J. Hennig, "Frequency resolved single-shot MR imaging using stochastic k-space trajectories," *Magn Reson Med*, vol. 35, pp. 569–576, Apr 1996.
- [104] C. E. Shannon, "Communication in the presence of noise," *Proceedings of the IRE*, vol. 37, pp. 10–21, Jan 1949.
- [105] A. J. Jerri, "The shannon sampling theorem: Its various extensions and applications: A tutorial review," *Proceedings of the IEEE*, vol. 65, pp. 1565–1596, Nov 1977.
- [106] H. J. Landau, "Necessary density conditions for sampling and interpolation of certain entire functions," *Acta Mathematica*, vol. 117, no. 1, pp. 37–52, 1967.
- [107] M. Doneva, *Advances in compressed sensing for magnetic resonance imaging*. PhD thesis, 2011.
- [108] D. Donoho, "Compressed sensing," *Information Theory, IEEE Transactions on*, vol. 52, pp. 1289–1306, April 2006.
- [109] E. J. Candès, J. K. Romberg, and T. Tao, "Stable signal recovery from incomplete and inaccurate measurements," *Communications on Pure and Applied Mathematics*, vol. 59, no. 8, pp. 1207–1223, 2006.
- [110] E. J. Candès, J. Romberg, and T. Tao, "Robust uncertainty principles: Exact signal reconstruction from highly incomplete frequency information," *Information Theory, IEEE Transactions on*, vol. 52, no. 2, pp. 489–509, 2006.

- [111] E. J. Candès and M. B. Wakin, “An introduction to compressive sampling,” *IEEE Signal Processing Magazine*, vol. 25, pp. 21–30, March 2008.
- [112] M. Lustig, D. L. Donoho, J. M. Santos, and J. M. Pauly, “Compressed sensing MRI,” *IEEE Signal Processing Magazine*, vol. 25, pp. 72–82, March 2008.
- [113] L. I. Rudin, S. Osher, and E. Fatemi, “Nonlinear total variation based noise removal algorithms,” *Phys. D*, vol. 60, pp. 259–268, Nov. 1992.
- [114] M. W. Taubman, David SMarcellin, *JPEG2000 Image Compression Fundamentals, Standards and Practice*. Springer US, 2002.
- [115] M. Lustig, *SPARSE MRI*. PhD thesis, STANFORD UNIVERSITY, 2008.
- [116] E. J. Candès and J. K. Romberg, “Signal recovery from random projections,” in *Electronic Imaging 2005*, pp. 76–86, International Society for Optics and Photonics, 2005.
- [117] Y. Tsaig and D. L. Donoho, “Extensions of compressed sensing,” *Signal Processing*, vol. 86, no. 3, pp. 549 – 571, 2006. Sparse Approximations in Signal and Image Processing.
- [118] H. Yan, *Signal Processing for Magnetic Resonance Imaging and Spectroscopy*. Signal processing and communications, CRC Press, 2002.
- [119] L. He, T. C. Chang, S. Osher, T. Fang, and P. Speier, “MR image reconstruction by using the iterative refinement method and nonlinear inverse scale space methods,” *UCLA CAM Report*, vol. 6, p. 35, 2006.
- [120] L. He, T.-C. Chang, S. Osher, T. Fang, and P. Speier, “MR image reconstruction from undersampled data by using the iterative refinement procedure,” *PAMM*, vol. 7, no. 1, pp. 1011207–1011208, 2007.
- [121] V. P. Gopi, P. Palanisamy, K. A. Wahid, and P. Babyn, “MR image reconstruction based on iterative split bregman algorithm and nonlocal total variation,” *Computational and Mathematical Methods in Medicine*, vol. 2013, pp. 1–16, 2013.
- [122] T. Goldstein and S. Osher, “The split bregman method for l1-regularized problems,” *SIAM Journal on Imaging Sciences*, vol. 2, no. 2, pp. 323–343, 2009.
- [123] Y. Wang, J. Yang, W. Yin, and Y. Zhang, “A new alternating minimization algorithm for total variation image reconstruction,” *SIAM Journal on Imaging Sciences*, vol. 1, no. 3, pp. 248–272, 2008.
- [124] Y. Shi and Q. Chang, “Efficient algorithm for isotropic and anisotropic total variation deblurring and denoising,” *Journal of Applied Mathematics*, vol. 2013, pp. 1–14, 2013.
- [125] P. Montesinos, J. F. P. Abascal, L. Cussó, J. J. Vaquero, and M. Desco, “Application of the compressed sensing technique to self-gated cardiac cine sequences in small animals,” *Magnetic Resonance in Medicine*, vol. 72, no. 2, pp. 369–380, 2014.

- [126] Z. Zhu, K. Wahid, P. Babyn, and R. Yang, “Compressed Sensing-based MRI Reconstruction Using Complex Double-density Dual-tree DWT,” *Journal of Biomedical Imaging*, vol. 2013, pp. 10:10–10:10, Jan. 2013.
- [127] S. Ma, W. Yin, Y. Zhang, and A. Chakraborty, “An efficient algorithm for compressed MR imaging using total variation and wavelets,” in *Computer Vision and Pattern Recognition, 2008. CVPR 2008. IEEE Conference on*, pp. 1–8, IEEE, 2008.
- [128] T. Goldstein, “[http://www.ece.rice.edu/~tag7/tom\\_goldstein/split\\_bregman.html](http://www.ece.rice.edu/~tag7/tom_goldstein/split_bregman.html).”
- [129] S. Osher, M. Burger, D. Goldfarb, J. Xu, and W. Yin, “An Iterative Regularization Method for Total Variation-Based Image Restoration,” *Multiscale Modeling & Simulation*, vol. 4, no. 2, pp. 460–489, 2005.
- [130] Y. Wang, W. Yin, and Y. Zhang, “A fast algorithm for image deblurring with total variation regularization”, caam,” tech. rep., 2007.
- [131] W. Mendenhall, R. Beaver, and B. Beaver, *Introduction to Probability and Statistics*. Cengage Learning, 2012.
- [132] K. V. Bulusu, S. Hussain, and M. W. Plesniak, “Determination of secondary flow morphologies by wavelet analysis in a curved artery model with physiological inflow,” *Experiments in Fluids*, vol. 55, no. 11, p. 1832, 2014.
- [133] T. A. Witten and L. M. Sander, “Diffusion-Limited Aggregation, a Kinetic critical phenomenon,” *Phys. Rev. Lett.*, vol. 47, pp. 1400–1403, Nov 1981.
- [134] P. Montesinos, J. Abascal, C. Chavarrías, J. Vaquero, and M. Desco, “Compressed Sensing for Cardiac MRI Cine Sequences: A Real Implementation on a Small-Animal Scanner,” in *XIII Mediterranean Conference on Medical and Biological Engineering and Computing 2013* (L. M. Roa Romero, ed.), vol. 41 of *IFMBE Proceedings*, pp. 214–217, Springer International Publishing, 2014.
- [135] K.-V. Nguyen, J.-R. Li, G. Radecki, and L. Ciobanu, “DLA based compressed sensing for high resolution MR microscopy of neuronal tissue,” *Journal of Magnetic Resonance*, vol. 259, pp. 186 – 191, 2015.
- [136] I. O. Jelescu, R. Nargeot, D. L. Bihan, and L. Ciobanu, “Highlighting manganese dynamics in the nervous system of *aplysia californica* using MEMRI at ultra-high field,” *NeuroImage*, vol. 76, no. 0, pp. 264 – 271, 2013.
- [137] G. Radecki, R. Nargeot, I. O. Jelescu, D. Le Bihan, and L. Ciobanu, “Functional magnetic resonance microscopy at single-cell resolution in *Aplysia californica*,” *Proceedings of the National Academy of Sciences*, vol. 111, no. 23, pp. 8667–8672, 2014.
- [138] A. Miranda Neto, A. Correa Victorino, I. Fantoni, D. Zampieri, J. Ferreira, and D. Lima, “Image processing using Pearson’s correlation coefficient: Applications on autonomous robotics,” in *Autonomous Robot Systems (Robotica), 2013 13th International Conference on*, pp. 1–6, April 2013.

- [139] R. E. London, G. Toney, S. A. Gabel, and A. Funk, "Magnetic resonance imaging studies of the brains of anesthetized rats treated with manganese chloride," *Brain Res. Bull.*, vol. 23, pp. 229–235, Sep 1989.
- [140] C. A. Massaad and R. G. Pautler, "Manganese-enhanced magnetic resonance imaging (MEMRI)," *Methods Mol. Biol.*, vol. 711, pp. 145–174, 2011.
- [141] N. Baxan, U. Kahlert, J. Maciaczyk, G. Nikkhah, J. Hennig, and D. von Elverfeldt, "Microcoil-based MR phase imaging and manganese enhanced microscopy of glial tumor neurospheres with direct optical correlation," *Magnetic Resonance in Medicine*, vol. 68, no. 1, pp. 86–97, 2012.
- [142] P. Pandit, J. Rivoire, K. King, and X. Li, "Accelerated  $t1\rho$  acquisition for knee cartilage quantification using compressed sensing and data-driven parallel imaging: A feasibility study," *Magnetic Resonance in Medicine*, vol. 75, no. 3, pp. 1256–1261, 2016.
- [143] W. Li, M. Griswold, and X. Yu, "Fast cardiac  $t1$  mapping in mice using a model-based compressed sensing method," *Magnetic Resonance in Medicine*, vol. 68, no. 4, pp. 1127–1134, 2012.
- [144] M. M. Mukaka, "Statistics corner: A guide to appropriate use of correlation coefficient in medical research," *Malawi Med J*, vol. 24, pp. 69–71, Sep 2012.
- [145] C. Prieto, M. E. Andia, C. von Bary, D. C. Onthank, T. Schaeffter, and R. M. Botnar, "Accelerating three-dimensional molecular cardiovascular MR imaging using compressed sensing," *Journal of Magnetic Resonance Imaging*, vol. 36, no. 6, pp. 1362–1371, 2012.
- [146] T. M. Shepherd, P. E. Thelwall, G. J. Stanisiz, and S. J. Blackband, "Aldehyde fixative solutions alter the water relaxation and diffusion properties of nervous tissue," *Magnetic Resonance in Medicine*, vol. 62, no. 1, pp. 26–34, 2009.
- [147] H. Berg, *Random Walks in Biology*. Princeton paperbacks, Princeton University Press, 1993.
- [148] J. Zhong and J. C. Gore, "Studies of restricted diffusion in heterogeneous media containing variations in susceptibility," *Magnetic Resonance in Medicine*, vol. 19, no. 2, pp. 276–284, 1991.
- [149] J. E. Tanner and E. O. Stejskal, "Restricted Self-Diffusion of Protons in Colloidal Systems by the Pulsed-Gradient, Spin-Echo Method," *JCP*, vol. 49, pp. 1768–1777, Aug. 1968.
- [150] D. S. Grebenkov, "NMR survey of reflected Brownian motion," *Reviews of Modern Physics*, vol. 79, no. 3, p. 1077, 2007.
- [151] T. Weber, C. H. Ziener, T. Kampf, V. Herold, W. R. Bauer, and P. M. Jakob, "Measurement of apparent cell radii using a multiple wave vector diffusion experiment," *Magnetic Resonance in Medicine*, vol. 61, no. 4, pp. 1001–1006, 2009.

- [152] D. Le Bihan, J.-F. Mangin, C. Poupon, C. A. Clark, S. Pappata, N. Molko, and H. Chabriat, “Diffusion tensor imaging: Concepts and applications,” *Journal of Magnetic Resonance Imaging*, vol. 13, no. 4, pp. 534–546, 2001.
- [153] S. Mori and J. Zhang, “Diffusion Tensor Imaging (DTI) ,” in *Encyclopedia of Neuroscience* (L. R. Squire, ed.), pp. 531 – 538, Oxford: Academic Press, 2009.
- [154] P. Basser, J. Mattiello, and D. LeBihan, “MR diffusion tensor spectroscopy and imaging,” *Biophysical Journal*, vol. 66, no. 1, pp. 259 – 267, 1994.
- [155] P. B. Kingsley, “Introduction to diffusion tensor imaging mathematics: Part I. tensors, rotations, and eigenvectors,” *Concepts in Magnetic Resonance Part A*, vol. 28A, no. 2, pp. 101–122, 2006.
- [156] D. V. Nguyen, J.-R. Li, D. Grebenkov, and D. L. Bihan, “A finite elements method to solve the bloch–torrey equation applied to diffusion magnetic resonance imaging,” *Journal of Computational Physics*, vol. 263, pp. 283 – 302, 2014.
- [157] L. Beltrachini, Z. A. Taylor, and A. F. Frangi, “A parametric finite element solution of the generalised bloch–torrey equation for arbitrary domains,” *Journal of Magnetic Resonance*, vol. 259, pp. 126 – 134, 2015.
- [158] J.-R. Li, D. Calhoun, C. Poupon, and D. L. Bihan, “Numerical simulation of diffusion MRI signals using an adaptive time-stepping method,” *Physics in Medicine and Biology*, vol. 59, pp. 441–454, 12 2013.
- [159] S. Chabert, N. Molko, Y. Cointepas, P. Le Roux, and D. Le Bihan, “Diffusion tensor imaging of the human optic nerve using a non-CPMG fast spin echo sequence,” *Journal of Magnetic Resonance Imaging*, vol. 22, no. 2, pp. 307–310, 2005.
- [160] A. F. Frohlich, J. hlich, L. Ostergaard, and V. G. Kiselev, “Effect of impermeable boundaries on diffusion-attenuated MR signal,” *Journal of magnetic resonance (San Diego, Calif. : 1997)*, vol. 179, p. 223—233, April 2006.
- [161] J. H. Jensen, J. A. Helpert, A. Ramani, H. Lu, and K. Kaczynski, “Diffusional kurtosis imaging: The quantification of non-gaussian water diffusion by means of magnetic resonance imaging,” *Magnetic Resonance in Medicine*, vol. 53, no. 6, pp. 1432–1440, 2005.
- [162] J. H. Jensen and J. A. Helpert, “MRI quantification of non-Gaussian water diffusion by kurtosis analysis,” *NMR in Biomedicine*, vol. 23, no. 7, pp. 698–710, 2010.
- [163] R. Gillies, *NMR In Physiology and Biomedicine*. Elsevier Science, 2013.
- [164] M. Webster, K. L. Witkin, and O. Cohen-Fix, “Sizing up the nucleus: nuclear shape, size and nuclear-envelope assembly,” *Journal of Cell Science*, vol. 122, no. 10, pp. 1477–1486, 2009.
- [165] OpenMP, “<https://computing.llnl.gov/tutorials/openmp>.”
- [166] B. Chapman, G. Jost, and R. van der Pas, *Using OpenMP: Portable Shared Memory Parallel Programming*. No. Volume 10 in Scientific Computation Series, MIT Press, 2008.

**Titre:** Microscopie du tissu neuronal par IRM: accélération des acquisitions, modélisation et validation expérimentale de la diffusion de l'eau

**Mots clé:** imagerie par résonance magnétique (IRM) , échantillonnage compressif, microscopie par résonance magnétique (MRM), segmentation cellulaire, agrégation limitée par la diffusion (DLA), variation totale

**Résumé:** La technique d'acquisition comprimée ou compressed sensing (CS) exploite la compressibilité de différents types d'images pour reconstruire des données sous-échantillonnées sans perte d'informations. Cette technique peut être appliquée à l'IRM pour réduire les temps d'acquisition. CS est basée sur trois composantes majeures: (1) la représentation parcimonieuse du signal dans un domaine de transformation, (2) des mesures incohérentes et (3) une méthode de reconstruction non-linéaire avec une contrainte de parcimonie. Si le nombre total de points dans une image est plus grand que quatre fois le nombre de coefficients de décomposition alors la reconstruction de données sous-échantillonnées est réalisable. Dans la partie IV de cette thèse, nous proposons un nouveau modèle de sous-échantillonnage basé sur la théorie de l'agrégation limitée par la diffusion (DLA) et montrons qu'il est plus performant que la méthode de sous-échantillonnage aléatoire. Le modèle de sous-échantillonnage DLA a été utilisé pour implémenter la technique de CS pour l'imagerie haute résolution pondérée T2 et T1 sur un champ magnétique très intense (17.2T). Pour chacune des pondérations, le temps d'acquisition a été réduit de 50 % tout en conservant la qualité des images en termes de résolution spatiale, rapport contraste sur bruit et quantification de l'intensité du signal. Les deux nouvelles séquences d'impulsions CS (csRARE et csFLASH) ont été implémentées sur le logiciel commercial ParaVision 5.1. La partie V de la thèse est centrée sur l'étude de la dépendance en temps de la diffusivité dans le ganglion abdominal de l'*Aplysia californica*. Le ganglion abdominal de l'aplysie a été choisi pour cette étude d'imagerie car l'IRM à haute résolution permet la description anatomique fine du réseau cellulaire (taille des neurones individuels et orientation des axones). Utiliser les tissus neuronaux de l'aplysie pour étudier la relation entre la structure cellulaire et le signal d'IRM de diffusion peut permettre de comprendre cette relation pour des organismes plus complexes. Le signal d'IRM de diffusion (IRMd) a été mesuré à différents temps de diffusion dans le ganglion abdominal et des simulations de la diffusion de l'eau dans des géométries obtenues à partir de la segmentation d'images haute résolution pondérées T2 et l'incorporation d'informations sur la structure cellulaire trouvées dans la littérature ont été réalisées. Pour comparer le signal d'IRMd dans des neurones composés d'une seule cellule avec le signal des simulations numériques, des cellules de grande taille ont été segmentées à partir d'images anatomiques pondérées T2. A l'intérieur des cellules, un noyau à forme irrégulière a été généré manuellement (environ 25-30% en fraction volumique). Les petites cellules ont été modélisées comme des petites sphères avec un petit noyau sphérique concentrique (environ 25% en fraction volumique). Le nerf a été modélisé en combinant des axones (cylindres) de différents diamètres en cohérence avec la littérature. Le signal numérique d'IRMd a été simulé en résolvant l'équation de Bloch-Torrey pour les domaines géométriques décrits ci-dessus. En fittant le signal expérimental avec le signal simulé pour différents types de cellules comme les grandes cellules neuronales (diamètre entre 150 et 420  $\mu\text{m}$ ), des agrégats de petites cellules neuronales ayant la forme d'un sac (jusqu'à 400 cellule chez l'aplysie adulte dans chaque sac avec une taille cellulaire entre 40 et 100  $\mu\text{m}$  de diamètre), des nerfs (groupes d'axones de forme cylindrique avec un diamètre de moins de 1 à 25  $\mu\text{m}$ ) pour une grande gamme de temps de diffusion, nous avons obtenu des estimations du coefficient de diffusion intrinsèque dans le noyau et le cytoplasme (pour les neurones) et le coefficient de diffusion intrinsèque dans les axones (pour les nerfs). Nous avons aussi évalué la pertinence d'utiliser une formule préexistante décrivant la dépendance en temps du coefficient de diffusion pour estimer la taille des cellules.



**Title:** MR microscopy of neuronal tissue: acquisition acceleration, modeling and experimental validation of water diffusion

**Keywords:** magnetic resonance imaging (MRI), compressed sensing (CS), magnetic resonance microscopy (MRM), cell segmentation, diffusion limited aggregation (DLA), total variation (TV)

**Abstract:** Compressed sensing (CS) exploits the compressibility of different types of images to reconstruct undersampled data without loss of information. The technique can be applied to MRI to reduce the acquisition times. The CS is based on three major components: (1) sparsity representation of the signal in some transform domain, (2) incoherent measurements, and (3) sparsity-constrained nonlinear reconstruction method. If the total number of points in the image is larger than four times the number of sparse coefficients then the reconstruction of undersampled data is feasible. In the part IV of this thesis, we propose a new undersampling model based on the diffusion limited aggregation (DLA) theory and show that it performs better than the random variable undersampling method. The DLA undersampling model was used to implement the CS for T2-weighted and T1-weighted high resolution imaging at the ultra-high magnetic field (17.2T). In both cases, the acquisition time was reduced by 50% while maintaining the quality of the images in terms of spatial resolution, contrast to noise ratio, and signal intensity quantification. Both new CS pulse sequences (csRARE and csFLASH) were implemented in ParaVision 5.1 commercial software.

In the part V of the thesis is focused on the study of the time-dependent diffusivity in the abdominal ganglion of *Aplysia californica*. The *Aplysia* abdominal ganglion was chosen in this imaging study because high resolution MR imaging allows the fine anatomical description of the cellular network (size of individual neurons and orientation of axons). Using the *Aplysia* ganglia to study the relationship between the cellular structure and the diffusion MRI signal can shed light on this relationship for more complex organisms. We measured the dMRI signal at several diffusion times in the abdominal ganglion and performed simulations of water diffusion in geometries obtained after segmenting high resolution T2-weighted images and incorporating known information about the cellular structure from the literature. To match the dMRI signal in the single cell neurons with numerical simulations signal, the large cell outline was segmented from the anatomical T2 weighted image. Inside this cell shape, an irregularly shaped nucleus was manually generated (around 25-30% volume fraction). The small cells were modeled as small spheres with a smaller concentric spherical nucleus (around 25% volume fraction). The nerve was modeled by combining axons (cylinders) of different diameters consistent with the literature. The numerical dMRI signal can be simulated by solving Bloch-Torrey equation under the geometries domain described above. By fitting the experimental signal to the simulated signal for several types of cells such as: large cell neurons (diameter between 150  $\mu\text{m}$  and 420  $\mu\text{m}$ ); cluster of small neuron cells gathered in the shape of a bag (up to 400 cells in adult *Aplysia* in each bag with cell size between 40  $\mu\text{m}$  to 100  $\mu\text{m}$  in diameter); and nerves (group of axons cylindrical shape diameter from less than 1  $\mu\text{m}$  to 25  $\mu\text{m}$ ) at a wide range of diffusion times, we obtained estimates of the intrinsic diffusion coefficient in the nucleus and the cytoplasm (for cell neurons) and the intrinsic diffusion coefficient in the axons (for the nerves). We also evaluated the reliability of using an existing formula for the time-dependent diffusion coefficient to estimate cell size.

